U.PORTO
FEUP FACULDADE DE ENGENHARIA
UNIVERSIDADE DO PORTO

Design, Analysis and Optimization of a tail for a civil UAV

Diogo Pinheiro Rodrigues

Thesis submitted to Universidade do Porto – Faculdade de Engenharia
in partial fulfillment of the requirements for the degree of
Master in Mechanical Engineering

Supervisor
Prof. Dr. Volnei Tita

Company Supervisors
Eng. Carlos Fonte
Eng. Nuno Matos

Mestrado em Engenharia Mecânica (M.EM)
Departamento de Engenharia Mecânica (DEMec)
Faculdade de Engenharia (FEUP)
Universidade do Porto (UP)

© Porto, 2024

"All our dreams can come true, if we have the courage to pursue them"

Walt Disney

Acknowledgments

Firstly, I would like to express my sincere gratitude to engineers Carlos Fonte and Nuno Costa, my mentors within the company throughout this period, for the good moments, support and advice, and for being available at all times to contribute to my growth as an engineer and as a person.

I wish to extend my sincere thanks to Prof. Dr. Volnei Tita for his clear and dedicated guidance throughout my master's degree, culminating in the guidance of this thesis, where he was available from the first moment, bringing his wealth of knowledge to each meeting, and was fundamental in guiding the decision-making process.

I would like to extend my appreciation to my colleagues in this adventure and future engineers Dinis Piris and João Salvador, who accompanied and contributed to the success of this project, providing peace of mind and joy in the most difficult moments, as well as allowing the optimization tool to perform better in the end.

I extend my gratitude to my family, especially my father, mother and brothers, who saw me grow up and became the man I am today, for their love and dedication, unconditionally supporting all my efforts and decisions throughout this journey, allowing me to dream and fight for my goals. A special acknowledgement to my girlfriend, who has been a fundamental part of completing this stage, for her love and patience, not letting me give up in my weakest moments, advising me and bringing a smile to my face in every circumstance.

Finally, I'd like to thank all my friends, from the earliest friendships to those made during my time at university and in the Formula Student project, for the good times and memories that will never be forgotten, which have been fundamental in making this whole journey more joyful and memorable.

Abstract

This thesis, developed in collaboration with Tekever, a leading Portuguese company in unmanned aerial systems (UAS), focuses on the structural design and optimization of the tail and boom components of the ARX, Tekever's future UAV, with a focus on versatile missions, including ISAR operations and cargo transportation, with an expected launch in 2025. The main objective of this research is to design a lightweight and structurally robust tail and boom system, in compliance with ASTM F3116-18 standards, while simultaneously optimizing operational efficiency and performance using heuristic optimization tools.

Within the scope of optimizing weight efficiency, the ARX's tail and boom structure was successfully designed, analyzing different structural reinforcements for the boom, different positions for the main spar, comparisons between C and I profiles for spar applications, as well as a study of the impact of reducing the number of ribs in the vertical and horizontal stabilizer and the feasibility of a single spar structure, for 6 critical load cases identified through the aircraft's V-n diagram and calculated with the help of the XFLR5 softwere. Culminating in an iterative process with a final result lighter while maintaining its structural efficiency.

Additionally, the project aims to validate and improve in terms of computational efficiency a heuristic algorithm optimization tool initiated in the 2022/2023 academic year to predict the minimum number of layers and the optimal fiber orientations for the composite material used in the critical points of the Tail boom structure developed for the ARX seeking better performance and structural optimization. The tool is based on a unique evolutionary algorithm to explore the search space, with limits based on Hashin matrix and fiber failure indices. To accommodate these limitations, a surrogate model was developed, combining the Abaqus finite element program and Python, building the training data for the surrogate model using the Latin hypercube sampling technique and a Gaussian regression model. As a final phase, it was possible to obtain an approximate 73% computational efficiency over the initial tool, through the fine-tuning of the genetic algorithm and Gaussian regression, greater flexibility in applying the tool to complex cases after direct implementation of .Cae files and an improved condition of the failure criterion and studying the application of LAr05 and Hashin criteria, culminating in an ARX tail boom structure 14% lighter than the initial reference.

Overall, this research not only advances the structural design of Tekever's ARX but also contributes to the broader field of UAV development by demonstrating effective methodologies for lightweight, high-performance aerostructure optimization.

Keywords: Composite Materials, Finite Element Analysis, Genetic Algorithms, Optimization Tool, Structural Analysis, Structural Optimization,Tail-Boom Structure, Unmanned Aerial Vehicle, Weight Reduction.

Resumo

Esta tese, desenvolvida em colaboração com a Tekever, uma empresa portuguesa líder em sistemas aéreos não tripulados (UAS), centra-se na conceção estrutural e otimização dos componentes da Tail e do boom do ARX, o futuro UAV da Tekever, com foco em missões versáteis, incluindo operações ISAR e transporte de carga, com lançamento previsto para 2025. O principal objetivo desta investigação é conceber um sistema de Tail e Boom leve e estruturalmente robusto, em conformidade com a norma ASTM F3116-18, optimizando simultaneamente a eficiência e o desempenho operacionais utilizando ferramentas de otimização heurística.

No âmbito da otimização da eficiência de peso, foi projectada com sucesso a estrutura da Tail e do boom do ARX, analisando diferentes reforços estruturais para o boom, diferentes posições para a longarina principal, comparações entre perfis C e I para aplicação de longarinas, bem como um estudo do impacto da redução do número de nervuras no estabilizador vertical e horizontal e a viabilidade de uma estrutura de longarina única, para 6 casos críticos de carga identificados através do diagrama V-n da aeronave e calculados com o auxílio do softwere XFLR5. Culminando num processo iterativo com um resultado final mais leve, mantendo a sua eficiência estrutural.

Adicionalmente, o projeto visa validar e melhorar em termos de eficiência computacional uma ferramenta de otimização de algoritmos heurísticos iniciada no ano letivo de 2022/2023 para prever o número mínimo de camadas e as orientações óptimas das fibras para o material compósito utilizado nos pontos críticos da estrutura do Tail boom desenvolvida para o ARX, procurando um melhor desempenho e otimização estrutural. A ferramenta baseia-se num algoritmo evolutivo único para explorar o espaço de pesquisa, com limites baseados nos índices de falha de Hashin para matriz e fibras. Para acomodar estas limitações, foi desenvolvido um modelo substituto, combinando o programa de elementos finitos Abaqus e Python, construindo os dados de treino para o modelo substituto utilizando a técnica de amostragem do hipercubo latino e um modelo de regressão gaussiano. Como fase final, foi possível obter uma eficiência computacional de cerca de 73% em relação à ferramenta inicial, através da afinação do algoritmo genético e da regressão gaussiana, uma maior flexibilidade na aplicação da ferramenta a casos complexos após a implementação direta de ficheiros .Cae e uma melhoria da condição do critério de falha e do estudo da aplicação dos critérios LAr05 e Hashin, culminando numa estrutura Tail-Boom para o ARX 14% mais leve que a referência inicial.

De um modo geral, esta investigação não só faz avançar a conceção estrutural do ARX da Tekever, como também contribui para o domínio mais vasto do desenvolvimento de UAV´s, demonstrando metodologias eficazes para a otimização de aeroestruturas de elevado desempenho.

Keywords: Algoritmo Genético,Análise de Elementos Finitos,Análise Estrutural,Estrutura Tail-Boom,Ferramenta de Otimização,Materiais Compositos,Otimização Estrutural,Redução de Peso,Veículo Aéreo Não Tripulado

Abbreviations

AIS Automatic Identification System

ASTM American society for Testing and Materials

AMC Acceptable Means of Compliance

AC Advisory Circulars

ATS Air Traffic Service

BVLOS Beyond Visual Line of Sight

CAD Computer Aided Design

CAE Computer Aided Engineering

CD Coefficient of Drag

CFD Computer Fluid Dynamics

CFRP Carbon Fiber Reinforced Polymer

CL Coefficient of Lift

CPU Central Processing Unit

CS Certification Specifications

DoE Design of Experiments

EASA European Union Aviation Safety Agency

EO Electro-Optical

ERP Emergency Response Plan

EU European Union

FAA Federal Aviation Administration

FAR Federal Aviation Regulations

FEA Finite Element Analysis

FEM Finite Element Model

GA Genetic Algorithm

GPR Gaussian Regression Regression

ICAO International Civil Aviation Organization

IR Infrared

ISTAR Intelligence Surveillance Target Acquisition and Reconnaissance

JAR Joint Aviation Requirements

LARC Lamina Analysis and Research Composite

LM Loyal Wingman

LHS Latin Hypercubic sampling

MSE Mean Squared Error

MTOM Maximum take-off mass

NACA National Advisory Committee for Aeronautics

NASA National Aeronautics and Space Administration

OEM Original Equipment Manufactures

RSS Residual Sum of Squares

SAR Synthetic Aperture Radar

SMT Surrogate Model Toolbox

TSAIH Tsai Hill failure index

UAS Unmanned Aerial System

UAV Unmanned Aerial Vehicle

UCAV Unmanned Combat Aerial Vehicle

US United States

Va Design Maneuvering Speed

Vc Design Cruising Speed

Vd Maximum Dive Speed

VTOL Vertical Take-Off and Landing

WWFE World-Wide Failure Exercise

Contents

Contents xi

List of Figures xv

List of Tables xix

1 Introduction 1
- 1.1 Motivation . . . 1
- 1.2 Objectives . . . 2
- 1.3 Structure of the Thesis . . . 2

2 Literature review 3
- 2.1 Unmanned Aerial Vehicles (UAVs) . . . 3
  - 2.1.1 UAVs Review . . . 3
  - 2.1.2 UAVs Fixed-wings evolution in patrol and surveillance . . . 5
  - 2.1.3 UAVs fixed-wings tail typs . . . 6
  - 2.1.4 UAVs fixed-wings Certification . . . 9
- 2.2 Composite materials . . . 11
  - 2.2.1 Evolution and introduction in aeronautics . . . 11
  - 2.2.2 Certification of composite materials . . . 13
  - 2.2.3 Design UAV . . . 15
  - 2.2.4 Failure Mechanisms in Composite . . . 17
- 2.3 Optimization . . . 22
  - 2.3.1 Genetic Algorithm . . . 24
- 2.4 Surrogate model . . . 31
  - 2.4.1 Regression methods . . . 34
- 2.5 Aircraft sizing . . . 37
  - 2.5.1 V-n Diagram . . . 37

3 Tail-Boom Concept Design 39
- 3.1 Tail configuration concept . . . 39
- 3.2 Structural Design concept . . . 41
  - 3.2.1 Tail Structural Design . . . 41
  - 3.2.2 ARX tail Structure . . . 44
    - 3.2.2.1 Iteration 1 . . . 44
    - 3.2.2.2 Iteration 2 . . . 45
  - 3.2.3 Boom Structural Design . . . 46
  - 3.2.4 ARX Boom Structure . . . 48
    - 3.2.4.1 Boom with Internal Pipe Iteration 1 . . . 48

3.2.4.2 Boom with Stringers Iteration 1 . . . 48
3.2.4.3 Boom with Internal Pipe and Stringers Iteration 1 . . . 49
3.2.4.4 Boom with Internal Pipe Iteration 2 . . . 49
3.2.4.5 Boom with Stringers Iteration 2 . . . 50
3.2.4.6 Boom with Internal Pipe and Stringers Iteration 2 . . . 50

4 ARX Load analysis 51
4.1 Load Case . . . 51
4.1.1 V-n diagram . . . 52
4.1.1.1 Maneuver . . . 52
4.1.1.2 Gust . . . 55
4.1.1.3 Total Envelope . . . 56
4.1.2 XFRL5 load case analysis . . . 56
4.1.2.1 Aerofoil analysis . . . 56
4.1.2.2 ARX XFLR5 design . . . 59
4.1.2.3 Load cases calculation for Horizontal stabilizer . . . 63
4.1.2.4 Load cases calculation for Vertical stabilizer . . . 69
4.2 Inertia Loads . . . 71
4.2.1 Inertia loads horizontal stabilizer . . . 71
4.2.2 Inertia loads vertical stabilizer . . . 72
4.2.3 Inertia loads Boom . . . 73
4.2.3.1 Boom with internal pipe . . . 74
4.2.3.2 Boom with Stringers . . . 75
4.2.3.3 Boom with Stringers and internal pipe . . . 77

5 Structural Analysis 79
5.1 FEM model . . . 79
5.1.1 Material Properties . . . 81
5.1.2 Boundary Conditions . . . 81
5.1.3 Aerodynamic Loads application . . . 82
5.1.4 Inertial Loads application . . . 84
5.1.5 Validation FEM model . . . 86
5.1.6 Mesh convergence . . . 88
5.2 Tail-Boom Structural analysis . . . 89
5.2.1 Tail and Boom with internal pipe . . . 90
5.2.2 Tail and Boom with Stringers . . . 91
5.2.3 Tail and Boom with internal pipe and Stringers . . . 93
5.2.4 Comparison of the 3 structural solutions . . . 94

6 Structural Optimization 97
6.1 Main spar position . . . 97
6.2 Spars I vs C Configuration . . . 100
6.3 2 Spar vs 1 Spars . . . 103
6.3.1 Spar C profile . . . 103
6.3.2 Spar I profile . . . 104
6.3.3 1 Spar C vs 1 Spar I . . . 105
6.4 Spars I different configurations . . . 106
6.5 Ribs Analysis . . . 109
6.6 Final solution . . . 110

7 Carbon Fiber Reinforced Panel (CFRP) Optimization **115**
7.1 Overview of the Optimization algorithmic 115
7.1.1 Algorithm Validation 118
7.1.1.1 Traction Plate 118
7.1.1.2 Plate in Shear 119
7.2 Improved Optimization Code 120
7.2.1 Validating changes to the fault model 122
7.2.1.1 Hashin Plate in Traction 122
7.2.1.2 Hashin Plate in Shear 122
7.3 ARX Skin Boom Optimization 123
7.3.1 Sampling parameters 125
7.3.2 Gaussian Regression Parameters 125
7.3.3 Genetic Algorithmic Parameters 125
7.3.4 Skin Boom Optimization Results 126

8 Conclusions and future work **129**

References **131**

APPENDIX **137**

A XFLR5 Load Cases Results Horizontal Stabilizer **139**

B Aero loads FEM model Horizontal Stabilizer **145**

C XFLR5 Load Cases Results Vertical Stabilizer **147**

D Aero Loads FEM model Vertical Stabilizer **153**

E Classical Optimization cases- LARC05 Failure Criteria **155**

F Skin Boom Optimization case - Hashin Failure Criteria **157**

List of Figures

1.1 TEKEVER ARX [1] . . . 1

2.1 Fixed-wing vs Multi-Rotor UAV´s . . . 3
2.2 TEKEVER fixed-wing AR3 UAV with VTOL capabilities [9] . . . 4
2.3 Missions involving fixed-wing UAVs [13] . . . 5
2.4 RQ-4 Global Hawk , Norhrop Grumman [15] . . . 6
2.5 Fixed-wing UAV with a more typical tails . . . 6
2.6 Deep Stall [20] . . . 7
2.7 V-Tail Control Surfaces . . . 8
2.8 Most popular twin boom configuration types [22] . . . 8
2.9 Evolution of the weight percentage of composite materials in aircraft [31] . . . 12
2.10 Schematic example of aircraft pyramid of testes [36] . . . 13
2.11 Sequence of thought to define Design Criteria . . . 15
2.12 Sequence of thought to define design philosophy [39] . . . 16
2.13 Major damage models in carbon fiber-reinforced composite laminates [47] . . . 17
2.14 Comparison test data and failure envelopes - unidirectional composite E-Glass/LY556 [49] . . . 20
2.15 Sequence of Topological Optimization [56] . . . 22
2.16 Flow diagram for a generic GA . . . 25
2.17 Binary code [61] . . . 26
2.18 Selection by roulette method [61] . . . 28
2.19 Uniform Crossover [61] . . . 29
2.20 Flip-Bit Mutation [65] . . . 29
2.21 Pure Genetic code vs with Surrogate model [3] . . . 31
2.22 Latin hypercube sampling technique involving two variables and eight samples [75] 32
2.23 Examples of Latin hypercube sampling and random sampling in two dimensions are compared (every row and column is sampled with LHS) [73] . . . 33
2.24 V-N Diagram [2] . . . 38

3.1 Different tail configurations for the type of boom : (a) Twin boom conventional, (b) Twin boom T, (c) Twin boom V invertida, (d) semi-inverted V-tail boom [23] 39
3.2 Full body H-tail and inverted V-tail arrangement volume flow visualization [89] . 40
3.3 ARX CAD model . . . 41
3.4 Tail flight control surfaces [92] . . . 42
3.5 Esquematic assembly of Ribs in a wing [93] . . . 42
3.6 Typical stringers configurations [96] . . . 43
3.7 Esquematic assembly of vertical and horizontal stabilzier [93] . . . 43
3.8 ARX tail structure iteration1 . . . 44
3.9 Ribs Holes Sketchs . . . 44
3.10 ARX tail structure iteration2 . . . 45

3.11 Horizontal Ribs Holes Sketchs . . . 45
3.12 Boom Truss type [93] . . . 46
3.13 Boom monocoque vs Semi-Monocoque [93] . . . 47
3.14 ARX Boom with internal pipe - iteration1 . . . 48
3.15 ARX Boom with stringers - iteration1 . . . 48
3.16 ARX Boom with internal pipe and stringers - iteration1 . . . 49
3.17 ARX Boom with internal pipe - iteration2 . . . 49
3.18 ARX Boom with stringers - iteration2 . . . 50
3.19 ARX Boom with internal pipe and stringers - iteration2 . . . 50

4.1 Manouver Diagram esquematic representation . . . 52
4.2 Manouver Diagram with simplifications esquematic representation . . . 53
4.3 ARX Manouver Diagram . . . 54
4.4 ARX Gust lines . . . 55
4.5 ARX V-N Diagram . . . 56
4.6 Tail symmetric airfoil . . . 57
4.7 C_L vs alpha Tail symmetric airfoil . . . 57
4.8 Main wing cambered airfoils . . . 58
4.9 Tail symmetric vs Main-wing cambered airfoils . . . 58
4.10 Tail symmetric airfoils with variations for control surfaces . . . 58
4.11 ARX model at XFLR5 . . . 59
4.12 Contact interference vertical surface and elevator . . . 60
4.13 ARX elevator at maximum deflexion . . . 60
4.14 Tail symmetric airfoils for different elevator deflection angles . . . 61
4.15 Angle of trim flight to different velocity . . . 61
4.16 ARX rudder at at maximum deflexion 25° . . . 61
4.17 ARX elevator at maximum deflection . . . 62
4.18 Visual lift representation for V_a with elevator positive deflection . . . 62
4.19 Visual lift representation for V_a with elevator negative deflection . . . 62
4.20 Visual lift representation for V_a with left rudder negative deflection and right rudder positive deflection . . . 63
4.21 XFLR5 vs experimental results [98] . . . 63
4.22 Pitching moment XFLR5 vs experimental results [98] . . . 64
4.23 Example of lift on horizontal and vertical stabilizer - Load case V_d with elevator negative deflection . . . 64
4.24 Horizontal stabilizer drag and lift along the semi-span . . . 65
4.25 Decomposition of Aerodynamic loading . . . 67
4.26 Vector decomposition of Lift with the angle of attack=4.72 degrees . . . 68
4.27 Vector decomposition of Drag with the angle of attack=4.72 degrees . . . 68
4.28 Vertical stabilizer lift per unit span . . . 69
4.29 Horizontal Stabilizer . . . 72
4.30 Vertical Stabilizer . . . 73
4.31 Boom with internal pipe . . . 74
4.32 Boom with stringers . . . 75
4.33 Boom with internal pipe and stringers . . . 77

5.1 Comparison of the front view of the Real model and the FEM model made . . . 80
5.2 Comparison of the top view of the Real model and the FEM model made . . . 80
5.3 Comparison of the lateral view of the Real model and the FEM model made . . . 80

5.4 Boundary conditions applied to the Fem model . . . 82
5.5 Boundary conditions detail . . . 82
5.6 Applying loads to the Horizontal surface . . . 83
5.7 Applying loads to the Vertical surface . . . 83
5.8 Load case with left rudder negative deflection and right rudder positive deflection 84
5.9 Application of reference points in the finite element model . . . 85
5.10 Applying Inertial loads to the Horizontal stabilizer . . . 85
5.11 Applying Inertial loads to the Vertical stabilizer . . . 86
5.12 Applying Inertial loads to the Boom structure . . . 86
5.13 Lateral view - Stress S11 [MPa] comparison for the Total model . . . 87
5.14 Lateral view - Deformation comparison for the Main spar [mm] . . . 87
5.15 Front view - Stress S11 [MPa] comparison for the Main spar . . . 87
5.16 Front view - Stress S11 [MPa] comparison for the Secound spar . . . 88
5.17 Mesh refinement for Ribs - Global size 15 [mm] . . . 89
5.18 Mesh refinement for Skin - Global size 15 [mm] . . . 89
5.19 Reference points for analysis . . . 90
5.20 Lateral view Internal structure Boom with internal pipe Stres S11 - Load case Vd- 91
5.21 Lateral view Internal structure Boom with Stringers, Stress S11 - Load case Vd- 92
5.22 Isometric view Internal structure Boom with internal pipe and Stringers, Stress S11 - Load case Vd- . . . 93
5.23 Stress analysis S11 point (1 and 2) - Load case Vd- . . . 95
5.24 Stress analysis S11 point (8 and 9) - Load case Vd- . . . 95
5.25 Analysis point 1 at load case Va+ . . . 96
5.26 Analysis point 1 at load case Va+ . . . 96

6.1 Horizontal Ribs Holes Sketchs for main spar at 35% of chord . . . 97
6.2 Vertical Ribs Holes Sketchs for main spar at 35% of chord . . . 98
6.3 Horizontal Ribs Holes Sketchs for main spar at 25% of chord . . . 98
6.4 Stress analysis S11 - Main Spar 35% chord and secound spar C - load case Rudder Vd . . . 99
6.5 Stress analysis S11 - Main Spar 30% chord and secound spar C - load case Rudder Vd . . . 99
6.6 Stress analysis S11 - Main Spar 25% chord and secound spar C - load case Rudder Vd . . . 100
6.7 Illustrative example of manufacturing an I-profile using semi-separated elements . 101
6.8 Stress analysis S11- Main Spar 30% chord and secound spar I - load case Rudder Vd102
6.9 Stress analysis S11 - Main Spar 35% chord and secound spar I - load case Rudder Vd102
6.10 Isometric view - Comapration structure for 2 spars and 1 spar . . . 103
6.11 Isometric view - Comapration structure for 1 spar in C and I - Load case Rudder Vd 106
6.12 Different spar configurations in I studied . . . 107
6.13 Isometric view - Stress analysis S11 point 8 - Load case Va+ . . . 108
6.14 Case of study 7 ribs - load case Va+ . . . 109
6.15 Stress analysis - Centre hole horizontal rib for the 7 Ribs analysis case - load case Va+ . . . 110
6.16 ARX final Tail structure . . . 110
6.17 Stress analysis1 - Frontal hole Vetical Rib for the 7 Ribs analysis case - load case Vd-111
6.18 Stress analysis2 - Frontal hole Vetical Rib for the 7 Ribs analysis case - load case Vd-112
6.19 Stress analysis - Section of the centre hole of the horizontal rib for the 7 Ribs analysis case . . . 112

6.20 Stress analysis - Main spar and control surface reforce for the 7 Ribs - load case Vd- 112
6.21 Stress analysis - Boom and main spar curve for the 7 Ribs analysis case - load case Vd- . . . 113

7.1 Flow Chart surrogate model [3] . . . 116
7.2 Representation line of thought Genetic code [4] . . . 117
7.3 Test with plate in traction . . . 118
7.4 Tsi-Hill Failure Criteria - Plate in Traction . . . 119
7.5 Tsi-Hill Failure Criteria - Plate in Traction for 0 degrees . . . 119
7.6 Test with plate in shear . . . 119
7.7 Tsi-Hill Failure Criteria - Plate in Shear for 45 degrees . . . 120
7.8 Tsi-Hill Failure Criteria - Plate in Shear . . . 120
7.9 Hashin Failure Criteria - Plate in Traction . . . 122
7.10 Hashin Failure Criteria - Plate in Shear for 0 degrees . . . 122
7.11 Hashin Failure Criteria - Plate in Shear for 45 degrees . . . 123
7.12 Hashin Failure Criteria - Plate in Shear . . . 123
7.13 Boundery conditions Symetric model . . . 123
7.14 Analysis sections Front Boom (yellow) and Rear Boom (blue) . . . 124
7.15 Fiber direction reference analysis section . . . 124
7.16 Schematic example cantilever beam . . . 126
7.17 Skin Boom Optimized regions . . . 127

E.1 LARC05 Failure Criteria- Plate in Traction for 0 degrees . . . 155
E.2 LARC05 Failure Criteria- Plate in traction . . . 155
E.3 LARC05 Failure Criteria- Plate in shear for 45 degrees . . . 156
E.4 LARC05 Failure Criteria- Plate in shear . . . 156

F.1 Hashin Failure Criteria- skin boom section1 for 0 degrees . . . 157
F.2 Hashin Failure Criteria- skin boom section1 . . . 157
F.3 Hashin Failure Criteria- skin boom section2 for 0 degrees . . . 158
F.4 Hashin Failure Criteria- skin boom section2 . . . 158

List of Tables

2.1 European Drone Classes [24] [25] 10
2.2 Advantages of composites materials [27] 12

4.1 Derived gust velocities for ASTM 3116 55
4.2 C_L, C_D and C_m along the semi-span of Horizontal stabilizer- XFLR5 data 65
4.3 Aerodynamic loads along the semi-span: my [N], Vz [N/m] , Vx [N/m] 66
4.4 Aerodynamic loads in rib positions 67
4.5 Lift decomposition for ribs 67
4.6 Aerodynamic load decomposition with safety factor=1.5 69
4.7 Aerodynamic loads equivalent for the Finite Element Model. 69
4.8 Aerodynamic loads along the span: My [N*m], Vz [N/m] , Vx [N/m] 70
4.9 Aerodynamic loads in rib positions 70
4.10 Aerodynamic Loads with safety factor=1.5 71
4.11 Weight estimation for Horizontal stabilizer structural elements 71
4.12 Inertia Loads for Horizontal Stabilizer 72
4.13 Weight estimation for Vertical stabilizer 72
4.14 Inertial Loads for Vertical Stabilizer 73
4.15 Weight estimation for Boom with innternal pipe 74
4.16 Inertial Loads for Boom with internal pipe 75
4.17 Weight estimation for Boom with stringers 76
4.18 Inertial Loads for Boom with stringers 76
4.19 Weight estimation for Boom with internal pipe and stringers 77
4.20 Inertial Loads for Boom with internal pipe and stringers 78

5.1 Laminate Elastic mechanical properties 81
5.2 Laminate Elastic failure stresses 81
5.3 Mesh Convergence 88
5.4 Stress analysis S11 of iteration 2 for Tail and boom with inner tube reinforcement 90
5.5 Stress analysis S11 of iteration 2 for Tail and boom with Stringers reinforcement . 92
5.6 Stress analysis S11 iteration 2 for Tail and boom with inner tube and stringers reinforcement 93
5.7 Weight comparison of structures 94

6.1 Stress analysis S11 - Comparing different main spar positions along the chord . . . 98
6.2 Stress analysis S11 - Comparative between Main spar at 30% chord with 2 spars I and 2 spars C 101
6.3 Stress analysis S11 - Comparative between Main spar at 35% chord with 2 spars I and 2 spars C 102
6.4 Stress analysis S11- Comparison of the reduction from 2 C spars to just 1 C - main spar at 30 % of the chord 103

List of Tables

6.5 Stress analysis S11 - Comparison of the reduction from 2 C spars to just 1 C - main spar at 35 % of the chord . . . 104
6.6 Stress analysis S11 - Comparison of the reduction from 2 I spars to just 1 I - main spar at 30 % of the chord . . . 104
6.7 Stress analysis S11 - Comparison of the reduction from 2 I spars to just 1 I - main spar at 35 % of the chord . . . 105
6.8 Stress analysis S11 - Comparison of the length without secound spar - Main spar : profile C vs Peril I . . . 105
6.9 Weight of the main spar with different I and C profile configurations . . . 107
6.10 Stress analysis S11 - Comparing different profile configurations I . . . 107
6.11 Stress analysis S11 - Comparing the best I-profile configurations and the best C-profile configurations . . . 108
6.12 Stress analysis S11 - Comparing 13/11/9/7 Ribs on the horizontal stabiliser . . . 109
6.13 Stress analysis S11 Final iteration Tail boom ARX . . . 111

7.1 Genetic algorithmic parameters . . . 121
7.2 Mean eror and R-squared value of each section of analysis . . . 125
7.3 Genetic algorithmic parameters . . . 126
7.4 Optimized Layep skin of the Boom . . . 126
7.5 Hashin Failure criterion for optimized sections . . . 127

A.1 Cl, Cd and Cm along the semi-span of Horizontal stabilizer- XFLR5 data for Vd+ 139
A.2 Cl, Cd and Cm along the semi-span of Horizontal stabilizer- XFLR5 data for Rudder Vd . . . 140
A.3 Cl, Cd and Cm along the semi-span of Horizontal stabilizer- XFLR5 data for Va- . 141
A.4 Cl, Cd and Cm along the semi-span of Horizontal stabilizer- XFLR5 data for Va+ 142
A.5 Cl, Cd and Cm along the semi-span of Horizontal stabilizer- XFLR5 data for Rudder Va . . . 143

B.1 Aerodynamic Loads equivalent for the Finite Element Model - Load case Vd+ . . 145
B.2 Aerodynamic Loads equivalent for the Finite Element Model - Load case rudder Vd 145
B.3 Aerodynamic Loads equivalent for the Finite Element Model - Load case Va- . . . 145
B.4 Aerodynamic Loads equivalent for the Finite Element Model - Load case Va+ . . . 145
B.5 Aerodynamic Loads equivalent for the Finite Element Model - Load case Rudder Va 145

C.1 Cl, Cd and Cm along the semi-span of Vertical stabilizer- XFLR5 data for Vd- . . 147
C.2 Cl, Cd and Cm along the semi-span of Vertical stabilizer- XFLR5 data for Vd+ . . 148
C.3 Cl, Cd and Cm along the semi-span of Vertical stabilizer- XFLR5 data for rudder Vd149
C.4 Cl, Cd and Cm along the semi-span of Vertical stabilizer- XFLR5 data for Va- . . 150
C.5 Cl, Cd and Cm along the semi-span of Vertical stabilizer- XFLR5 data for Va+ . . 150
C.6 Cl, Cd and Cm along the semi-span of Vertical stabilizer- XFLR5 data for rudder Va151

D.1 Aerodynamic Loads equivalent for the Finite Element Model - Load Vd+ 153
D.2 Aerodynamic Loads equivalent for the Finite Element Model - Load case Rudder Vd 153
D.3 Aerodynamic Loads equivalent for the Finite Element Model - Load case Va+ . . . 153
D.4 Aerodynamic Loads equivalent for the Finite Element Model - Load Va- 153
D.5 Aerodynamic Loads equivalent for the Finite Element Model - Load Rudder Va . . 154

Chapter 1

Introduction

1.1 Motivation

The motivation for this project derives from the partnership with Tekever, founded in 2001 and the current leader in the development of unmanned aerial systems (UAS) technologies in Portugal, with a special focus on ISAR, for the development and optimization of the structural components of the vertical, horizontal and boom stabilizers of its new UAV aircraft.

Among the most prominent models developed by Tekever are the AR5, AR4 and AR3, each of these UAVs with distinct features to meet the specific requirements of their respective applications. The AR5, for example, stands out for its long-endurance flight capability and payload flexibility, making it suitable for a variety of surveillance and reconnaissance missions. The AR3, on the other hand, includes variants such as the vertical take-off AR3 Light Ray, and is known for its versatility and performance, with advanced autonomous flight characteristics and out-of-line-of-sight operation capabilities. Finally, the AR4 is a smaller fixed-wing unmanned aerial system designed for applications that require long endurance and the ability to cover large areas, such as environmental monitoring and maritime surveillance.

In this regard, Tekever plans to launch a new UAV aircraft called ARX in 2025 (Figure 1.1), under the European funds project, which is the company's largest project to date, with the design of an aircraft weighing around 600 kg, versatility, performance and payload capacity to operate in different environments and conditions, with different versions of ARX also planned, with a special focus on ISAR missions and cargo transportation.

Figure 1.1: TEKEVER ARX [1]

1.2 Objectives

The objectives of this thesis can be divided into two parts. The first and most important is to design the next generation tail and boom structure for the new UAV aircraft developed by Tekever, focusing on reducing weight and increasing structural reliability, while ensuring that the design can withstand the various critical cases established by the ASTM F3116-18 standard [2] for vertical and horizontal stabilizers. In this context, the study includes flight envelope analysis, calculation of loading conditions and development in flight dynamics software (XFLR5) through aerodynamic and stability analysis, as well as the process of designing and sizing the structure and evaluating the performance of the various iterations developed through finite element analysis (FEA), contributing to Tekever's structural improvement and operational efficiency in the development of high-performance aeronautical solutions.

The second objective of the project is to validate and improve the heuristic algorithm optimization tool started in the 2022/2023 academic year by engineers Douglas [3] and Dilki [4], in order to predict the minimum number of layers and the preferred direction of the fibres of the composite material for the most critical structures identified, with the aim of improving structural performance, reducing manufacturing costs and reducing the total weight of the UAV. It should also be mentioned that this study aims to provide data related to the use of GA to improve composite structures, such as the selection of input parameters and fitness functions.

1.3 Structure of the Thesis

In line with the objectives presented above, this section aims to describe the sequence taken into account for the development of the Tail Boom structure of the ARX aircraft, its structural optimization and improvement and the application of the optimization tool.

Chapter 2 presents the state of the art and literature review on unmanned aircraft (UAVs), their certification and the different types of tail that are typically used, as well as composite materials and their failure criterion, types of optimization algorithms, regression models and substitute models.

The 3^{rd} chapter presents the various conceptual studies carried out to choose the type of Tail and structural elements, culminating in iteration 1 and later iteration 2 of the ARX Tail and Boom structures.

The 4^{th} chapter presents the calculation of the aircraft's V-n diagram and the respective development in the XFLR5 software to obtain the aerodynamic forces of the critical cases identified, in addition to the respective calculation of the inertia forces for each structure.

Chapter 5^{th} is dedicated to presenting the work carried out in the CAE software, presenting the FEM model developed and comparing it with the CAD model supplied by the company. Comparing and defining the most suitable structure for the Boom, among the different ones developed.

The 6^{th} chapter aims to present the results of the various tests carried out on the structure defined in chapter 5, such as testing the position of the main spar, reducing the number of Ribs, comparing C and I profiles for the spar flange, among others, culminating in a structurally optimized final version.

The 7^{th} chapter is based on the introduction, validation and improvement of the optimization tool, allowing it to be applied to the most critical sections identified in chapter 6. The conclusions and prospects for future work are presented in chapter 8.

Chapter 2

Literature review

2.1 Unmanned Aerial Vehicles (UAVs)

2.1.1 UAVs Review

Unmanned Aerial Vehicles (UAVs), colloquially known as drones, represent a diverse category of aircraft capable of controlled movement along all three axes without the need for onboard pilots. In recent years, they have emerged as formidable tools for a wide range of tasks, from the military branch that carries out surveillance, strategic patrol in support of ground groups (known as Strategic ISTAR) or even attack (known as UCAV and Target), to the civilian branch that carries out functions ranging from leisure, cinematography and entertainment (known as Utility UAV) to surveillance and tactical patrol (known as Tactical ISTAR). This surge in popularity is largely attributed to technological advancements, which have simultaneously reduced production costs and increased reliability, versatility, and operational range, often allowing for the completion of intended missions without endangering the safety of a crew or pilot.

Thus, we can classify UAVs into two groups: Fixed-Wing (Figure 2.1 a) and Multi-Rotor (Figure 2.1 b). Each type presents distinct advantages and disadvantages, making them suitable for various applications depending on specific requirements and mission .

a) Fixed- Wing UAV, AR5 Tekever [5]

b) Multi-rotor UAV [6]

Figure 2.1: Fixed-wing vs Multi-Rotor UAV´s

Starting with fixed-wing UAVs, these are distinguished by their aerodynamic design, which uses the wings to generate lift and enable flight.

This leads to more energy-efficient, long-range flights, often lasting more than 10 or 30 hours, depending on the size of the aircraft, as well as the ability to reach higher speeds (they can reach cruising speeds of more than 100 km/h). In addition, due to their more robust construction, fixed-wing UAVs have greater endurance and flight stability. However, due to their larger size, they generally have less maneuverability and are also more expensive to produce and maintain. In addition, they require a runway or other launching devices, such as catapults, to take off [7] [8]. Therefore, given their characteristics, they are excellent for work such as large-scale surveillance operations, agricultural monitoring and aerial mapping. More concrete examples of their application would be mapping the growth of unwanted vegetation over a wide area, monitoring vast agricultural areas or patrolling and mapping large maritime areas to facilitate maritime traffic control.

On the other hand, multirotor UAVs use multiple rotors to ensure lift and flight, which allows not only for vertical takeoff and landing (VTOL) but also for static flight and superior maneuverability and control. Additionally, they typically have lower maintenance and manufacturing costs and higher payload capacity. However, due to their less aerodynamic design and typically smaller motors, they typically have endurances of less than 1 hour of flight and much lower flight speeds compared to fixed-wing aircraft. Therefore, they are ideal for inspections, photography, and short-distance filming, allowing the UAV to fly very close to the target and even hover statically over it. Thus, some specific applications of these UAVs can predominantly be observed in civilian applications such as in construction through 3D mapping of construction areas, in the mining sector allowing mapping and investigation of dangerous access locations, or in structure inspection where RGB cameras or infrared sensors can identify leaks and insulation defects [7] [8].

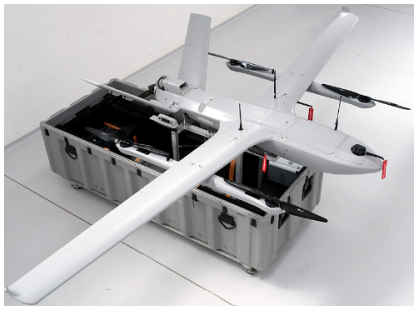

Figure 2.2: TEKEVER fixed-wing AR3 UAV with VTOL capabilities [9]

With that in mind, it is important to note that fixed-wing drones can also be adapted with additional rotors allowing for vertical takeoff and landing (VTOL) capabilities, giving them intermediate characteristics between the two previous cases. Consequently, some of the advantages of this configuration naturally include not requiring a runway for takeoff or landing, enabling take-off and landing on a variety of surfaces, including uneven terrain, making them perfect for operations in urban and maritime areas where landing on a ship is necessary. Additionally, they have the ability to hover in a single location, which is useful for mapping, inspection, and surveillance missions requiring greater precision and proximity.

However, this change introduces some of the problems of multi-rotor UAVs, as hovering requires more energy than fixed-wing drones, usually resulting in shorter flight durations and slower maximum speeds. An example of this type is the fixed-wing model AR3 from Tekever (Figure 2.2), which can be equipped with a VTOL system; however, this impacts its performance, reducing its autonomy from 16 hours to just 8 hours [10]. Finally, compared to traditional fixed-wing drones, production and maintenance costs are higher due to their mechanical complexity and additional propulsion systems.

2.1.2 UAVs Fixed-wings evolution in patrol and surveillance

Unmanned Aerial Vehicles have their roots in the mid-18th century, with the first experiments in Great Britain during the First World War, where the first autonomous vehicles appeared, exemplified by the British Aerial Target - a small radio-controlled plane tested in March 1917 [11]. Since then, drones have been widely used in civilian markets, despite their initial military design for strategic, patrol and detection tasks.

Today, there are thousands of drone operators and manufacturers around the world, which demonstrates the rapid growth of the sector. A survey carried out in 2019 by the European Commission revealed that 76% of participants predicted a rapid development of drones with a maximum take-off mass (MTOM) of more than 150 kg, which indicates a positive trajectory for their continued application in various sectors [12].

Therefore, taking into account the conclusions of a statistical study carried out in 2023 (Figure 2.3) in which six types of missions carried out by fixed-wing UAVs were taken into account, we can infer that the majority of missions (74%) are associated with intelligence, surveillance, target acquisition and reconnaissance (ISTAR), with a greater predominance of the Tactical sector which refers to operations typically monitoring large areas, tracking long-term trends or assessing potential threats to national security, with 48.3% compared to 26.2% for the strategic sector, which generally focuses on supporting ground forces or localized operational areas. On the other hand, combat missions (UCAV) account for 13.4% of the total and are the third strongest group, with their evolution and use in the military sector becoming increasingly common. Finally, target drones and LM have single-digit percentages [13].

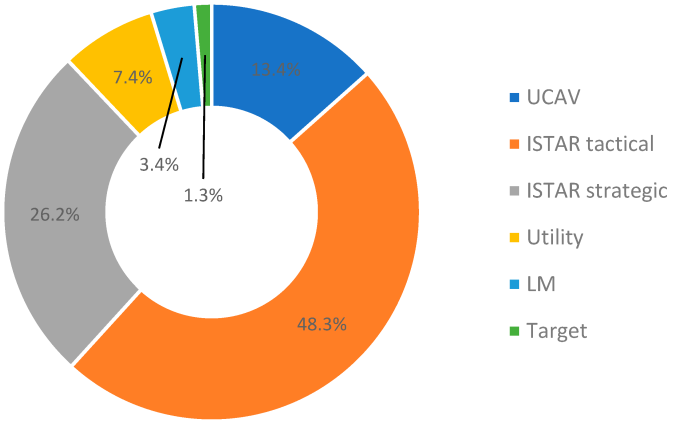

Figure 2.3: Missions involving fixed-wing UAVs [13]

In the national and European context, one of the companies most present in the UAV field for ISTAR tactical of the Mediterranean Sea is the company Tekever, whose drone, such as the AR3 launched in 2019 (Figure 2.2), is designed for a variety of maritime and land missions, such as ISTAR, pollution monitoring and communications support. With an endurance of more than 10 hours and communications range of up to 80 km, it is ideal for medium-range missions. Its features include high-definition video retrieval, processing and transmission, payload flexibility, reduced logistics and ease of operation. It can be launched with a mobile catapult system and recovered using parachutes and airbags over rough terrain. In addition, it is tested for shipboard operations and is capable of carrying out autonomous surveillance, multi-mission support and near-shore missions [9].

Another ISTAR tactical example of greater endurance is Tekever's AR5 (Figure 2.1a), which, with a maximum speed of 100 km/h and around 20 hours of autonomy, specializes in maritime missions and offers advanced on-board processing, simultaneous EO, IR, radar and AIS observation, along with satellite communications. Flexible and safe, it was chosen in 2021 to lead maritime surveillance systems in Europe, with automatic take-off and landing on short runways [14].

Finally, one example of a strategic ISTAR UAV is the RQ-4 Global Hawk (Figure 2.4) , which was introduced in 2001 and has over 320,000 flight hours, an extended flight capability of up to 30 hours, and the ability to take high-resolution images in any weather. Its primary duties involve assisting civil authorities in responding to natural disasters and weather forecasting, as well as supporting military operations by identifying threats and providing vital intelligence [15].

Figure 2.4: RQ-4 Global Hawk , Norhrop Grumman [15]

2.1.3 UAVs fixed-wings tail typs

The design of tails for unmanned aerial vehicle (UAV) aircraft is a critical aspect that can significantly impact performance and functionality. Various tail configurations exist, each tailored to specific needs dictated by mission requirements, design constraints, manufacturing considerations, and operational demands. So,understanding the characteristics and trade-offs of different tail types is essential for optimizing UAV performance [16].

Among the array of tail configurations available, four primary types dominate the UAV industry landscape: the conventional tail, T-tail, H-tail, and V-tail, Figure 2.5, [17] [18].

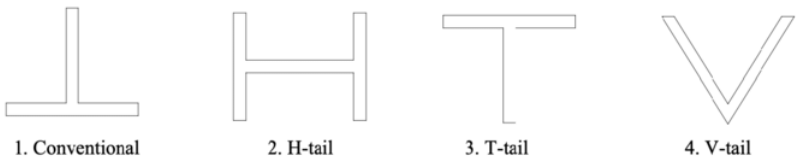

Figure 2.5: Fixed-wing UAV with a more typical tails

Starting with the conventional tail, also referred to as the inverted T-shape configuration, is recognized for its simplicity and versatility in fulfilling essential tail functions such as trim, stability, and control. This configuration comprises a horizontal tail divided into left and right sections positioned at the aft fuselage, along with a single vertical tail section placed atop the aft fuselage, ensuring a balanced distribution of tail functions. While the horizontal tail primarily addresses longitudinal trim and stability, the vertical tail focuses on directional requirements. It is often recommended for designers with limited experience due to its well-understood dynamics, although professionals exploring alternative configurations must possess advanced expertise in trim, stability, and control analysis. Notably, around 60 % of current aircraft in service utilize conventional tail configurations, highlighting their widespread adoption and effectiveness in meeting flight dynamics requirements [16] [19].

The T-tail configuration places the vertical tail over the horizontal tail, offering advantages such as reduced interference, less vibration and improved maneuverability. However, it also presents challenges, such as a heavier and more robust vertical tail structure due to the greater moments created by the control surfaces, greater structural complexity, potential interference problems and limited payload space and especially the possibility of it becoming totally immersed in the turbulent flow generated by the fuselage and tail of the aircraft at high angles of attack, which causes a loss of aerodynamic efficiency, better known as deep stall (Figure 2.6) which can lead to critical failure of the aircraft. Design solutions therefore involve ensuring stable initial stall, increasing the horizontal spans of the tail, implementing mechanisms for full down elevator angles and using protective devices to mitigate the associated risks and ensure safe operation.As a result, it has become increasingly popular, mainly on military cargo planes and smaller Cs-23 aircraft, with around 25 % of current aircraft using the T-tail configuration. [16].

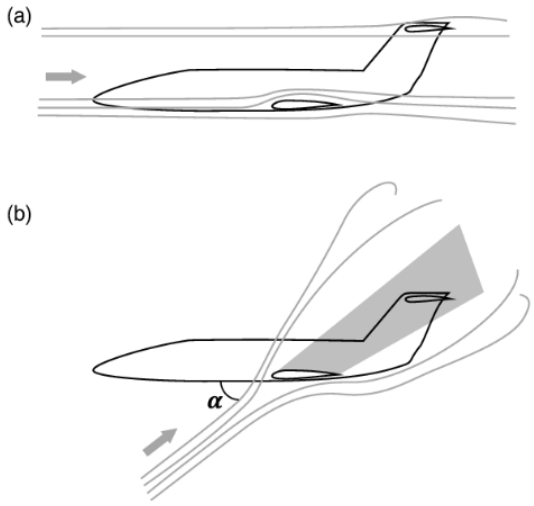

Figure 2.6: Deep Stall [20]

In the other hand,the H-tail configuration, resembling the letter "H", consists of one horizontal tail situated between two vertical tails. This design offers various advantages, including reduced influence of fuselage turbulent flow at high angles of attack. The presence of vertical tails enhances the aerodynamic performance of the horizontal tail through the end-plate effect. In military aircraft, the H-tail configuration can help conceal very hot exhaust gases from radars or infrared missiles, aids in parking in confined spaces, and improves lateral control. However, it is slightly heavier due to the need for the horizontal tail to support both vertical tails, and its structural design is more complex compared to conventional tail configurations. In contrast, while the H-tail setup featuring two horizontal stabilizers flanking the vertical stabilizer offers benefits such as redundancy, enhanced directional stability, and potential stowability advantages, it comes with drawbacks such as increased weight, complexity, and potential interference problems between the tail components [16] [19].

A different alternative is the V-tail configuration, chosen to minimize the total tail area, comprising two V-shaped sections, integrating the functions of horizontal and vertical tail, more commonly referred to as Ruddervators, generating lift in both the y and z directions. Although it offers satisfactory longitudinal and directional trim, the V-tail encounters stability difficulties, especially with Dutch roll tendencies; however, it reduces resistance. Control is managed through movable directional fins linked to the control wheel, with differential movements of the rudder pedals providing directional control, as shown in Figure 2.7 a. Here we can observe an example of yaw movement induced by deflection in opposite directions of the Ruddervators, which induces a vertical force

component canceling yaw control but with a secondary adverse rolling effect. In Figure 2.7 b, we can see an exemplification of pitch movement occurring through the combined deflection of both Ruddervators, generating a horizontal force component on each control surface that cancels out, resulting in pure pitch control. Despite its complexity, the V-tail control system can induce adverse roll-yaw coupling, which can be mitigated by an inverted V-tail configuration, presenting advantages, especially for Boom-style UAV aircraft as we will see in Section 3.1. Overall, V-tails offer lightweight construction and simplified design due to their symmetry but may compromise control authority and yaw stability, especially in crosswinds [16] [19].

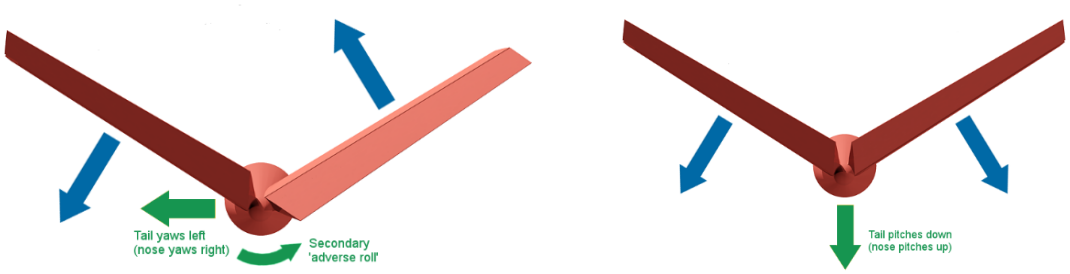

a) Ruddervator Ruder control [21] b)Ruddervator Elevator Control [21]

Figure 2.7: V-Tail Control Surfaces

Beyond what has already been mentioned, we can also take into consideration configurations for two booms such as Twin boom conventional ,Twin boom H,Twin boom T and Twin boom inverted V, (Figure 2.8) which we will address in more detail in Section 3.1.1 due to their application in the aircraft under development in this project.

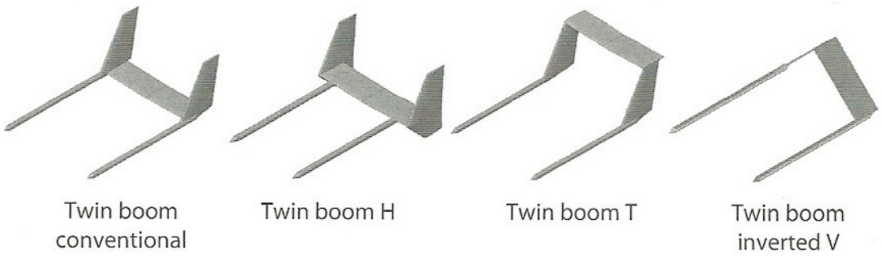

Figure 2.8: Most popular twin boom configuration types [22]

Some of the main advantages of using two booms include improved force distribution along with enhanced stability, especially in pitch, which makes the aircraft easier to handle during flight, allowing for safer and smoother maneuvering. Additionally, the structural support provided by the booms adds rigidity to the empennage, facilitating the assembly of tail components and reducing bending and vibrations, in addition to their notable accessibility provided by the open layout, which simplifies access to tail section components, expediting equipment installation, maintenance, and repair operations. Finally, by eliminating the conventional tail portion, the aircraft's center of gravity and flight performance are optimized due to the flexibility in cargo positioning [23].

On the other hand, there are some disadvantages compared to single-boom aircraft designs. The presence of two booms may result in a slight reduction in performance due to increased aerodynamic drag, potentially leading to reduced maximum speeds or increased fuel consumption, thereby decreasing overall operational efficiency. Additionally, the extra structural elements add weight, which could affect flight range and payload capacity, as well as reducing the amount of space

within the main fuselage, affecting cabin or cargo capacity and potentially limiting the aircraft's adaptability for certain uses, especially those requiring a large interior volume. Finally, there may be additional challenges involved in the construction of a two-boom structure from an engineering and manufacturing perspective, as careful attention must be paid to ensure that the booms and fuselage are properly aligned, balanced, and integrated, which could delay production. Comparing these elements with more typical designs, the need for extended flight testing results in higher engineering and production costs [23].

2.1.4 UAVs fixed-wings Certification

At the same time as drone operations are on the rise, their certification is accompanying the process, with certification criteria currently being defined taking operational risk into account. For this purpose, the European Aviation Safety Agency (EASA) has defined three categories of operation and the corresponding regulatory framework for them have been created: Open, Specific and Certified, taking into account the wide variety of drone types and operations (Article 3 of Implementing Regulation (EU) 2019/947 [24]).

Before delving into the specifics of each of these categories, it's important to highlight the new European regulations that came into force in January 2021, creating a system of C0, C1, C2, C3, C4, C5 and C6 class (based on Delegated Regulation (EU) 2019/945 [25]) labels to distinguish the various types of open and specific category drones, based on their characteristics and operational limitations, taking into account factors such as maximum take-off mass (MTOM), maximum speed and other specific technical requirements [25]. The Table 2.1 therefore provides a summary of all this information.

Drones in the open operation category (Article 4 of Implementing Regulation (EU) 2019/947 [24]) allows low-risk activities without Aviation Authority involvement or airworthiness approval. This category is separated into three certification subcategories, A1, A2, and A3, due to the vast number of drones that fall under it. Despite their differences, they are all founded on publicly available regulations that demand adherence to particular flight parameters, such as staying in the operator's visual range and staying no higher than 120 meters above the ground, unless lower altitudes are mandated by regional geographic restrictions. Furthermore, it is strictly prohibited to carry hazardous materials or drop any objects, fly over crowds, or fly higher than is permitted in the operational protection zones of international airports.

Subcategory A1: Includes drones with class C0 and C1 markings (Table 2.1), as well as equipment with non-European markings, up to 250 grams (payload included) and a maximum speed of less than 19 m/s are used in operations. Typically used for leisure applications or small events [24].

Subcategory A2: It covers operations with drones with a maximum take-off mass of less than 4 kg and with class C2 markings (Table 2.1). Only people who are not involved in the operation may be at a minimum distance of 30 meters from the drones, or at a minimum distance of 50 meters if the drones do not have class markings. Typically used by commercial or recreational operators [24]).

Subcategory A3: Addresses the use of drones with class C3 and C4 markings (Table 2.1) that have a maximum take-off mass of less than 25 kg. The drone should only be flown if it is certain that no one who is not directly involved will be in danger while the aircraft is in the area. The flight must take place more than 150 meters away from any residential, commercial, industrial or recreational area [24]).

2.1. Unmanned Aerial Vehicles (UAVs)

Table 2.1: European Drone Classes [24] [25]

Class	Description
C0	MTOM $\leq 0.250g$ Maximum speed $\leq 10m/s$ Maximum altitude $\leq$ 120 m
C1	MTOM$\leq 0.9g$ Maximum speed $\leq 19m/s$ Maximum altitude $\leq 120m$ Function for adjusting or limiting flight height Spatial geo-recognition feature included
C2	MTOM$\leq 4kg$ Maximum speed $\leq 19m/s$ Maximum altitude $\leq 120m$ Function for adjusting or limiting flight height Spatial geo-recognition feature included Selectable low-speed mode ($\leq 3m/s$, except for fixed-wing) Lights for night flying and altitude control
C3	MTOM$\leq 25kg$ Maximum speed $\leq 19m/s$ Maximum altitude $\leq 120m$ Function for adjusting or limiting flight height Spatial geo-recognition feature included Lights for night flying and altitude control Maximum wingspan $\leq 3m$
C4	MTOM$\leq 25kg$ Includes higly specialized aircraft, racing drones, and model or homemade aircraft
C5	MTOM$\leq 25kg$ Spatial geo-recognition feature included Selectable low-speed mode ($\leq 5m/s$, except for fixed-wing) Lights for night flying and altitude control Failsafe mechanism for ending flight or data retrieval upon failure Tailored for operation within the specific Category, STS-01 Scenario
C6	MTOM$\leq 25kg$ Maximum horizontal flight speed$\leq 50m/s$ Spatial geo-recognition feature included Lights for night flying and altitude control Failsafe mechanism for ending flight or data retrieval upon failure or loss Tailored for operation within the specific Category, STS-02 Scenario

Moving to the category of specific operations (Article 5 of Implementing Regulation (EU) 2019/947 [24]), stricter measures are applied to mitigate risks, considering medium-risk operations. Operators must carry out safety risk assessments approved by the national aviation authority or self-approved with the agreement of the provider. An "Operations Authorization" is issued, which defines the conditions of a single operation or a series of operations, as well as airworthiness assessments, procedures, personnel competence and airspace, in accordance with industry standards, defining the UAV's operations manual.In addition, a drone operator's ERP (Emergency Response Plan) is required [12]. Compared to the open category, this category allows flights beyond the pilot's vision (BVLOS), flights over people in restricted areas, transport and delivery of non-hazardous cargo and aircraft with greater weight capacity, altitude and maximum speed, encompassing classes C5 and C6 (Table 2.1). This category therefore typically includes professional operators with more complex operations.

Finally, the Certified category, which encompasses high-risk operations (Article 6 of Implementing Regulation (EU) 2019/947 [24]) proposes a regulatory framework that mirrors aircraft certification processes, ensuring that drones, even large ones, meet strict standards while maintaining public and operational safety. Certification thus covers environmental, airworthiness and noise aspects, with separate approvals for control stations and maintenance organizations. Compared to previous cases, pilots and operators would need licenses and integration into the airspace would depend on the safety assessments of ATS providers [12]. With this in mind, these UAVs are typically intended for people transport operations, flying over concentrations of people and transporting dangerous goods.

However, despite continued efforts to keep up with rapid technological and industry advances, there are still security risks, such as collisions with structures or other aircraft, as well as possible damage caused by drone accidents or low battery levels, even with current attempts to certify and control UAV operations. In addition, privacy concerns are also raised by unauthorized data collection and surveillance, and security risks include the possibility of drone weaponization, cyber attacks and breaches in perimeter defense. Thus, some regulatory issues that have yet to be fully addressed include air traffic management, operator compliance and enforcement of airspace laws. [26].

2.2 Composite materials

2.2.1 Evolution and introduction in aeronautics

Historically, metals have dominated aircraft construction due to their consolidated knowledge of design, performance, manufacturing processes and material costs. Age hardened aluminum alloys, usually from the 7000 series, are the most widely used due to their greater resistance to yielding, compression and fatigue, however, the 2000 and 8000 series are also used for applications requiring greater ductility, fracture toughness or corrosion resistance, respectively [27]. In addition, steel is used in components that require greater rigidity and strength, such as landing gear and engine mounts, while magnesium is mainly used in secondary aircraft structures due to its low weight, although it is more expensive and has inferior structural properties to aluminum or titanium, which were first used in military aircraft in the 1950s, especially in the development of supersonic aircraft due to its better mechanical properties and resistance to high temperatures.

However, due to the industry's constant demand for more efficient and cost-effective aircraft, weight is a crucial factor, which has led to the introduction of composite materials. These materials offer a high strength-to-weight ratio, allowing weight to be reduced, thus improving efficiency

and reducing fuel consumption without compromising structural integrity, making their presence increasingly prominent. Furthermore, composite materials have superior resistance to corrosion and fatigue, extending the useful life of aircraft components and reducing maintenance costs. In addition, they are characterized by their inherent design flexibility, allowing for the creation of complex shapes and smoother aerodynamic profiles, further improving performance. Table 2.2 shows a summary of the advantages of composites vs. metals in an operational context.

Table 2.2: Advantages of composites materials [27]

Weight redction	Reduced Acquisition Cost	Improved Performance	Reduced through-Life Support Cost
-increased range -reduced fuel cost -higher pay load -increased maneuverability	-reduced fabrication cost -improved "fly-to-by" ratio -reduced assembly costs	-smoother, more aerodynamic form -special aeroelastic properties -increased temperature	-resistance to fatigue and corrosion -resistance to mechanical damage

Given all these advantages, and given that the major advance in UAVs is considerably more recent than the rest of aviation, composites presented themselves as an attractive option almost from the start. As such, they are typically used in structures such as wings, fuselages and landing gear [28] [29]. An example of this was the Leading Systems Amber, considered the first endurance unmanned aerial vehicle (UAV), developed under a joint program (Teal Rain) with the US Navy, which could fly for more than 38 hours straight and reached an altitude of 25,000 feet in 1988, with structures such as landing gear and part of the fuselage made mainly of composite materials, mainly Kevlar. In addition a more recent example is the MQ-9 launched in 2021 by General Atomics, which presents itself as one of the most advanced drones today and has about 89% of the fuselage structure made of carbon fiber [30].

On the other hand, in a general context, if we look at the evolution of its integration into aircraft (Figure 2.9), we can see that the first integrations were carried out in military environments aircraft in the 70s such as the F-15 and F-16 in secondary structures, representing a very small percentage of their weight (less than 5%), it was only in the 80s with the McDonnell Douglas F/A-18 Hornet in the military and later with the Airbus A320 in the civil sector, where composites made their first big leap, representing around 10% of the weight of the structure and integrating primary aircraft structures (e.g Vertical Tail Plain in the A320). With greater knowledge of the materials and advanced manufacturing and control technologies, confidence in their use has increased, with aircraft such as the Boeing 787 or Airbus A350 having around 50% composite content, from the fuselage, wingskin to control surfaces [31].

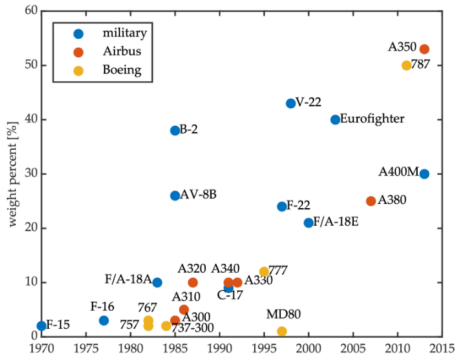

Figure 2.9: Evolution of the weight percentage of composite materials in aircraft [31]

Although CFRP (carbon fiber reinforced polymers) continue to be the main material used in most UAV projects, hybrid composites have been investigated, recently gaining popularity due to environmental concerns raised by the low recyclability of common composite materials such as CFRP.

In addition, these materials represent a significant advance in UAV design, being able to obtain specific performance attributes by combining different materials, such as glass fibers, carbon fiber composites and Kevlar, allowing the material to be modified to meet specific needs. This provides particularly good solutions for reducing vibration and increasing impact resistance when combining materials with greater impact resistance, such as glass fibers or Kevlar, absorbing and dissipating energy more effectively compared to CFRP, thus increasing the resilience and durability of UAVs.

Another possibility of hybrid composite structures is the possibility of generating more economical options, balancing performance and cost by carefully integrating less expensive fibers, such as glass or natural fibers, in areas where high strength is not so important. For example, carbon fibre composites can reinforce areas that require rigidity and strength, while Kevlar or aramid fibres can be used in areas that require flexibility and impact resistance, making it easier to design UAV structures to specific operational requirements and optimized for reliability, weight reduction and improved performance [32] [30] [33].

2.2.2 Certification of composite materials

To guarantee safety and reliability, the certification of aeronautical materials is an essential and thorough procedure that must be completed. In order to meet the strict standards set by regulatory bodies such as the European Aviation Safety Agency (EASA) in Europe or the Federal Aviation Administration (FAA) in the United States, the materials used are subjected to exhaustive testing and certification procedures called the "Pyramid of Tests" (Figure 2.10) [34].

This involves testing samples of materials, creating a database of their mechanical properties and assessing characteristics such as fatigue and strength. Then moving on to testing components and sub-assemblies to assess the strength and load capacity of the materials used in real aircraft components, guaranteeing overall integrity and extending the assessment to larger sections of the aircraft, respectively, and finally, exhaustive analyses are carried out to reproduce the operating conditions of the real aircraft structure [35].

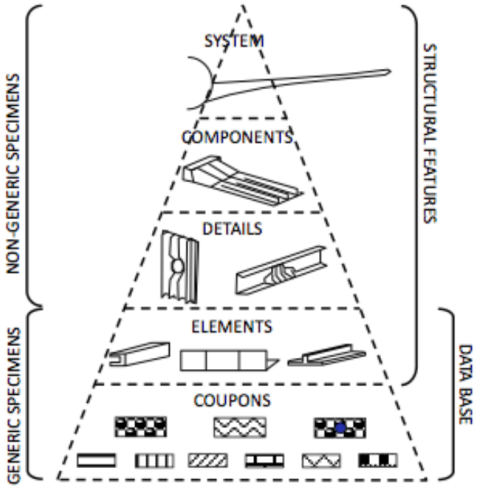

Figure 2.10: Schematic example of aircraft pyramid of testes [36]

Based on these procedures, creating a wealth of information on materials and the operational expertise accumulated over the decades has led to the establishment of well-established certification processes for metallic components.

However, despite their advantages, composites present a series of challenges and barriers that have forced authorities to evolve and reformulate certification processes to incorporate these materials into aeronautical structures, guaranteeing the same level of safety through tighter certification processes. Therefore, we will discuss some of the most important barriers created by the introduction of composites in aeronautics, as well as the solutions adopted for each of them [35] [37].

Anisotropic Behavior: Unlike metals, composites have an anisotropic behavior, with mechanical properties that vary with direction, so in the direction perpendicular to the fibers, the mechanical properties tend to be lower than those parallel to the fibers, due to less adhesion between the matrix and the fibers and a less uniform distribution of loads, typically resulting in lower tensile, compressive and flexural strengths in this direction.

Impact on certification: Adapted certification procedures that take into account directional variations in mechanical properties (e.g. multidirectional tests)

No Material Standerization Lack of a common standardization framework (like the Aluminium Association, for example) that would provide an initial database for the engineering properties and ensure a minimum material quality level independent of the supplier.

Impact on certification: Every applicant needs to create their own database and material qualification system. If a component has already received certification, any material changes must be addressed in detail and supported by the necessary evidence.

Reduced Ductility This directly affects impact loads, including crash loads, due to a material's decreased capacity to absorb energy through plastic deformation. When combined with laminates' low through-the-thickness mechanical properties, this renders the material especially vulnerable to low velocity accidental impact damage, making it challenging to visually assess the extent of the damage. Damage of this kind will lower residual static strength.

Impact on certification: Requirement for Special Conditions to show that, in terms of impact resistance (such as crashworthiness), they are just as safe as metals. In pertinent, impact-prone zones, it is necessary to assume the regular occurrence of low velocity impact damage and to demonstrate residual static strength capability in the event that damage is discovered.

Poor Electrical Conductivity: Laminates made of carbon fiber are far less electrically conductive than those made of aluminum. They only function as a weak electrical shielding and behave like dielectric materials.

Impact on certification: Creation of new regulations and appropriate compliance strategies to support composite structures against the direct and indirect effects of lightning strikes ,such as metals foil expanded into skin, are used to cover the composite surface(e.g Conductive materials like copper, bronze, and aluminum are the most frequently used). To provide the current with multiple safe exit routes from the aircraft, these conductive paths must be connected to the remainder of the aircraft.

Manufacturing Variability: Significant dependence exists between the processing parameters and the final mechanical properties. Potential introduction of inherent manufacturing flaws (voids, porosities, dry patches, etc.) during the material consolidation stage.

Impact on certification: emphasizes the importance of quality assurance, particularly in process control. The structures used in structural substantiations must be representative of the lowest quality permitted by the quality control system (e.g., by adding artificial voids, delaminations, and realistic impact scenarios).

Therefore, the successful integration of carbon fiber reinforced polymer (CFRP) into civil aviation was a complex process that took place over decades and involved close collaboration between industry stakeholders and regulatory authorities, allowing for the amendment of certification specifications, the acceptance of special conditions, the adaptation of acceptable means of compliance (AMC) for CFRP and the publication of advisory circulars (AC) with the input of original equipment manufacturers (OEM). Culminating in a larger and more extensive pyramid testing process, requiring a greater volume of samples due to the need to analyze numerous and complex failure modes, less confidence in the numerical analysis of these materials, the need to explore different stacking sequences and greater variability in mechanical properties [34].

2.2.3 Design UAV

The process of establishing design criteria in aircraft is a fundamental step that guides the entire project development. Therefore, it takes into account two major groups of considerations: the design specifications, which include considerations regarding the mission type, directing design choices to achieve certain properties of maneuverability, maximum speed, aerodynamic efficiency, range, endurance, cargo capacity, among others, which in turn are refined according to the intentions of the customer/operator , (Figure 2.11). As an example, let's consider the design of a UAV with a long-range ISAR mission and, on the other hand, a UAV with a mission of cargo and supply distribution.

In these two cases, both UAVs are designed and delineated to achieve characteristics that lead them to perform better in carrying out their mission. In this particular case, the long-range ISAR UAV would prioritize a design that is as lightweight as possible, with greater aerodynamic efficiency and less weight, opting for a fixed-wing structure. On the other hand, the cargo or supply distribution UAV would probably need to prioritize other areas such as greater structural resilience and additional space in the fuselage for cargo transportation or additional mechanisms such as floats for its transport, potentially utilizing a multi-rotor or fixed-wing with VTOL capability to drop cargo more precisely and closer to the target [38].

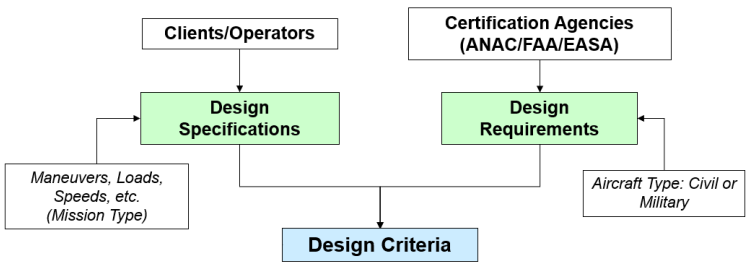

Figure 2.11: Sequence of thought to define Design Criteria

However, after this phase, it is important to consider that changes can be made taking into account the preferences of the customer/operator. Taking back the previous example of the cargo UAV, it could initially be designed as a fixed-wing with the capacity for launching and transporting cargo using a float, but then adapted to a fixed-wing with VTOL capability to operate the aircraft in more challenging terrains such as caves or urban centers.

In the context of composite materials, it is at this stage that consideration is given to which philosophy should be taken into account for each of the aircraft's elements, opting between Safe-life, Fail-safe, or damage tolerance design (Figure 2.11).

2.2. Composite materials

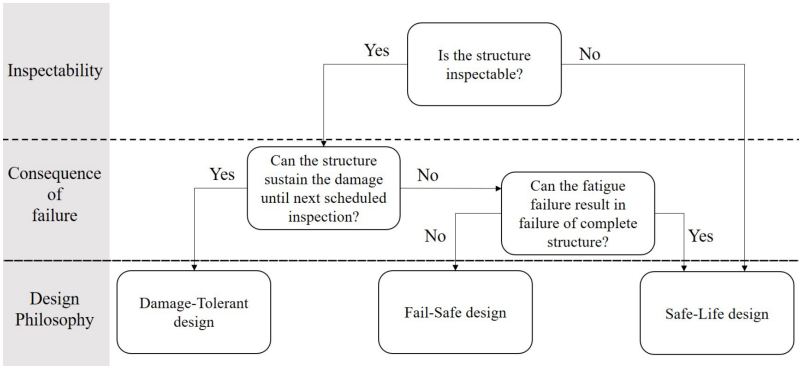

Figure 2.12: Sequence of thought to define design philosophy [39]

Safe-Life - *"Safe-life is when a structure or component is designed to remain free from any defect during its service life."*

Although safer, these structures are typically heavier and are conveniently limited to applications with structures that are difficult to inspect, such as the ribs closest to the fuselage, or where high strength is required, such as landing gear. However, there are differences in this definition when it comes to metals or composite materials. In the first case, the metal structure must remain free of any kind of damage or failure until the end of its useful life. On the other hand, in the case of a composite material structure, it must remain free of any critical defect, damage or degradation until the end of its useful life, referred to as the original defect-tolerant useful life [40].

Fail-Safe - *"The fail-safe approach requires multiple load paths to be included at the design stage so that even after the failure of a structural element, the structural integrity of the aircraft is not impaired, allowing sufficient time for scheduled inspections to find and repair the damage."*

In this case, this criterion results in lighter structures compared to the previous case, and this design criterion is the most widely used in all metal aeronautical structures, although it requires proper maintenance in order to carry out possible repairs to the structure [41].

Damage-Tolerance - *"Damage tolerance is the attribute of the structure that allows it to retain its necessary residual strength for a period of use after the structure has experienced a certain level of fatigue, corrosion, accidental damage, or discrete source damage."*

Finally, this criterion gives rise to the lightest structures of the three criteria, typically used in structures such as wing skins or other components that are easy to inspect and monitor, requiring the monitoring of the structure to detect cracks and defects and the creation of a maintenance plan to monitor them [42].

As mentioned in the previous section, composite materials have low ductility, and in the vast majority of cases their damage is created by small manufacturing defects or low-speed impacts during aircraft operation or maintenance, creating internal defects that result in rapid and difficult-to-predict propagation of these materials. For this reason, the EASA and FAA agencies do not normally allow the certification of primary structures made of composite materials with damage tolerance design criteria [40][38].

Finally, it's important to note that these requirements are initially defined according to the type of UAV (civilian or military), with civilian criteria being stricter when compared to military criteria, since the need for maximum performance and greater risk tolerance capacity dictate more extreme and innovative design paths for military aircraft, which are not allowed in civilian contexts where safety is the main factor to consider [40].

2.2.4 Failure Mechanisms in Composite

There are several ways in which failure can occur in composite materials, the two most important being matrix failure and fiber failure (Figure 2.13). When the polymer matrix that holds the reinforcing fibers in a composite material is damaged or breaks, this is referred to as matrix failure and can occur under different loading scenarios, including shear, compression, tension or a mixture of these. In addition, other failures can arise due to ageing factors of the matrix material or excessive stresses or strains, and cracking, detachment, delamination and plastic deformation of the polymer matrix can occur [43].

On the other hand, fiber failure refers to the failure of the reinforcing fibers of the composite material (e.g. glass, aramid or carbon fibers), arising from the tearing or separation of the fiber-matrix interface, due to tensile, compressive or shear loads, this being due to factors such as fiber strength, fiber-matrix adhesion and fiber misalignment [44] [45] [46].

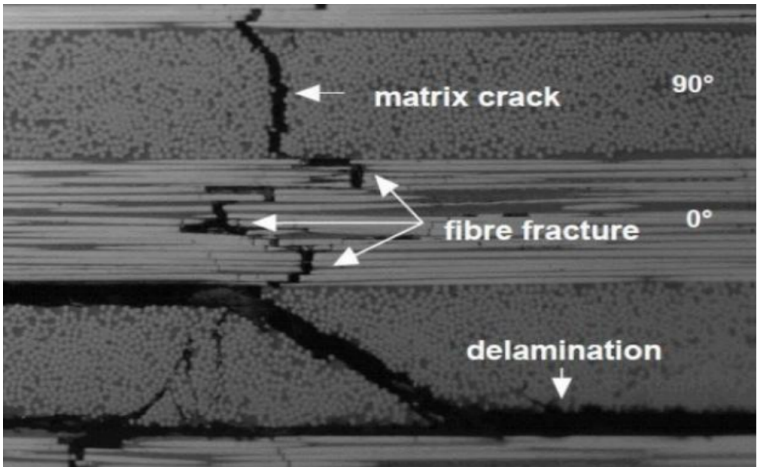

Figure 2.13: Major damage models in carbon fiber-reinforced composite laminates [47]

To deal with this complexity, several different Lamine failure criteria have been devised, which can be divided into two main categories:

1. **Criteria that account for the interconnections between the various stress factors-** forming each of the three components of stress (or strain) in the plane, an inequality [48]. Some examples are the quadratic Hoffman criterion, Tsai-Wu, Liu-Tsai, Tsai-Hill, stress/strain and maximum strain/energy.

2. **Criteria that account for the interaction between several stress factors-** and loads in other directions, such as shear, can affect failure in one direction, and this group can be further divided into criteria that combine interactive and non-interactive requirements and criteria that define a single inequality to define the failure envelope [49]. Some examples of these criteria are Hashin and Rotem, Hashin, Puck and Schuermann, LARC03, LARC04 and LARC05, which aim to differentiate between the various failure processes, considering phenomenological approaches.

Finally, for predicting failure in laminates, methods such as Hart-Smith, the sudden failure method and the layer-by-layer discount method are commonly used [49] [48]. With this in mind, we will analyse the three models present in the Abaqus software, Hashin, Tsai-Hill and Tsai-Wu, and then compare them with the most recent model presented by NASA LARC03, which is widely used in aeronautical structure applications.

2.2. Composite materials

Starting with the Tsai-Hill failure criterion, Hill began by adjusting the von Mises criterion for anisotropic ductile metals and Tsai later modified it for unidirectional composite plates with transversal isotropy [50]. Consequently, this failure criterion, known as Tsai-Hill (deviatoric strain energy), allows for a significant interaction between the stress components, which is expressed in terms of a single criterion , Equation 2.1.

$$\left(\frac{\sigma_1}{X}\right)^2 - \left(\frac{\sigma_1\sigma_2}{X^2}\right) + \left(\frac{\sigma_2}{Y}\right)^2 + \left(\frac{\tau_{12}}{S}\right)^2 = 1 \tag{2.1}$$

where,

σ_1 - Applied normal stress
σ_2 - Applied transverse stress
τ_{12} - Applied shear stress
X - Limit normal stress (Compression or tensile)
Y - Limit transverse stress (Compression or tensile)
S - Limit shear stress (Compression or tensile)

On the other hand, for orthotropic or transversely isotropic slabs, the Tsai-Wu failure criterion (Equation 2.2), a modified tensor polynomial criterion, can be presented, which makes it possible to distinguish between compressive and tensile strengths in this situation, also taking into account the interaction between normal stresses [50].

$$F_1\sigma_1 + F_2\sigma_2 + F_3\tau_{12} + F_4{\sigma_1}^2 + F_5{\sigma_2}^2 + F_6{\tau_{12}}^2 + 2F_7\sigma_1\sigma_2 = 1 \tag{2.2}$$

where,

- $F_1 = \frac{1}{X^{\mathrm{T}}} + \frac{1}{X^{\mathrm{C}}}$, $F_2 = \frac{1}{Y^{\mathrm{T}}} + \frac{1}{Y^{\mathrm{C}}}$
- $F_3 = 0$, $F_4 = -\frac{1}{X^{\mathrm{T}}X^{\mathrm{C}}}$
- $F_5 = -\frac{1}{Y^{\mathrm{T}}Y^{\mathrm{C}}}$, $F_6 = \frac{1}{S_{12}^2}$
- $F_7 = \frac{1}{2Y^{\mathrm{T}}}\left[1 - (F_1 + F_2)\,Y^{\mathrm{T}} - (F_4 + F_5)\left(Y^{\mathrm{T}}\right)^2\right]$

where,

X^{T} - Limit tensile normal stress
X^{C} - Limit compressive normal stress
Y^{T} - Limit tensile transverse stress
Y^{C} - Limit compressive transverse stress
S_{12} - Limit shear stress

When determining whether a composite material is likely to fail under a given stress state, the failure index is used in the Tsai-Hill and Tsai-Wu criteria. Thus, under the specified stress conditions, failure is likely to occur in the composite material if the calculated value of the failure index is greater than 1. In other words, a rupture index greater than 1 denotes a higher probability of rupture because the applied stress state exceeds the material's resistance to rupture. Finally, it is important to remember that the Tsai-Hill and Tsai-Wu criteria do not specify the exact failure mode that will occur, but only use the combination of stress components to predict the total occurrence of failure [50].

Next up is the Hashin failure criterion, which is presented in the Abaqus software as one of the most accurate and efficient criteria. Developed by Tsu-Wei Hashin in 1980, unlike the previous cases, this criterion calculates critical stresses in each main direction of the composite material, taking into account the properties of the constituents, fibre orientation and geometry of the structure, differentiating between failures in the matrix and in the fibres, resulting from tension or compression, using four interactive and non-interactive factors [49] [48].

Thus, the following inequalities Equation [2.3 to 2.6], provide the failure criteria for Hashin's interactive criterion, expressing the different possible failure modes, establishing a limit for the principal stresses that can be withstood without leading to material failure.

Fiber failure for compression with $\sigma_{11} \geq 0$:

$$-\frac{\sigma_{11}}{X^C} \geq 1. \tag{2.3}$$

Fiber failure for compression with $\sigma_{11} < 0$:

$$\left(\frac{\sigma_{11}}{X^T}\right)^2 + \left(\frac{\tau_{12}}{S^L}\right)^2 \geq 1. \tag{2.4}$$

Matrix failure for compression with $\sigma_{22} \geq 0$:

$$\left(\frac{\sigma_{22}}{Y^T}\right)^2 + \left(\frac{\tau_{12}}{S^L}\right)^2 \geq 1. \tag{2.5}$$

Matrix failure for tension with $\sigma_{22} < 0$:

$$\left(\frac{\sigma_{22}}{2S^T}\right)^2 + \left[\left(\frac{Y^C}{2S^T}\right)^2 - 1\right]\frac{\sigma_{22}}{Y^C} \geq 1. \tag{2.6}$$

where,

S^T - Transverse shear strength
S^L - Longitudinal shear strength

In continuation, the LARC03 failure criterion is one of the most advanced models currently used mainly in the aeronautics and aerospace industry to predict failure in fibre-reinforced polymer laminates, incorporating five interactive conditions to detect crack initiation in the matrix and fibre compression failure, along with a separate condition for fibre tensile failure. As such, it was developed post-WWFE at the Langley Research Centre, offering accurate predictions without relying on curve-fitting parameters, making it a valuable tool for ensuring structural integrity in aerospace and high-performance applications [51] [48]. Thus, this criterion is at the same time the most complex of all those presented so far, and a simplified overview of its various formulas for predicting the different failure modes is provided, which can be seen in Equations [2.7 to 2.12] below:

Matrix cracking for tension with $\sigma_{22} \geq 0$

$$(1-g)\left(\frac{\sigma_{22}}{Y_n^T}\right) + g\left(\frac{\sigma_{22}}{Y_n^T}\right)^2 + \left(\frac{\tau_{12}}{S_n^L}\right)^2 \geq 1 \tag{2.7}$$

Matrix cracking for compression with $\sigma_{22} < 0$ and $\sigma_{11} < Y^c$

$$\left(\frac{\tau_{eff}^{mT}}{S^T}\right)^2 + \left(\frac{\tau_{eff}^{mT}}{S_n^L}\right)^2 \geq 1 \tag{2.8}$$

Matrix cracking for compression with $\sigma_{22} < 0$ and $\sigma_{11} \geq Y^c$

$$\left(\frac{\tau_{eff}^T}{S^T}\right)^2 + \left(\frac{\tau_{eff}^T}{S_n^L}\right)^2 \geq 1 \tag{2.9}$$

Failure for fiber tension with $\sigma_{11} \geq 0$

$$\left(\frac{\epsilon_{11}}{\epsilon_{11}^T}\right) \geq 1. \tag{2.10}$$

Failure for fiber compression with $\sigma_{22} < 0$

$$\tau_{12}\left(\frac{1}{(S^L)^2} + \frac{1}{(Y^C)^2}\right) \geq 1 \tag{2.11}$$

Failure for fiber compression with $\sigma_{22} \geq 0$

$$(1-g)\left(\frac{\sigma_{22}^m}{Y_n^T}\right) + g\left(\frac{\sigma_{22}^m}{Y_n^T}\right)^2 + \left(\frac{\tau_{12}^m}{S_n^L}\right)^2 \geq 1. \tag{2.12}$$

where, g is the material constant

Having presented the Tsi-hill, Tsi-wu, Hashin and LARC03 criteria, we can turn to the study carried out in [49], which compares the four failure criteria in a τ_{12} vs σ_{22} plane, correlating them with experimental data, Figure 2.14, we can see that the LARC03 and Hashin criteria are more accurate than the others, which in most of the test points do not achieve a satisfactory correlation [49], [48]. This is justified by the more complex and in-depth approach of the initial criteria, which allows different failure modes to be separated, giving a better insight into the behavior of the composite material.

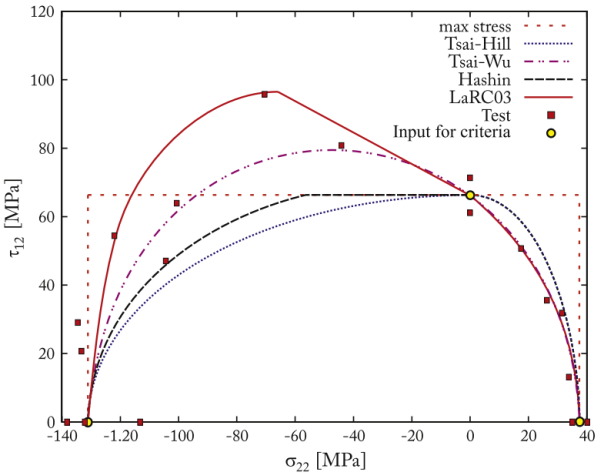

Figure 2.14: Comparison test data and failure envelopes - unidirectional composite E-Glass/LY556 [49]

Finally, it should be noted that the LARC03 criterion is not available for analysis in the CAE Abaqus software, which makes it impossible to use it in this project. However, its most recent version LARC05, established during the World-Wide Failure Exercise (WWFE-II), allows it to be integrated into Abaqus in plug-in format. This principle maintains the calculation of solutions for blades and laminates like LARC03, but integrates the latest knowledge of physics related to the breaking process at the micro-mechanical level [52] [53]. So this criterion takes into account the following four damage initiation processes: Matrix Cracking (Equation 2.13), Fiber Kinking (Equation 2.15), Fiber Splitting (Equation 2.15), and Fiber Tensile failure (Equation 2.18).

Matrix Cracking

$$FI_M = \left(\frac{\tau_T}{S_T^n - \eta_L \sigma_N}\right)^2 + \left(\frac{\tau_L}{S_L^n - \eta_T \sigma_N}\right)^2 + \left(\frac{\sigma_N}{Y_T^n}\right)^2 \tag{2.13}$$

$$\begin{cases} \sigma_N &= \frac{\sigma_2+\sigma_3}{2} + \frac{\sigma_2-\sigma_3}{2}\cos(2\alpha) + \tau_{23}\sin(2\alpha) \\ \tau_T &= -\frac{\sigma_2-\sigma_3}{2}\sin(2\alpha) + \tau_{23}\cos(2\alpha) \\ T_L &= \tau_{12}\cos(\alpha) + T_{31}\sin(\alpha) \end{cases} \tag{2.14}$$

Fibre Kinking ($\sigma_1 < -\frac{X^c}{2}$) and for Splitting ($\sigma_1 > -\frac{X^c}{2}$)

$$FI_{KINK} = Fl_{SPLIT} = \left(\frac{\tau_{23}^m}{S_T^n - \eta_L \sigma_2^m}\right)^2 + \left(\frac{\tau_{12}^m}{S_L^n - \eta_T \sigma_2^m}\right)^2 + \left(\frac{\sigma_2^m}{Y_T^n}\right)^2 \tag{2.15}$$

Thus, rotation to the kink-band plane (ψ) is the focus of stress rotation Equations:

$$\begin{cases} \sigma_2^\psi = \cos^2\psi\sigma_2 + \sin^2\psi\sigma_3 + 2\sin\psi\cos\psi\tau_{23} \\ \tau_{12}^\psi = \tau_{12}\cos\psi + \tau_{31}\cos\psi \\ \tau_{23}^\psi = -\sin\psi\cos\psi\sigma_2 + \sin\psi\cos\psi\sigma_3 + (\cos^2\psi - \sin^2\psi)\tau_{23} \\ \tau_{31}^\psi = \tau_{31}\cos\psi - \tau_{12} + \sin\psi \end{cases} \tag{2.16}$$

As well as for the rotation that follows to the misaligned frame:

$$\begin{cases} \sigma_2^m = \sin^2\theta\sigma_1 + \cos^2\theta\sigma_2^\psi - 2\sin\theta\cos\theta\tau_{12}^\psi \\ T_{12}^m = -\sin\theta\cos\theta\sigma_1 + \sin\theta\cos\phi\sigma_2^\psi + (\cos^2\phi - \sin^2\phi)\tau_{12}^\psi \\ \tau_{23}^m = \tau_{23}^\psi\cos\theta - \tau_{31}\psi\sin\theta \end{cases} \tag{2.17}$$

Fibre Tensile Failure

$$FI_{FT} = \frac{\sigma_1}{X_t} \tag{2.18}$$

where,

α is the represents the angle of the fracture plane under pure compression (α_0 =53 deg);
η_T indicates the friction coefficient caused by transverse shear;
η_L represents the coefficient of longitudinal shear friction;
σ_N, τ_L and τ_T do the traction elements lie in the plane of potential fracture

Where ψ is the bending band angle, which is determined numerically in the interval [0, π] to maximise the failure index of Equation 2.15 and the misalignment angle θ, representative of a coordinate system aligned with the manufacturing defect, the initial misalignment angle θ_0 being caused by the manufacturing problem.

2.3 Optimization

Optimizing the structural weight of aircraft is essential for engineering efficiency, especially in cases where weight is such a determining factor as in aeronautics, making it possible to reduce fuel consumption, increase the aircraft's range and consequently improve its efficiency. Therefore, in the context of composite materials, innovation is fueled by a variety of optimization techniques that are developed to achieve performance and weight reduction objectives without compromising operational safety, ranging from topological and computational algorithms to the use of artificial intelligence.

Topological optimization

Starting with topological optimization, this essentially involves an iterative redistribution of the material using the finite element model and sophisticated algorithms as a guide. To obtain an optimised topology, the process begins by defining the geometry of the structure and the loads applied in the finite element model (FEM), then iteratively going through different design alternatives, gradually eliminating regions of excess material [54], allowing for the creation of lighter but equally robust components, which are particularly useful in aeronautics for wings, fuselage components and to create ribs or reinforcement supports (Figure 2.15). Nowadays, tools such as Virtual.Pyxis [55] can be used in combination with FEM software such as Ansys, Abaqus or Nastran, speeding up the evaluation of creative aircraft structures and enabling rapid prototyping.

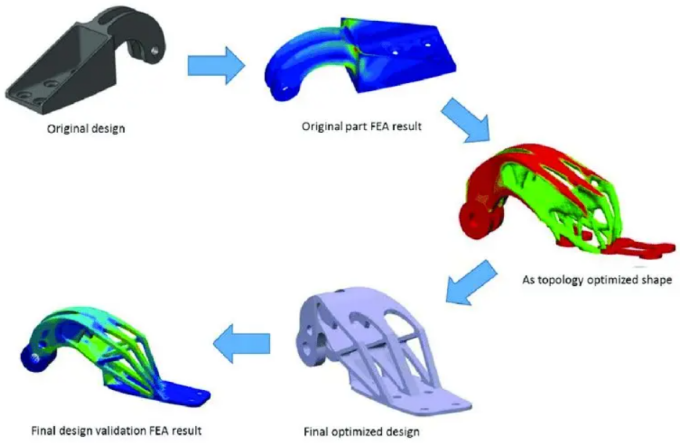

Figure 2.15: Sequence of Topological Optimization [56]

Material composition optimization

On the other hand, we have the optimization of composite materials in terms of their composition, where unlike the previous case where we tried to maintain the composition of the material and reduce its mass by removing material from certain areas of the part, in this case we want to reduce the mass of the part structure by changing the composition/disposition of the material, changing parameters such as stacking sequence, fiber orientation and number of layers. [57].

Composites are therefore highly customisable materials, and all these factors have a direct impact on the final mechanical properties of the laminate, since changing the orientation of the fibres in a particular section can alter and negatively or positively affect load transfer and stress distribution in adjacent sections, affecting the entire structure. This leads to an intensive and iterative study by optimization algorithms of this type to evaluate and compare different variations of the material, trying to obtain the optimum solution in terms of weight, stiffness and resistance for the requirements demanded, with the computational time needed depending on the complexity of the structure and the number of variables and layers, with CAE software playing a leading role in increasing the performance/precision of these algorithms by allowing different versions of the material to be analysed under different load and involvement conditions. In addition, it is important to note that these codes must take into account certain limitations, such as the manufacturing process and regulatory restrictions, since certain stacking sequences or less conventional orientations can make the manufacturing process more difficult, especially in more basic cases such as manual manufacturing. Therefore, the angles available for optimization must be limited from the outset, taking into account the manufacturing conditions and the regulatory process required [57].

Optimization softwares

With this in mind, it is possible to review some of the most important optimization software available, such as the Isight plugin and OptiStruct with the Abaqus software and OptiSLang with the Ansys software.

Starting with OptiSLang, this is a tool provided by Ansys that offers a powerful solution for the optimization, uncertainty quantification, and sensitivity analysis of composite structures, including methodologies such as response surface and genetic algorithms, which allow the structure to be optimized automatically in terms of pairing, fiber direction and thickness, allowing for better material performance, which is evaluated in parallel by the Ansys software and provides comprehensive results on displacements, stresses and deformations at the layer level, allowing for an in-depth analysis of local behavior and possible failure regions. [58] [4].

On the other hand, we have the Isight plugin developed by Firehole Composites and designed to work with Abaqus software, enabling the analysis and optimization of composite materials in addition to reliability analysis and progressive failure analysis, providing features such as damage modelling, visualization of stresses and strains layer by layer and failure criteria. As in the previous case with Isight, users can use sophisticated algorithms to automatically generate optimized layer shapes and orientations to meet specific design objectives, such as maximizing stiffness or minimizing weight, generating The program provides comprehensive reports and graphical representations of layer orientations, as well as visualization tools to evaluate the optimized results. [59].

Finally, OptiStruct created by Altair Engineering, like the previous cases, provides a wide range of optimization tools, but with a focus on gradient-based optimization algorithms specifically designed for structural optimization, including composite structures. In addition, OptiStruct can be easily integrated into widely used finite element analysis (FEA) software programs, allowing the optimization of composite layers according to a variety of design parameters, such as weight, stress and fatigue.[60].

It is important to remember that all these software programs allow for an improvement in design efficiency, minimizing manual iterations and saving time by optimizing the process, however, the fact that they are commercial programs can make the process very expensive, with high license fees, as well as requiring a lot of processing power, especially for large and complicated models, requiring a lot of time and resources to obtain the best results, which can make it difficult to acquire and use them, especially for small companies or individual users.

Optimization algorithms [Evolutionary vs Gradient]

Bearing this in mind and recognizing the importance and added value of structural optimization for an engineering project, this work aims to address the challenges of structural weight optimization in the context of designing tails for ISAR unmanned aerial vehicles (UAVs), through the evolution of a computational tool that is suitable for this specific application and that is customizable.

Therefore, the two main approaches are evolutionary methods, including genetic algorithms, memtics, swarm intelligence, among others, and gradient-based methods, such as Newton or quasi-newton, each of which presents different ways of approaching optimization problems, each with its own advantages and disadvantages [61].

Evolutionary methods, such as genetic algorithms and evolutionary strategies, are inspired by biological evolution, operating by taking into account populations of candidate solutions, applying selection, recombination and mutation operators to find better solutions over time. One of their main advantages is their robustness in complex search spaces, with the ability to explore a wide range of solutions. In addition, they are naturally parallelizable, allowing them to be implemented efficiently in distributed systems; however, they can converge more slowly in simple problems than gradient strategies, requiring careful adjustments to the algorithm's parameters in order to correctly balance the diversity of search (exploration) with the elitist exploitation of solutions (explotation) [61].

On the other hand, gradient methods, such as the descending gradient method, are based on calculating the derivatives of the objective function in relation to the decision variables, using this information to determine the most promising search direction in each iteration. Their great advantage is rapid convergence in well-behaved and convex problems, and they are computationally more efficient, especially in continuous and smooth search spaces, where the derivatives can be calculated accurately and economically. However, they are sensitive to initialization and can get stuck in local minima or saddle points in non-conventional problems, making them more difficult to apply in more complex and highly non-linear situations, such as the optimization of orthotropic materials [61].

With this in mind, throughout this work we will stick to the genetic algorithm approach, sacrificing time and computational resources but ensuring a better guarantee of accuracy in the final result. To this end, we will delve deeper into this type of algorithm in the next section.

2.3.1 Genetic Algorithm

Genetic Algorithms (GA), first proposed by John Holland in 1975, are a powerful class of optimization algorithms inspired by the principles of natural selection and genetics. They offer a versatile approach to solving complex optimization problems in various domains, from engineering to computational biology, making it possible to navigate large solution spaces efficiently, particularly in scenarios where traditional optimization techniques prove inadequate [62].

In the context of optimizing composite structures, genetic algorithms offer distinct advantages, including the ability to efficiently explore large solution spaces, deal with non-linearity and accommodate constraints inherent in the problem domain. For example, optimizing the number of layers in a composite structure requires consideration of factors such as strength, stiffness and weight, which have non-linear relationships, and GA excels in such scenarios, efficiently evaluating various solutions and incorporating constraints into the optimization process through the fitness function. In addition, genetic algorithms mitigate the risk of getting stuck in local optima , which

is a common challenge in optimization, by employing stochastic elements such as random mutation and recombination. This stochastic nature allows genetic algorithms to traverse the solution space more comprehensively, increasing the likelihood of discovering globally optimal solutions [63] [62]. With this in mind, here is a brief summary of how these algorithms work, with Figure 2.16 providing a schematic line of thought.

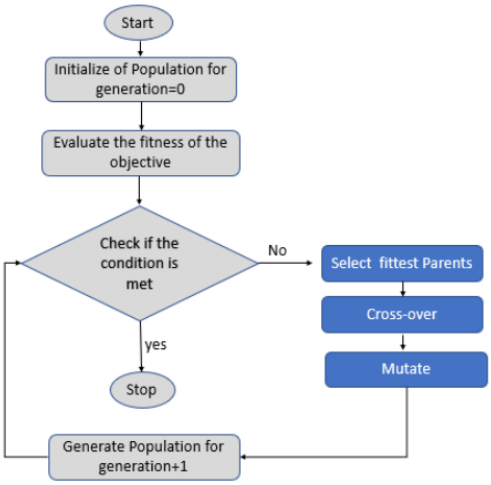

Figure 2.16: Flow diagram for a generic GA

Initial population - A genetic algorithm begins by creating an initial population of random chromosomes representing potential answers to the problem to be solved, in order to match the set of solutions to a set of individuals.

To generate this randomness, quasi-random sequences of integers or a pseudo-random technique can be used, the most popular method of generating randomness being the former. Since it is impossible to produce completely independent random numbers, classical generators such as the Fibonacci quadratic congruent can be used. On the other hand, in quasi-random sequencing, the goal of the generation is linked to both the dispersion and independence of the subsequent values, in order to cover the entire search space, in which case the diversity of the population in a quasi-random generation is usually higher than in a pseudo-random generation.

In light of this, it is crucial to keep in mind that the population size should be appropriate for the complexity of the issue and the available computational resources. This is because the goal is always to strike a balance between computational cost and efficiency, keeping in mind that a large population would result in significantly higher computational costs, while a small population would not allow for adequate space to explore the research domain. [61]. It is also important to remember that large and small populations have negative effects on the system. On the one hand, a small population implies that too many generations are needed to reach the desired solution, while a large population indicates that not enough generations are generated to find an optimum, which can decrease genetic drift and the loss of alleles, while improving overall results by increasing merit more slowly in the early stages. This leads to the conclusion that the unique requirements and attributes of each problem determine the optimal parameter value.

Research Space - After defining the initial population, it is necessary to define the search space by encoding the different potential solutions to the problem (the phenotype) in the genetic material of each individual (the genotype). The term "representation" is another term used in the literature. Thus, the most common coding method is classical binary coding (Figure 2.17), or other variants of it, such as Gray's code. It follows five steps [61]:

1. Specifying the variables for the project, Equation 2.19:

$$X = (x_1, x_2, ..., x_n) \tag{2.19}$$

2. Representation in binary, Equation 2.20:

$$S = b_1 b_2 ... b_n \tag{2.20}$$

3. Defining each project variable's domain, Equation 2.21:

$$l_i = 2^{l_{c_i}} - 1 \tag{2.21}$$

where l_{c_i} is the bit-count allotted to every design variable;

4. Decoded subsequence computation, Equation 2.22:

$$x_{i,bin} = \sum_{k=0}^{l_i - 1} 2^k b_{i,k} \tag{2.22}$$

5. Find each design variable's real value, Equation 2.23:

$$x_i = x_i^{inf} + \frac{x_i^{sup} - x_i^{inf}}{2^{l_i - 1}} x_{i,bin} \tag{2.23}$$

with $x_{inf}^i \leq x_i \leq x_{sup}^i, 1 \leq i \leq n$.

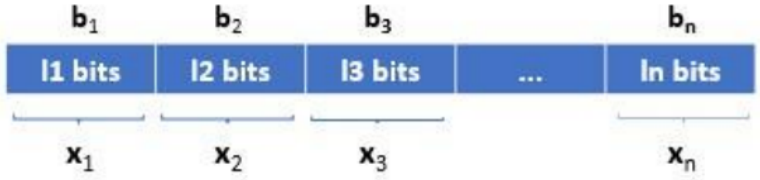

Figure 2.17: Binary code [61]

Function of Merit - Once the initial population has been built, it is possible to evaluate from an evolutionary point of view the relative value of a solution/individual in the context of the population it is part of. This evaluation can be carried out using a merit function based on the objective function.

- Objective function - *"Measure of performance with respect to a particular set of gene values, independently of any other chromosome (String)"*[61].
- Merit function - *"Transforms the objective function into an allocation of reproductive opportunities in relation to other members of the population"* [61].

Thus, each chromosome is evaluated using a fitness function after initializing the population, which objectively evaluates the quality of the solution and its adherence to the objectives and constraints of the task, and the resulting fitness values are fundamental for selecting parents for reproduction. To this end, the construction of the merit function must take into account a few key factors. Firstly, it must be smooth and regular to ensure that the chromosomes with adequate fitness are spatially close to the chromosomes with the highest fitness, secondly, it must

objectively reflect the value of the chromosome and, thirdly, the non-admissible solutions (invalid chromosomes) must take on the role of leading in the direction of the space of admissible solutions [61].

Therefore, the fitness or merit function can be used to mathematically express the quantification of the relative value of a solution or an individual in its population, seeking to convert the objective function - a measure of performance in relation to a particular set of genes - into a "pool" of breeding opportunities in relation to other members of the population.

This procedure can be carried out using a normalization process or a merit function by evaluation value. The application of a normalization process that takes into account the presence of defective chromosomes - which are the consequence of violating the rules and are associated with unacceptable solutions - provides an example of a merit function. The Equation 2.24 provides an expression for the merit function that is based on a normalization method.

$$Mer\left(\mathbf{x_i}\right) = \frac{1}{f\left(\mathbf{x_i}\right) + \Gamma\left(\mathbf{x_i}\right)}, com\left(\mathbf{x_i}\right) + \Gamma\left(\mathbf{x_i}\right) \neq 0 \tag{2.24}$$

Inclusion of restrictions - Constraints are present in most real-world situations and have a substantial impact on the performance of the optimization algorithm, so it is important to evaluate how they are incorporated. There is no uniform approach to integrating constraints into the search process. Further study is therefore required to determine which technique most improves the effectiveness of the genetic algorithm. The external penalty is an example of this type of approach, which creates a penalty function according to the "distance" of the solution being analyzed from the set of acceptable solutions, the penalty being introduced by a set of punishment functions u_j, which are stated as follows, Equation 2.25:

$$u_j(\mathbf{x}) = \max\left[0, g_j(\mathbf{x})\right], se1 \leq j \leq q \tag{2.25}$$

Thus, the adaptive penalty approach, as follows, is used to evaluate the solutions to the minimization problem at each iteration, as we can see in Equation 2.26 .

$$Aval(\mathbf{x}) = f(\mathbf{x}) + (Ck)^{\alpha} \sum_{j=1}^{m} \left[u_j(\mathbf{x})\right]^{\beta} \tag{2.26}$$

Genetic selection operator - A method of identifying individuals (chromosomes) for reproduction or population survival is called selection. The proportional selection method is one way of choosing candidates based on their merits, while the ranked selection method is another way of choosing candidates based on their ranking rather than their merits.

The chromosomes with the highest fitness are then preferred for reproduction during the selection phase. In this phase, a set of superior chromosomes can be assembled using selection techniques such as roulette or selection based on universal stochastic sampling or selection based on sorting such as linear sorting, exponential sorting, tournament selection, trick selection, among others.

The roulette wheel approach (Figure 2.18), which was the first selection strategy suggested for genetic algorithms and remains the most popular among academics, is an illustration of a proportional selection methodology. It has the advantage of having a probability of selection based on merit, with the candidates being organized in a wheel, with the most capable and deserving being chosen more often, as they will take up more space on the wheel.

However, due to the presence of over-fit and under-fit individuals, the strength of selection is typically low, convergence occurs prematurely and the rate of convergence decreases with successive generations [61]. Equation 2.27, a stochastic function, provides the likelihood of choosing an individual.

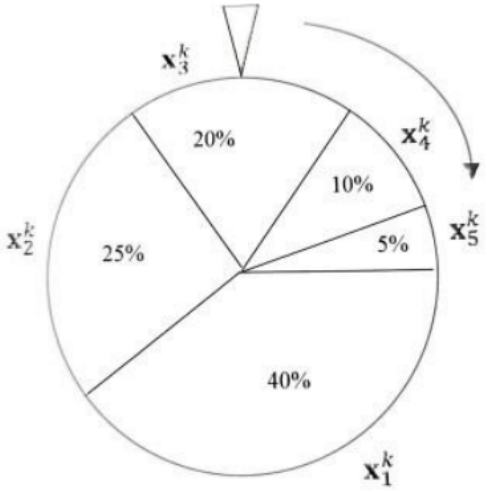

Figure 2.18: Selection by roulette method [61]

$$P\left(\mathbf{x_j}^k\right) = \frac{f\left(\mathbf{x_j}^k\right)}{\sum_{j=1}^{N_{pop}} f\left(\mathbf{x_j}^k\right)} \tag{2.27}$$

, $f\left(\mathbf{x_j}^k\right)$ represents the value of the merit function

Crossover - Is considered in the literature to be the most important operator in evolutionary research [61]. This is a genetic operator that combines the genetic material of two parents already chosen to create a new set of solutions or individuals. It is a complementary operation to mutation and is normally used when two offspring chromosomes are produced for each pair of parents, involving the exchange of genetic material between specific parental chromosomes. This operation simulates genetic recombination and promotes genetic diversity through the use of strategies such as segmented, uniform, multi-point and single-point crossing, among others that affect the exploration of the solution space. It is essential to remember that the nature of the problem to be solved and the biased combination associated with the operator's search style in the design space determine the operator's effectiveness, with each approach being more suitable for dealing with a certain type of problem [64].

As mentioned above, an example of this process is uniform crossover. It starts by choosing two parent solutions from the current population, then generating a random number between 0 and 1 for each gene position in the offspring. If the random number is less than 0.5 (or any predefined probability), the gene is inherited from the first parent, otherwise it is inherited from the second parent, repeating this process until a complete offspring solution is generated. The main characteristic of this method is that each gene in the offspring has the same probability of coming from one of the parents, hence the term "uniform". This randomness helps to introduce diversity into the offspring, helping to explore the search space more effectively, preventing the algorithm from getting stuck in local optima and helping to find global solutions. However, it can also lead to the loss of potentially beneficial genetic information due to its randomness, and should be combined with elitist strategies (Figure 2.19).

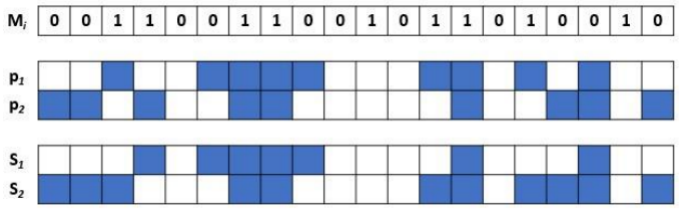

Figure 2.19: Uniform Crossover [61]

Mutation operator - Last but not least, mutations are a type of genetic operator that introduces small changes to a subset of the population, with a corresponding probability (P_m) of each gene being mutated. This causes random changes in the chromosomes of the offspring, guaranteeing genetic diversity and avoiding early convergence of the genetic algorithm, and is controlled by a mutation rate that balances the trade-offs between exploration and exploitation, allowing the discovery of new solution zones. It is also important to take precautions when defining and applying a mutation operator to ensure that valid solutions are generated and that all solutions in the search space can be reached, respecting ergodicity and validity, respectively. Thus, controlling the probability of mutation is also crucial in order to minimize the change that the mutation operator induces (locality), i.e. that small modifications to the genotype result in small modifications to the phenotype [61].

Uniform mutation, regularly distributed mutation and gene swap/flip-bit mutation are some examples of this process. The latter is a mechanism that induces random changes with a probability P_m in the binary code (and therefore in its genetic material), which can occur bit by bit or in a sequence of bits , Figure 2.20.

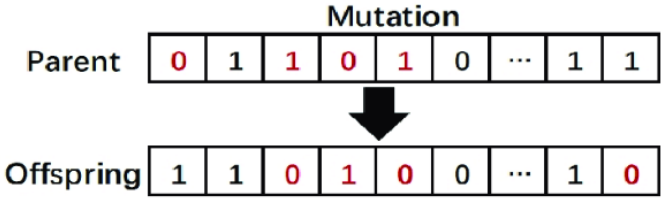

Figure 2.20: Flip-Bit Mutation [65]

After crossover and mutation, the offspring replaces certain individuals in the current population, with the replacement strategies, typically generational or elitist replacement, shaping the next generation, improving the solutions over the iterations and influencing the speed of convergence and the preservation of the solution [66].

Convergence and stopping criteria - Normally, there are two main categories of stopping conditions that guide the search of a genetic algorithm:

- The first stopping criterion is based on the genotype and ends when the population converges to a specific degree with respect to its chromosomes. In other words, the genetic algorithm ends when the population reaches the convergence point of the number of genes that have converged on an allele.
- The second criterion is based on phenotyping, evaluating the success of the algorithm over the last n generations, as determined by the designer. The algorithm is considered to have converged when this measure, which is often the average merit value of the population, produces a value greater than a predetermined threshold, at which point evolution is abruptly halted.

Thus, the maximum number of generations, the increasingly rare changes in the subsequent generations, the maximum computational time limit, or even proximity to the solution or level of merit achieved for x part of the population can all be defined as convergence and stopping criteria, while at the same time avoiding either an excessively long convergence or an excessively early convergence. The research is guided based on a set of criteria that specify its field of action. Determining a suitable value for, say, a fixed number of generations, can be challenging when defining these requirements. Other issues include specifying appropriate values for the corresponding parameters [61].

Setting the algorithm parameters - In order to properly define and create an executable version of a genetic algorithm, additional details must be considered in addition to those mentioned above. One such detail is how to control the "algorithm parameters," which constitute the genetic algorithm's complete definition. Setting parameter values can be done in two major ways:

- The first method is to run the code with these values after determining appropriate values for the parameters before running the programmed code. This is how algorithms are defined in the industry. This modification is made by experimenting with various parameter values and choosing the ones that get the best outcomes for the issue being resolved [61].
- Parameter control, on the other hand, refers to starting a run with initial parameter values that are modified while it runs. Therefore, it is acknowledged that depending on the issue at hand, genetic algorithms may need parameter modifications. Ideally, the algorithm should regulate the parameters in the evolutionary search to make the precise adjustments required for each challenge [61].

Elitist strategies and the balance between free and regulated exploitation - To ensure that the genetic algorithm (GA) seeks optimal solutions to problems with high quality, it is typically necessary to incorporate elitist methods, which seek to protect the most exceptional members of society - known as the elite - for future generations. This is important because it prevents beneficial characteristics from being lost during the evolutionary process. Elitist methods contribute to better convergence of the GA and a shorter time to the optimal solution, protecting the elite. They also improve the quality of the finished product, since the advantageous features are preserved and passed down through the generations. This is especially significant for complicated problems where the quality of the answer is crucial [61].

In addition,another crucial factor is finding the right balance between extensive unconstrained exploration and controlled exploration.In order to avoid early convergence and ensure that various parts of the design space are searched, extensive unconstrained exploration allows the GA to explore the search space widely at the beginning of the search. On the other hand, controlled exploration, also known as intensification, uses the best solutions already discovered to guide the search to more promising regions of the search space as it progresses. Both thorough free exploration and controlled exploration are essential to the GA's success, thus striking a balance between them is critical.

While excessively restricted exploration might cause early convergence and stagnation in local optima, excessively comprehensive free exploration can result in ineffective searches and lack of convergence. Typically, a well-programmed genetic algorithm should favor a more pronounced initial exploration and, over the generations, favor the search for optimal solutions. In other words, at the beginning we should favor exploration and greater versatility and as the code progresses we should favor the search for optimal solutions by favoring the individuals with the greatest fitness [61].

2.4 Surrogate model

Surrogate models, or substitute models, are simplified representations of complex systems that are used in place of the system itself during analysis or optimization processes. They are built on the basis of available data from the original system or simpler computer simulations, representing an important relevance in the field of optimization, providing a faster and more efficient way of exploring the search space, allowing more detailed analyses to be carried out at a better cost/time ratio. To build these surrogate models, various statistical or machine learning techniques can be applied, such as regression, neural networks, support vector machines, among others, and especially in an industrial context, these models are a fundamental aid, especially in software that performs complex numerical analysis, such as computational fluid dynamics (CFD) and the finite element method (FEM), allowing for faster numerical approximation and the need for fewer iterations [67] [68].

Therefore, when compared to approaches such as pure genetic algorithms which employs a direct evaluation method, carefully analyzing all potential solutions through practical simulations, often requiring the execution of finite element simulations for each iteration of the genetic code, a greater need for computational and time resources is created, making it especially limited in large scenarios. On the other hand, an improved GA that uses a surrogate model employs a more resource-efficient strategy allowing for a more efficient exploration of the search space, as it does not require the direct evaluation of the original system at each iteration, significantly reducing the time needed to run the simulations or experiments required during optimization, making the most of the available CPUs, making it ideal for large-scale situations such as the CFRP optimization carried out in this report [68].

So in Figure 2.21 we can see a comparison between a pure genetic-assisted optimization algorithm thinking scheme Figure 2.21 a and in Figure 2.21 b the improved version with the integration of the surrogate model.

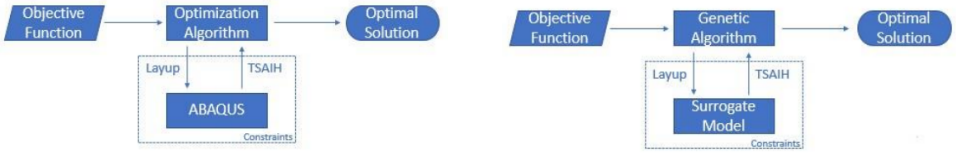

a) Flow chart of a Pure Genetic code

b) Flow chart of a Surrogate Genetic code

Figure 2.21: Pure Genetic code vs with Surrogate model [3]

However, surrogate models also have some disadvantages compared to pure genetic algorithms, typically presenting a lower accuracy, since the pure GA directly evaluates the solutions through detailed simulations, the surrogate model introduces approximations, which can generate deviations from the exact solutions, and this balance between accuracy and efficiency is a compromise to select the most appropriate optimization approach. On the other hand, another difficulty is ensuring the accuracy of the substitute model, as it must be able to accurately capture the behavior of the original system, which can be difficult in cases where the system is highly complex or non-linear, or when there is limited data available to build the model. As such, the quality and efficiency of these forecasting models is typically associated with the ability to understand the link between the input variables and the corresponding system response, leading to a correct selection of data points and investigation of the input space, and it is crucial to obtain a large and representative data set that sufficiently covers the input space [3] [69].

In this context, methods such as Design of Experiments (DoE), based on a statistical approach, have emerged as a crucial approach to ensuring the efficiency of these models, providing a systematic methodology for planning, executing and analyzing experiments, with the aim of understanding and improving processes, products and systems, properly structuring the data collection process and ensuring that the information obtained is significant and representative of the system under study, manipulating the input variables (factors) to observe their impact on the output variables, products and systems, structuring the data collection process appropriately and ensuring that the information obtained is meaningful and representative of the system under study, manipulating the input variables (factors) to observe their impact on the output variables (responses) and identifying the optimal configurations that lead to the desired results. It is therefore important to note that an ineffective sampling strategy can result in biased or insufficient data, which in turn can generate incorrect models and unreliable forecasts. [70] [71].

One of the most widely used DoE sampling techniques is Latin Hypercube Sampling (LHS). Originating in 1970, this method is based on the definition of a Latin square where for a given order n an n x n matrix (grid) is generated, which includes values from a sample, where for each row or column there are only one, spreading this context to multiple directions where only one hypercube includes a given sample in each coordinate axis or axial direction, the main objective being to achieve a uniform distribution of samples across multidimensional space. To do this, the LHS divides each variable into p equally probable intervals or bins, and then includes the samples ensuring that only one is allocated per interval [72] [73] [74]. An example of a Latin hypercube sample with two variables and eight samples can be seen in Figure 2.22.

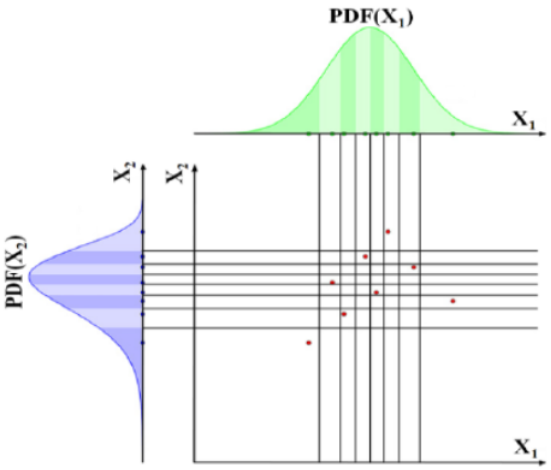

Figure 2.22: Latin hypercube sampling technique involving two variables and eight samples [75]

So some advantages of this method over other alternatives are its flexibility and efficiency, allowing effective coverage of design spaces of any size, guaranteeing a comprehensive representation of the relationships between the variables involved, also providing an efficient allocation of samples, distributing the points in a balanced way, which maximizes the representatives of the data and minimizes redundancy. Another significant advantage is the ease of optimization, since it can be adjusted to meet specific objectives, such as maximizing the distance between data points or ensuring uniform coverage of the sampling space. Finally, it makes it possible to carry out a quasi-random selection, avoiding repetition and guaranteeing effective coverage of the sampling space.

In contrast to the LHS, there are other sampling techniques adapted for computational experiments, ranging from simple techniques such as direct sampling and stratified sampling to more

complex models such as Hammersley designs, Box-Behnken designs, fractional factorials, response surface designs, orthogonal sampling and others. Hammersley designs, Box-Behnken designs, fractional factorial designs, response surface designs, orthogonal sampling and others. In Figure 2.23 we can see a comparison between LHS and random sampling where we can observe the better uniformity and search efficiency of the LHS compared to the random model, which although simpler, reduces efficiency and can introduce efficiency problems when it comes to properly exploring the possibilities of samples. This is due to the fact that the sample points are generated completely randomly, not taking into account points from past samples, nor is it necessary to know in advance how many sample points will be needed, which strongly conflicts with the LHS where it is necessary not only to know how many points will be used in the sample and to have a reference of their position (row and column), but also a guarantee that the random numbers generated adequately represent the real variability [73] [74].

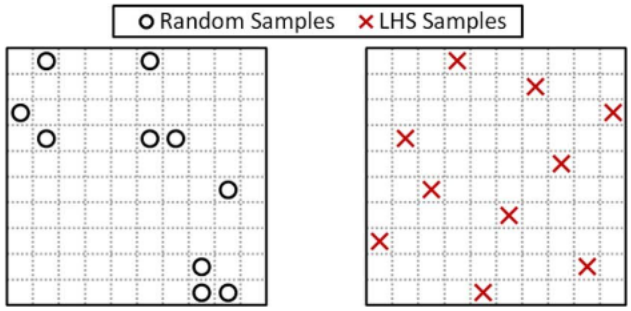

Figure 2.23: Examples of Latin hypercube sampling and random sampling in two dimensions are compared (every row and column is sampled with LHS) [73]

With this in mind, these experimental designs are integrated into the alternative model building process, where they are used to generate a diverse set of training data, used to train the substitute model, whether based on regression, machine learning or another suitable technique. Once trained, the substitute model can be used to make quick and accurate predictions about the system's behavior under different input conditions. Finally, it is important to note that the choice between these methodologies depends on the specific requirements of the project, based on considerations such as the desired levels of accuracy, the computational resources available and time constraints.

It is also important to note that there are several software tools available to help build and analyze surrogate models, such as Matlab with its toolboxes that include functionalities for fitting regression models and global optimization such as MATSuMoTo and several Python libraries, including PyDoE, Scikit-learn and Surrogate Modeling Toolbox (SMT), offering integrated functionalities for design of experiments (DoE) and regression methods.

To evaluate the performance of these methods, there are several common evaluation metrics, such as the coefficient of determination (R^2) and the mean squared error (MSE), which can be applied to both regression models and surrogate models to assess their accuracy and performance. In the case of the R^2, present in Equation 2.28, it shows the proportion of the variation in the data that the model can explain, being represented in a range of [0, 1], being better for values closer to 1 and worse for values close to 0. The mean squared error (MSE), shown in Equation 2.29, determines the average variation between the predicted values and the actual values, and the quality of this parameter is better the closer it is to 0 [76].

$$R^2(y, \hat{y}) = 1 - \frac{\sum_{i=1}^{n}(y_i - \hat{y}_i)^2}{\sum_{i=1}^{n}(y_i - \bar{y})^2} \tag{2.28}$$

$$MSE(y, \hat{y}) = \frac{1}{n}\sum_{i=1}^{n}(y_i - \hat{y}_i)^2 \tag{2.29}$$

where,

$\hat{y}-$ Predicted values (surrogate model)
$y-$ Real value
$\bar{y}-$ average value of y and $\hat{y}$
$n-$ Quantity of test specimens

Note that other methods often used to evaluate model performance are the mean absolute error, median absolute error and the relative average absolute error [76].

2.4.1 Regression methods

The creation of surrogate models relies heavily on regression techniques, which are used to estimate the associations between a dependent variable and one or more independent variables, and can be used to simulate the future relationship between variables and assess how strongly the variables are related to each other. With this in mind, in the environment of this project, more specifically in the realization and improvement of the optimization code, regression techniques are crucial for analyzing complex data sets, the influence of many variables, which can be considered at once when using multiple regression, facilitating hypothesis testing and informed decision-making.

Thus, there are several versions of regression analysis, including multiple linear, non-linear and linear, with linear models being the simplest and multiple linear models the most commonly used. Non-linear models are usually used when dealing with increasingly complex data sets, where there is a non-linear relationship between the independent and dependent variables [77].

With this in mind, we are going to look at various techniques in the field of regression and multiple regression, each with unique assumptions, advantages and disadvantages, among which we can list some such as Gaussian process regression, linear regression, polynomial regression and regression using regularization techniques (such as Lasso, Ridge or elastic net) [77] [78].

Linear Regression: models the relationship between input characteristics and a target variable, with coefficients $w = (w_1, w_2, ..., w_p)$, by fitting a linear equation, with the aim of minimizing the sum of squared residuals. As such, it can deal with simple and multiple linear regression problems, integrating perfectly with software features such as data pre-processing and cross-validation, and is widely used not only for its simplicity and interpretability, but also for its effectiveness in capturing linear relationships between variables. However, it assumes linearity between variables and is sensitive to outliers and may not capture complex non-linear relationships. Equation 2.30 represents Linear Regression [79] [80] [81], which can be mathematically simplified as follows.

$$y = w_0 + w_1x_1 + +w_2x_2 + ... + w_nx_n + \epsilon_i \tag{2.30}$$

$$\min_{\mathbf{w}} ||\mathbf{X}\mathbf{w} - \mathbf{y}||_2^2$$

where,

y - Dependent Variable
w_0 - Population y intercept
w_1, w_2, w_n - Population Slope Coefficient
x_1, x_2, x_n - Independent Variable
ϵ_i - Random Error term

Polynomial Regression: It is an expanded concept of the previously explained linear regression, which introduces polynomial terms in the independent variables. In this way, unlike the linear version, it allows us to model a relationship between the dependent variables and one or more independent variables, using a polynomial of degree n. This makes it possible to capture and represent non-linear relationships and patterns. Finally, it is important to bear in mind that the degree of the polynomial n chosen determines the complexity and flexibility of the model, and Equation 2.31 shows the representation of this model [81].

$$y = w_0 + w_1x_1 + w_2x_2 + ... + w_nx_n + w_{1+1}x_1^2 + w_{1+2}x_1x_2 + ... + w_{1+n}x_n^2 + ... + \epsilon_i \tag{2.31}$$

Ridge Regression: is a technique used in statistics and machine learning to mitigate the problem of multicollinearity in linear regression models and avoid overfitting. In linear regression, multicollinearity occurs when the independent variables are highly correlated with each other, leading to unstable estimates of the regression coefficients, making the model sensitive to small changes in the data. Ridge regression solves this problem by adding a penalty term proportional to the squared coefficients to the loss function, trying to drive the coefficients towards 0, but not to 0, controlling not only the complexity of the model but also reducing the impact of the multicollinearity explained earlier [81] [82].

$$\min_{\mathbf{w}} ||\mathbf{X}\mathbf{w} - \mathbf{y}||_2^2 + \alpha||\mathbf{w}||_2^2$$

where, α is the regularization parameter.

The term [$\alpha||\mathbf{w}||_2^2$] in Equation 2.4.1 is the penalty term, also known as the regularization term (L2), which penalizes large values of the coefficients, reducing them to zero. The higher the value of α, the greater the amount of shrinkage applied to the coefficients, resulting in a simpler model with less variance, but potentially more biased.

With this in mind, this model is particularly useful when dealing with high-dimensional data (i.e. data with a large number of predictor variables) and when there is multicollinearity. By penalizing large coefficients, Ridge Regression helps stabilize coefficient estimates and reduces the model's sensitivity to collinearity, thus improving its predictive performance.

Lasso Regression: is a type of linear regression technique used for variable selection and regularization, and is particularly useful when dealing with data sets that contain a large number of characteristics, some of which may be irrelevant or redundant.

In standard linear regression, the aim is to minimize the sum of the squared differences between the observed and predicted values. However, in situations where there are many predictors (features), overfitting can occur, leading to poor generalization performance on new data. Lasso regression addresses this issue by adding a penalty term to the objective function of standard linear regression, which encourages sparsity in the coefficient estimates [81] [83].

$$\min_w \frac{1}{2n_{samples}}||\mathbf{Xw} - \mathbf{y}||_2^2 + \alpha||\mathbf{w}||_1$$

The term $\alpha||\mathbf{w}||_1$ is the penalty term also known as the regularization term (L1), where α represents the absolute values of the coefficients. This penalty encourages small coefficient values and effectively reduces some coefficients to zero, effectively performing feature selection by eliminating irrelevant predictors from the model.

Thus, the similarity between Lasso Regression and Ridge Regression is visible, both being regularization techniques used in linear regression models to avoid overfitting and improve generalization performance. However, they also have distinct differences in their penalties and effects on the resulting models. In Lasso regression, the penalty is the sum of the absolute values of the coefficients, while in Ridge regression, it is the sum of the squares of the coefficients.In addition, Lasso regression has the effect of shrinking the coefficients of the least important features exactly to zero, performing automatic feature selection, which makes it suitable for dealing with high dimensionality. On the other hand, Ridge shrinks the coefficients towards zero, but rarely sets them to exactly zero, making it more suitable for dealing with multicollinearity without eliminating features. So, while Lasso can produce sparse solutions, Ridge generally does not. However, the choice between Lasso and Ridge depends on the specific characteristics of the data set and the objectives of the model.

ElasticNet Regression: ElasticNet regression is a type of linear regression that combines the penalties of both L1 (Lasso) and L2 (Ridge) regularization techniques. It is particularly useful when dealing with high-dimensional data where there may be multicollinearity among the predictors [81] [84].

$$\min_{\mathbf{w}} \frac{1}{2n_{samples}}||\mathbf{Xw} - y||_2^2 + \alpha\rho||\mathbf{w}||_1 + \frac{\alpha(1-\rho)}{2}||w||_2^2$$

where, α and ρ are regularization parameters that control the strength of the penalties for L1 (ρ) and L2 (α) regularization.

So, ElasticNet regression balances between Lasso and Ridge penalties, when $\rho = 0$, it becomes Ridge regression, and when $\alpha = 0$, it becomes Lasso regression. Therefore, this method aims to minimize the aforementioned objective function, adjusting the coefficients (w) accordingly, taking into account the model's fit to the data (RSS) and the regularization penalties, helping to reduce overfitting and deal effectively with multicollinearity. In practice, the optimal values of ρ and α are usually determined using techniques such as cross-validation, and libraries such as scikit-learn in Python provide implementations for ElasticNet regression.

Gaussian Regression (GPR): is a machine learning method used for regression and classification tasks. It is an example of a non-parametric Bayesian technique which, instead of estimating specific parameters, models the distribution of a function. The fundamental idea behind GPR is to consider a function as a set of random variables, representing it as a Gaussian process, drawing a distribution over functions, making it possible to model the uncertainty inherent in predictions.

To do this, GPR performs three fundamental tasks, drawing a prior distribution over functions, conditioning the prior distribution on the observed data and creating forecasts for new inputs based on the posterior distribution. The selection of the prior distribution is crucial because it establishes the space of functions that the model can produce and has a major impact on the forecasts. On the other hand, Bayes' theorem is used to update the prior distribution to a posterior distribution based on the observation of the data, taking into account the likelihood of the model parameters, creating as a consequence a posterior distribution on functions, which represents the knowledge obtained from the data. The mean and variance of this posterior distribution are then calculated to generate predictions for new inputs, since the mean indicates the expected value of the output variable, while the variance denotes the uncertainty related to the prediction.

Finally, it is important to note that the adaptability and effectiveness of GPR derive from its ability to provide probabilistic forecasts and capture the intrinsic uncertainty of the data, making it especially useful for tasks where estimating uncertainty is crucial, such as making decisions in the face of ambiguity or in situations where data sets are scarce. However, it is important to note that the calculation and inversion of covariance matrices required for large data sets can result in higher processing costs.[81].

2.5 Aircraft sizing

2.5.1 V-n Diagram

In aeronautics, regardless of the flight situation we find ourselves in, whether in still air, in a maneuvering situation or during in-flight turbulence such as gusts, there are always load factors (n) that are responsible for the increased loads on the aircraft. This leads to the need to establish and limit load factors (representing the relationship between Lift and the weight of the aircraft) and maximum speed values in order to determine the aircraft's performance. In this way, the flight envelope is responsible for graphically defining the operational limits of an aircraft, in relation to the maximum speed and load factor given by a given atmospheric density, being the region in which it is safe to operate an aircraft, and it can also be said that if an aircraft flies outside the envelope it may suffer damage and the limits must not be exceeded. It therefore consists of two independent analyses, the maneuvering analysis and the gust analysis (Figure 2.24) [2].

Starting with the Maneuver Sub-Diagram, this represents the region in which the aircraft can maneuver without suffering structural damage, beginning with the positive and negative stall curves which represent the relationship between the minimum lift for which the aircraft can make the flight viable and the load factor (n) of the maneuver performed, which represents the relationship between the weight of the aircraft (W) and the Lift aerodynamic force (L), n=L/W. In this phase, there are some speeds of particular interest, such as positive and negative V_S (Figure 2.24), which represent the stall limit condition in which the aircraft is still able to generate enough lift to maintain straight and level flight, and V_A and V_G (Figure 2.24), which represent the maximum speed for fully extended flaps at which the upper and lower limit of the load factor is reached, respectively. Next we have two straight lines, which define the lower and upper levels of this sub-

diagram and represent the maximum value for the positive and negative load factors, ending with a vertical limitation referring to the maximum dive speed, representing the highest certified speed and consequently the highest speed at which the aircraft can fly without suffering structural damage determined by the strength of the components under maximum dynamic load, which should not typically be less than 1.4 times the cruising speed, (Figure 2.24)[85][2].

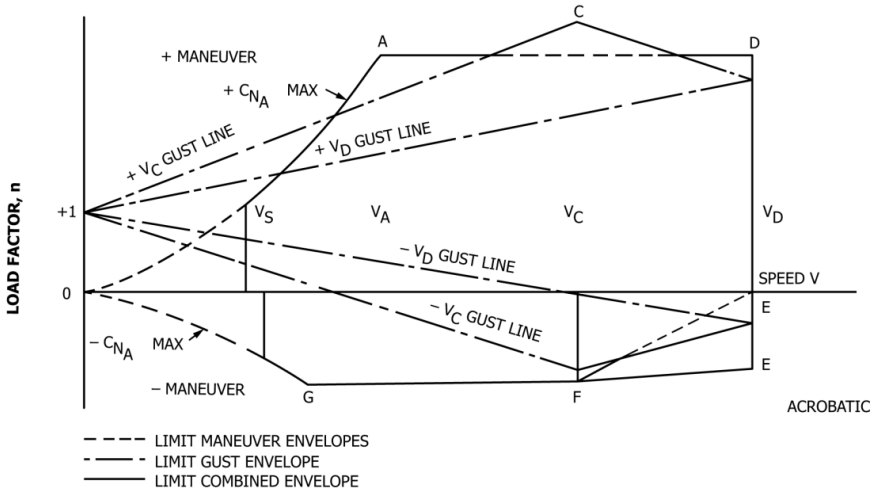

Figure 2.24: V-N Diagram [2]

The second analysis is the gust sub-diagram, which graphically represents the limits within which an aircraft can safely operate under gust load conditions, defining the combination of gust intensity and aircraft speed that the aircraft structure can withstand without exceeding the design limits. This calculates the load factor value for negative and positive gusts for V_C and V_D speeds, linearly intersecting these values typically with the load factor axis of ordinate 1. Note that in more conservative analyses, the negative gust lines are intersected at ordinate 0 of the load factor axis. Therefore, this analysis is of great importance since agitations caused by turbulence can worsen the flight condition by sharply increasing the load factor (Figure 2.24) [85].

Finally, the total envelope is made up of the intersection of these two sub-diagrams, allowing for a balance between these two independent analyses. It should be noted that these factors are typically subject to a safety factor of around 1.5, differentiating the situation of Limit condition from Ultimate condition, and simplifications such as removing the area of the diagram for speeds below V_S are generally applied, as they represent flight situations that are not very representative of reality [85][2].

It is also important to note that small differences in V-n diagrams may exist according to the specific regulations of different aviation authorities, such as the FAR (Federal Aviation Regulations), JAR (Joint Aviation Requirements) or CS (Certification Specifications) regulations of EASA (European Aviation Safety Agency). Due to the greater or lesser demands and redundancy of the regulations and the difference in aircraft configuration, it is easy to see that the safety margins applied to, for example, commercial aircraft (CS-25), or an aerobatic aircraft, require different approaches.

Chapter 3

Tail-Boom Concept Design

3.1 Tail configuration concept

This project began by studying and identifying various twin boom tail configurations, already introduced in Section 2.3.1, such as conventional twin boom, Twin boom T, Twin boom H and twin boom V for inverted configuration, (Figure 3.1), analyzing their possible integration into the ARX and making comparisons in terms of stability, performance, maneuverability and adaptability, allowing not only to define the starting point and working basis of the project but also to improve the framework of the project.

Figure 3.1: Different tail configurations for the type of boom : (a) Twin boom conventional, (b) Twin boom T, (c) Twin boom V invertida, (d) semi-inverted V-tail boom [23]

The first comparative analysis taken into account was the adaptability of the tails to the positioning of the aircraft's propeller, since unlike most civilian aircraft, fixed-wing UAVs often have the propeller in the center rear area of the aircraft, which has a negative impact both on the performance and efficiency of the control surfaces (elevator and rudder), but also on the drag and efficiency of the aircraft, due to the turbulent wake created by the rotation of the engine blades. As such, configurations such as twin boom conventional or twin boom H are typically interesting for situations where the aircraft's propellers are located on the wings, and twin boom inverted V or twin boom T are especially useful for situations where the propeller is located in the center of the aircraft, reducing the impact of turbulence created by the engine and the downwash of the wing, reducing drag and allowing the Tail's wing profiles to work on less turbulent fluid, increasing their efficiency [86][87][88].

This can be seen in the study carried out in 2020 by Khadka,[89], which compared a fixed wing UAV with two different twin boom configurations (H-tail and inverted V-tail), observing a reduction of approximately 19 % in the drag of the aircraft when using inverted V-tail compared

to H-tail. Figure 3.2 shows a CFD streamline analysis of the turbulence created by the engine, and shows the greater interaction with the tail in the H-tail configuration compared to the inverted V-tail configuration.

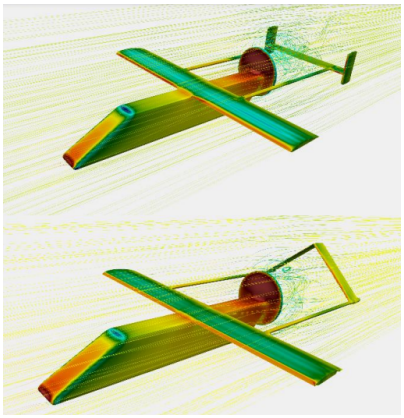

Figure 3.2: Full body H-tail and inverted V-tail arrangement volume flow visualization [89]

Taking into account the previous analysis, it was possible to reduce the analysis options to inverted twin boom V or Twin boom T. The second analysis proposed was a comparison of stability, performance, maneuverability, manufacturing and cost, in which, after consulting various comparative studies in the literature, was possible conclude the following points:

Stability/Maneuverability

Starting with the T-shaped twin boom, this is the best alternative to the conventional configuration, when it cannot be used due to factors such as those mentioned in the previous study, as mentioned in [23], also allowing according to [23], to maintain a short turning radius even past the critical angle of the aircraft, thus being considered optimal for situations requiring high maneuverability, presenting greater stability at higher angles of attack compared to the inverted V-tail configuration, however this configuration has the major problem of being subject to deep stall as discussed in Section 2.1.3, [87] [90]. On the other hand, the inverted V-shaped configuration can offer other advantages such as greater lateral and directional stability, especially in crosswind situations, but it is important to take into account its greater complexity in controlling flight surfaces due to mixed control, which is typically better for smaller angles of attack [91] [23], and unlike the previous configuration, according to [90] unable to maintain a short turning radius past the aircraft's critical angle.

It is also important to note that both configurations can increase their vertical stability by introducing vertical extensions called Fins, which help to distribute the aerodynamic loads more evenly. However, this means that the distance to the ground at the drop-off is reduced, requiring greater care when riding[86].

Efficiency/Performance

In this field, the T-shaped twin boom has a more efficient weight distribution between the wings and the tail, which can result in improved response during maneuvers and greater stability in various flight conditions, offering comparable efficiency to the conventional design, with some additional advantages such as avoiding turbulence and down-wash of the fuselage/wings and thrust [22]. The inverted V-shaped twin boom, on the other hand, can offer other advantages such as reduced aerodynamic drag due to typically having a smaller frontal area, which can lead to lower consumption and consequently greater range. However, despite this advantage, according to the studies [23] and [91] this configuration typically has less lift.

Manufacturing/Cost

Finally, the T-shaped twin boom, although offering advantages in terms of aerodynamic efficiency and maneuverability, may require a more robust structure, due to the arrangement of the horizontal stabilizer, which is responsible for a greater moment on the control surfaces compared to the other configurations, forcing a consequently heavier structure [86], which may also result in slightly higher manufacturing costs [22]. On the other hand, the inverted V-shaped twin boom, due to its symmetry, usually offers greater ease of manufacture, in addition to the improved aerodynamic efficiency that can offer long-term fuel economy benefits[87].

Taking into account all the information gathered, it was quickly concluded that since the ARX is an aircraft designed for ISAR purposes and its propeller is located in the center rear, between the two options the Twin boom T could bring more advantages, due to its simplicity of design and operation and good maneuverability. Therefore, after presenting the conceptual study to the company, the Twin boom T configuration was chosen, since this was also the configuration previously chosen internally. Once the tail configuration was well defined, as can be seen in Figure 3.3, it was possible to begin the conceptual study for the ARX tail and boom structure.

To do this, the geometry of the ARX prototype was provided (Figure 3.3a), in which the general configurations of the aircraft were already defined, such as dimensions, position and number of propellers, in addition to the geometry of the Tail and Boom, Figure 3.3b previously designed by the company. It is important to note that the boom has two disassembly zones, the first in the main wing connection zone and the second corresponding to the section located 40% of its length (Figure 3.3), making it possible to disassemble the rear boom and tail.

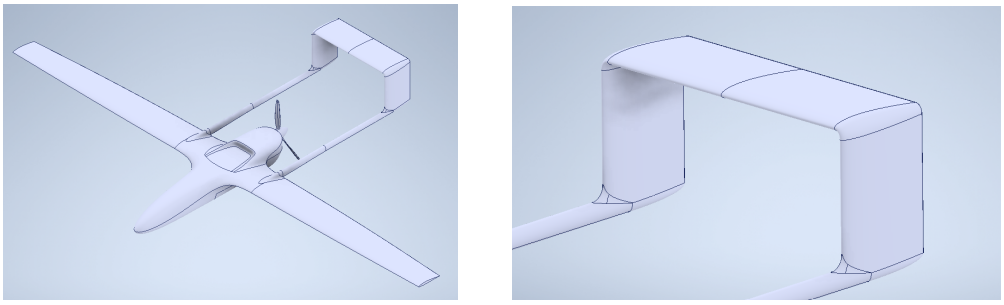

a)TEKEVER ARX prototype b)ARX Tail prototype

Figure 3.3: ARX CAD model

3.2 Structural Design concept

Aircraft structures play a fundamental role in safety, efficiency and performance during all phases of operation. Their main function is to withstand the forces applied to the aircraft, maintaining its integrity in extreme flight conditions. Therefore, throughout Section 3.3.1 and Section 3.3.2, we will take into account the studies carried out to design the tail and boom structures of the ARX aircraft, for the Twin-T boom configuration defined.

3.2.1 Tail Structural Design

Starting with the Tail, it is made up of two large surfaces, the vertical stabilizer, which contains the Rudder control surface (Figure 3.4) which allows the Yaw movement (movement along the vertical axis) providing directional stability to the aircraft and in the case of the chosen T configuration is also responsible for supporting the second large structure, the horizontal stabilizer,

which in turn contains the Elevator control surface (Figure 3.4) which allows the pitch movement of the aircraft (movement along the lateral axis) providing longitudinal stability.

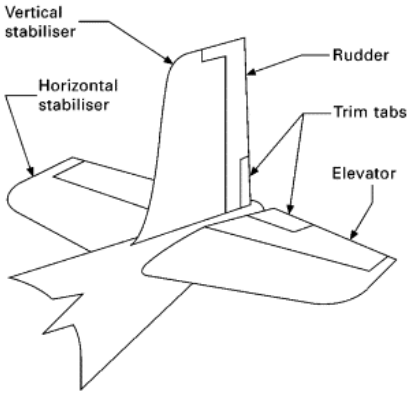

Figure 3.4: Tail flight control surfaces [92]

Therefore, the constructive elements typically used to reinforce the structure of these surfaces are:

Ribs: They are, together with the spars, the main structural element of the aircraft's stabilizers and wings. They are located along the wing's trailing edge and are responsible, together with the stringers, for forming the wing's geometry, as well as providing rigidity and curvature to the wing and supporting torsional and compressive loads, transferring the weight of the skin and stringers to the spars and avoiding phenomena such as skin buckling. In the early days of aviation, these components were typically made of wood, but nowadays they are made of metal (e.g. aluminum) or composite material (e.g. CFRP), the latter being the most common in the UAV industry.

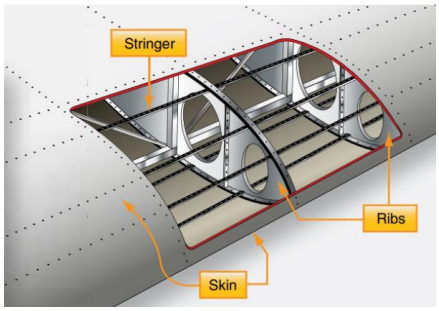

Figure 3.5: Esquematic assembly of Ribs in a wing [93]

As for their configuration, they can take on different geometries, but there are typically three main types, the Former Rib, used in the vast majority of aircraft, consisting of a central vertical section (core) and a component folded upwards (flange), with the main focus on balancing strength and weight, typically including holes to reduce weight (Figure 3.5). On the other hand, we have Reinforced Ribs, which have a more robust construction, with upper and lower layers joined by a reinforced core, providing greater strength and are used in areas of the aircraft subject to high stresses. And finally, Truss Ribs with simple, lightweight structures made up only of diagonal and vertical transverse elements, offer a good weight/strength ratio and are preferred for smaller aircraft or in situations where weight savings are crucial [94] [93].

Stringers: They are fixed to the structure in the longitudinal orientation of the aircraft and are responsible for supporting the axial loads induced by the bending of the wing, serving as reinforcing elements, having the ability to transmit the aerodynamic loads acting on the covering to the structures, avoiding the deformation of the covering under pressure, compression or shear

loads. Currently, stringers can typically be manufactured in aluminum or composite materials, and can have a variety of cross-sections such as HAT, I, T, Y and Z, Figure 3.6, each of which has characteristics that make them especially useful for different stresses [95].

As an example, the T-configuration is especially useful in situations where bending and compression loads are to be resisted, due to its high moment of inertia around its vertical neutral axis, while the I-configuration is especially effective in longitudinal and transverse loading situations due to its greater moment of inertia around the horizontal neutral axis. On the other hand, configurations such as the Z allow loads to be distributed in two opposite directions, resulting in less weight for the same resistance, while HAT configurations due to their robustness are generally only applied in loading situations in different directions where the previous configurations do not allow sufficient performance [93].

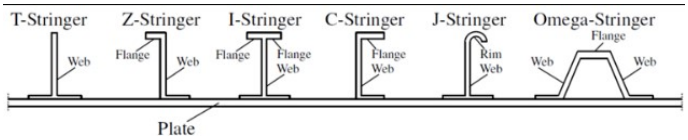

Figure 3.6: Typical stringers configurations [96]

Spars: They are located parallel to the aircraft's lateral axis, from the fuselage to the wing and are, together with the Ribs, the main components of the wing, supporting all its weight, distributed loads and concentrated weights, such as the fuselage, landing gear and engines, They are typically made up of a central body called the Web, which can include reinforcements in the most stressed areas, or holes to relieve weight, and flanges at the top and bottom to support bending loads. Their thicknesses and configurations can vary, with the two most commonly used types being the C and I profiles [95] [93].

In aircraft construction, there are usually at least two spars, the main spar, located about [15-35]% from the chord, and the secondary spar, located [60-75]% from the chord, which together create a region of high torsional strength typically called the Wing-box. Currently, the majority of aircraft produced consist of aluminum extrusions that are riveted together to create the spar, solid extruded aluminum wings or composite material as is more common in the UAV industry.

They are coated with a skin typically made of composite materials or light metals such as aluminium, which insulates the aforementioned elements, protecting against corrosion and degradation, and plays a fundamental aerodynamic role in maintaining the laminar flow possible, guaranteeing the proper functioning of the wings and control surfaces. With this in mind, an example of a schematic assembly of a wing is shown in Figure 3.7.

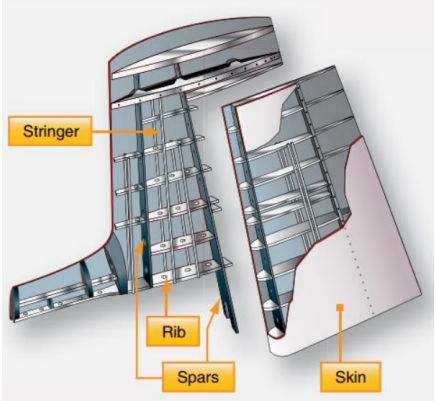

Figure 3.7: Esquematic assembly of vertical and horizontal stabilzier [93]

3.2.2 ARX tail Structure

3.2.2.1 Iteration 1

After the analyses carried out in the previous section on the various structural elements, we began by making a conceptual model of what would become of Tail's structure, which allowed us to understand, together with the company, which parameters should be improved and maintained, allowing us to create iteration 2, represented in Subsection 3.3.2.2, which is the starting point for the various structural analyses carried out in this project.

Therefore, for iteration 1, we took into account a structure composed of a main spar at 30% of the chord (approximately 188 [mm] from the leading edge of the wing profile) and a secound spar at 75% of the chord (approximately 563 [mm] from the leading edge of the wing profile), these positions being arbitrated initially based on references of positions usually used by aircraft of similar configuration found in the literature. Also with regard to the Spars, a C-shaped profile was taken into account at this stage, as can be seen in Figure 3.8, since it was the profile used by the company on previous aircraft, thus seeking a more accurate approximation to the desired one.

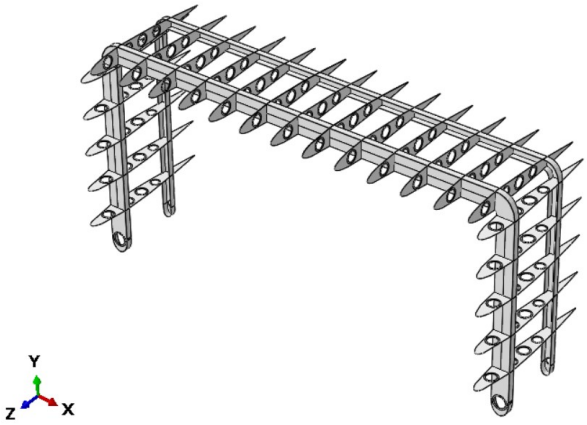

Figure 3.8: ARX tail structure iteration1

As for the Ribs, in the same way as the previous case, a distance ratio of 1/4 chord was initially taken into account, which was considered a good initial weight/strength ratio, allowing a margin of optimization in the next iterations of the structure, corresponding to approximately one Rib every 170 [mm], obtaining 13 Ribs for the Horizontal stabilizer and 5 Ribs for each Vertical stabilizer, In addition, 4 holes (20 and 25 [mm]) were inserted in all the Ribs of the structure, taking into account a spacing between 70 and 100 [mm] and respecting a safety margin of the edge of the Rib, avoiding stress concentrations that could jeopardize the integrity of the structure, while trying to reduce the weight of the structure (Figure 3.9).

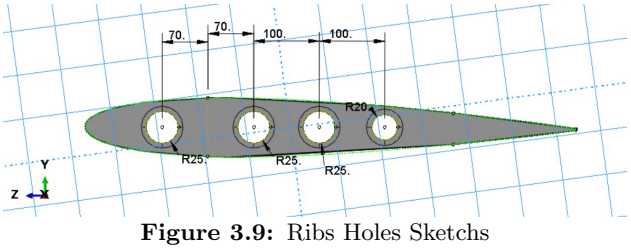

Figure 3.9: Ribs Holes Sketchs

3.2.2.2 Iteration 2

After finalizing the first iteration of the Tail structure and presenting it to the company, several modifications were taken into account in order to make the structure not only more geared towards the company's objectives and goals, but also to be able to meet some mandatory requirements such as the margins of the Rudder and Elevator control surfaces. Thus, the first change that was taken into account was to change the positioning of the secondary spar, from an initial position corresponding to 75% of the chord to 55% of the chord in the case of the horizontal stabiliser and from 75% of the chord to 70% of the chord in the case of the vertical stabiliser, in order to delimit the wing box from the aircraft's control surfaces. The second change that was taken into account was the positioning of the vertical surface ribs, since unlike the horizontal surface where the elevator is actuated at 100% of the span, in the case of the vertical stabilizer, the rudder is only actuated at 80% of the chord, making it necessary to position a rib at its upper and lower limit in order to delimit the control surface equally, opting to space the two central ribs equally within this limit.

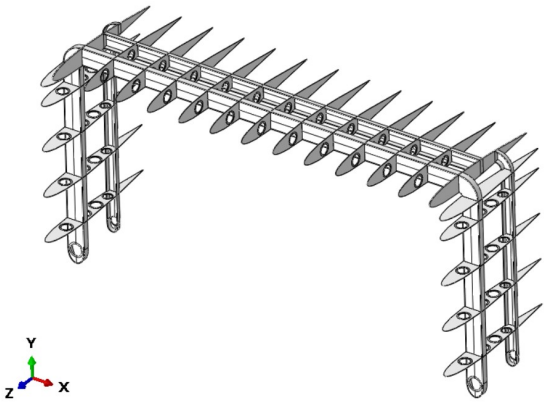

Figure 3.10: ARX tail structure iteration2

The third change made was to alter the size and position of the holes in the horizontal ribs, due to the drastic reduction in the size of the wing box. Figure 3.11 shows the configuration used. Finally, it was decided to remove the holes from the connecting ribs between the vertical and horizontal surfaces and the previous rib on the vertical surface, since these two ribs would have integrated a connection system between the two stabilizers, as well as a combination of holes that would allow for a floor change in the horizontal stabilizer's tilt setup, which had not yet been designed at this stage of the project (Figure 3.10).

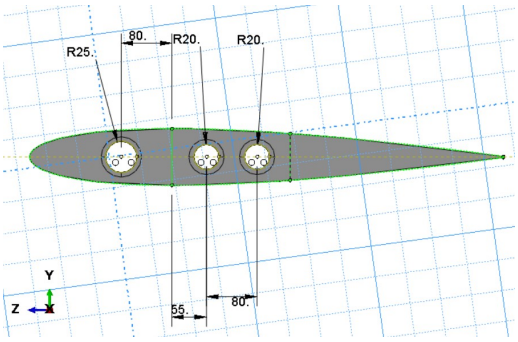

Figure 3.11: Horizontal Ribs Holes Sketchs

3.2.3 Boom Structural Design

After the conceptual design of the tail structure, it was necessary to carry out the same process for the boom, which has the main responsibility of connecting the airplane's fuselage structure to the tail. We therefore began by carrying out a conceptual study of the different configurations and structural elements typically used in this structure, starting by identifying the two main construction groups: Truss Boom and Monocoque Boom [94] [93].

As far as the Boom truss group is concerned, these are typically rigid structures made up of beams, trusses and bars, designed to resist the deformation caused by the loads applied to the structure, and there are typically two most popular customary forms, Pratt (Figure 3.12a) and Warren (Figure 3.12b).

Pratt-type trusses are characterized by having compressed vertical members and tensioned diagonal members, which makes it possible to reduce the thickness of the diagonal elements, reducing the cost of the structure and allowing a more effective design for simple horizontal structures, where the forces act predominantly in the vertical direction, and also work well for mixed loads.

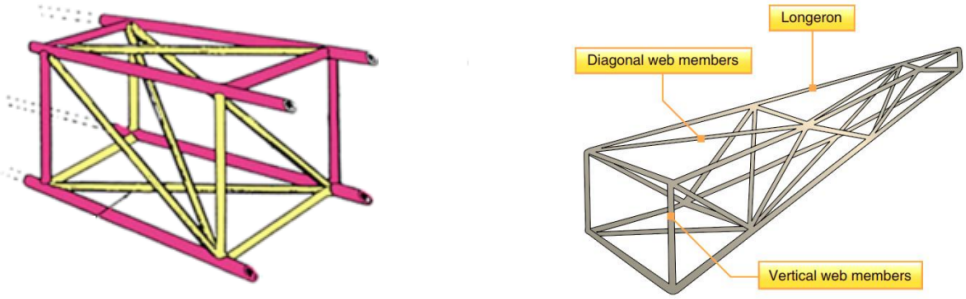

a) Pratt Truss b) Warren Truss

Figure 3.12: Boom Truss type [93]

On the other hand, the Warren truss has as its main characteristic the ability to distribute the load fairly evenly across its members, since it is characteristically built with equilateral triangles, presenting a simpler design, however it can be less efficient in situations of concentrated loading, being useful in situations of long spans and uniformly distributed loads. Therefore, it is understood that truss structures are typically used for simpler situations and where a cost-effective design project is required. It is important to note that the material of choice for their manufacture is light metals such as aluminum, which is a difficult option for composite materials [94] [93].

A second analysis was the monocoque structure, often known as a "single shell", which can be classified into two main types, semi-monocoque and monocoque, based mainly on the strength of the skin or covering to support the primary loads. Starting with the monocoque (Figure 3.13a), this construction method uses elements such as skin, Bulkheads and Formers to give shape to the fuselage, with the main limitation being the weight/strength ratio, since the skin is responsible for supporting the primary tensions, implying a more exposed configuration, in addition to the need for greater care with the positioning of the heaviest loads in order to reduce concentrated loads.

On another hand, the semi-monocoque type (Figure 3.13b) appears as an alternative solution to the weight/resistance limitation of the previous configuration, adding to the elements already present in the monocoque, the longitudinal reinforcements called stringers, which allow not only a better distribution of the forces in the structure, but also less dependence on the skin to support

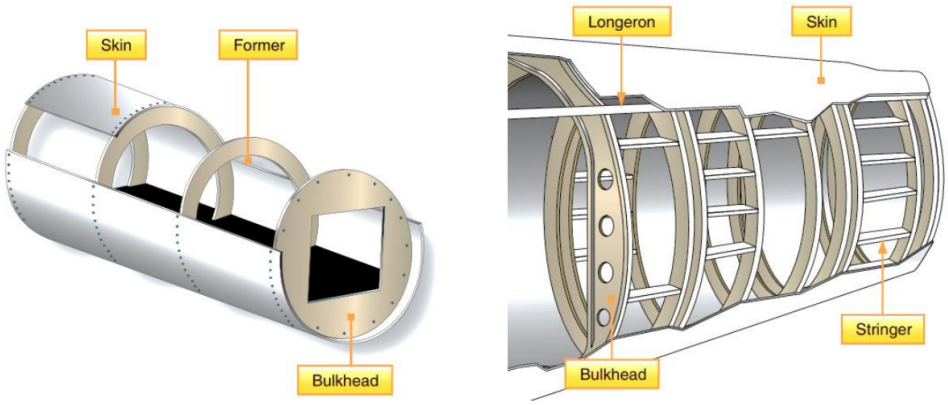

a) Monocoque b) Semi-Monocoque

Figure 3.13: Boom monocoque vs Semi-Monocoque [93]

them, helping to support the primary bending loads, preventing deformation of the structure due to forces such as traction and compression, allowing a considerable reduction in the thickness of this element. It is also important to bear in mind that monocoque and semi-monocoque construction is predominantly made of aluminum and magnesium alloys. In areas subject to high temperatures, other materials such as steel and titanium can be used. In the case of the UAV industry, composite materials are typically used and are often joined to the rest of the structure using riveting techniques, welding, fasteners and, in the case of composite structures, in some cases adhesive joints [94] [93].

Finally, as in the previous section on the structural elements of the tail, it is important to give a brief summary of some of the unique components integrated into these monocoque and semi-monocoque constructions:

Bulkheads are the structures located at the ends of the boom, typically more robust in relation to the Formers, since they are responsible for connecting the structure to the fuselage and tail, being subject to a greater concentrated effort (Figure 3.13a and Figure 3.13b). In addition, together with the formers properly spaced along the structure, they are responsible for ensuring the shape of the structure.

Formers are the structural elements distributed along the longitudinal axis of the structure, properly spaced in order to maintain the structural integrity of the structure, avoiding, together with the stringers, phenomena such as buckling or deformation of the skin along the structure and ensuring its geometric shape (Figure 3.13a and Figure 3.13b). In addition, they can take a variety of shapes, being less robust than Bulkheads and being connected to each other by stringrs in the case of the semi-monocoque configuration.

Longerons are structural elements very similar to stringers, designed to increase the stiffness and strength of the structure by supporting bending and axial loads, connecting to the aforementioned structural elements, providing greater longitudinal support (Figure 3.13b). However, unlike stringers, which are typically connected between formers in greater numbers and smaller thicknesses, longerons are typically more robust and connect the entire structure longitudinally, dividing the skin into smaller panels and increasing the buckling and rupture stress of the skin.

3.2.4 ARX Boom Structure

After analyzing the various structural elements typically used in Boom structures, we quickly came up with three different configurations for making the structure of this component. In the following subsections, we will identify and illustrate the three proposed solutions.

3.2.4.1 Boom with Internal Pipe Iteration 1

The first constructive solution taken into account was a boom reinforced by formers with an external radius equal to that of the boom section where they are located and an internal radius equal to that of the inner tube which reinforces the structure in an attempt to reduce the total deformation and stress to which the boom skin in particular would be subjected. As for its geometry, it has a constant radius of 30 [mm], conically reducing its section between the main spar and secound spar to 25 [mm], extending to the end of the wing profile, conically reducing its section radius to 20 [mm]. As for its connection to the structure, the aim was to create a connection zone between the inner tube and the main and secondary spar, as can be seen in Figure 3.14, increasing its robustness.

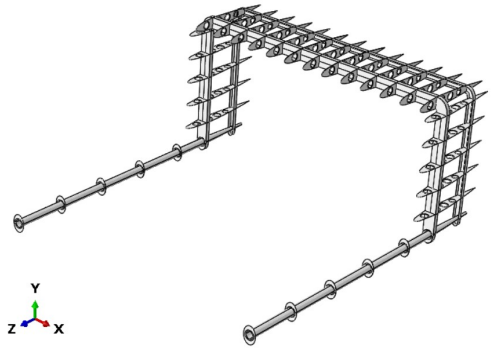

Figure 3.14: ARX Boom with internal pipe - iteration1

3.2.4.2 Boom with Stringers Iteration 1

The second construction solution was to replace the inner tube fixed to the main and secondary spar with four T-profile longerons. As mentioned in Subsection 3.3, this profile is especially useful in situations where bending loads are likely due to its high moment of inertia around its vertical neutral axis, so it was dimensioned with 30[mm] of flange and 30[mm] of web following references supplied by the company. This was intended not only to reduce the weight compared to the previous case, but also to reduce two potential critical zones of the previous option, relating to the connection holes between spars and booms.

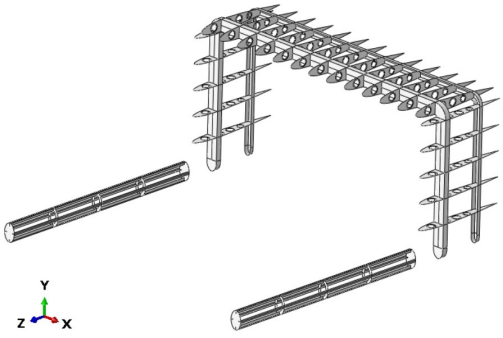

Figure 3.15: ARX Boom with stringers - iteration1

3.2.4.3 Boom with Internal Pipe and Stringers Iteration 1

As for the third construction option, it consists of merging the two previous ones, trying to compare the two previous solutions with a more robust one and obviously creating a more conservative option in case the two previous ones don't have the necessary capacity to reinforce the structure.

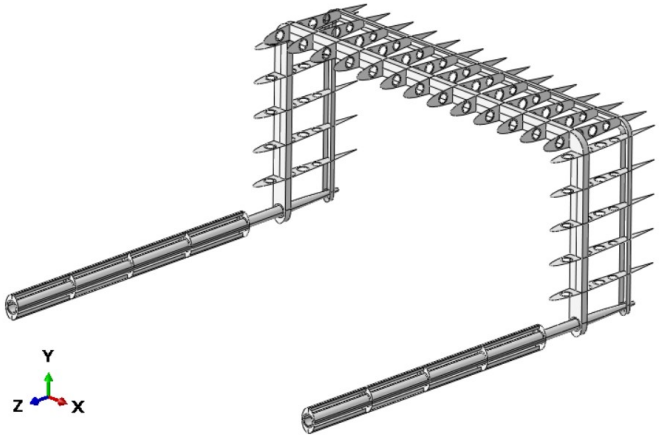

Figure 3.16: ARX Boom with internal pipe and stringers - iteration1

3.2.4.4 Boom with Internal Pipe Iteration 2

As was done for the tail structure, the previous configurations were presented to the company, detecting what could be some problems, trying to anticipate them with their correction, and iteration 2 emerged for the Boom's construction solutions. The first change that was taken into account was the increase in the Boom's analysis section, and at an early stage we were projecting about 50% of the length of this element, with the final section corresponding to the first disassembly zone of the Tail and rear boom, however some doubts arose as to how the boundary conditions could be faithfully represented in this zone, and the simplest and most practical solution found was to extend the analysis section to the second disassembly zone of the boom, corresponding to the connection zone to the main wing. Therefore, the reinforcement tube made up of this new analysis section has a constant radius equivalent to the internal radius of the tube in the previous section, recessed into it by 200[mm], maintaining the same formers as the previous approach, as shown in Figure 3.17.

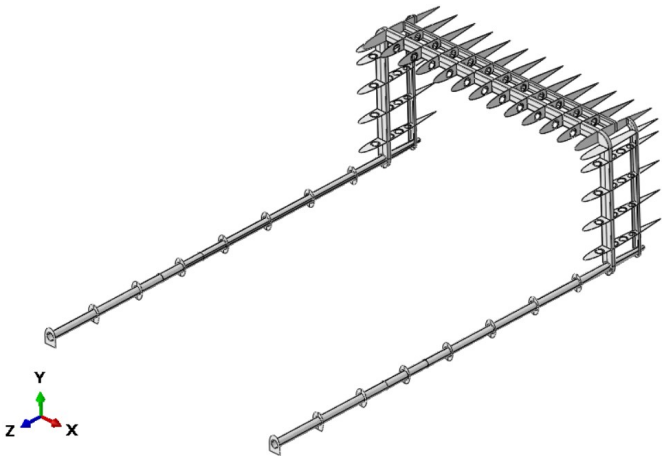

Figure 3.17: ARX Boom with internal pipe - iteration2

3.2.4.5 Boom with Stringers Iteration 2

As for iteration 2 of the boom solution reinforced with stringers, it followed the same line as the previous alteration, extending the existing structure up to the main wing. As for the connection zone between the two booms, since in this version there is no internal tube designed to make this connection, two tubes were designed along the same lines as the previous one, the first with an external radius of 30[mm] and the second with a radius equal to the internal radius of the previous one, maintaining the recess for a length of 200[mm]. The aim was not only to represent in the best possible way a possible stress concentration zone in relation to the connection of the two booms, but also to seek a similarity between solutions in terms of the connection zone, making future comparisons simpler and more accurate, as can be seen in the Figure 3.18.

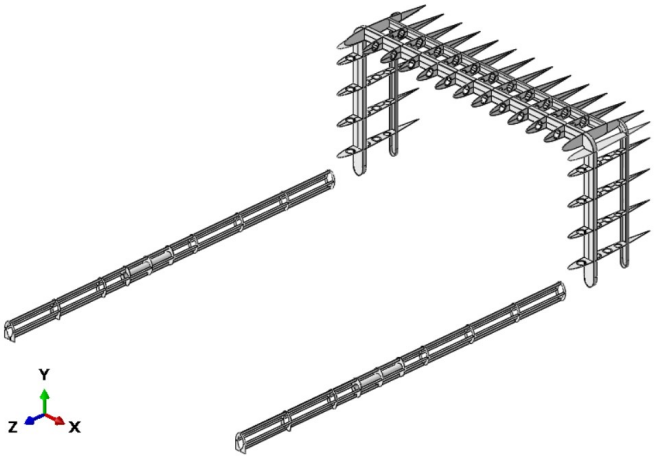

Figure 3.18: ARX Boom with stringers - iteration2

3.2.4.6 Boom with Internal Pipe and Stringers Iteration 2

Finally, the same procedure was carried out for the version that combines the two previous solutions, in which case the connection between sections of the boom was guaranteed in the same way as in the version of the boom with internal tube reinforcement, as shown in Figure 3.19.

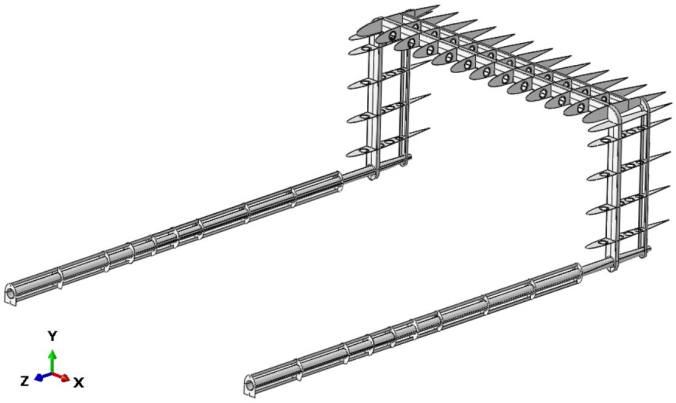

Figure 3.19: ARX Boom with internal pipe and stringers - iteration2

Concluding this initial design phase, we will explain in the next chapter 4 how the procedure for obtaining the aerodynamic and inertial loads was carried out, as well as the work carried out in the XFLR5 tool and the consequent projection of the aircraft's V-n diagram.

Chapter 4

ARX Load analysis

After the initial concept phase, when the structural solutions for both the tail and the boom of the ARX had been designed, it was necessary to begin the process of analysing and calculating the various forces that would be applied during the flight of the aircraft. Therefore, in this chapter we will begin by presenting the characteristics of the aircraft, calculating its V-n flight diagram, enabling the identification of the critical cases in accordance with ASTM F3116/F3116M-18e2 [2], followed by the modelling and analysis of the ARX in the XFLR5 software, enabling the previously identified critical cases to be translated into force reports that allow us to later apply the forces in the finite element model.

4.1 Load Case

One of the fundamental aspects of the design process is the understanding and analysis of load cases to ensure the application of appropriate safety margins. This is essential for guaranteeing structural integrity and avoiding catastrophic failures. To determine the critical load cases for a proper structural analysis, it was necessary to model the aircraft's V-n Diagram. This was carried out in accordance with the "Standard Specification for Design Loads and Conditions ASTM F3116/F3116M-18e2" [2]. The following section illustrates the procedure considered for its realization, followed by the aircraft parameters necessary for its execution:

- V_c = Cruise Speed = 194 $[ft/s^2]$
- V_d = Dive Speed = 1.4 x Vc = 271.7 $[ft/s^2]$
- n^+ = Maximum load factor = 3.8
- n^- = Minimum load factor = 0.4 x n^+ = 1.52
- a = Slope of the airplane normal force coefficient = 5.6 [rad]
- C = Geometric Chord = 0.840 [m]
- S = Wing area = 10.085 $[m^2]$
- Cl_{max} = Maximum Lift coefficient = 1.5
- Cl_{min} = Minimum Lift coefficient = -0.8
- ρ = air density = 0.00238 $\left[\text{slugs}/\text{ft}^3\right]$

- W = Airplane gross weight (force) = 1322.77 [slug ft/s^2]

4.1.1 V-n diagram

4.1.1.1 Maneuver

Regarding the maneuvering diagram, as already introduced in Section 2.5.1, it consists of the horizontal limits of the Maximum Load Factor (n^+) and the minimum (n^-), the maximum vertical limit Dive Speed (V_d), and the minimum vertical limits, the Positive and Negative Stall curves. As we can observe in the sketch of Figure 4.1, the points [I, II, III, IV] correspond to four limit maneuvering situations.

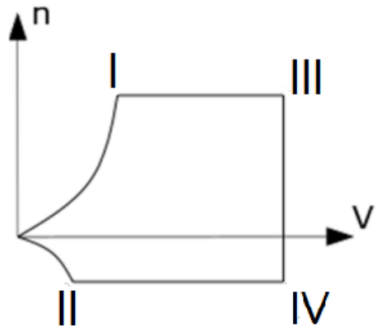

Figure 4.1: Manouver Diagram esquematic representation

Relativamente ao ponto III e IV, estes correspondem a interseção do maximo load factor (n^+) e minimo load factor (n^-), respetivamente com a velocidade V_d, obtendo:.

$$\begin{aligned} III &= \left(V_D, n^+\right) = (271.7, 3.8) \\ IV &= \left(V_D, n^-\right) = (271.7, -1.52) \end{aligned} \tag{4.1}$$

Regarding the positive and negative stall curves (total loss of aerodynamic lift), these can be obtained by the equality L=W represented in the following Equations:

$$n^+_{C_{l_{\max}}} = \frac{1}{2}\frac{\rho S V^2 C_{l_{\max}}}{W} \tag{4.2}$$

$$n^-_{C_{l_{\min}}} = \frac{1}{2}\frac{\rho S V^2 C_{l_{\min}}}{W} \tag{4.3}$$

Thus, substituting in Equation 4.2 and Equation 4.3 the initially presented values for the ARX, we have:

$$n^+_{C_{n_{\max}}} = \frac{1}{2}\frac{0.00238\left[\frac{\text{slug}}{ft^3}\right] * 10.085\left[ft^2\right] * 3.8}{1322.77\left[\frac{\text{slug } ft}{s^2}\right]}V^2 \tag{4.4}$$

$$n^-_{C_{n_{\min}}} = \frac{1}{2}\frac{0.00238\left[\frac{\text{slug}}{ft^3}\right] * 10.085\left[ft^2\right] * -0.8}{1322.77\left[\frac{\text{slug } ft}{s^2}\right]}V^2 \tag{4.5}$$

$$n^+_{C_{l_{\max}}} = 0.000034476 * V^2 \tag{4.6}$$

$$n^{-}_{\overline{C_{l_{\min}}}} = -0.0000072582 * V^2 \tag{4.7}$$

By now intersecting these curves with our upper and lower limits, $n^+ = 3.8$ and $n^- = -1.5$, it is possible to obtain the positive and negative stall speed values:

$$V_{S(+)} = 161.062 \left[\text{ft}^2\right] \tag{4.8}$$

$$V_{S(-)} = 139.483 \left[\text{ft}^2\right]. \tag{4.9}$$

The intersection points being:

$$I = (161.062, 3.8) \tag{4.10}$$

$$II = (139.483, -1.52) \tag{4.11}$$

Finally, we also take into account two simplifications to our diagram, the first by drawing a line joining the intersection point of V_c with the negative load factor $n^- = -1.52$, with the intersection point of V_d and zero load factor $(n = 0)$,discarding the posterior area, the second simplification being the intersection of the positive and negative stall curves with the load factors $(n = 1)$ and $(n = -1)$ respectively, discarding the previous area. Both simplifications are justified since the aircraft is unable to fly in the conditions of the discarded areas and remembering that the purpose of the diagram is to obtain the flight conditions of the aircraft, it is not valid to include these areas in our diagram. A sketch of the above is shown below (Figure 4.2):

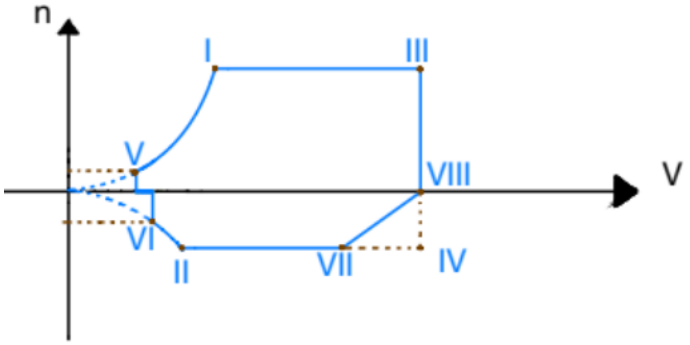

Figure 4.2: Manouver Diagram with simplifications esquematic representation

The calculations required to achieve these simplifications are presented below:

$$1 = \frac{1}{2} \frac{0.00238 \left[\frac{\text{slug}}{ft^3}\right] * 10.085 \left[ft^2\right] * 3.8}{1322.77 \left[\frac{\text{slug } ft}{s^2}\right]} V^2 \tag{4.12}$$

so that:

$$V_V = 82.623 \left[ft^2\right] \tag{4.13}$$

and point V is:

$$V = (82.623, 1). \tag{4.14}$$

and, for point VI:

$$-1 = \frac{1}{2}\frac{0.00238\left[\frac{\text{slug}}{ft^3}\right] * 10.085\left[ft^2\right] * -0.8}{1322.77\left[\frac{\text{slug}\ ft}{s^2}\right]}V^2 \tag{4.15}$$

so that:

$$V_{VI} = 113.14\left[ft^2\right] \tag{4.16}$$

and point VI is:

$$VI = (113.14, -1). \tag{4.17}$$

Regarding the intersection points we have of cruising and diving speeds, all values are already known being:

$$VII = (146.6, -1.5). \tag{4.18}$$

$$VIII = (205.24, 0). \tag{4.19}$$

Thus, in Figure 4.3, we can observe the obtained maneuvering diagram.

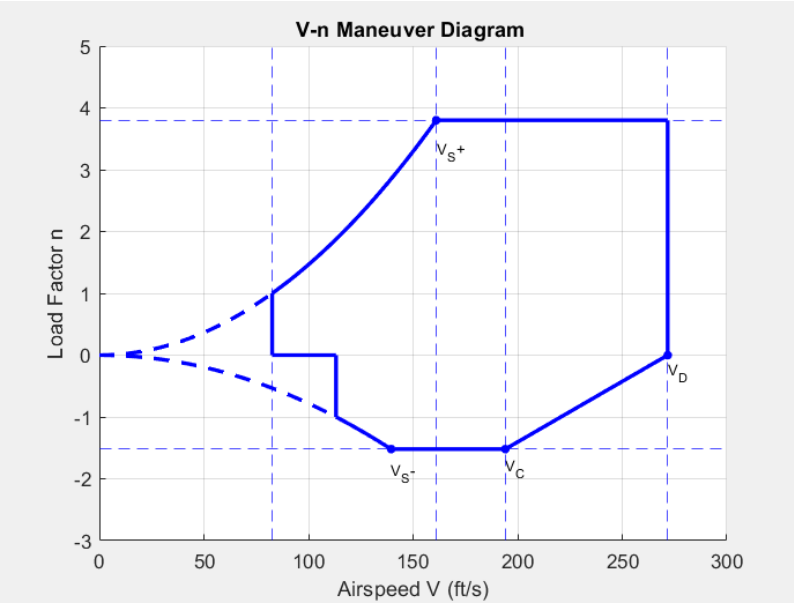

Figure 4.3: ARX Manouver Diagram

4.1.1.2 Gust

For the construction of the gust diagram, the first step is to define the two Derived Gust Velocities prescribed by the ASTM 3116 standard, as shown in Table 4.1.

Table 4.1: Derived gust velocities for ASTM 3116

Velocity	Ude [ft/s]
Vc	50
Vd	25

Taking this into account and the values provided in the initial section, we can calculate the coordinates relative to the critical points, which can be obtained as shown in Figure 4.4, by adding an amount Δn, depending on the velocity (dive or cruise), to the reference value (n), Equation 4.20 and Equation 4.21. Finally, connecting from point [0,1] to the corresponding critical points yields the corresponding gust lines.

$$n_g^+ = 1 + \Delta n \tag{4.20}$$

$$n_g^- = 1 - \Delta n \tag{4.21}$$

with:

$$\Delta n = \frac{K g U_{de} V a}{498(W/S)} \tag{4.22}$$

where:

- $K_g = \frac{0.88\mu_g}{5.3+\mu_g}$ = gust alleviation factor
- $\mu_g = \frac{2(M/S)}{\rho C a g}$ = airplane mass ratio

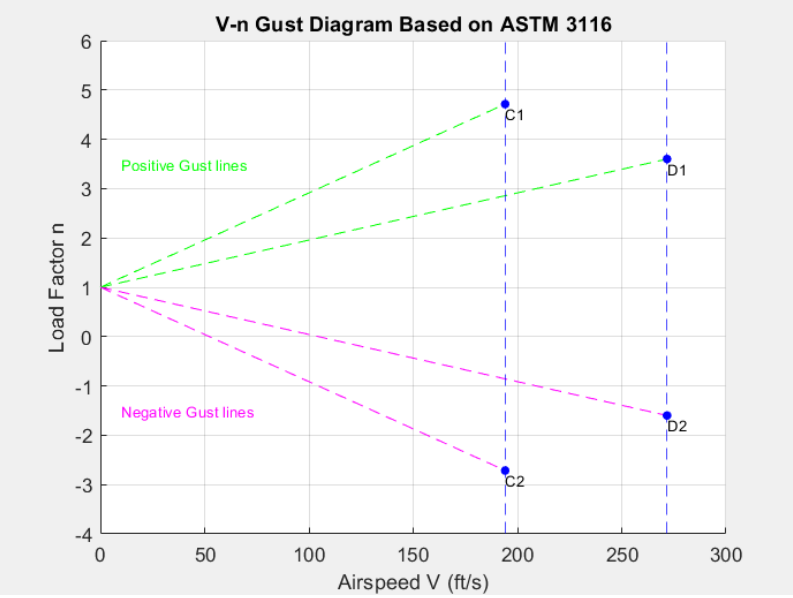

Figure 4.4: ARX Gust lines

Therefore, the obtained values for the extreme cases are shown in Figure 4.4.

- Positive Dive (D_1) – (271.737/3.6)
- Negative Dive (D_2) – (271.737/ – 1.6)
- Positive Cruise (C_1) – (194.98/4.714)
- Negative Cruise (C_2) – (194.094/ – 2.714)

4.1.1.3 Total Envelope

Taking into account the previous sequence, we can obtain the total flight envelope (Figure 4.5) by expanding the maneuvering diagram (Figura 4.3), through linear segments to points C1, C2, D1, and D2 calculated from the Gust Lines (Figura 4.4). Analyzing the ASTM 3116 standard for modeling vertical and horizontal surfaces, we can conclude that the critical analysis cases for the Tail would involve the two points marked in red in Figure 4.5, The leftmost point corresponds to the stall speed condition for maximum control surface deflection, and the rightmost point corresponds to the dive speed condition for 1/3 maximum control surface deflection. These critical points will be considered for our analyses in the upcoming sections, ensuring proper sizing of the internal Tail structure.

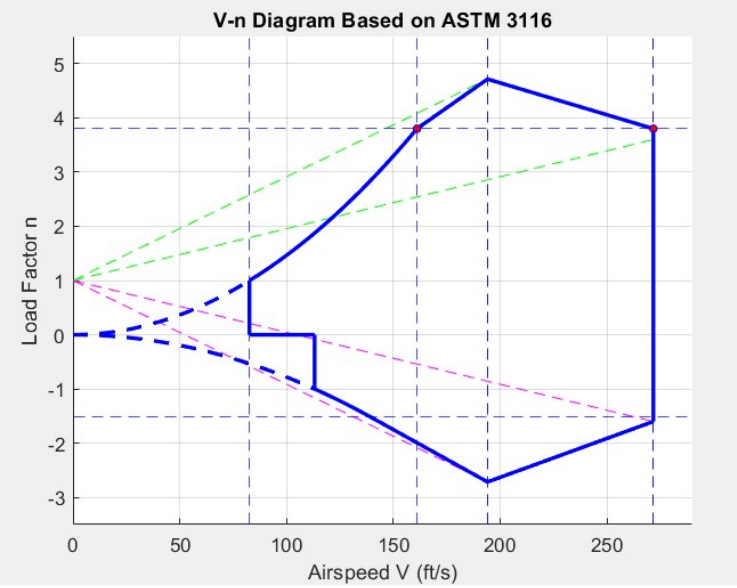

Figure 4.5: ARX V-N Diagram

4.1.2 XFRL5 load case analysis

4.1.2.1 Aerofoil analysis

Having defined the critical load cases for the analysis of our structure, the next step was to transition to software capable of analyzing the forces exerted on the aircraft. We chose the XFLR5 software due to its simplicity and extensive support materials available. This allowed us to approximate the forces of drag, lift, and pitching moments applied to the horizontal and vertical surfaces. Additionally, we had the opportunity to access analyses such as visualization of streamline patterns on the model surface (streamlines), coefficient of pressure analyses, among others.

To initiate this process, it was necessary to identify and analyze the airfoil profiles used for the different wings of the aircraft. This choice marks the first step in ensuring proper aircraft control during flight, guaranteeing good performance and stability of the control surfaces under various flight conditions.

Starting with the horizontal and vertical surfaces that constitute the Tail, these are typically composed of symmetric airfoils which provide a more balanced and predictable response to control inputs, due to their more uniform load distribution along the surface compared to cambered airfoils. In this case, the symmetric airfoil has been chosen, as shown in Figure 4.6. It is important to note that symmetric airfoils do not generate aerodynamic force at 0 degrees angle of attack (Figure 4.7),which typically leads designers to introduce a small angle of attack on the horizontal surface to maintain tail effectiveness during cruise flight conditions. In this particular case, an angle of attack of 0.35 degrees is chosen.

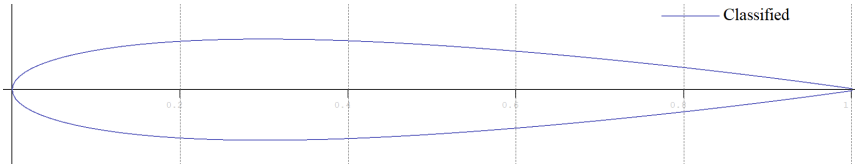

Figure 4.6: Tail symmetric airfoil

In Figure 4.7,we can observe a comparison between the C_L vs alpha graph of the Tail symmetric profile obtained from the Airfoil Tool [97] and the corresponding comparison obtained in the XFLR5 software.

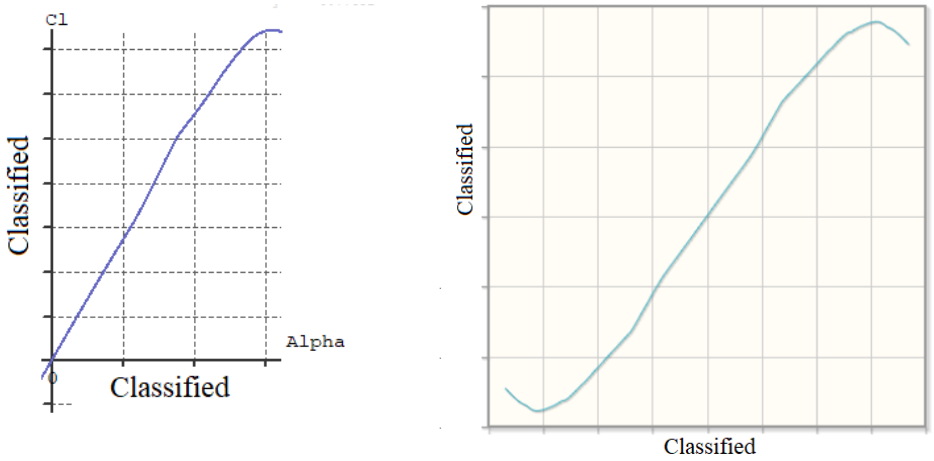

a)XFLR5 Software - Reynols=10000 b)Airfoil Tool - Reynols=10000 [97]

Figure 4.7: C_L vs alpha Tail symmetric airfoil

On the other hand, when it comes to the main wing, the approach is typically different, often opting for curved profiles to generate maximum aerodynamic force (lift). In this case, the main wing is made up of an optimized aerofoil with variable curvature along the span, as can be seen in Figure 4.8.

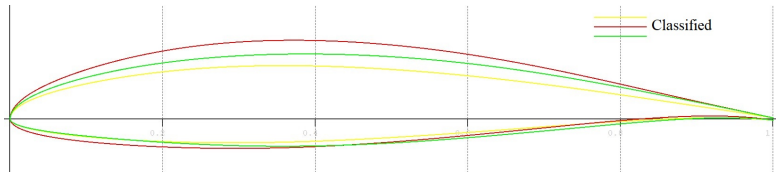

Figure 4.8: Main wing cambered airfoils

In Figure 4.9a we see a comparison obtained in the XFLR5 software for the four profiles. It can be seen that the symmetrical tail profile (in blue) has C_L=0 for alpha=0, as expected due to its symmetrical characteristics. However, for the profile of the curved main wing, we can see that the profile in red shows a higher C_L value for different angles of attack, compared to the other versions. On the other hand, the yellow version has the lowest C_L value for the different alphas, while the green version provides an intermediate relationship between the two. Furthermore, we can see that the red version has a higher critical angle of stall.

In a further analysis in Figure4.9b, we can also see a comparison between the four profiles for the C_L vs C_D ratio. It's clear that the red profile is considerably more efficient, while the symmetrical tail profile is the least effective. The other versions of the curved main wing profile show intermediate efficiency between the red and symmetric profiles, with very similar C_D values across the range.

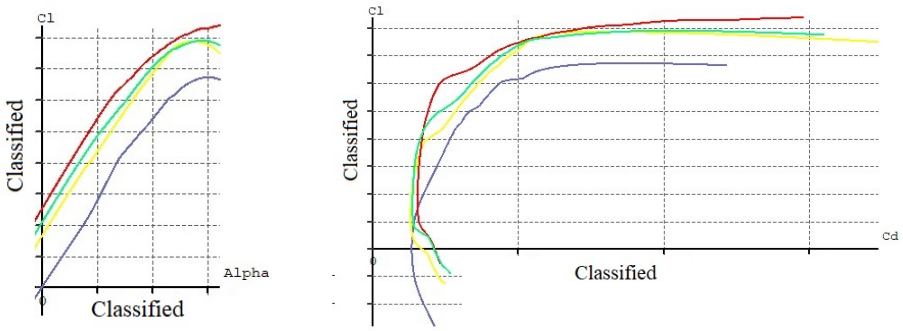

a)Cl vs alpha profiles b)Cl vs C_D profiles

Figure 4.9: Tail symmetric vs Main-wing cambered airfoils

After the definition and study of the default profiles, the Tail symmetric profile were also analyzed for the different configurations of maximum deflection and 1/3 of the maximum deflection representative of the critical conditions of the structure as defined in the previous section, and the Figure 4.10 shows the case of maximum positive deflection simulating the Rudder control surface (in red) and elevator (in blue).

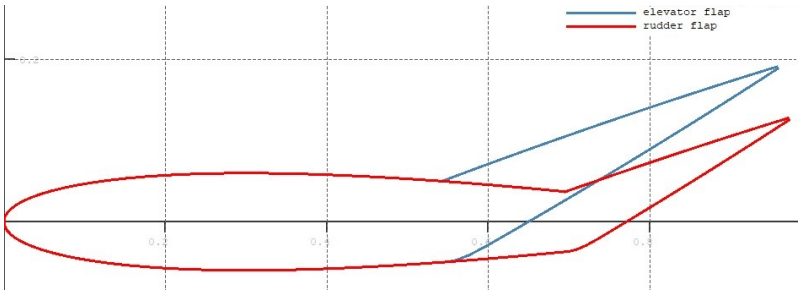

Figure 4.10: Tail symmetric airfoils with variations for control surfaces

Finally, in order to guarantee a good analysis by the XFLR5 software, it was essential to ensure that all flight conditions in terms of Reynolds and angles of attack were taken into account, allowing the software to have as much information as possible to estimate the forces exerted on the aircraft as accurately as possible. Therefore, for all the profile analyses in this report, we opted for the largest possible range of Reynolds, [234.375 - 1.536e+09] and an angle of attack range between -5 and 16 degrees.

4.1.2.2 ARX XFLR5 design

After completing the analysis of the various necessary airfoil profiles, the next step involved modeling the aircraft geometry in the XFLR5 software. In Figure 4.11 the final aircraft and the various payloads provided by the company can be observed, which meet the requirements to initiate the analysis process in the software.

It is noteworthy that in addition to the previously mentioned 0.35 degrees angle of attack for the horizontal stabilizer, a 4-degree angle of attack was also defined for the main wing.

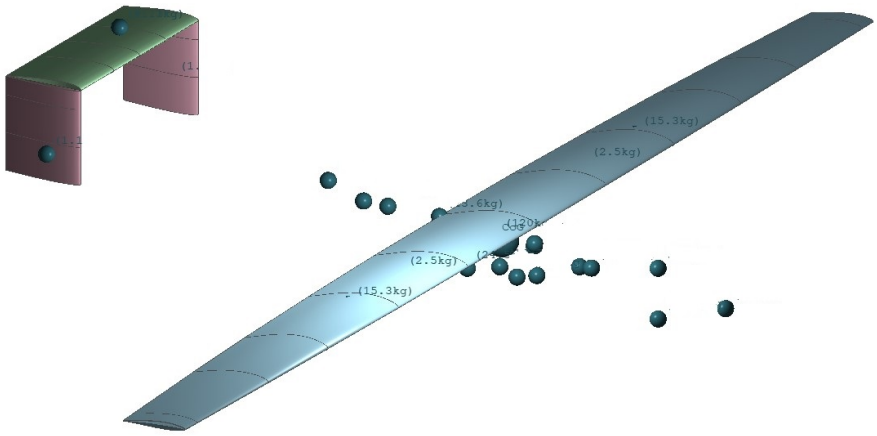

Figure 4.11: ARX model at XFLR5

It's important to note that in the case of the elevator control surface, it operates across the entire span of the horizontal surface(Figure 4.16) unlike the rudder control surface, which operates over only 80% of its span. This difference can lead to some interferences in the XFLR5 software when the elevator is deflected, potentially causing deviations in the calculated results, as seen in Figure 4.12. To address this issue, two possibilities were considered: either moving the horizontal stabilizer away from the vertical stabilizer by raising the position of the horizontal stabilizer, or increasing the lateral position of the vertical stabilizer. Ultimately, the latter option was considered more appropriate because raising the horizontal stabilizer position would have a more direct impact on the aircraft's stability and flight dynamics conditions, potentially interfering with the subsequent analysis. On the other hand, the interference caused by widening the lateral position of the vertical stabilizer is much less significant.

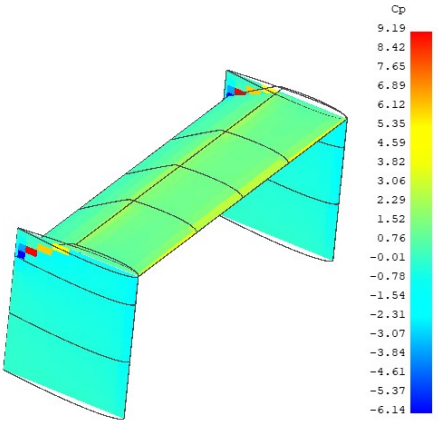

Figure 4.12: Contact interference vertical surface and elevator

As can be seen in Figure 4.13, the drag coefficient begins to converge to the estimated value at 8 [mm] from the reference position, while the lift coefficient is minimally affected by the gradual increase to the reference position. With this in mind, the 8 [mm] distance from the reference position was taken into account for our analyses. We can then begin the analysis process for the load cases required by the ASTM 3116 standard, which includes analysing at speed V_a with the maximum deflection of the control surface and at speed V_d with 1/3 of the maximum deflection of the control surface.

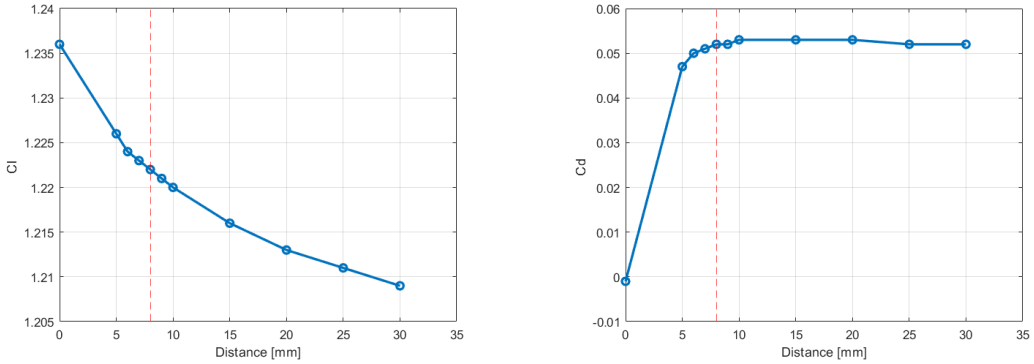

a) C_L b) C_D

Figure 4.13: ARX elevator at maximum deflexion

With this, the process began with a stability analysis using the 3D panel method along with the Ring Vortices method (VLM2) for trimmed flight (load factor=1). Iterating through different deflection angles of the Elevator control surface (a small representation of angles in Figure 4.14), it was possible to determine at which angle the aircraft achieved trimmed flight for speeds V_a and V_d. The values obtained were $\alpha_{Va} = 3.35°$ and $\alpha_{Vd} = 4.72°$ respectively. In Figure 4.15 we can observe the curve showing the relationship between the angle of attack of the control surface and the trim flight speed of the aircraft.

Note that in both the previous and subsequent analyses, the viscous analysis has been disabled as it is good practice and recommended by the software itself for situations where control surfaces are deflected, which can cause some contact interference in the software (between the elevator and vertical stabilizer in the case of the Tail, since the former operates over 100% of the span).

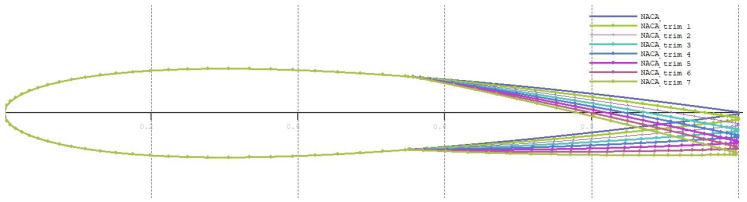

Figure 4.14: Tail symmetric airfoils for different elevator deflection angles

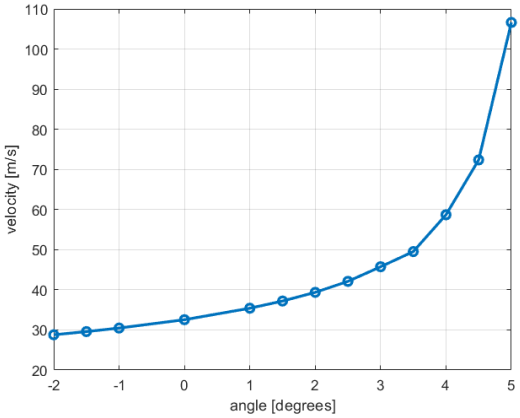

Figure 4.15: Angle of trim flight to different velocity

Having obtained the trim flight angles, four fixed-speed analyses (type 1 in XFLR5) were then conducted using the 3D panel method along with the Ring Vortices method (VLM2), aiming for better accuracy. These analyses provided detailed information on the lift and drag forces generated for the different analysis cases mentioned below:

- V_a for maximum deflection (+) of the elevator and an angle of attack of 3.35° (Figure 4.17a)
- V_a for maximum deflection (-) of the elevator and an angle of attack 3.35° (Figure 4.17b)
- V_a for maximum deflection of the rudder control surface (Figure 4.16)
- V_d for 1/3 of maximum deflection (+) of the elevator and an angle of attack de 4.72°
- V_d for 1/3 of maximum deflection (-) of the elevator and an angle of attack 4.72°
- V_d for 1/3 of maximum deflection of the rudder control surface

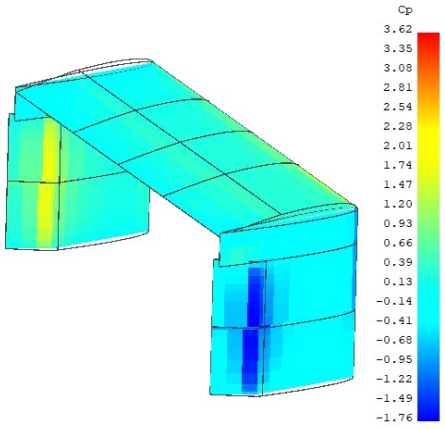

Figure 4.16: ARX rudder at at maximum deflexion 25°

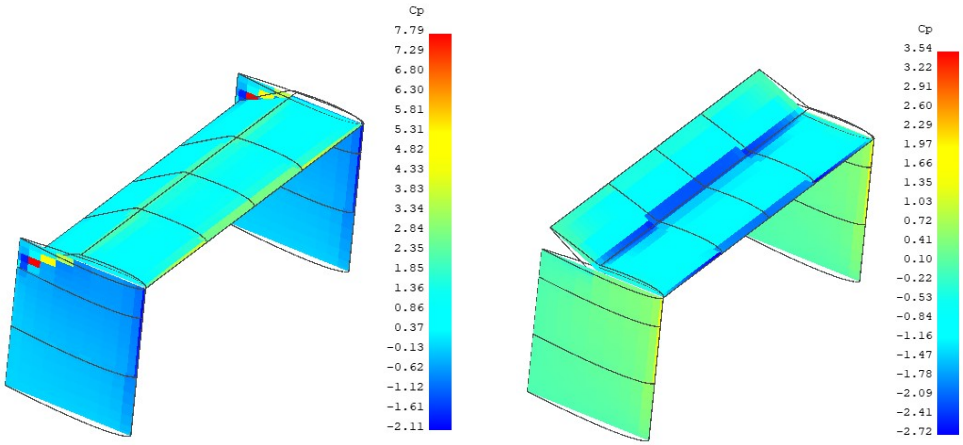

a) ARX elevator at -25° b) ARX elevator at 25°

Figure 4.17: ARX elevator at maximum deflection

At this point, it is important to analyze the obtained results, ensuring that they follow a logical train of thought. Therefore, in Figure 4.18, we can observe a frontal view of the lift estimation for the main wing and tail of the ARX under the load case of positive elevator deflection at speed V_a (Figure 4.17a) in which we can observe that both the vertical stabilizer and the horizontal stabilizer estimate negative forces, resulting in an expected negative moment, and upon analysis using finite element analysis, a negative deflection of the structure is anticipated.

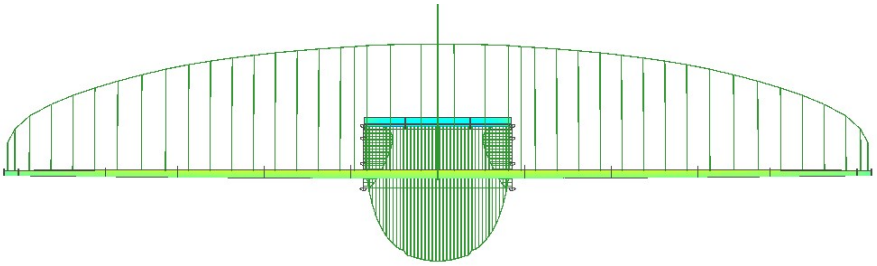

Figure 4.18: Visual lift representation for V_a with elevator positive deflection

On the other hand, in Figure 4.19, a frontal view is represented for the lift estimation of the main wing and tail of the ARX under the load case of negative elevator deflection at speed V_a (Figure 4.17b), here, we observe the opposite scenario to the previous case, with both the vertical and horizontal stabilizers estimating positive forces, indicating an expected positive pitching moment and potentially a positive deflection of the structure in the future.

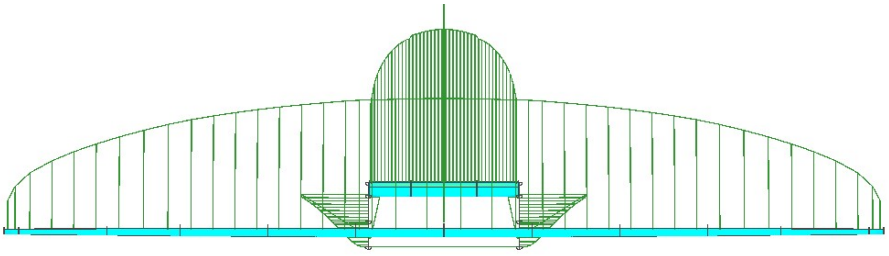

Figure 4.19: Visual lift representation for V_a with elevator negative deflection

Finally, in Figure 4.20 a frontal view is depicted for the lift estimation of the main wing and tail of the ARX under the load case of rudder negative deflection and right rudder positive deflection at speed V_a (Figure 4.16), here we observe an asymmetric case caused by the different directions of deflection of the rudder control surface, resulting in a positive lift estimation for the horizontal stabilizer. This lift increases from the right vertical stabilizer to the left vertical stabilizer. Therefore, a positive pitching moment is expected, similar to the previous case. Additionally, we anticipate a higher lift estimation for the left vertical stabilizer compared to the right one, with the latter predicting a force in the opposite direction.

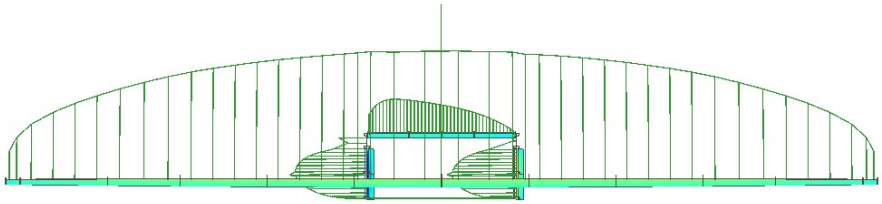

Figure 4.20: Visual lift representation for V_a with left rudder negative deflection and right rudder positive deflection

Taking this into account, throughout the next subsection, we will explain in detail the process of calculating how to convert the values obtained from the XFLR5 software into the forces applied on the structural model.

4.1.2.3 Load cases calculation for Horizontal stabilizer

Before starting this subsection, it is important to take into account some factors that are relevant to our future analysis. Like commercial CFD software, XFLR5 also suffers from some prediction errors, mainly associated with values such as the drag coefficient (C_D) and pitching moment (M_c). There is only greater confidence in the values it can predict for the lift coefficient (C_L), but it is subject to equal care when confirming it in a wind tunnel or testing it against experimental data. A visual example of this disparity can be seen in the study carried out by İbrahim, Yüksel and Mehmet in [98], where we can see in Figure 4.21, the differences between the drag and lift values in the software and experimentally and in Figure 4.22, the same comparison for pitching moment.

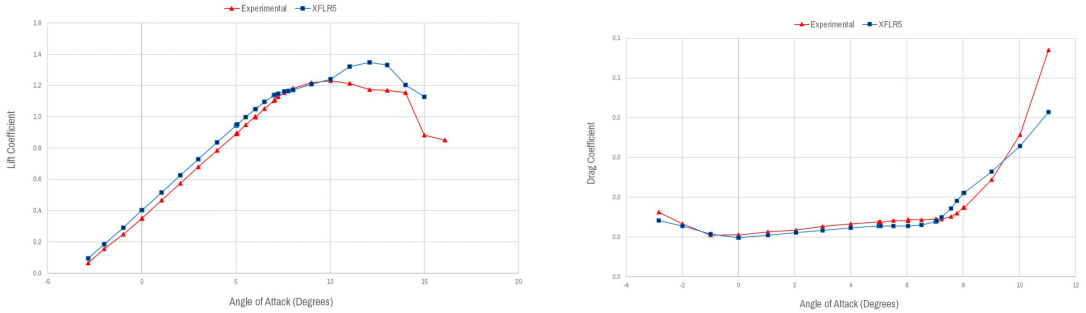

a) Lift comparation b) Drag comparation

Figure 4.21: XFLR5 vs experimental results [98]

It is important to emphasize that since this project is at a conceptual stage, the error associated with the predictions provided by the software can be passed over, although these should be reviewed and updated when the company has experimental values or a more accurate approximation of the final result of these values.

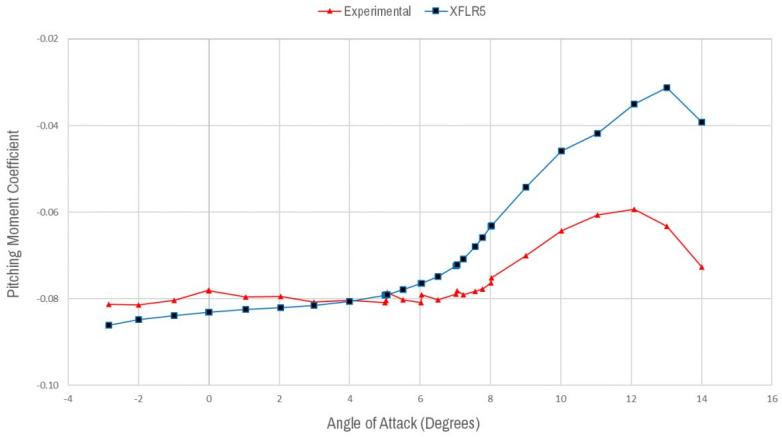

Figure 4.22: Pitching moment XFLR5 vs experimental results [98]

Taking into account that the process follows the same steps for all the cases being analysed, we'll look in detail at the situation for speed V_d and 1/3 of the maximum negative deflection of the elevator control surface (Figure 4.17a), replicating the process in the following subsection for the vertical surface, and we can find the data obtained for the other load cases in [Appendix A-Appendix D]. The process begins by obtaining the report provided by XFLR5, which breaks down the values of lift coefficient, drag coefficient and Cm along the span, as can be seen in Table 4.2, where these values are broken down for half the span of the wing, the rest being symmetrical.

It is important to note that the last section of span in bold in the Table 4.2, was added manually since the software cannot accurately estimate the values mentioned above for the entire span. We therefore considered a conservative approach in which the span would have exactly the same values as the previous section (span = 0.9963), since we know from theory that both drag and lift forces decrease with the approach to the tip of the wing, as can be seen in the XFLR5 software and visualized as an illustrative example in Figure 4.23, for a generic situation.

Figure 4.23: Example of lift on horizontal and vertical stabilizer - Load case V_d with elevator negative deflection

Finally, it should be noted that we are going to keep the Abaqus reference already presented in chapter 3 as a basis, but we are going to change the nomenclature of the axes to approximate the nomenclature typically used for these calculations, with the vertical axis being [Z], the longitudinal [X] and the transversal [Y].

Table 4.2: C_L, C_D and C_m along the semi-span of Horizontal stabilizer- XFLR5 data

Span	**C_L**	**C_D**	**C_m@25%c**
0	0.618131	0.039312	-0.07547
0.025	0.617082	0.039167	-0.07547
0.075	0.616418	0.039169	-0.07542
0.125	0.615082	0.039174	-0.07531
0.175	0.613061	0.039181	-0.07516
0.225	0.61033	0.039191	-0.07494
0.275	0.606859	0.039207	-0.07466
0.325	0.602608	0.039237	-0.07431
0.375	0.597532	0.039302	-0.07388
0.425	0.591707	0.040228	-0.07348
0.4738	0.583196	0.037405	-0.07152
0.5212	0.575999	0.038997	-0.0712
0.5687	0.567141	0.038946	-0.07043
0.6162	0.556815	0.038812	-0.06945
0.6638	0.544817	0.038591	-0.06825
0.7113	0.530825	0.038256	-0.06678
0.7588	0.514372	0.037759	-0.06497
0.8063	0.49476	0.037022	-0.06271
0.8538	0.470881	0.035919	-0.05989
0.9013	0.440778	0.034247	-0.05633
0.9487	0.400166	0.031615	-0.05172
0.9963	0.334156	0.026043	-0.04485
1.02	**0.33415**	**0.026043**	**-0.04485**

Next, taking into account the values in Table 4.2, it is possible to obtain the values for lift, drag and pitching moment per unit of span, taking into account the following sequence of Equations [Equation 4.23 to 4.27], with the results of the aerodynamic forces summarized in Table 4.3. Also, we can see in Figure 4.24 the respective distribution of lift and drag along the semi-span, and in all cases we can see their reduction when approaching the wing tip. It should be noted that in Figure 4.24b, there is a slight interference in the values obtained by the software for the 0.5 semi-span, which can be explained by small interference's in the mesh created in that region. Finally, we can also see the position of the Ribs of the horizontal stabilizer from iteration 2 along the span with the vertical blue lines in Figure 4.24.

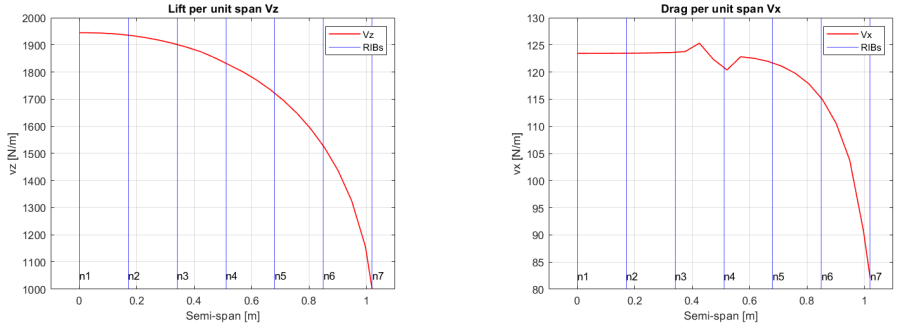

a) Lift per unit span b) Drag per unit span

Figure 4.24: Horizontal stabilizer drag and lift along the semi-span

$$q = \frac{1}{2}\rho V^2 \tag{4.23}$$

$$vz_i = q * \frac{c(Cl_i + Cl_{i+1})}{2} \tag{4.24}$$

$$vx_i = q * \frac{c(Cd_i + Cd_{i+1})}{2} \tag{4.25}$$

$$My_i = q * c * -(Cm_{i+1} + Cm_i) \tag{4.26}$$

$$my_i = \frac{My_{i+1} + My_i}{2(y_{i+1} - y_i)} \tag{4.27}$$

Table 4.3: Aerodynamic loads along the semi-span: my [N], Vz [N/m] , Vx [N/m]

Span [mm]	**Vz [N*m]**	**Vx [N*m]**	**my [N]**
0	1944.660	123.430	475.663
0.025	1943.613	123.433	475.663
0.075	1940.462	123.444	475.502
0.125	1935.172	123.463	475.014
0.175	1927.685	123.490	474.185
0.225	1917.912	123.531	473.000
0.275	1905.745	123.603	471.431
0.325	1891.048	123.753	469.445
0.375	1873.872	125.315	467.006
0.425	1851.283	122.326	464.390
0.4738	1826.532	120.386	456.928
0.5212	1801.234	122.814	449.755
0.5687	1771.006	122.522	446.336
0.6162	1735.830	121.963	440.818
0.6638	1694.878	121.087	433.951
0.7113	1646.906	119.776	425.534
0.7588	1590.079	117.832	415.185
0.8063	1521.551	114.932	402.371
0.8538	1436.492	110.560	386.378
0.9013	1325.067	103.778	366.244
0.9487	1157.064	90.851	340.494
0.9963	999.233	82.071	304.335
1.02	—	—	—

Up to this point, it has been possible to obtain the aerodynamic forces for the load case being analyzed. However, as mentioned above, the load case has a distribution of forces for the sections defined by the XFLR5 software. In order to allow them to be properly applied in the finite element software, it was necessary to reduce these points of application to the Ribs of the horizontal stabilizer. This process can be carried out by interpolating using the trapezoidal rule, considering the area under the curve for Vz[N/m], Vx[N/m] and my[N], taking into account the values in the Table 4.3, dividing the wingspan evenly around each Rib, as can be seen in the Table 4.4, where the Rib is placed in a central position with the region of integration being half the distance between the ribs adjacent to each side. Finally, it is important to note that the results obtained in Table 4.4 refer to half a wingspan since the structure is symmetrical, with rib n1 referring to the centre position and rib n7 to the position of one of the wingtips.

Table 4.4: Aerodynamic loads in rib positions

Rib id	Rib position	Lim of integ		Vz	Vx	My
-	[m]	[m]		[N]	[N]	[N*m]
n1	0	0	0.0850	330.512	20.983	80.850
n2	0.17	0.0850	0.2550	328.873	20.989	80.593
n3	0.34	0.2550	0.4250	323.031	21.059	79.652
n4	0.51	0.4250	0.5950	311.369	20.798	76.949
n5	0.68	0.5950	0.7650	292.185	20.652	73.139
n6	0.85	0.7650	0.9350	257.92	19.429	65.489
n7	1.02	0.9350	1.020	103.000	8.116	27.018

Once the forces have been reduced to the Ribs of the structure, it is important to note that the representation of the forces has also been adapted so that the vertical forces (Vz) can be equivalent to the aerodynamic moment (My), decomposing them into *Vz1* and *Vz2* applied respectively to the main spar and secound spar of the FEM model, seeking a more realistic distribution of forces throughout the structure, as suggested in Figure 4.25. The forces (Vx) can be applied to the main spar as suggested in Figure 4.25.

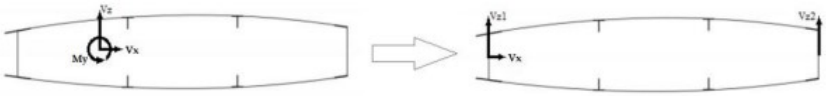

Figure 4.25: Decomposition of Aerodynamic loading

Thus, this process can be carried out taking into account the system of Equations 4.28 which can be simplified to obtain the system of Equations 4.29, which allows the calculation of the load distribution, *Vz1* and *Vz2*. It is important to note that the suggested calculation took into account that the aerodynamic centre would be located at 25% of the aerodynamic chord and the relative positions of the stringers (L1 at 30% and L2 at 55%) in relation to the chord. Where c is the length of the aerodynamic chord and li is the relative position of the spar. The results obtained at the end of this process can be seen in the 4.5.

$$\begin{cases} V_z = V_{z1} + V_{z2} \\ M_y = V_{z1}(l_1 - 0.25)c + V_{z2}(l_2 - 0.25)c \end{cases} \tag{4.28}$$

$$\begin{cases} V_{z1} = \frac{\frac{My}{c} + V_z(12-0.25)}{12-11} \\ V_{z2} = \frac{\frac{My}{c} + V_z(0.25-11)}{12-11} \end{cases} \tag{4.29}$$

Table 4.5: Lift decomposition for ribs

Rib id	Rib position	Vz1	Vz2
-	[m]	[N]	[N]
n1	0	102.325	228.187
n2	0.170	101.336	227.536
n3	0.340	97.900	225.131
n4	0.510	93.793	217.576
n5	0.680	84.909	207.276
n6	0.850	71.861	186.058
n7	1.020	25.813	77.187

Next, it was necessary to decompose the loads obtained into their vertical and horizontal components, as shown in Figure 4.26 for *Vz1* and *Vz2* and Figure 4.27 for *Vx*, since unlike the analysis carried out in XFLR5 where the tail had an angle of attack of 4.72 degrees, the finite element model has an angle of attack of 0 degrees. This process can therefore be carried out by applying the Equations 4.30 to Equation 4.35, and the Table 4.6 shows the results obtained.

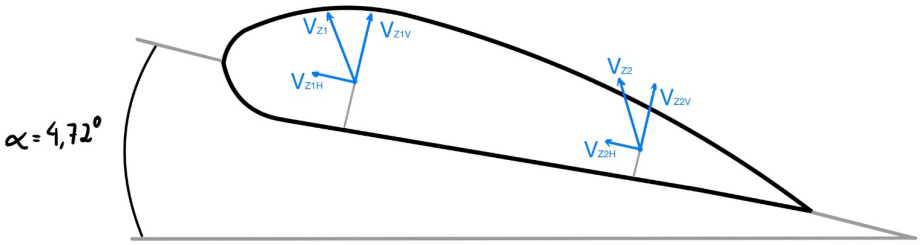

Figure 4.26: Vector decomposition of Lift with the angle of attack=4.72 degrees

$$Vz_{1V} = Vz_1 \cos(4.72°) \tag{4.30}$$

$$Vz_{1H} = Vz_1 \sin(4.72°) \tag{4.31}$$

$$Vz_{2V} = Vz_2 \cos(4.72°) \tag{4.32}$$

$$Vz_{2H} = Vz_2 \sin(4.72°) \tag{4.33}$$

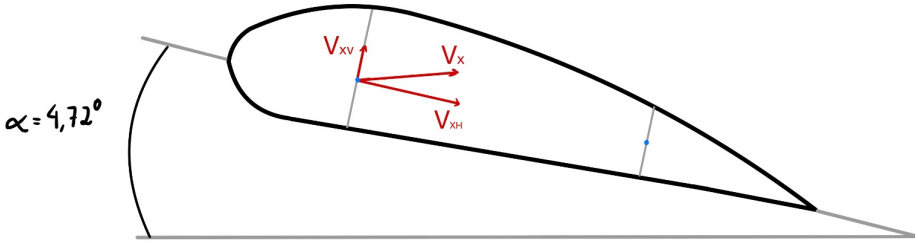

Figure 4.27: Vector decomposition of Drag with the angle of attack=4.72 degrees

$$Vx_V = V_x \sin(4.72°) \tag{4.34}$$

$$Vx_H = V_x \cos(4.72°) \tag{4.35}$$

Table 4.6: Aerodynamic load decomposition with safety factor=1.5

Rib id	Rib position	Vz1 V	Vz1 H	Vz2 V	Vz2 H	Vx V	Vx H
-	[m]	[N]	[N]	[N]	[N]	[N]	[N]
n1	0	101.978	8.423	341.119	28.177	1.727	-20.912
n2	0.170	100.993	8.342	340.147	28.096	1.728	-20.917
n3	0.340	97.475	8.059	336.550	27.799	1.734	-20.988
n4	0.510	93.475	7.7212	325.256	26.866	1.712	-20.728
n5	0.680	84.621	6.989	309.858	25.595	1.700	-20.582
n6	0.850	71.618	5.9158	278.140	22.975	1.599	-19.366
n7	1.020	25.725	2.1250	115.388	9.531	0.668	-8.089

Finally, the final loads applied to the finite element model can be represented by two sets, Vz in its vertical component (sum of $Vz1\ V$ and $Vx\ V$) and its horizontal component (sum of $Vz1\ H$ and $Vx\ H$), which are applied at the intersection of the ribs with the main spar, and $Vz2$ in its vertical and horizontal components, which are applied at the intersection of the ribs with the secound spar, as can be seen in Table 4.7 considering the Abaqus reference axis. Note that in this last step a safety factor of 1.5 was also taken into account.

Table 4.7: Aerodynamic loads equivalent for the Finite Element Model.

Rib id	Rib1	Rib2	Rib3	Rib4	Rib5	Rib6	Rib7
VZ1 H [N]	-18.7329	-18.8636	-19.393	-19.5101	-20.3886	-20.1718	-8.945974358
VZ1 V [N]	155.5578	154.0812	148.9529	142.7812	129.4822	109.8262	39.59041651
VZ2 V [N]	341.1195	340.1469	336.5503	325.2565	309.8588	278.1402	115.388696
VZ2 H [N]	28.177	28.09666	27.79958	26.86669	25.59481	22.97481	9.531284659

4.1.2.4 Load cases calculation for Vertical stabilizer

Once the loads had been defined for the horizontal structure, an identical process was taken into account for the vertical surface, starting by extracting the reports provided by XFLR5 (which can be consulted in Appendix C), allowing the lift (Vz) and drag (Vx) forces to be calculated for the various sections estimated by the software following Equation 4.23 to 4.27, with the pitching moment in this case being 0, since it is a symmetrical profile with an angle of attack equal to 0 degrees, and the results can be seen in Table 4.8. In addition, in Figure 4.28 we can also observe the lift (Vy) per unit span, and we can see an interference in the final section, justified by the contact interference generated by the deflection of the elevator control surface.

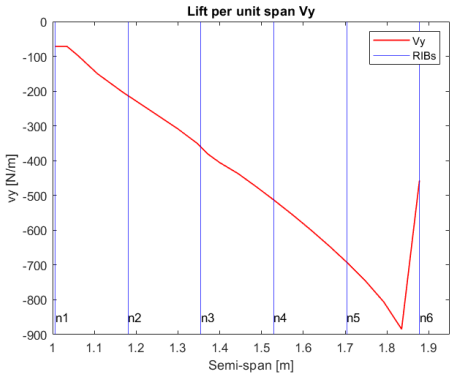

Figure 4.28: Vertical stabilizer lift per unit span

Table 4.8: Aerodynamic loads along the span: My [N*m], Vz [N/m] , Vx [N/m]

Span [m]	Vz [N*m]	Vx [N*m]	My [N*m]
1.0066	**-71.7065**	**15.97592**	**0**
1.0347	-71.7065	15.97434	0
1.0603	-97.4265	15.97434	0
1.1076	-150.281	15.97277	0
1.1695	-204.49	15.96804	0
1.2365	-257.725	15.96331	0
1.2984	-307.497	15.96016	0
1.3457	-349.945	15.95544	0
1.3713	-380.794	15.95228	0
1.3999	-405.649	15.95071	0
1.4436	-437.054	15.94598	0
1.4874	-475.07	15.93968	0
1.5311	-514.831	15.9318	0
1.5749	-556.406	15.92077	0
1.6186	-600.031	15.90816	0
1.6624	-645.993	15.89556	0
1.7061	-694.726	15.88295	0
1.7494	-747.053	15.86877	0
1.7921	-806.028	15.86405	0
1.8349	-884.403	15.87508	0
1.8776	—	—	0

Taking into account the values from the Table 4.8 , the same procedure used in the previous subsection was used to obtain the loads on the Ribs of the vertical stabilizer, using the integration intervals from the Table 4.9, referring to iteration 2 of the structure.

Table 4.9: Aerodynamic loads in rib positions

Rib id	Rib Position	Lim of integ		Vz	Vx
-	[m]	[m]		[N]	[N]
n1	1.0066	1.0066	1.0576	-5.881	1.222
n2	1.1086	1.0576	1.2253	-44.603	4.0163
n3	1.3419	1.2253	1.4586	-122.327	5.584
n4	1.5752	1.4586	1.6919	-195.795	5.572
n5	1.8776	1.6919	1.8776	-208.374	4.421

Finally, it is important to note that although the pitching moment generated is 0, the moment created by the lift (Vy), when applied to the main spar at 30% of the chord, generates a moment that will have to be compensated for so as not to create an unreasonable twist in the vertical stabilizer, so the decomposition in Figure 4.25, for the Lift (Vy), in the components *Vz1* and *Vz2*, applied respectively to the main and secound spar (70% of the chord), it can also be noted that since the drag force (Vx) remains applied to the main spar. Therefore, in Table 4.10 we can see the loads taken into account for the Vertical surface in the finite element model, applying a safety factor of 1.5 as was done for the Horizontal surface. Note that this load case is symmetrical and therefore the second vertical stabilizer will have symmetrical conditions.

Table 4.10: Aerodynamic Loads with safety factor=1.5

Rib id	Rib1	Rib2	Rib3	Rib4	Rib5
Vx [N]	-1.22207	-4.016274	-5.584284	-5.571479	-4.420857
Vy1 V [N]	-6.616	-50.18	-137.6	-220.3	-234.4
Vy2 V [N]	0.735087	5.575388	15.29094	24.47438	26.0468

4.2 Inertia Loads

Considering the six critical load cases calculated in terms of aerodynamic forces, it was necessary to approximate the inertia forces of the vertical stabilizer, horizontal stabilizer, and boom structure.

Since the ribs are the main structural elements responsible for supporting the weight of the structure, a reasonable approximation was made by considering that each rib would support at its center of mass the respective inertia force corresponding to half the weight of the section to its left and right, with the ribs at the limit positions of the structures only supporting one side, as detailed in the following subsections.

To estimate the weight, it's important to note that since various iterations of the structure were directly performed in the finite element software, to avoid meshing issues that could arise from imported CAD structures, the Abaqus mass prediction tool was utilized.

Finally, before proceeding to the subsections, it's important to consider that throughout the iterative analysis process in a later phase of the project, the estimated weight values will vary. This variation will occur due to testing different versions of spars and reducing the number of ribs in a later part of the project. Therefore, this subsection aims to exemplify how the process was approached for iteration 2, with the procedure being similar for subsequent iterations.

4.2.1 Inertia loads horizontal stabilizer

Starting with the horizontal stabilizer (Figure 4.29) presented in Subsection 3.3.2.2, this is made up of 13 ribs, part of the main Spar and the secondary Spar and the respective skin that surrounds the structure. It's important to note that the 2 end ribs are heavier because they don't have any holes and have a double thickness because they represent the connection zone between the vertical and horizontal stabilizer, while the remaining 11 ribs are lighter and all have the same weight. Therefore, using the "Query - Mass Properties" tool, it was possible to arrive at the mass values of the aforementioned elements, shown in the Table 4.11 . Note that once the ribs are equally spaced, the section between them is the same and is represented in the Table 4.11 as "Section (Skin+Spars)", representing the software's estimate for the weight of the skin, main and secound spar in that section.

Table 4.11: Weight estimation for Horizontal stabilizer structural elements

Elements	Weight [kg]
rib with hole	0.332
rib without hole	0.145
Section (skin+Spars)	1.07

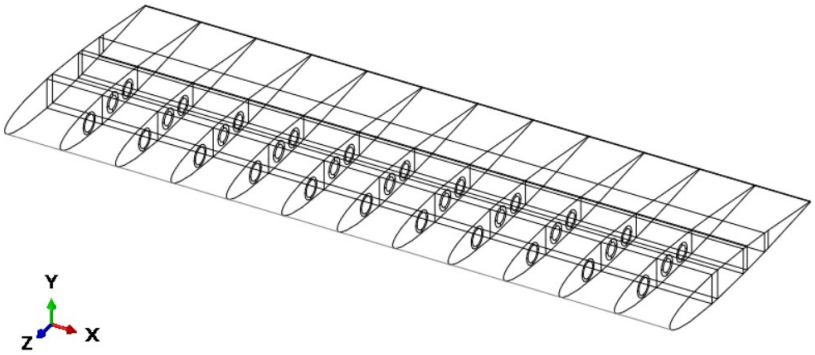

Figure 4.29: Horizontal Stabilizer

Based on the values from Table 4.11, the inertial forces for each rib were calculated using Equations 4.36 and 4.37, where MS represents a margin of safety of 1.5 and g denotes the gravitational acceleration of 9.81 m/s^2. The results obtained are shown in Table 4.12.

$$W_{rib_{ends}} = (0.332 + \frac{1.07}{2})gMS \tag{4.36}$$

$$W_{rib_{holes}} = (0.145 + 1.07)gMS \tag{4.37}$$

Table 4.12: Inertia Loads for Horizontal Stabilizer

Elements	Inertia load [N]
Rib without holes	12.75791
Rib with holes	17.9523

4.2.2 Inertia loads vertical stabilizer

For the vertical stabilizer (Figure 4.30) the same procedure as previously mentioned was followed, with the peculiarity that sections mostly represent different dimensions, necessitating individual calculations for each rib. Thus, it consists of 4 ribs with holes (R1-R4 in Figure 4.30), each weighing the same, and one rib without holes, with the same thickness as the 4 aforementioned ribs. It's important to note that the rib at the connection point has already been accounted for in the horizontal stabilizer, considering that the weight of the curved section would be the responsibility of the subsequent rib (without holes). In addition to these elements, it also includes corresponding sections of the main spar, secondary spar, and the skin. Lastly, despite the vertical stabilizer sharing the connection zone with the boom structure towards its end, it was assumed that the last rib would be responsible for supporting the weight of this section. The calculation of inertial forces for the boom starts from the first former, as detailed in the following subsection.

Table 4.13: Weight estimation for Vertical stabilizer

Elements	Weight [kg]
Rib without holes	0.166
Rib with holes	0.141
Curved initial section	0.589
Section after curve	0.637
Central section	1.46
Final section	1.85

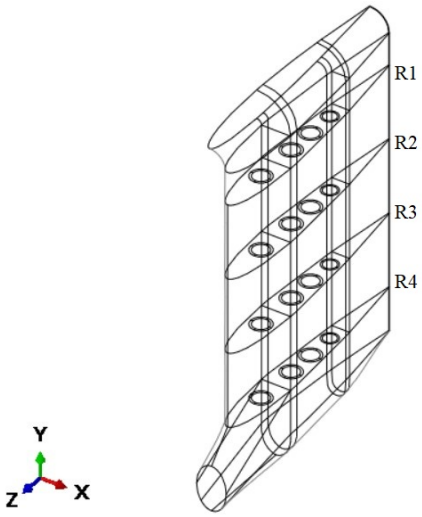

Figure 4.30: Vertical Stabilizer

Therefore, in Table 4.13 the estimated weight values by the software for the different sections of the vertical stabilizer are shown. Using Equations [4.38 to 4.42], the inertial forces for each vertical rib were calculated, as presented in Table 4.14.

$$W_{rib_{start}} = (0.166 + 0.589 + \frac{0.637}{2})gMS \tag{4.38}$$

$$W_{rib_{holes1}} = (0.141 + \frac{1,46}{2} + \frac{0.637}{2})gMS \tag{4.39}$$

$$W_{rib_{holes2}} = (0.141 + 1.46)gMS \tag{4.40}$$

$$W_{rib_{holes3}} = (0.141 + 1.46)gMS \tag{4.41}$$

$$W_{rib_{holes4}} = (0.141 + 1.85 + \frac{1.46}{2})gMS \tag{4.42}$$

Table 4.14: Inertial Loads for Vertical Stabilizer

Elements	Inertial Force [N]
Rib without holes	15.79655
Rib with holes 1	17.87137
Rib with holes 2	23.55872
Rib with holes 3	23.55872
Rib with holes 4	40.03952

4.2.3 Inertia loads Boom

Finally, regarding the Boom, it was necessary to analyze three different structures: reinforced Boom with internal tube, reinforced Boom with stringers, and reinforced Boom with stringers and internal tube. It's important to note that throughout this section, the counting of sections and elements starts from the former located next to the Vertical Stabilizer, with sections corresponding to the space between formers.

4.2.3.1 Boom with internal pipe

Starting with the case of the boom reinforced with an internal tube (Figure 4.31), it consists of 9 formers with slight variations in weight due to the varying section of the boom along its length, and two internal tubes. One tube, of larger diameter, starts at the main wing and ends at the boom mounting area (F6 in Figure 4.31). The second tube, of smaller diameter, starts at the same connection point and ends at the connection to the secondary spar of the Tail, as explained in Subsection 3.3.4.1.

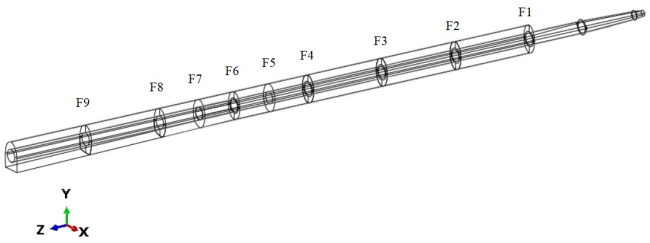

Figure 4.31: Boom with internal pipe

Therefore, in Table 4.15,the estimated weight values are presented for the 9 formers and the estimated weight of the 9 sections delimited by the formers, including the weight of the skin and tube for each respective section. Additionally, the weight of the boom extension from this structure to the secondary spar is shown.

As a special condition, in this and the following case, two extra inertial forces corresponding to the extension of this element were added. It was considered more accurate to assume that these forces would be supported by the main and secondary spars at the connection regions.

Table 4.15: Weight estimation for Boom with innternal pipe

Elements	Weight [kg]
Former1	0.0263
Former2	0.0271
Former3	0.0279
Former4	0.0287
Former5	0.0291
Former6	0.0295
Former7	0.0285
Former8	0.0292
Former9	0.031
Section1	0.847
Section2	0.851
Section3	0.855
Section4	0.453
Section5	0.409
Section6	0.555
Section7	0.472
Section8	0.911
Section9	0.981
Internal pipe final section	0.0186
Internal pipe from main spar to secound spar	0.182
Internal pipe from first former to main spar	0.206

Based on the values from Table 4.15, Equations [4.43 to 4.47], the procedure that was taken into account to obtain the values of the inertial forces for the different formers and spars represented in Table 4.16, with Equation 4.44 represents the generic process for obtaining the inertial force for the boom sections, with the remaining equations referring to the two extreme boom sections and their respective spars.

$$W_{rib_{start}} = (0.0263 + \frac{0.847}{2} + \frac{0.206}{2})gMS \tag{4.43}$$

$$W_{rib_{holes1}} = (0.02 + \frac{0.847}{2} + \frac{0.851}{2})gMS \tag{4.44}$$

$$W_{rib_{holesfinal}} = (0.031 + 0.981 + \frac{0.911}{2})gMS \tag{4.45}$$

$$W_{spar_{main}} = (\frac{0.206}{2} + \frac{0.182}{2})gMS \tag{4.46}$$

$$W_{spar_{secound}} = (\frac{0.0186}{2} + \frac{0.182}{2})gMS \tag{4.47}$$

Table 4.16: Inertial Loads for Boom with internal pipe

Elements	Inertial force [N]
Former1	8.947897
Former2	14.18099
Former3	14.25869
Former4	11.05052
Former5	7.447409
Former6	8.279395
Former7	8.773083
Former8	11.66561
Former9	23.75369
Main spar	3.140181
Secound Spar	1.77404

4.2.3.2 Boom with Stringers

Having defined the inertial forces for the all-internal boom, it was necessary to carry out the same process for the second structural option of a boom reinforced by stringers (Figure 4.32).

Figure 4.32: Boom with stringers

Therefore, the procedure follows the same parameters as before, with this structure comprising the same 9 formers and replacing the inner tube with 4 longerons, including the connecting tubes in the central assembly area and losing the need to estimate the inertial forces for the extension of the boom that would be supported by the spars. So, as shown in the previous subsection, in the Table 4.17 we can find the estimated weights for the different formers and sections that make up the structure.

Table 4.17: Weight estimation for Boom with stringers

Elements	Weight [kg]
Former1	0.0263
Former2	0.0271
Former3	0.0279
Former4	0.0287
Former5	0.0291
Former6	0.0295
Former7	0.0285
Former8	0.0292
Former9	0.031
Section 1	0.794
Section 2	0.801
Section 3	0.808
Section 4	0.429
Section 5	0.501
Section 6	0.625
Section 7	0.439
Section 8	0.844
Section 9	0.912

Taking into account the values obtained in Table 4.17, we were able to calculate the values in Table 4.18, following the same line of thought presented in the previous Equations [4.43 to 4.45]. It should be noted that compared to the values obtained previously in Table 4.16, this second constructive solution is slightly lighter, with a decrease of approximately 3.36 %, with only an increase in weight in sections 5 and 6 since they correspond to the sections where the connecting tubes are included, approximating the geometry of the first constructive solution, but including the stringers in that section.

Table 4.18: Inertial Loads for Boom with stringers

Elements	Weight [kg]
Former1	6.851745
Former2	13.34739
Former3	13.47364
Former4	10.4759
Former5	7.99775
Former6	9.590501
Former7	9.072533
Former8	10.85629
Former9	14.71353

4.2.3.3 Boom with Stringers and internal pipe

To finalize, the same procedure had to be applied to the Boom with Stringers and internal pipe version (Figure 4.33), expecting beforehand that it would be considerably heavier, being made up of the same 9 formers, 4 longerons and the two internal pipe sections as explained above. So in Table 4.19 we can see the estimated weights for the various sections.

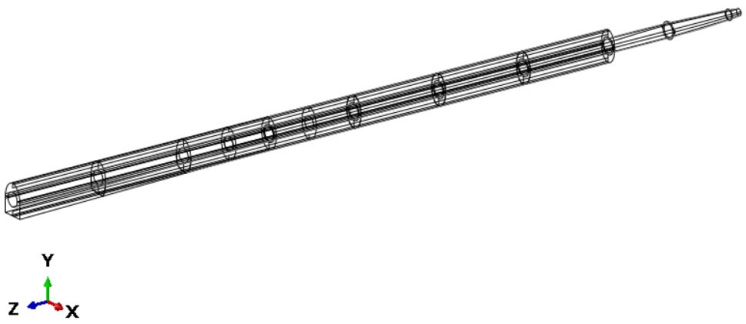

Figure 4.33: Boom with internal pipe and stringers

Table 4.19: Weight estimation for Boom with internal pipe and stringers

Elements	Weight [kg]
Former1	0.0263
Former2	0.0271
Former3	0.0279
Former4	0.0287
Former5	0.0291
Former6	0.0295
Former7	0.0285
Former8	0.0292
Former9	0.031
Section 1	1.06
Section 2	1.06
Section 3	1.07
Section 4	0.567
Section 5	0.513
Section 6	0.66
Section 7	0.592
Section 8	1.14
Section 9	1.18
Internal pipe final section	0.0186
Boom from main spar to secound spar	0.182
Boom from first former to secound spar	0.206

Having obtained the values from Table 4.19, the same thinking applied in Equations [4.43 to 4.47] was taken into account, with this case again requiring the estimation of the inertial forces for the Boom's extension from the first Former to its end at the secound spar. Note that as estimated at the beginning of the subsection, this version shows an average increase of 14.10 % compared to the lighter case.

Table 4.20: Inertial Loads for Boom with internal pipe and stringers

Elements	Weight [kg]
Former1	10.67176
Former2	17.59634
Former3	17.69023
Former4	13.7132
Former5	9.211737
Former6	9.970884
Former7	10.59406
Former8	14.49015
Former9	28.82816
Main Spar	3.140181
Secound Spar	1.77404

Chapter 5

Structural Analysis

Having defined the structural concept for the different versions of the tail and boom structure in Chapter 3, and identified the inertial and aerodynamic forces for the critical load cases in Chapter 4, in the initial phase of Chapter 5 we will present the FEM model of the tail and boom of the ARX aircraft, explaining how the various forces and boundary conditions were applied to the model, the characteristics of the material used and finally the validation of the model. In a second phase, we will also compare the three different versions of iteration 2 previously designed in the concept phase, so that, taking into account the results obtained, we can define which will be the most suitable for the company's conditions and objectives, allowing us to iterate an optimized version of it at structural level in Chapter 6 and at orientation level and number of material layers in Chapter 7.

5.1 FEM model

In the aeronautics industry, there are typically two ways of approaching a finite element model representing a structure to be tested: representing it in finite element software while carefully respecting all the dimensions of the real structure, or exporting the CAD model of the same structure. Engineers often opt for the first option whenever possible, as it has advantages such as better mesh generation, reducing the number of interference and points with poor mesh quality, since the software creates the references based on a model already created within the software, as well as allowing greater design freedom by being able to alter and rectify small details of the structure more easily. On the other hand, importing a CAD model into Finite Element software is typically associated with the creation of countless mesh interference, since the software creates the references based on an exported model, and often doesn't have the capacity to properly distribute the number of mesh elements across the edges of the structure, thus requiring extra work in the creation of countless partitions, and it is typical to use external software such as hyper mesh to facilitate this process.

In the case of this project, since we had the objective not only of carrying out a vast amount of analysis and alterations to the structure, but also its optimization in the programming tool developed in Chapter 7, this required programming the structure, which, together with the problems already mentioned, led to the need to replicate the real CAD model supplied by the company in the finite element software.

Therefore, in Figure 5.1 , Figure 5.3 and Figure 5.2 we can see three comparisons of the CAD model supplied by the company and the FEM model developed in the Abaqus software, which was developed taking into account a meticulous collection of dimensions from the real model, in order to guarantee a correct analysis and validation of the results obtained for the real structure.

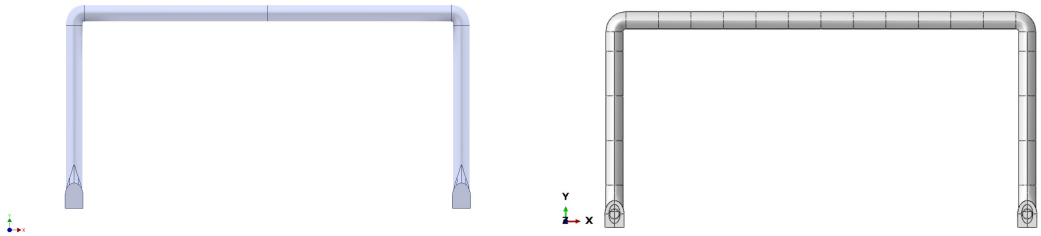

a) CAD model b) FEM model

Figure 5.1: Comparison of the front view of the Real model and the FEM model made

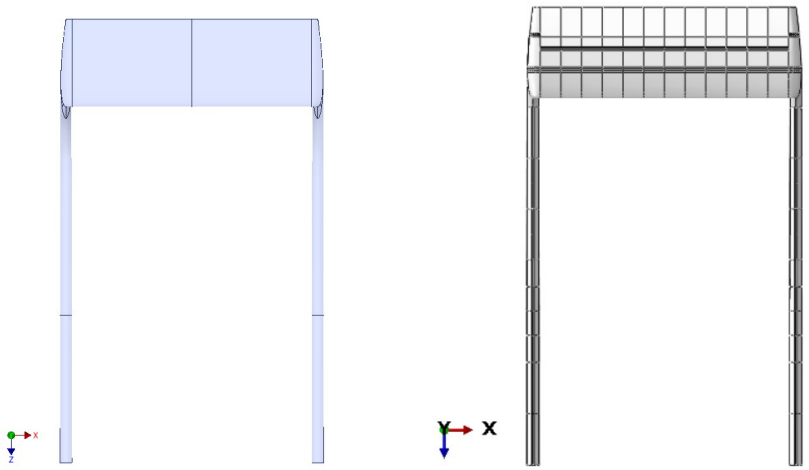

a) CAD model b) FEM model

Figure 5.2: Comparison of the top view of the Real model and the FEM model made

It is important to note that the only area that could not be replicated with the same perfection as the rest of the structure was the area between the vertical stabiliser and the Boom, although this approximation is considered reasonable as it maintains the position and dimensions of the real case. However, in order to confirm that the FEM model drawn up at an early stage of the project, corresponding to iteration 1, was working properly, a CAD version was tested by comparing it with the one modelled entirely in the software, and its consistency could be verified, as can be seen in more detail in Subsection 5.1.5.

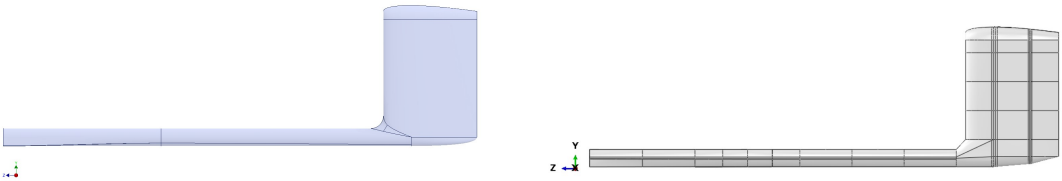

a) CAD model b) FEM model

Figure 5.3: Comparison of the lateral view of the Real model and the FEM model made

5.1.1 Material Properties

With regard to the material used in the FEM model in the Abaqus software, a unidirectional CFRP laminate was taken into account, chosen over other non-directional options available from the company in order to facilitate better operation of the optimization tool applied in the following chapter. As such, the material supplied has a thickness(t) of 0.25 [mm] and a specific mass of (ρ_{CFRP}) is 1.8*10-9 [tonne/mm3]. The remaining mechanical properties can be found in Table 5.1, and the properties in Table 5.2, provided by the company. It should be noted that the properties of Elastic failure Strain are not shown, since at the time this project was realized these values were not yet known by the company.

Table 5.1: Laminate Elastic mechanical properties

	E1	E2	E3	v12	v13	v23	G12	G13	G23
Elastic mechanical properties	*Classify*	*Classify*	*Classify*	*Classify*	*Classify*	*Classify*	*Classify*	*Classify*	*Classify*

Table 5.2: Laminate Elastic failure stresses

	Ten Stress Fiber Dir	Com Stress Fiber Dir	Ten Stress Transv Dir	Com Stress Transv Dir	Shear Strength
Elastic failure stresses	*Classify*	*Classify*	*Classify*	*Classify*	*Classify*

Where,

E1- stiffness of the composite along the fiber direction

E2- composite in-plane stiffness perpendicular to the direction of the fibers.

E3- transverse lamina stiffness.

G13/G12- in-plane shear modulus

G23- transverse shear modulus

v12- in-plane 1-2 Poisson ratio

5.1.2 Boundary Conditions

Regarding the boundary conditions, in collaboration with the colleague who was developing the rib connecting the boom to the aircraft fuselage, it was possible to conclude that the displacements and rotations in the final section of the boom, corresponding to the area where the structure is mounted to the main wing, would be approximately 0. At first glance, the two options closest to this situation were the "pinned" condition and the "encaster" condition provided by the software. However, it is important to bear in mind that, according to the De Saint-Venant principle, the total clamping of the last former would lead to an unrealistic concentration of stresses in the rounds of the constrained face, creating an artificial change in the results obtained in the structure which was not desired.

It was therefore decided to apply support (U1=U2=U3=0) to the edges of the last former and to fix (U1=U2=U3=UR1=UR2=UR3=0) in the case of a boom with an inner tube to the edge of that tube, since it would be a point of attachment and connection to the wing, and in the case of the customary solution of a boom with stringeres, to fix only the final edges of the stringeres, since these would be fixed to the final connection section. Therefore, in Figure 5.4, we can see an isometric view of the general structure, where we can visualise the point of application, and in Figure 5.5, two detail views for the two cases mentioned above.

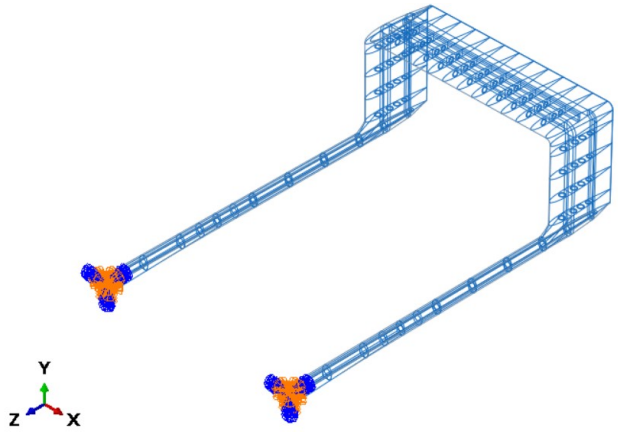

Figure 5.4: Boundary conditions applied to the Fem model

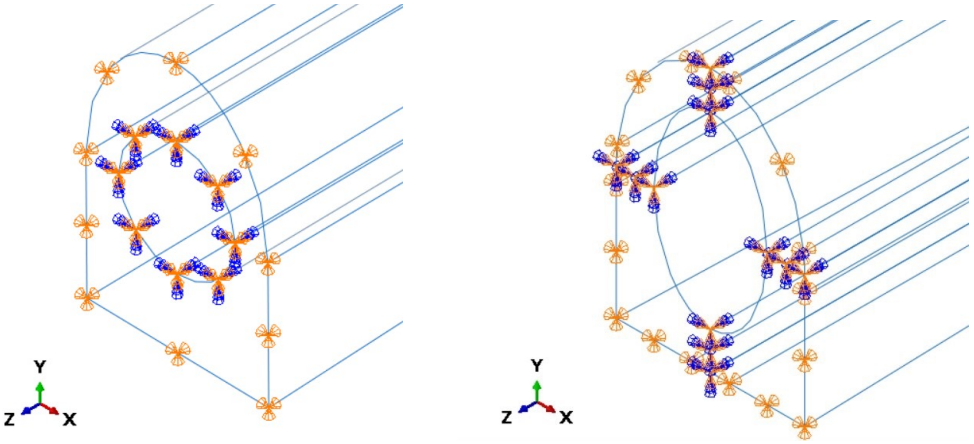

a) Boom with internal pipe b) Boom with stringers

Figure 5.5: Boundary conditions detail

5.1.3 Aerodynamic Loads application

After the detailed calculation described in Subsection 4.1.2.3, where it was possible to illustrate the procedure for obtaining the aerodynamic loads to which the horizontal stabilizer (Subsection 4.1.2.3) and vertical stabilizer (Subsection 4.1.2.4) would be subject in the 6 critical loads identified in the V-n diagram, it was necessary to apply this information to the aircraft's FEM model.

It is therefore essential to remember that the strategy used to apply these loads to the model involved the direct application of a system of equivalent concentrated forces at the junction between the stringers and the ribs, which ensures that the areas furthest from the load application points are not unduly deformed due to the creation of concentrated forces, providing a more accurate simulation. In addition, it is important to note that the ideal application of the forces would be at the aerodynamic center, which is located approximately 25% from the chord and between 50% and 60% of the thickness of the wing profile, in the vertical direction, however a good approximation to this application can be made along the center line of the stringers, the path followed due to its simplicity. Therefore, in Figure 5.6a we can see an example of the aerodynamic forces applied to the horizontal surface calculated for Load case with positive elevator deflection and in Figure 5.6b for Load case with negative elevator deflection.

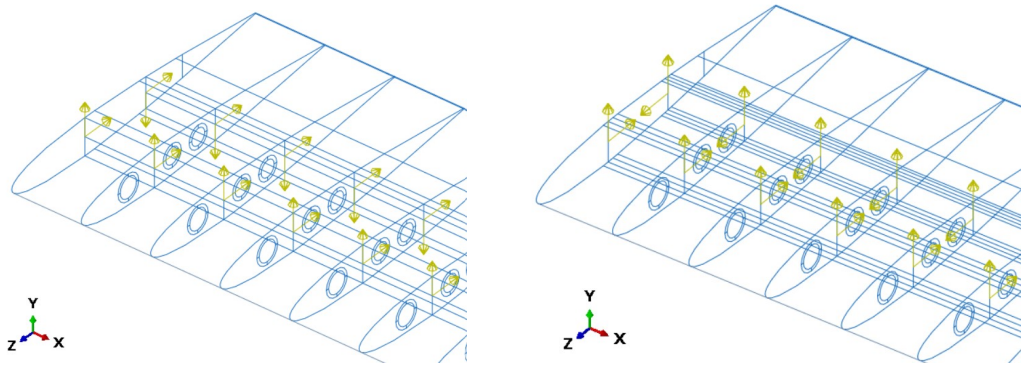

a) Load case with elevator positive deflection b) Load case with negative elevator deflection

Figure 5.6: Applying loads to the Horizontal surface

As predicted in Chapter 4, after obtaining the estimates for the critical cases in the XFLR5 software, we can see that the predictions made at an early stage (Figures 4.18, 4.19 and 4.20) are confirmed, with the moment created on the horizontal stabiliser being negative in the case of Figure 5.6a and positive in the case of Figure 5.6b. In a second analysis, in Figure 5.7 we can see the application of the forces on the vertical stabiliser, with Figure 5.7 referring to the case of positive elevator deflection, expecting a positive force as estimated by sofwere XFLR5 in Figure 4.19 and a negative force for the vertical stabiliser in the load case for positive deflection, as initially estimated in Figure 4.18.

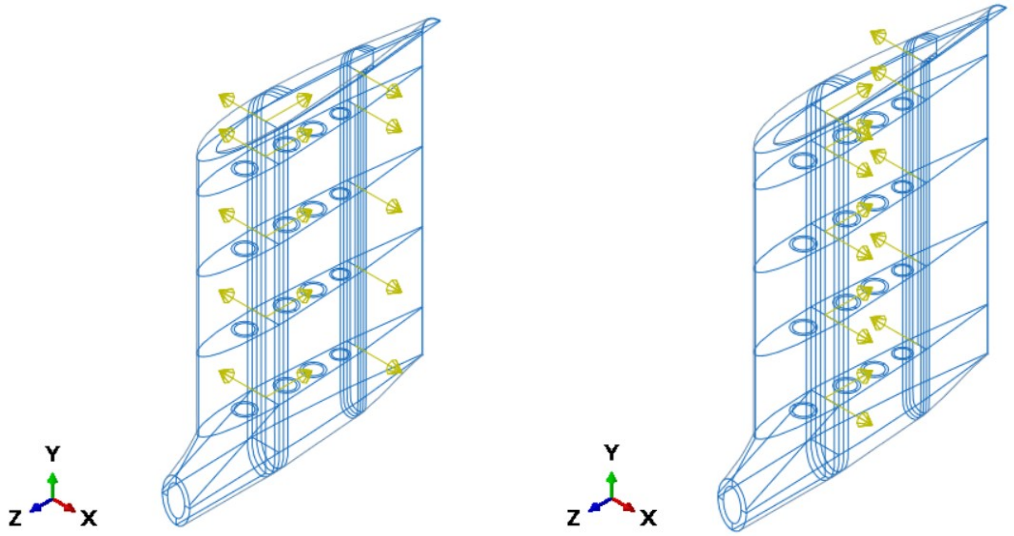

a) Load case with elevator positive deflection b) Load case with elevator negative deflection

Figure 5.7: Applying loads to the Vertical surface

Finally, we can see in Figure 5.8, the application of the forces estimated for the vertical stabiliser in the deflection load case of the Rudder control surface, and we can confirm that opposite directions were obtained for the two stabilisers, as initially estimated in the software in Figure 4.20.

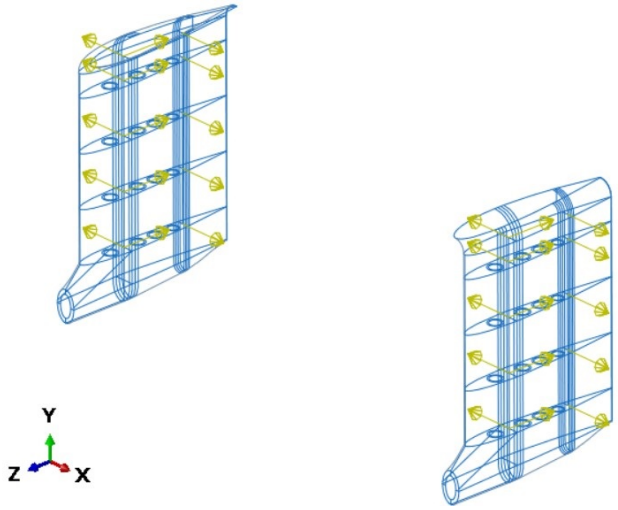

Figure 5.8: Load case with left rudder negative deflection and right rudder positive deflection

5.1.4 Inertial Loads application

In terms of the inertial forces, calculated in Chapter 4 in Section 4.2, it was necessary to translate them as correctly as possible into the Finite Element model, so the first task was to obtain the centre of mass values for each Rib and formers, creating a series of reference points that represent them (Figure 5.9), allowing the values obtained in Tables 4.12 4.14,4.16,4.18 and 4.20 to be applied to each corresponding element.

It should be noted that, typically, the more application points that are created, the greater the approximation to the real case of the distribution of inertial forces. In this case, the model had 41 application points, which was considered sufficient to obtain a reasonable approximation to the distribution of weight throughout the structure. However, the application of a force concentrated at a reference point would end up representing the real case in an unrepresentative way, since the weight is not distributed at one point but throughout the structure. Therefore, in order to create as realistic an approximation as possible, "coupling- Structural distribution" constraints were created following the "Uniform" wheithing method in order to guarantee a uniform distribution of the force throughout the element (Rib or former).

It's important to note that the Abaqus user manual [99] provides other coupling options such as "Kinetic" or "Continuem distribution", however the method mentioned above was chosen because it couples the displacement and rotation of each attachment point (in this case the reference point) to the average displacement and rotation of the surface nodes within the radius of influence (in this case the element frame), unlike Continuem distribution which only couples the average displacement and "Kinetic" which restricts the movement of the coupling nodes to the movement of the rigid body of the reference node. The same applies to the decision made for the wheithing method. There are others such as "Linear", "Quadratic" and "Cubic", representing non-uniform forms of weight distribution along the element, which are considered less realistic for the application being analyzed.

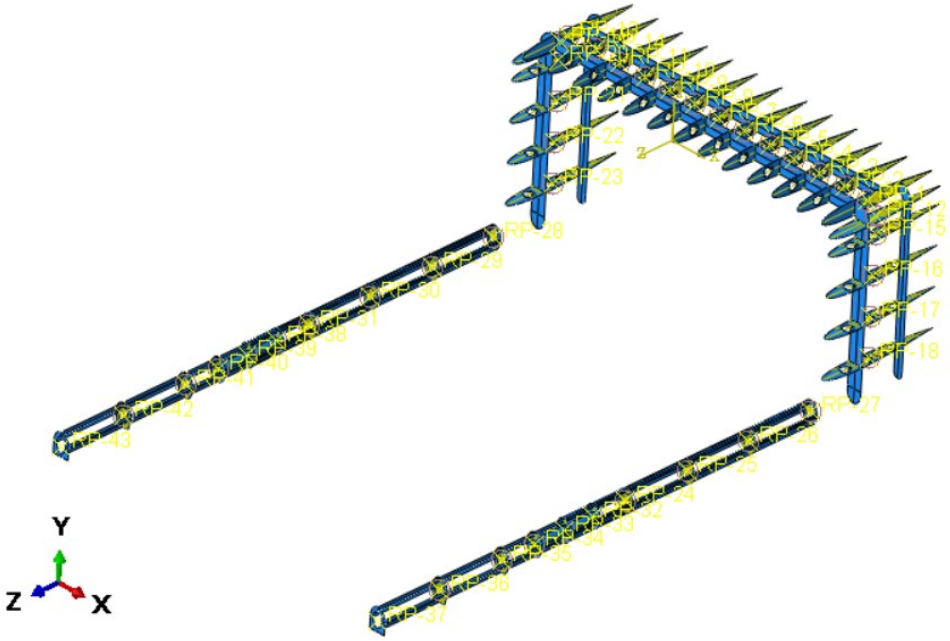

Figure 5.9: Application of reference points in the finite element model

With this in mind, in Figure 5.10, we can see the final result of the couplings applied to the various Ribs of the Horizontal surface, with the forces applied at each respective reference point and then distributed by Rib through the constraint as explained above.

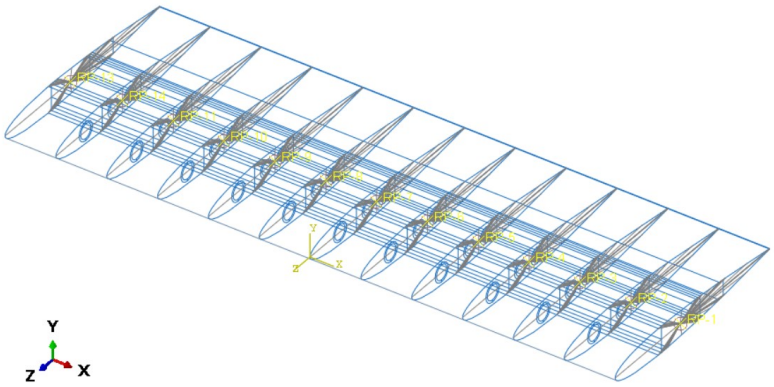

Figure 5.10: Applying Inertial loads to the Horizontal stabilizer

In the same way, we can see in Figure 5.11, the distribution of the inertial forces across the different Ribs of the vertical surface, with Figure 5.11a representing the case for the constructive solution of a boom reinforced by strigners with no inertial force in the spars, while Figure 5.11b, the case of a boom reinforced with an internal tube, showing the two reference points created in the holes of the main and secound spar and the respective coupling of the force in this lower region of the spar.

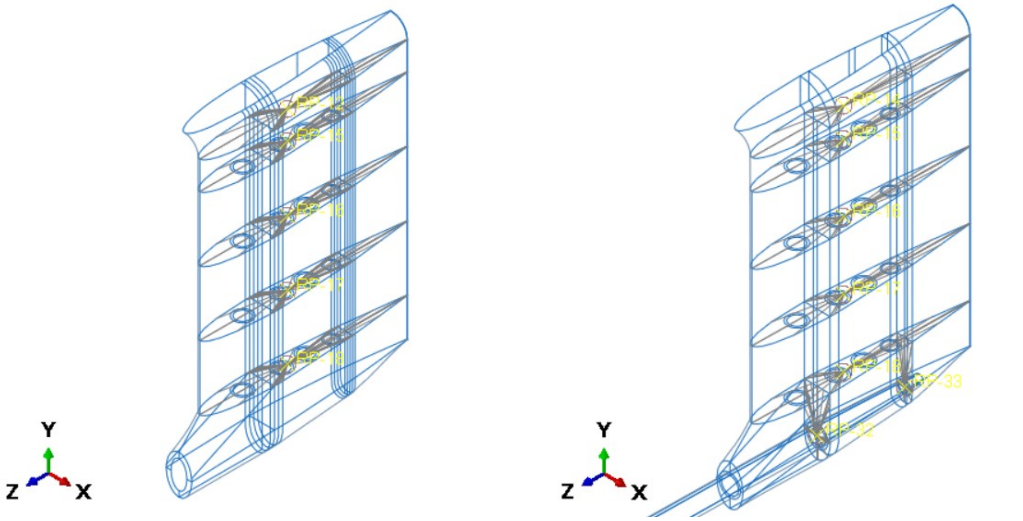

a) Inertial loads in Boom with stringeres b) Inertial loads in Boom with internal pipe

Figure 5.11: Applying Inertial loads to the Vertical stabilizer

Finally, in Figure 5.12, we can see a detail view of the result of this same process on the Boom formers for the example case of a boom with reinforcing stringers. It is important to note that, as explained in the section on calculating the inertial forces for this component, it was decided not to apply any shape to the last former since it would be the point of application of the boundary conditions, with the penultimate former being responsible for bearing the weight of this last section.

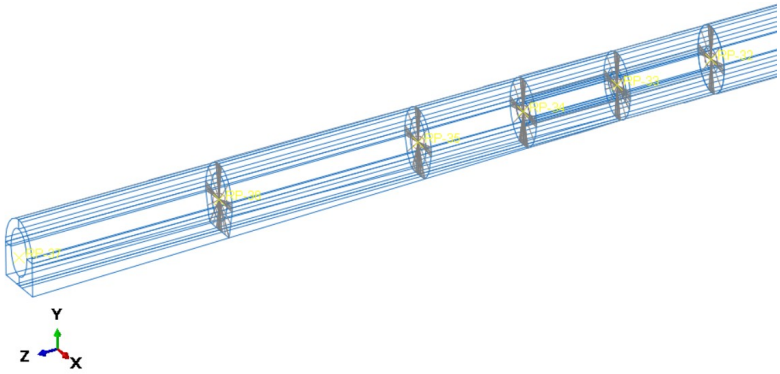

Figure 5.12: Applying Inertial loads to the Boom structure

5.1.5 Validation FEM model

As mentioned at the beginning of this chapter, at an early stage of the project when iteration 1 of the various Tail and Boom construction solutions was designed, the need arose to confirm that the structure modelled entirely in the FEM software obtained the same results as the iteration exported from the CAD model supplied by the company. Therefore, in this subsection we will illustrate the results obtained, which allowed us to demonstrate that the FEM model worked properly and to move on to the structural analyses of iteration 2.

Therefore, below we can see a series of comparisons made for the load case of positive deflection of the elevator for speed Va. It is important to note that since this geometry refers to iteration 1

and this process was carried out at a very preliminary stage of the project, it is important to bear in mind that the results obtained are only useful for direct comparison between the two structures, and it is not valid to compare them with the results of the following sections. Therefore, in Figure 5.13, we can see the first comparison of two side views of the CAD model (right) and the respective model modelled in ABAQUS (left), where we can see that the maximum stress estimate of the total structure is practically identical in both models, with the most stressed region being the Boom.

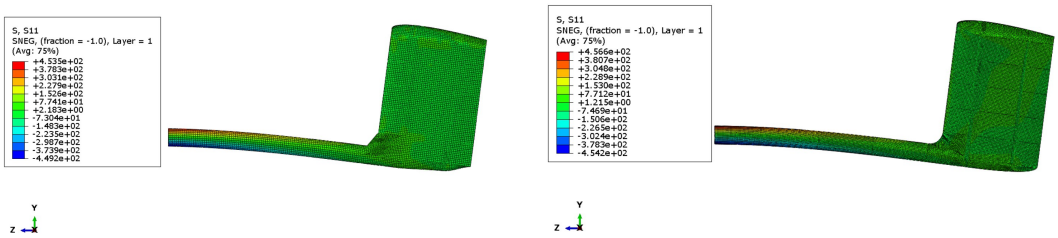

a) Stress analysis to FEM model b) Stress analysis to CAD model

Figure 5.13: Lateral view - Stress S11 [MPa] comparison for the Total model

In Figure 5.14, we can see a comparison of the deformation in the two models, where we can see that in general both structures show the same deformation throughout the structure, with the maximum value also being very similar.

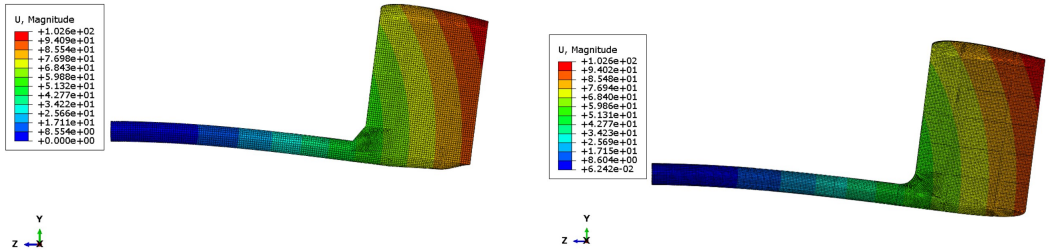

a) Deformation analysis to FEM model b) Deformation analysis to CAD model

Figure 5.14: Lateral view - Deformation comparison for the Main spar [mm]

On the other hand, when looking at internal structural components such as the main and secound spar, (Figure 5.15 and Figure 5.16 respectively), we can see that in both cases the areas of greatest stress are the same, highlighting in the case of the main spar, the accumulation of stress in the central area, which would be expected since it is the most heavily loaded area of the structure, in addition to the accumulation of stress in the folds of the main spar.

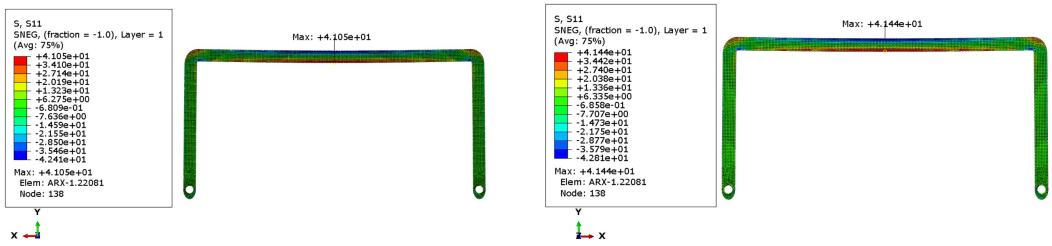

a) Stress analysis to FEM model b) Stress analysis to CAD model

Figure 5.15: Front view - Stress S11 [MPa] comparison for the Main spar

In terms of values, we can see a slight increase in the maximum stress. In the case of the main spar there is a difference between the models of approximately 0.4 MPa and in the case of the secound spar approximately 1.5 MPa, this difference being justified by small differences in modelling or simply small differences in the mesh of both structures.

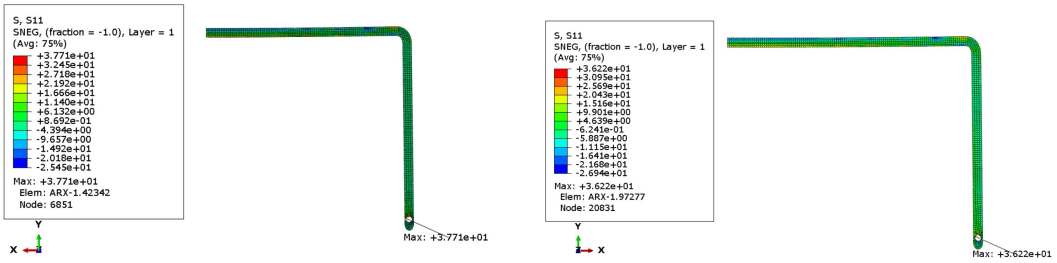

a) Stress analysis to FEM model b) Stress analysis to CAD model

Figure 5.16: Front view - Stress S11 [MPa] comparison for the Secound spar

With regard to the other elements of the structure, we can see a continuity with the previous one, with the differences between the models never exceeding 6 MPa, thus validating the correct behaviour of the structure modelled directly in the finite element software and allowing us to move on to the structural iteration 2 developed with greater confidence. Therefore, in the following sections we will begin the process of analysing the various structural options developed for iteration 2.

5.1.6 Mesh convergence

In order to guarantee a good computational cost/precision ratio, a convergence study was carried out for the mesh of the FEM model of the sturcture, in order to find the most suitable mesh refinement for the case under study. To do this, a Global mesh size range between 30 and 10 [mm] and 3 analysis measures were taken into account, these being the maximum stress, maximum value estimated by the Hashin criterion and displacement, evaluating in parallel how computational time and the number of elements accompany these parameters, for the Tail with Boom structure with reinforcement with stringers, for the load case of negative deflection of the elevator control surface for speed Vd. Thus, in Table 5.3, we can see the results of the study, for an element of the boom skin, located approximately halfway along the length of the structure, in order to avoid interference induced by the boundary conditions.So, we can conclude in terms of number of elements and computational time, that for sizes of less than 15 [mm], these values increase considerably compared to the variation in the analysis parameters, this being the value chosen for carrying out the structural analyses in chapter 5 and chapter 6.

Table 5.3: Mesh Convergence

Mesh Global Size	Number of elments	Job Time	Max Stress	Max displacment	Max Hashin value
30	89025	68	457.333	25.7575	0.145168
25	93639	69	453.231	25.0578	0.14254
18	111763	72	451.214	24.802	0.141264
15	126247	81	447.906	24.7222	0.1392
13	144107	127	449.236	24.8516	0.140033
10	193935	149	448.122	24.4755	0.13934

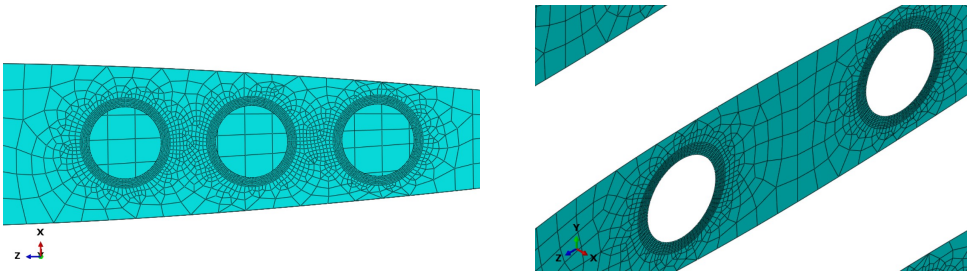

a) Vertical ribs b) Horizontal ribs

Figure 5.17: Mesh refinement for Ribs - Global size 15 [mm]

In Figure 5.17 we can see the mesh refinements carried out in the region of the holes in the rib structure, allowing the creation of a mesh structure in this region and better precision for the stress estimates made. In Figure 5.18, we can see the overall state of the mesh that we will be taking into account when carrying out the structural analyses.

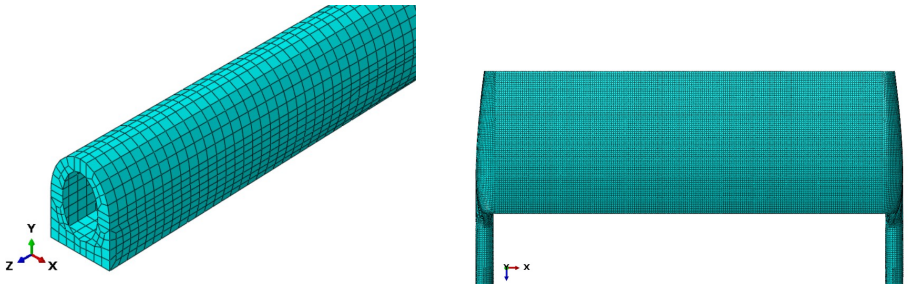

a) Boom b) Tail

Figure 5.18: Mesh refinement for Skin - Global size 15 [mm]

5.2 Tail-Boom Structural analysis

After the validation process has been completed and all the relevant information about the FEM model has been described in the previous subsections, in this section we will analyse the 3 constructive alternatives from iteration 2 designed for the boom and tail of the ARX aircraft. Therefore, in order to create a standardization of the following analyses, it was decided to create a series of critical point references for which we will directly compare throughout all the analyses carried out. These sections are as follows:

1. Maximum Total Stress

1.1 Maximum Total Stress ignoring elements in the vicinity of boundary conditions

2. Maximum Stress of Tail structure only (main spar, secound spar and Ribs)
3. Maximum Stress Vertical Ribs
4. Maximum stress of Main Spar
5. Maximum Stress of Secound Spar
6. Maximum Stress Horizontal Ribs
7. Maximum Stress of Main Spar Curve (Figure 5.19)
8. Maximum stress of the mounting region (Figure 5.19)

9. Maximum Stress of the Skin in the Vertical Stabiliser-Boom Transition Region (Figure 5.19)
10. Maximum stress of the main Spar hole (Figure 5.19)
11. Maximum deformation of the entire structure
12. Highest value estimated by Hashin's criterion for the entire structure
13. Location of the highest value estimated by the Hashin criterion

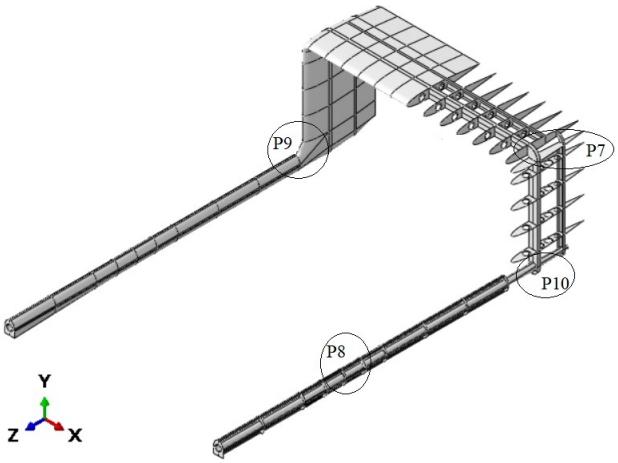

Figure 5.19: Reference points for analysis

It's also important to note that we're going to create a short code name for the load cases realised, with the load case for positive elevator deflection at speed Va being called "Va+", the same situation for negative elevator deflection "Va-" and consequently for the load case with deflection of the rudder control surface, "rudder Va", with the remaining three load cases for speed Vd following the same nomenclature.

5.2.1 Tail and Boom with internal pipe

Starting with the Boom case reinforced by an inner tube, we can see in Table 5.4 the compiled stress values for all the points mentioned above over the 6 critical load cases calculated.

Table 5.4: Stress analysis S11 of iteration 2 for Tail and boom with inner tube reinforcement

Points of analysis	Iteration 2 Boom with internal Pipe					
	Va-	Va+	Rudder Va	Vd -	Vd +	Rudder Vd
	[MPa]					
Maximum Stress [1]	-664.2	774.8	111.7	-846.1	584.6	-599.1
Maximum stress, ignoring boundary conditions [1.1]	-543.52	634.21	91.34	-692.5	478.81	-490.24
Maximum stress Tail [2]	35.82	66.23	40.43	50.5	50.84	99.75
Maximum stress Vertical Rib [3]	35.82	66.23	34.38	50.5	50.84	99.75
Maximum stress Main Spar [4]	28.41	38.89	-37.75	-36.23	27.39	63.24
Maximum stress Secound Spar [5]	24.29	23.46	-12.87	29.85	-16.52	-24.96
Maximum stress Horizontal Rib [6]	17.73	18.85	4.907	15.61	18.46	12.31
Maximum stress Main spar curve [7]	12.13	8.84	40.43	16.32	7.18	63.24
Maximum stress Boom assembly region [8]	-157.0	187.4	17.32	-201.3	141.2	-130.80
Maximum stress Skin vertical stabilizer-Boom [9]	111.6	162.4	-81.62	148.2	123.6	-234.8
Maximum stress Furo Main spar [3]	26.27	38.89	15.99	36.68	27.39	52.24
Maximum deformation Total [cm]	29.05	34.53	3.096	37.14	26.06	24.29
Higher Hashin Value	0.3063	0.2668	0.1476	0.4972	0.1519	0.2492
Location	[1] [8]	[1] [8]	[4] [7]	[1][8]	[1] [8]	[1]

Looking at the values obtained, we can quickly see that the most stressed area of the entire structure is the boom skin [points 1 and 1.1], which is especially high for the Va+,Vd- and Rudder Vd load cases, representing the most critical cases for the structure. In addition, we can see that the second most critical points of the structure would be both the boom assembly area [point 8] and the transition skin between the boom and the vertical stabilizer [point 9], which is as expected since the forces exerted along the Tail structure create a negative moment (load cases Va+ and Vd+) or a positive moment (load cases Va- and Vd-, Rudder Va and Rudder Vd), on the point of application of the boundary conditions (boom recessed into the main wing), concentrating greater stresses on the skin in the weakest region corresponding to the transition point between the vertical stabilizer and the boom and in the connection between the two sections of the boom's inner tube. With regard to deformation, we can see a maximum value for the load case Vd- of 37.14 [cm], which although high is within expectations. Finally, with regard to the highest values estimated by the Hashin criterion, we can see a value of 0.4972 for the same load case Vd-, for the boom skin and boom assembly regions.

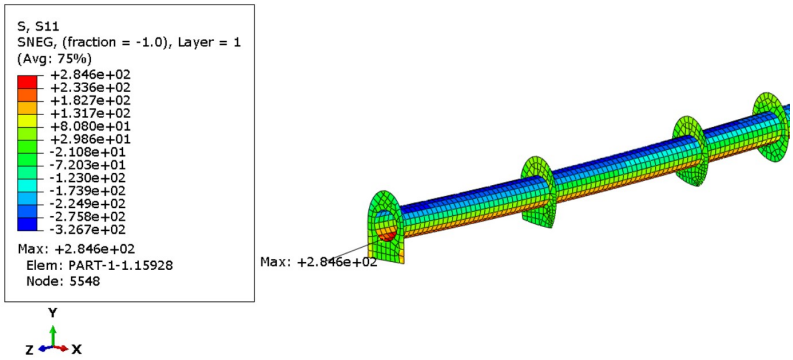

Figure 5.20: Lateral view Internal structure Boom with internal pipe Stres S11 - Load case Vd-

Finally, we can see in Figure 5.20, an isometric view of the internal part of the boom structure in its most stressed final section, near the main wing connection, for the Vd- load case, and we can see in the continuation that for this load case the boom presents the upper part in compression and the lower part in traction, with a greater concentration of Stresses near its boundary condition restriction zone, decreasing until it is practically 0 near its connection to the Tail in the main spar and secondary spar.

5.2.2 Tail and Boom with Stringers

Moving on to the case of Boom reinforced stringers, we can see in Table 5.5, the compiled stress values for all the analysis points over the 6 critical load cases calculated, with the color map referring to the comparison with the previous case.

Looking at the results obtained, we can see that the analysis follows the same pattern as the previous case, with the Vd-, Va+ and Rudder Vd load cases being the most critical for the structure. We can also see that the boom skin [points 1 and 1.1] remains the most stressed point in the entire structure, with the assembly zone of the boom sections [point 8] and the region where the skin of the vertical stabilizer transitions to the boom [point 9] being the second most critical zones. Comparing the values obtained in the different load cases to those obtained in the previous situation, we can see that in general it is possible to observe an average reduction of 32 MPa in the estimated maximum stress value in the entire structure corresponding to the boom skin, while increasing by an average of 13 MPa for the connecting skin in the transition zone from the vertical stabilizer to the boom and approximately 15 MPa in the case of the assembly region.

5.2. Tail-Boom Structural analysis

Table 5.5: Stress analysis S11 of iteration 2 for Tail and boom with Stringers reinforcement

Points of analysis	Iteration2 Boom with Stringers					
	Va-	Va+	Rudder Va	Vd+	Vd-	Rudder Vd
	MPa					
Maximum Stress [1]	-640.5	734.3	171.5	552.7	-814.4	-575.6
Maximum stress, ignoring boundary conditions [1.1]	-420.42	504.23	135.2	381.5	-565.38	-415.2
Maximum stress Tail [2]	42.3	74.67	57.88	57.59	59.26	100.9
Maximum stress Vertical Rib [3]	42.3	74.67	57.88	57.59	59.26	100.9
Maximum stress Main Spar [4]	28.72	-28.12	52.47	-19.48	36.15	64.33
Maximum stress Secound Spar [5]	24.65	-23.58	13.63	-16.7	30.20	21.17
Maximum stress Horizontal Rib [6]	17.1	18.01	7.181	18.81	14.48	11.07
Maximum stress Main spar curve [7]	9.25	7.74	52.51	6.32	14.92	63.41
Maximum stress Boom assembly region [8]	172.9	200.8	31.57	151.0	-220.5	150.6
Maximum stress Skin Vertical stabilizer-Boom [9]	123.8	-195.2	-149.4	-150.3	167.1	-250.2
Maximum stress Main spar hole [10]	9.576	13.96	13.14	10.57	12.8	14.83
Maximum deformation Total [cm]	23.57	27.59	4.338	20.77	30.09	19.83
Higher Hashin Value	0.2949	0.2559	0.1646	0.145	0.4609	0.2299
Location	[1]	[1]	[9][1]	[1]	[1]	[1]

This is in line with expectations, since the stringers allow for a more direct reinforcement of the skin, reducing the stress in the most critical area of the boom. However, it allows for a weakening of the connection area and the transition area between the vertical stabilizer and the boom, since this case, unlike the previous one, ends the reinforcement in the first former and not in the second spar.

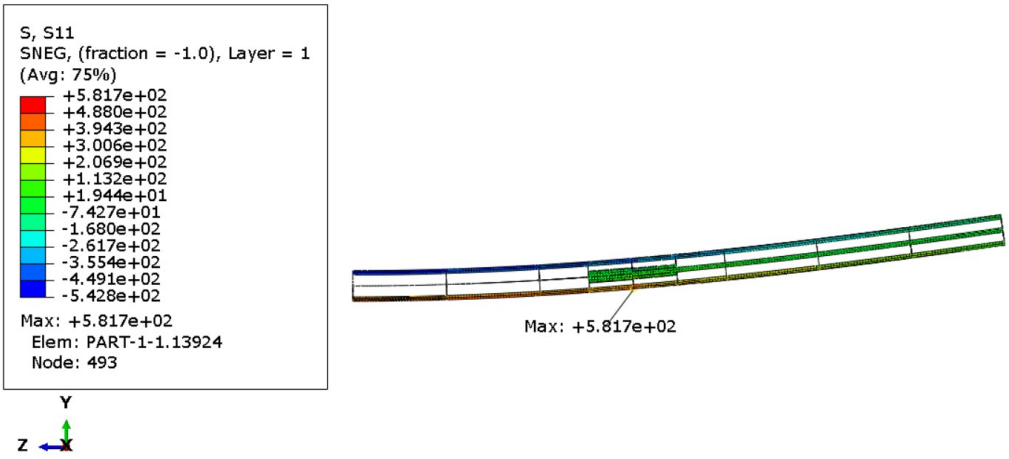

Figure 5.21: Lateral view Internal structure Boom with Stringers, Stress S11 - Load case Vd-

Therefore, we can see in Figure 5.21, a side view of the behavior of the stringers for the Vd-load case, showing, as in the previous case, the upper region in compression and the lower region in tension, presenting a greater stress concentration near the boundary conditions and the connection region between booms, gradually decreasing thereafter until the Tail, this value being higher than that observed for the boom, showing that this reinforcement is more effective in terms of reinforcing the skin. In addition, it is important to note that there is a marked reduction in stress in the area where the hole in the main spar and the secondary spar for connection to the boom are located in the previous case, thus making it possible to reduce 4 potential problem points in the context of real aircraft operation, both in terms of possible delamination of the material in this contact area creating potential structural failures, and in terms of the possible creation of stress concentrations causing potential fatigue problems. Finally, we can see that the total deformation of the structure has generally decreased by 7 [cm], compared to the previous case. This can be explained by the

greater capacity of the stringers to bend and prevent deflection of the skin of the structure, and we can also see a reduction in the maximum value estimated by the hashin criterion, accompanying the reduction in the maximum stress in the skin of the boom.

5.2.3 Tail and Boom with internal pipe and Stringers

Finally, we can see in Table 5.6, the compiled stress values for all the analysis points over the 6 critical load cases calculated, with the color map referring to the comparison with the previous case.

Table 5.6: Stress analysis S11 iteration 2 for Tail and boom with inner tube and stringers reinforcement

Points of analysis	Iteration2 Boom with Stringers					
	Va-	Va+	Rudder Va	Vd+	Vd-	Rudder Vd
	MPa					
Maximum Stress [1]	-594.5	693.2	158.5	523.0	-757.4	-531.1
Maximum stress, ignoring boundary conditions [1.1]	-403.02	468.23	119.32	354.21	-513.96	-380.24
Maximum stress Tail [2]	37.43	67.81	62.4	52.1	52.43	102
Maximum stress Vertical Rib [3]	37.43	67.81	62.4	52.1	52.43	102
Maximum stress Main Spar [4]	29.74	32.31	61.92	23.32	37.45	78.33
Maximum stress Secound Spar [5]	24.66	23.82	-13.65	-17.00	30.02	20.99
Maximum stress Horizontal Rib [6]	21.45	23.59	8.162	23.86	18.11	12.53
Maximum stress Main spar curve [7]	12.52	10.62	61.92	7.82	16.25	78.33
Maximum stress Boom assembly region [8]	-114.0	135.8	22.40	102.3	-146.1	-95.71
Maximum stress Skin Vertical stabilizer-Boom [9]	-102.9	173.8	-130.9	133.6	-140.1	-225.2
Maximum stress Main spar hole [10]	21.64	32.31	26	23.32	29.99	46.93
Maximum deformation Total [cm]	22.08	26.22	3.974	19.79	28.22	18.57
Higher Hashin Value	0.2455	0.2136	0.0579	0.1152	0.3983	0.1959
Location	[1]	[1]	[4] [7]	[1]	[1]	[1]

At first glance, we can see continuity in terms of the points of greatest stress and critical load cases. However, since this version of the structure combines the two previously used stiffeners, we can see a general reduction in stress at all points, taking advantage of the greater reinforcement of the skin by the stringers to reduce the maximum stress of the boom skin and its total deformation, while also including the advantages of the internal tube reinforcement, reducing the stress in the connection region of the boom sections and the transition of the skin from the vertical stabilizer to the boom. Consequently, the estimated maximum hashin value is also reduced in line with the rest of the structure's trend.

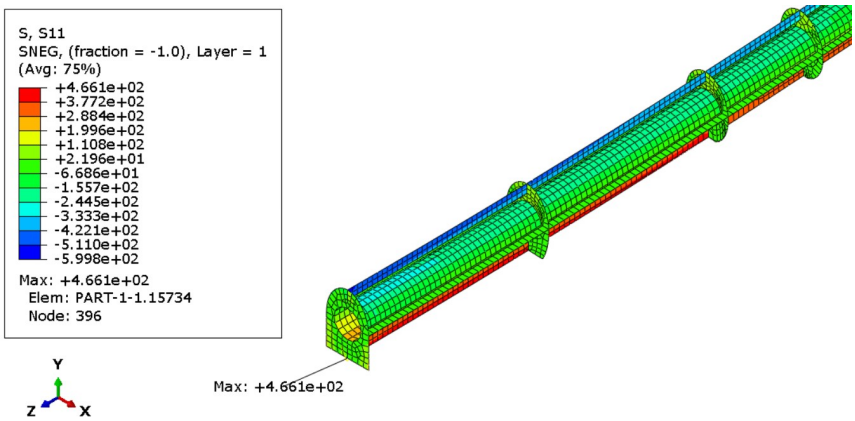

Figure 5.22: Isometric view Internal structure Boom with internal pipe and Stringers, Stress S11 - Load case Vd-

Finally, in Figure 5.22, we can see an isometric view of the internal structure of the two stiffeners in the most stressed section near the connection with the main wing, showing a continuation of what has already been observed, with the stringers being responsible for absorbing much more stress than the inner tube, although this is smaller compared to the previous cases, since the forces are divided by both stiffeners.

5.2.4 Comparison of the 3 structural solutions

Having already presented the results obtained for the three different structural cases, it was necessary to define which version was the most targeted at the company's and ARX's objectives, so the following priority factors were defined:

1. Total Weight of the structure
2. Maximum Stress of the structure
3. Number of critical points
4. Maximum Deformation of the structure

It is important to bear in mind that in a UAV aircraft the weight factor is of great importance and has a direct impact on the flight range and performance of the aircraft. Bearing this in mind, having already presented the data for points 2, 3 and 4, it was necessary to estimate the total weight of the ARX Tail+Boom structure for the three construction solutions, these values being shown in Table 5.7.

Table 5.7: Weight comparison of structures

Arx version	Weight [kg]
Tail+Boom with internal pipe reinforcement	45.2
Tail+Boom with Stringers reinforcement	44.2
Tail+Boom with internal pipe and Stringers reinforcement	48.4

We can see that the version of the boom reinforced only by stringers is approximately 1 kg lighter than the case of the Boom reinforced by inner tube and approximately 4.2 kg lighter than the version with both reinforcements, the latter being the heaviest structure.

Regarding the points of greatest stress and deformation of the different versions of the structure, we can say that the Boom case with total reinforcement has advantages over both individual cases, being the most robust situation. However, its considerably higher weight compared to the previous alternatives has made this alternative disposable, although it is useful in terms of knowledge for the company, and we can conclude that a union of both structures could be a structural solution to consider for a future aircraft with other more severe requirements.

Therefore, comparing the two simplest cases, we can recall that the case of the boom reinforced only by strigners shows an average reduction of 32 MPa in the estimated maximum stress value in the entire structure corresponding to the boom skin, while increasing by an average of 13 MPa for the connecting skin in the transition zone from the vertical stabilizer to the boom and approximately 15 MPa in the case of the assembly region, although the estimated maximum hashin value is lower and the maximum deformation of the structure is approximately 7 [mm] lower.

With each of these structures having advantages and disadvantages, and the difference in weight between the structures being smaller, the tie-breaker was the number of critical points in the structure. It can be seen that in the case of the Boom structure with internal tube reinforcement, it has a higher overall critical point, limiting the reduction in the number of layers of material in

this region, presenting two additional points of possible crack creation and fatigue, corresponding to the main and secound spar holes, which the other solution does not contain.

Thus, the Tail+Boom structure with stringers reinforcement proved to be more balanced and closer to the desired objectives, being 1 [kg] lighter, presenting a lower critical point of the overall structure and a lower number of critical points, as well as a lower overall deformation, assuming a slightly higher concentration of stress in the connection zone and transition from the boom skin to the vertical stabilizer, the former being easily solved by creating a reinforcement zone.

To conclude this section, the points of greatest stress concentration for the chosen boom structure with stringer reinforcement, used to develop the analyses in Chapter 6, are shown below.

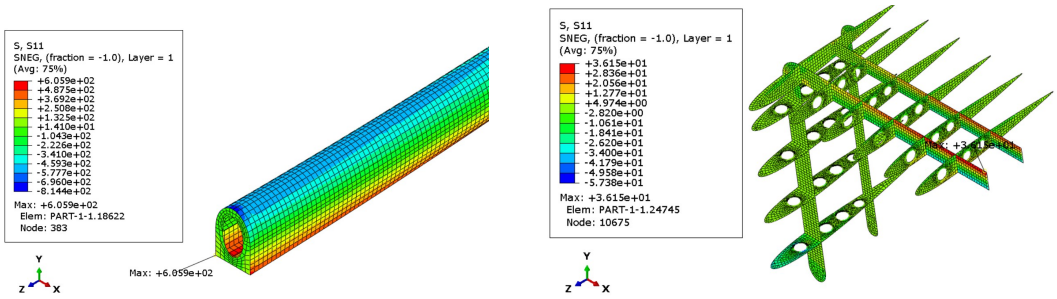

a) Skin Boom [point 1] b) Tail structure [point 2]

Figure 5.23: Stress analysis S11 point (1 and 2) - Load case Vd-

In Figure 5.23, we can see the concentration of stresses along the boom skin in the final section near the main wing and the stresses along the tail structure, highlighting the greater concentration in the central region of the main and secondary spars, with the upper region in tension and the lower region in compression. A concentration of stress in compression can also be seen in the hole in the lower region of the Vertical Rib, which is to be expected since a greater concentration of stress was identified in the transition region from the vertical stabilizer to the boom due to the bending created by the moment generated by the aerodynamic forces. In Figure 5.24, we can see the concentration of stresses in the region where the two sections of the tube meet, which is to be expected, and in Figure 5.24b the concentration of stresses in the skin of the transition region from the vertical stabilizer to the boom, as mentioned above.

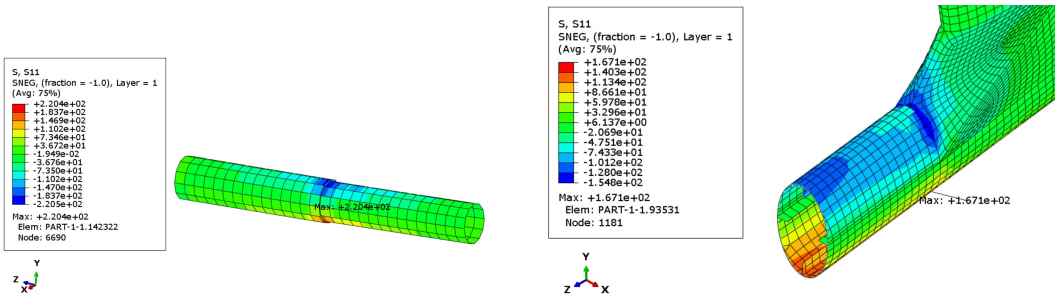

a) Boom conection [point 8] b) Skin transiton [point 9]

Figure 5.24: Stress analysis S11 point (8 and 9) - Load case Vd-

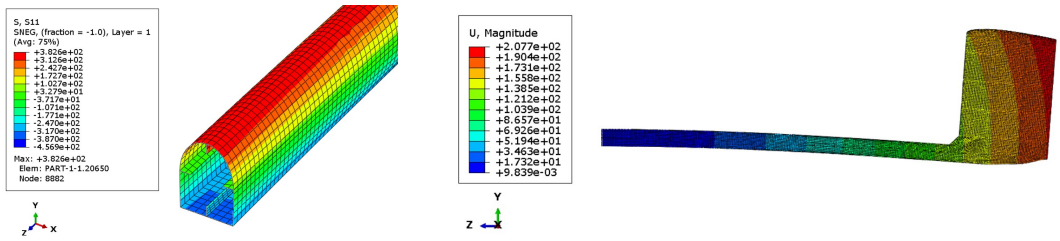

a) Stress S11 point 1 b) Lateral view total structure deformation

Figure 5.25: Analysis point 1 at load case Va+

Finally, in Figure 5.25 and Figure 5.26, we can see the stress analysis of the final section near the main wing of the boom skin corresponding to the most critical case of analysis, for load case Va+ and Rudder Vd respectively. Thus, in Figure 5.25a, we can see a case of analysis exactly the same as that observed in load case Vd- with the upper skin in tension and the lower skin in compression, since the structure flexes in the opposite direction, as we can see in Figure 5.25b. In Figure 5.26a we can observe the same analysis case but for the Rudder Vd case, in which we can see that we maintain a deflection identical to that of the Rudder Vd load case, but asymmetrical since the left and right Rudder create different loads on the structure, as suggested in Figure 5.26b, we can see that the upper skin is in compression and the lower skin is in traction, but their maximum points fall to more lateral areas, in opposite directions between the upper and lower parts.

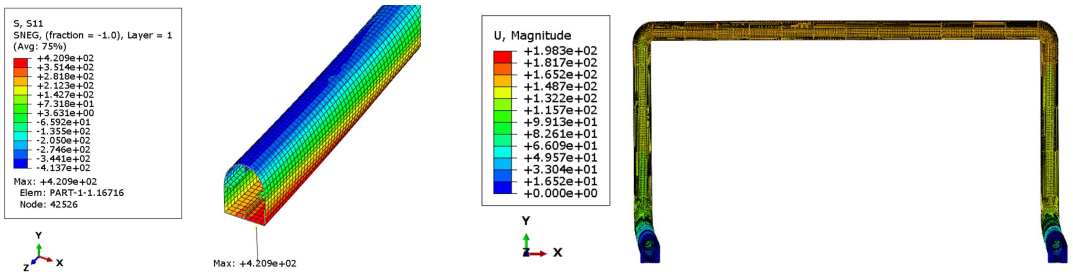

a) Stress S11 point 1 b) Front view total structure deformation

Figure 5.26: Analysis point 1 at load case Va+

Chapter 6

Structural Optimization

After choosing the Tail and Boom version with reinforcing stringers, we will carry out a series of tests throughout this chapter to iteratively arrive at a more structurally optimized version, testing different positions for the main spar, guiding the structure towards the possibility of using only 1 spar, as well as analyzing the differences between using a C profile and different I profiles for the spar flanges and finally reducing the number of Ribs for the vertical and horizontal stabilizers.

In addition, it is important to note that in Chapter 6, it was possible to verify the greater demand of the Va+, Vd- and Rudder Vd load cases on the structure, which made it possible to reduce the number of load cases analyzed from 6 to 3.

6.1 Main spar position

Starting with the test of varying the position of the main spar between the option presented in the previous study located at 30% of the chord and the respective alternatives at 35% and 25% of the chord, the aim was to understand the influence of the movement of this component on the structure, identifying its advantages and disadvantages and which would be the most suitable for the application of just one main spar. Therefore, before we begin the detailed analysis of the values obtained, it is important to bear in mind that changing the position of the main spar required small changes in the size and positioning of the holes in the vertical stabilizer ribs in the case of the main spar at 25% from the chord and also in the horizontal stabilizer ribs in the case of the main spar at 35% from the chord, since the spacing between spars varies, making the hole configuration initially proposed for the ribs unsuitable.

Starting with the case of the main spar at 35% of the chord in which the spacing between spars was 37.5 [mm], it was decided in the case of the horizontal stabilizer (Figure 6.1) to reduce it from 2 holes of 20 [mm] diameter to just 1 centered hole of 25 [mm] diameter, keeping the hole in the front section intact.

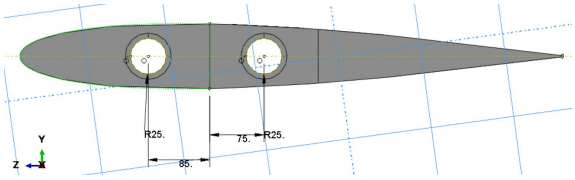

Figure 6.1: Horizontal Ribs Holes Sketchs for main spar at 35% of chord

6.1. Main spar position

As for the vertical stabilizer, despite the reduction in the 37.5 [mm] spacing between spars, there was no need to reduce the number of holes, only reducing the diameter of the 2 holes in the left wing-box region from 25 [mm] to 20 [mm], Figure 6.2.

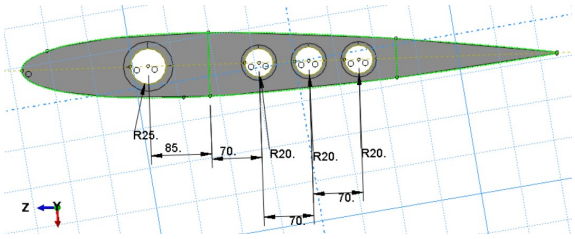

Figure 6.2: Vertical Ribs Holes Sketchs for main spar at 35% of chord

With regard to the configuration of the main spar at 25% of the chord, there is an increase of 37.5 [mm] in the spacing between spars, compared to the reference version. We therefore decided to keep the configuration of the vertical stabilizer's ribs, which remained optimal, but we felt the need to increase the diameter of the two holes in the horizontal stabilizer's wing-box from 20 [mm] to 25 [mm], since although they are larger, they allow for a more distant position, maintaining a similar situation of tension concentration of the ribs. Similarly, the hole in the front section of the Rib was not changed, Figure 6.3.

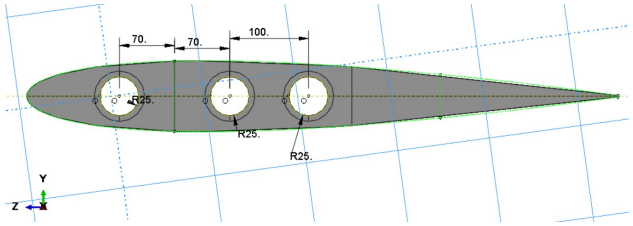

Figure 6.3: Horizontal Ribs Holes Sketchs for main spar at 25% of chord

Bearing this in mind, it is important to note that these changes have led to a slight difference in weight between the 3 options, with the main spar option at 25% of the chord being approximately 300 [g] lighter than the reference case, since it has a larger hole section in the horizontal Ribs and a slightly smaller main spar since the widest section occurs at 30% of the chord. As for the case of the main spar at 35% chord, the decrease in the section of the Rib holes ends up balancing out the decrease in the main spar due to the same phenomenon as before, being only approximately 50 [g] heavier than the reference option.

Table 6.1: Stress analysis S11 - Comparing different main spar positions along the chord

Points of analysis	Main spar at 25% Chord			Main spar at 30% Chord			Main spar at 35% Chord		
	Va+	Vd-	Rudder Vd	Va+	Vd-	Rudder Vd	Va+	Vd-	Rudder Vd
	MPa			MPa			MPa		
Maximum Stress [1]	748.7	-818.2	-579.6	734.3	-814.4	-575.6	716.9	-780.5	-540.2
Maximum stress, ignoring boundary conditions [1.1]	535.21	-588.74	-414.85	506.2	-565.2	-415.2	518.53	-561.23	-394.12
Maximum stress Tail [2]	97.93	75.26	129.8	74.71	59.07	100.09	38.4	35.63	67.55
Maximum stress Vertical Rib [3]	97.93	75.26	129.8	74.71	59.07	100.09	38.4	30.33	33.6
Maximum stress Main Spar [4]	-27.63	35.4	63.87	-28.12	36.15	64.33	-27.94	35.70	70.68
Maximum stress Secound Spar [5]	21.37	26.99	-27.35	-23.58	30.20	21.17	-21.35	27.23	27.58
Maximum stress Horizontal Rib [6]	21.7	18.44	10.3	18.01	14.48	11.02	23.81	17.06	13.42
Maximum stress Main spar curve [7]	9.23	15.4	67.8	7.521	15.12	63.08	9.96	18.8	67.55
Maximum stress Boom assembly region [8]	-195.5	120.0	74.54	200.8	-220.5	150.6	205.2	-221.6	147.4
Maximum stress Skin Vertical stabilizer-Boom [9]	174.9	-144.6	-222.3	-195.2	167.1	-240.2	205.5	-172.4	-319.7
Maximum stress Main spar hole [10]	7.77	6.864	13.78	13.96	12.77	14.86	6.675	52.81	16.74
Maximum deformation Total [cm]	29.62	31.94	21.04	27.59	30.07	19.83	28.69	30.79	20.28
Higher Hashin Value	0.231	0.4688	0.233	0.2559	0.4606	0.2301	0.284	0.423	0.2027
Location	[1]	[1]	[1]	[1]	[1]	[1]	[1]	[1]	[1]

It's important to note that in Table 6.1 a color scheme is presented to aid comparison, with the reference case being the lightest case (main spar at 25% of the chord), the dark pattern referring to an improvement or worsening of greater magnitude and the light pattern of lesser magnitude.

Starting with a general approach, it is important to bear in mind that the main spar at 30% of the chord is approximately in the area with the largest section of the wing profile in both the vertical and horizontal stabilizers, allowing for lower values of total deformation of the structure and slightly higher values in terms of maximum stress in the main and secound spar, due to their greater stress absorption capacity, as shown in Table 6.1. On the other hand, the main spar at 25% is closer to the leading edge, which benefits the reinforcement of the structure in the transition zone between vertical stabilizer and boom and in the assembly region, as can be seen in Table 6.1. Finally, the main spar position at 35%, although it moves away from the leading edge of the structure, is closer to the secound spar, creating a shorter and also more robust wing box.

In addition, Figure 6.4, Figure 6.5 and Figure 6.6, a comparison of the analysis carried out for the Rudder Vd case, since it proved to be the most critical case for the main spar, where we can see that in the region of the horizontal stabilizer, the web is the most stressed region and in all cases the transition fold between the horizontal and vertical surface is the second most stressed point, with the flange of the vertical stabilizer spar being the most critical point for all cases.

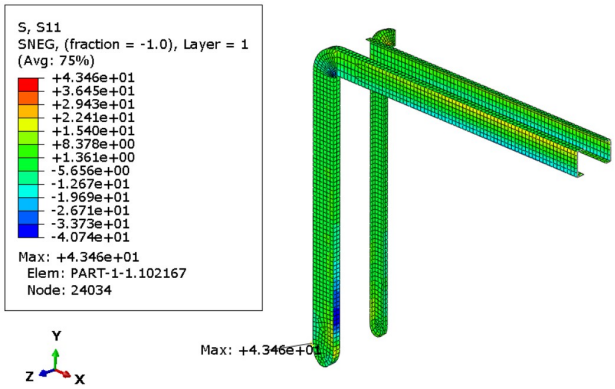

Figure 6.4: Stress analysis S11 - Main Spar 35% chord and secound spar C - load case Rudder Vd

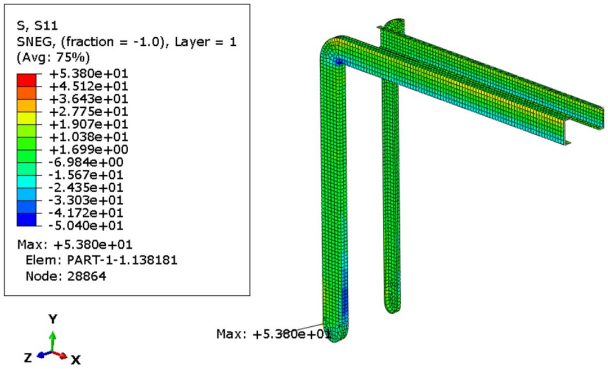

Figure 6.5: Stress analysis S11 - Main Spar 30% chord and secound spar C - load case Rudder Vd

We can also see how increasing the distance from the leading edge reduces the stress accumulated in the lower region of the main spar of the vertical stabilizer, as we gradually move away from the transition region between boom and vertical stabilizer, identified as one of the critical points of the structure. We can also see that increasing the distance between the position of the main spar and the leading edge has the advantage of reducing the maximum stress in both the most critical area of the structure (skin boom) and the most critical area of the Tail.

However, it can be seen that reducing the distance between the position of the main spar and the leading edge reduced the stress concentration in the region of the assembly and the transition skin from the vertical stabilizer to the boom.

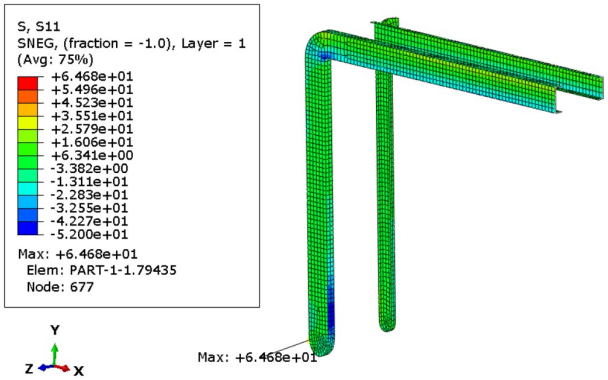

Figure 6.6: Stress analysis S11 - Main Spar 25% chord and secound spar C - load case Rudder Vd

Taking all this into account, balancing the advantages and disadvantages of each option analyzed, since it was a requirement of the company to test a possible structure with only one spar, it was decided to direct the following analyses with this objective, discarding the main spar configuration at 25% of the chord, since for a 2 spar configuration this could offer some advantages such as less weight and stress relief in the mounting region and boom vertical stabilizer transition skin, for a configuration with just one spar, this would not be the best option, as we want a position further away from the leading edge of the structure, looking for regions with a larger section, like the other two options, although the information will remain with the company for a potential future structure.

With this in mind, in the following analyses we will only consider the main spar version at 30% of the chord and 35% of the chord, trying to maximize its advantages and reducing the stress in the transition skin region between boom and vertical stabilizer by changing the C profile to the I profile, which has a greater static inertia.

6.2 Spars I vs C Configuration

Looking at previous aircraft manufactured by the company, we can see that it is typical to use Spar with a C profile flange, presenting itself as a simpler process in the context of manufacturing, thus giving rise to a new realtive analysis comparing the use of C and I profile in the flange of the spars, intending to identify the advantages and disadvantages of this possible change.

Analyzing the potential ways of manufacturing profile I, it can be seen that its manufacture in composite materials in a single element would be subject to serious problems at the time of rolling, since in the central region of the fringes there would be a division in the direction of the plys, potentiating a possible failure zone. It was therefore concluded that the most practical way for the company to carry out this process would be to glue two C profiles together, as shown in Figure 6.7a, or to manufacture the web and flanges separately and assemble them later, as shown in Figure 6.7b.

Comparing the two options, we can quickly see that the first option would have a much larger contact section than the second option, which, as it is a main structural element (main and secound spar), forces the choice of the first solution (Figure 6.7a).

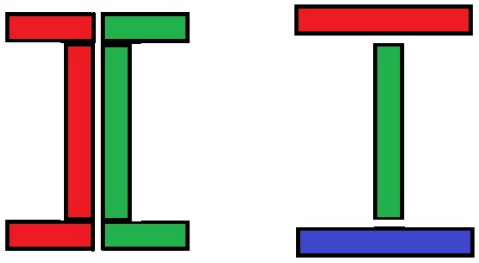

Figure 6.7: Illustrative example of manufacturing an I-profile using semi-separated elements

Bearing this in mind, it is important to remember that manufacturing using the chosen method can typically result in the web being twice as thick as the flange. Therefore, and remembering that the most important requirement of this work is weight, for the following comparisons we will take into account a profile manufactured from 2 C profiles of half the thickness compared to those used in the analysis of C profile spars, with the I profile having the same thickness in the web and half the thickness in the flange compared to the reference case, but with the total length and width of the web and flange of the I profile being the same as that of the C profile.Finally, importante to note that the I profile main spar will be approximately 480 g lighter.

Table 6.2: Stress analysis S11 - Comparative between Main spar at 30% chord with 2 spars I and 2 spars C

Points of analysis	Main spar at 30% chord-2 spars C			Main spar at 30% chord-2 spars I		
	Va+	Vd-	Rudder Vd	Va+	Vd-	Rudder Vd
	MPa			MPa		
Maximum Stress [1]	734.3	-814.4	-575.6	733.8	-814.4	-575.0
Maximum stress, ignoring boundary conditions [1.1]	506.2	-565.2	-415.2	505.7	-565.2	-410.91
Maximum stress Tail [2]	74.71	59.07	100.09	75.77	59.45	100.4
Maximum stress Vertical Rib [3]	74.71	59.07	100.09	75.77	59.45	100.4
Maximum stress Main Spar [4]	-28.12	36.15	64.33	-29.13	37.59	68.01
Maximum stress Secound Spar [5]	-23.58	30.20	21.17	-24.62	31.48	-23.63
Maximum stress Horizontal Rib [6]	18.01	14.48	11.02	18.38	14.78	11.11
Maximum stress Main spar curve [7]	7.521	15.12	63.08	7.521	15.12	67.58
Maximum stress Boom assembly region [8]	200.8	-220.5	150.6	200.8	220.5	150.5
Maximum stress Skin Vertical stabilizer-Boom [9]	-195.2	167.1	-240.2	-195.4	167.3	-256.2
Maximum stress Main spar hole [10]	13.96	12.77	14.86	12.59	11.62	18.98
Maximum deformation Total [cm]	27.59	30.07	19.83	27.59	30.08	19.83
Higher Hashin Value	0.2559	0.4606	0.2301	0.2559	0.4606	0.2301
Location	[1]	[1]	[1]	[1]	[1]	[1]

Analysing the values obtained in Table 6.2 and Table 6.3, we can quickly conclude that in both cases the change from profile C to profile I has a more significant impact on the load case in which a rotation of the Rudder control surface is indicated, while in general the changes in the rest of the structure for the various analysis points never exceed 3 MPa.

Looking in more detail at the rudder load case, we can also see that in the case of the main spar at 30% of the chord, this change does not benefit the structure, while in the case of the main spar at 35% of the chord, the change to an I profile proves to be advantageous not only for the overall structure in the Rudder Vd load case, but also for Vd- and Va+ in the transition skin between vertical stabilizer and boom. In terms of deformation, we were also able to observe that the values did not change in any way, indicating in this study that for a situation where 2 spars are used, the change from a C profile to an I profile with the same web thickness and half the flange thickness could prove to be advantageous when choosing a main spar 35% from the chord, in addition to its weight reduction of approximately 480g.

6.2. Spars I vs C Configuration

Table 6.3: Stress analysis S11 - Comparative between Main spar at 35% chord with 2 spars I and 2 spars C

Points of analysis	Main spar at 35% chord-2 spars C			Main spar at 35% chord-2 spars I		
	Va+	Vd-	Rudder Vd	Va+	Vd-	Rudder Vd
	MPa			MPa		
Maximum Stress [1]	716.9	-780.5	-540.2	717.0	-780.5	-540.0
Maximum stress, ignoring boundary conditions [1.1]	518.53	-561.23	-394.12	518.53	-561.23	-394.11
Maximum stress Tail [2]	38.4	35.70	70.68	39.12	36.92	63.36
Maximum stress Vertical Rib [3]	38.4	30.33	33.6	39.12	30.59	34.81
Maximum stress Main Spar [4]	-27.94	35.70	70.68	-28.89	35.21	63.36
Maximum stress Secound Spar [5]	-21.35	27.23	27.58	-22.26	26.79	28.30
Maximum stress Horizontal Rib [6]	23.81	17.06	13.42	24.34	17.66	10.66
Maximum stress Main spar curve [7]	9.96	18.8	70.68	9.96	18.8	61.42
Maximum stress Boom assembly region [8]	205.2	-221.6	147.4	205.3	-221.6	147.4
Maximum stress Skin Vertical stabilizer-Boom [9]	205.5	-172.4	-319.7	179.9	-156.8	-277.2
Maximum stress Main spar hole [10]	6.675	5.281	16.74	9.429	7.521	23.46
Maximum deformation Total [cm]	28.69	30.79	20.28	28.68	30.79	20.28
Higher Hashin Value	0.284	0.423	0.2027	0.284	0.423	0.2027
Location	[1]	[1]	[1]	[1]	[1]	[1]

To conclude this analysis, we can see in Figure 6.8 and Figure 6.9, as in the previous analysis, the main and scound pair for the two analysis cases, for the respective Rudder Vd load case. As expected, by comparing Figure 6.8 and Figure 6.9 with the results obtained in the previous section, we can conclude that changing the profile from I to C leads to a greater increase in the maximum stress of the main spar flange at 30% of the vertical stabilizer. We can also see that changing the profile does not change the regions of greatest stress in the structure.

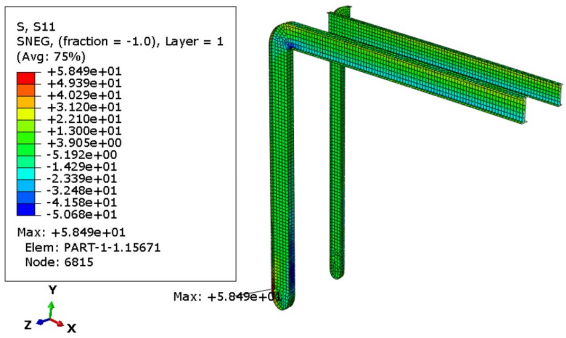

Figure 6.8: Stress analysis S11- Main Spar 30% chord and secound spar I - load case Rudder Vd

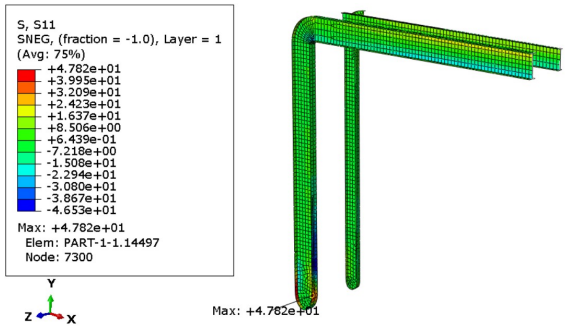

Figure 6.9: Stress analysis S11 - Main Spar 35% chord and secound spar I - load case Rudder Vd

6.3 2 Spar vs 1 Spars

As has already been mentioned throughout this chapter, one of the objectives proposed by the company, in addition to creating the lightest possible structure, was to study the possibility of using only one main spar. This study aimed to analyze the impact of reducing the secound spar for the different cases under analysis. In Figure 6.10, we can see the difference in structural terms of this change, and it is important to note that there is still a region of reinforcement where the secound spar used to be, since in a real context it will always be necessary to reinforce the limits of the control surfaces, which is why it is present in 100% of the span of the horizontal stabilizer and only in 80% of the span of the vertical stabilizer.

In addition, it is important to note that this new reinforcement region has only half the total thickness, being composed of a layep [0.+-45.90], translating these changes into a reduction of approximately 1.2 kg in the total weight of the structure for the C profile and 900 g in the total weight of the structure for the I profile, since the removed flange was half the thickness of the C version, with less weight lost by the change.

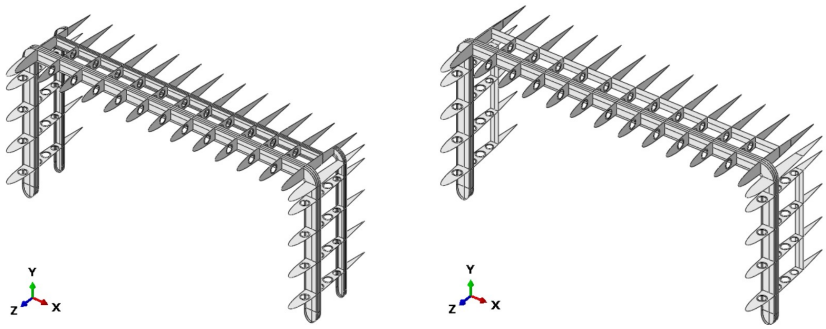

a) 2 spar FEM model b) 1 spar FEM model

Figure 6.10: Isometric view - Comapration structure for 2 spars and 1 spar

6.3.1 Spar C profile

Starting the study with the C profile, we can see in Table 6.4 and Table 6.5 the influence of the aforementioned change.

Table 6.4: Stress analysis S11- Comparison of the reduction from 2 C spars to just 1 C - main spar at 30 % of the chord

Points of analysis	Main spar at 30% chord-2 spars C			Main spar at 30% chord-1 spars C		
	Va+	Vd-	Rudder Vd	Va+	Vd-	Rudder Vd
	MPa			MPa		
Maximum Stress [1]	734.4	-814.4	-576.6	734.3	-814.4	-574.6
Maximum stress, ignoring boundary conditions [1.1]	506.2	-565.2	-411.23	506.2	-565.2	-411.23
Maximum stress Tail [2]	74.71	59.07	100.09	74.91	59.2	101.8
Maximum stress Vertical Rib [3]	74.71	59.07	100.09	74.91	59.2	101.8
Maximum stress Main Spar [4]	-28.12	36.15	64.33	-29.33	37.69	63.26
Maximum stress Secound Spar [5]	-23.58	30.20	21.78	-24.55	31.31	21.70
Maximum stress Horizontal Rib [6]	18.01	14.48	11.02	19.58	16.12	13.29
Maximum stress Main spar curve [7]	7.521	15.12	63.08	12.23	15.12	66.1
Maximum stress Boom assembly region [8]	200.8	-220.5	150.6	200.8	-220.5	150.5
Maximum stress Skin Vertical stabilizer-Boom [9]	-195.2	167.1	-240.2	-195.5	167.2	-248.9
Maximum stress Main spar hole [10]	13.96	12.77	14.86	14.02	12.81	15.59
Maximum deformation Total [cm]	27.59	30.07	19.83	27.61	30.07	19.86
Higher Hashin Value	0.2559	0.4606	0.2301	0.2559	0.4606	0.2301
Location	[1]	[1]	[1]	[1]	[1]	[1]

6.3. 2 Spar vs 1 Spars

Analyzing the results obtained, we can see that in general the alteration of spar 2 by the reinforcement zone has a negative impact in terms of the maximum stress of the various components of the structure, but never more than 5 MPa, with no significant changes being observed in the critical regions of the boom skin, the assembly zone and the transition skin between the vertical stabilizer and the boom, while the change in deformation and the maximum value estimated by the hashin criterion are considered insignificant.

Table 6.5: Stress analysis S11 - Comparison of the reduction from 2 C spars to just 1 C - main spar at 35 % of the chord

Points of analysis	Main spar at 35% chord-2 spars C			Main spar at 35% chord-1 spars C		
	Va+	Vd-	Rudder Vd	Va+	Vd-	Rudder Vd
	MPa			MPa		
Maximum Stress [1]	716.9	-780.5	-540.2	716.9	-780.5	-539.4
Maximum stress, ignoring boundary conditions [1.1]	518.53	-561.23	-394.12	518.53	-561.23	-394.12
Maximum stress Tail [2]	38.4	35.63	67.55	38.57	37.15	65.25
Maximum stress Vertical Rib [3]	38.4	30.33	33.6	38.57	35.24	33.1
Maximum stress Main Spar [4]	-27.94	35.70	70.68	-29.14	37.23	68.77
Maximum stress Secound Spar [5]	-21.35	27.23	27.58	22.38	28.15	17.59
Maximum stress Horizontal Rib [6]	23.81	17.06	13.12	25.9	19.26	14.17
Maximum stress Main spar curve [7]	9.96	18.8	67.55	12.2	20.1	65.25
Maximum stress Boom assembly region [8]	205.2	-221.6	147.4	205.6	-221.6	147.3
Maximum stress Skin Vertical stabilizer-Boom [9]	205.5	-172.4	-319.7	205.4	-172.4	-319.0
Maximum stress Main spar hole [10]	6.675	5.281	16.74	6.675	5.281	16.6
Maximum deformation Total [cm]	28.69	30.79	20.28	28.71	30.81	20.31
Higher Hashin Value	0.284	0.423	0.2027	0.284	0.423	0.2027
Location	[1]	[1]	[1]	[1]	[1]	[1]

Thus, we can conclude that for the main spar with C-profile flange located at 30 % and 35 % from the chord, the reinforcement region is able to maintain stability in the structure, making it feasible to remove the secound spar, the weight reduction provided by the change being more advantageous compared to the small overall increase in stress in the structure.

6.3.2 Spar I profile

As with the C profile, the same study is carried out for the I profile, and the influence of the change in structure can be seen in Table 6.6 and Table 6.7.

Table 6.6: Stress analysis S11 - Comparison of the reduction from 2 I spars to just 1 I - main spar at 30 % of the chord

Points of analysis	Main spar at 30% chord-2 spars I			Main spar at 30% chord-1 spars I		
	Va+	Vd-	Rudder Vd	Va+	Vd-	Rudder Vd
	MPa			MPa		
Maximum Stress [1]	733.8	-814.4	-575.0	733.8	-814.4	-574.0
Maximum stress, ignoring boundary conditions [1.1]	506.2	-565.2	-411.23	507.02	-565.2	-411.23
Maximum stress Tail [2]	75.77	59.45	100.4	75.92	59.52	100.12
Maximum stress Vertical Rib [3]	75.77	59.45	100.4	75.92	59.52	100.12
Maximum stress Main Spar [4]	-29.13	37.59	68.01	-30.05	38.76	66.12
Maximum stress Secound Spar [5]	-24.62	31.48	-23.63	25.06	32.15	22.30
Maximum stress Horizontal Rib [6]	18.38	14.78	11.11	19.68	16.11	13.35
Maximum stress Main spar curve [7]	7.521	15.12	67.58	8.24	16.4	68.3
Maximum stress Boom assembly region [8]	200.8	220.5	150.5	200.8	220.5	150.4
Maximum stress Skin Vertical stabilizer-Boom [9]	-195.4	167.3	-256.2	-195.6	167.4	-255.0
Maximum stress Main spar hole [10]	12.59	11.62	18.98	11.48	10.66	19.2
Maximum deformation Total [cm]	27.59	30.08	19.83	27.61	30.09	19.85
Higher Hashin Value	0.2559	0.4606	0.2301	0.2559	0.4606	0.2301
Location	[1]	[1]	[1]	[1]	[1]	[1]

Looking at the results obtained, we can conclude that the previous case is continuing, and we can also see a slight general increase in stress in the various structural elements that make up the structure, maintaining the maximum estimated stress at the critical points of the boom skin, the assembly region and the boom-vertical stabilizer transition skin. As for the deformation and maximum value estimated by the hashin criterion, as in the previous case, we can observe an insignificant change, confirming once again that the reduction is feasible, with the weight reduction provided by the change being more advantageous than the small overall increase in stress in the structure.

Table 6.7: Stress analysis S11 - Comparison of the reduction from 2 I spars to just 1 I - main spar at 35 % of the chord

Points of analysis	Main spar at 35% chord-2 spars I			Main spar at 35% chord-1 spars I		
	Va+	Vd-	Rudder Vd	Va+	Vd-	Rudder Vd
	MPa			MPa		
Maximum Stress [1]	717	-780.5	-540.0	717	-780.5	-540.0
Maximum stress, ignoring boundary conditions [1.1]	518.53	-561.23	-394.12	518.58	-561.23	-394.12
Maximum stress Tail [2]	39.12	36.92	63.36	39.33	37.93	59.9
Maximum stress Vertical Rib [3]	39.12	30.59	34.81	39.33	30.77	34.13
Maximum stress Main Spar [4]	-28.89	35.21	63.36	-29.70	37.98	60.46
Maximum stress Secound Spar [5]	-22.26	26.79	28.30	22.81	28.85	17.98
Maximum stress Horizontal Rib [6]	24.34	17.66	10.66	26.12	19.4	15.08
Maximum stress Main spar curve [7]	9.96	18.8	61.42	14.29	15.2	59.9
Maximum stress Boom assembly region [8]	205.3	-221.6	147.4	205.3	-221.6	147.2
Maximum stress Skin Vertical stabilizer-Boom [9]	179.9	-156.8	-277.2	179.8	-157.2	-278.3
Maximum stress Main spar hole [10]	9.429	7.521	23.46	11.37	9.344	23.46
Maximum deformation Total [cm]	28.68	30.79	20.28	28.71	30.82	20.32
Higher Hashin Value	0.284	0.423	0.2027	0.284	0.423	0.2027
Location	[1]	[1]	[1]	[1]	[1]	[1]

6.3.3 1 Spar C vs 1 Spar I

At this point, it was necessary to reduce the analysis cases to a single solution, in order to make it possible to covert to an optimal solution. The need therefore arose for the present study in order to directly compare the versions previously studied for the structure of just 1 spar.

Looking at the results in Table 6.8, where a color scheme is presented to facilitate the interpretation of the results, where dark green indicates the lowest value among the 4 cases and light green the 2nd lowest case, we can quickly state that in the context of using only one spar, its positioning at 35% of the chord, has the advantage of reducing the maximum stress value for practically all points of the structure, with the sole exception of the skin in the transition region between the vertical stabilizer and the boom, where the main spar option at 30% of the chord generally has lower stress values.

Table 6.8: Stress analysis S11 - Comparison of the length without secound spar - Main spar : profile C vs Peril I

Points of analysis	Main spar at 30 % chord-1 spars C			Main spar at 30 % chord-1 spars I			Main spar at 35 % chord-1 spars C			Main spar at 35 % chord-1 spars I		
	Va+	Vd-	Rudder Vd	Va+	Vd-	Rudder Vd	Va+	Vd-	Rudder Vd	Va+	Vd-	Rudder Vd
	MPa			MPa			MPa			MPa		
Maximum Stress [1]	734.3	-814.4	-574.6	733.8	-814.4	-574	716.9	-780.5	-539.4	717	-780.5	-540.0
Maximum stress, ignoring boundary conditions [1.1]	506.2	-565.2	-411.23	507.02	-565.2	-411.23	518.53	-561.23	-394.12	518.584	-561.23	-394.12
Maximum stress Tail [2]	74.91	59.2	101.8	75.92	59.52	100.12	38.57	37.15	65.25	39.33	37.93	59.9
Maximum stress Vertical Rib [3]	74.91	59.2	101.8	75.92	59.52	100.12	38.57	35.24	33.1	39.33	30.77	34.13
Maximum stress Main Spar [4]	-29.33	37.69	66.26	-30.05	38.76	68.12	-29.14	37.23	63.77	-29.70	37.98	60.46
Maximum stress Secound Spar [5]	-24.55	31.31	21.70	25.06	32.15	22.30	22.38	28.15	17.59	22.81	28.85	17.98
Maximum stress Horizontal Rib [6]	19.58	16.12	13.29	19.68	16.11	13.35	25.9	19.26	14.17	26.12	19.4	15.08
Maximum stress Main spar curve [7]	12.23	15.12	66.1	8.24	16.4	68.3	12.2	20.1	65.25	14.29	15.2	59.9
Maximum stress Boom assembly region [8]	200.8	-220.5	150.5	200.8	220.5	150.4	205.6	-221.6	147.3	205.3	-221.6	147.2
Maximum stress Skin Vertical stabilizer-Boom [9]	-195.5	167.2	-248.9	-195.6	167.4	-255.0	205.4	-172.4	-319.0	179.8	-157.2	-278.3
Maximum stress Main spar hole [10]	14.02	12.81	15.59	11.48	10.66	19.2	6.675	5.281	16.6	11.37	9.344	23.46
Maximum deformation Total [cm]	27.61	30.07	19.86	27.61	30.09	19.85	28.71	30.81	20.31	28.71	30.82	20.32
Higher Hashin Value	0.2559	0.4606	0.2301	0.2559	0.4606	0.2301	0.284	0.423	0.2027	0.284	0.423	0.2027
Location	[1]	[1]	[1]	[1]	[1]	[1]	[1]	[1]	[1]	[1]	[1]	[1]

In terms of deformation, we can see that increasing the distance from the leading edge of the main spar generates an increase of approximately 1 [cm], but promotes a reduction of approximately 0.3 in the maximum value estimated by the Hashin criterion.

Looking now at the two best cases in Table 6.8, referring to the main spar at 35% of the chord, we can see that the I profile has a clear advantage in the Vd rudder load case, making it possible to create a more uniform distribution of stress in the structure, avoiding such high stress concentration points. On the other hand, we can see how the C profile has an advantage in the other two load cases Va+ and Vd-.

To conclude this analysis, we can look at Figure 6.11, a comparison between the main spar and the respective reinforcement region for the two best cases observed above, where we can see that changing the secound spar by the reinforcement region does not alter the stress distribution along the structure, and we can also see a slight reduction in the maximum stress of the structure for the C profile.

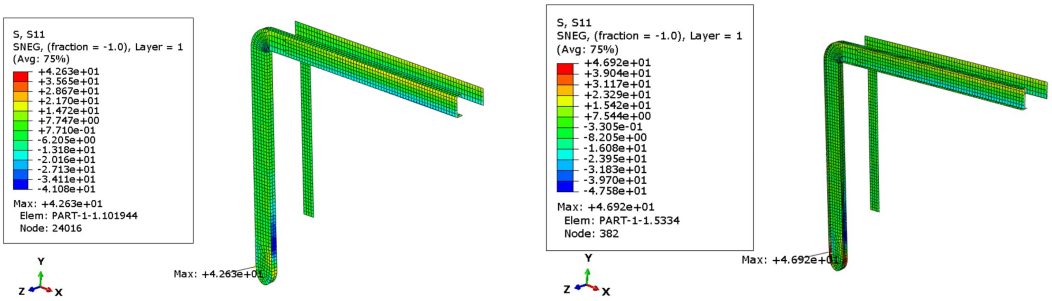

a) 1 spar C FEM model b) 1 spar I FEM model

Figure 6.11: Isometric view - Comapration structure for 1 spar in C and I - Load case Rudder Vd

Taking into account all this information gathered and the company's desire to explore the advantages of using the I-profile for the main spar flange, it was decided to opt for the structural solution of just one main spar located 35% from the chord and with its flange made up of an I-profile.

6.4 Spars I different configurations

Since the company already had consolidated experience in the use of spars with a C profile flange, the need arose to carry out this study in order to understand what advantages we could have gained by increasing the thickness of the web or the flange of the I profile, Bearing in mind that all the analyses carried out so far with the I-profile were based on its manufacture from 2 C-profiles, resulting in the same web thickness but half the flange thickness compared to the reference C-profile, which brought a weight advantage of approximately 480 g but a penalty in structural terms.

In order to have a mapping of the different configurations of the profile, the different configurations tested are shown in Figure 6.12, with profile 1 being the version studied so far. As for profile 2, it is made up of a web with the same thickness as profile 1, but the flange is 1.5 times thicker than the reference C profile, while in the case of profile 3, we can find a similar configuration to profile 2, changing only the thickness of the flange from 1.5 to 2 times thicker than the reference C profile. Finally, profile 4 refers to a flange with the same thickness as profile C, but a web twice as thick.

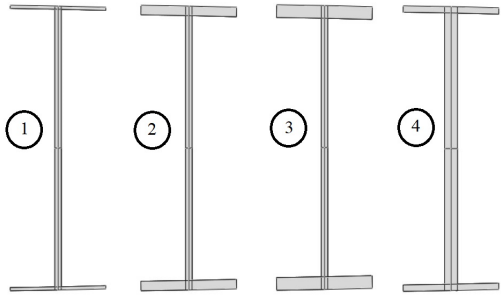

Figure 6.12: Different spar configurations in I studied

The first analysis that was taken into account was the weight variation generated by the different I-profiles in the main spar. Table 6.9 shows that the I-profiles [2, 3 and 4] (Figure6.12) show an increase in weight compared to the C-profile, which is 480 [g] for profile 2, 960 [g] for profile 3 and 1.35 [kg] for profile 4.

Table 6.9: Weight of the main spar with different I and C profile configurations

Spar configuration	Thickness Web	Thickness Flange	Main spar Weight[kg]
Spar C	1x	1x	3.24
Spar I	1x	0.5x	2.76
Spar I	1x	1.5x	3.72
Spar I	1x	2x	4.16
Spar I	2x	1x	4.59

After collecting the weights for the different configurations of I-profile, we can see the results of the comparison in Table 6.10, where the same color scheme used in the previous section is followed, with dark green representing the lowest stress value of all the cases and light green the second lowest, so we can quickly see as a first analysis that increasing the thickness of the flange is more beneficial compared to increasing the thickness of the web, with the flange configuration with 1.5 times thicker can obtain very similar stress values, even lower at some points compared to the configuration with double the web thickness, the latter being approximately 890 [g] heavier.

Table 6.10: Stress analysis S11 - Comparing different profile configurations I

Points of analysis	I profile- 0.5x flange			I profile - 2x web			I profile - 1.5x flange			I profile - 2x flange		
	Va+	Vd-	Rudder Vd	Va+	Vd-	Rudder Vd	Va+	Vd-	Rudder Vd	Va+	Vd-	Rudder Vd
	MPa			MPa			MPa			MPa		
Maximum Stress [1]	717	-780.5	-540.0	717	-780.5	-540.0	717	-780.5	-540.0	717	-780.5	-540.0
Maximum stress, ignoring boundary conditions [1.1]	518.584	-561.23	-394.12	518.53	-561.23	-394.12	518.53	-561.23	-394.12	518.53	-561.23	-394.12
Maximum stress Tail [2]	39.33	37.93	59.9	39.72	35.82	46.6	39.64	35.98	53.04	39.67	35.14	54.02
Maximum stress Vertical Rib [3]	39.33	30.77	34.13	39.72	31.07	34.71	39.64	30.99	34.34	39.67	30.99	34.5
Maximum stress Main Spar [4]	-29.33	37.69	63.26	-28.07	35.86	43.17	-28.17	36.05	56.62	-27.51	35.21	55.42
Maximum stress Secound Spar [5]	-24.55	31.31	21.70	21.47	26.96	16.72	-21.60	27.40	17.04	21.27	26.79	16.64
Maximum stress Horizontal Rib [6]	26.12	19.4	15.08	27.08	20.47	16.6	26.05	19.23	14.8	26.04	19.17	14.56
Maximum stress Main spar curve [7]	14.29	15.2	59.9	6.8	10.2	46.6	13.25	11.2	53.04	5.959	16.2	54.02
Maximum stress Boom assembly region [8]	200.8	-220.5	150.5	205.3	-221.6	147.4	205.3	-221.6	147.3	205.3	-221.6	147.3
Maximum stress Skin Vertical stabilizer-Boom [9]	-195.5	167.2	-248.9	179.6	-157.1	-278.8	179.8	-157.0	-279.0	179.8	-157.0	-279.0
Maximum stress Main spar hole [10]	11.37	9.344	23.46	9.962	8.491	21.53	7.56	6.225	17.77	6.78	4.908	13.51
Maximum deformation Total [cm]	28.71	30.82	20.32	27.69	30.79	20.3	28.7	30.8	20.31	28.69	30.79	20.29
Higher Hashin Value	0.284	0.423	0.2027	0.284	0.423	0.2027	0.284	0.423	0.2027	0.284	0.423	0.2027
Location	[1]	[1]	[1]	[1]	[1]	[1]	[1]	[1]	[1]	[1]	[1]	[1]

With this in mind, the final analysis was to compare the two best I-profiles previously observed with the C-profile, in order to see if the change was really justified. Table 6.11 shows a gradual reduction in the maximum stresses estimated for the different structural elements with the increase in flange thickness. Of particular importance is the average reduction of 25 MPa in the region of the transition skin between the boom and vertical stabilizer, which is justified by the greater static inertia of the I-profile compared to the C-profile, which reduces the deflection of the structure and consequently the concentration of stress in the aforementioned area.

6.4. Spars I different configurations

Table 6.11: Stress analysis S11 - Comparing the best I-profile configurations and the best C-profile configurations

Points of analysis	C profile - 1x flange			I profile - 1.5x flange			I profile - 2x flange		
	Va+	Vd-	Rudder Vd	Va+	Vd-	Rudder Vd	Va+	Vd-	Rudder Vd
	MPa			MPa			MPa		
Maximum Stress [1]	716.9	-780.5	-539.4	717	-780.5	-540	717	-780.5	-540
Maximum stress, ignoring boundary conditions [1.1]	518.53	-561.23	-394.12	518.53	-561.23	-394.12	518.53	-561.23	-394.12
Maximum stress Tail [2]	38.57	37.15	65.25	39.64	35.98	53.04	39.67	35.14	54.02
Maximum stress Vertical Rib [3]	38.57	35.24	33.1	39.64	30.99	34.34	39.67	30.99	34.5
Maximum stress Main Spar [4]	-29.14	37.23	68.77	-28.17	36.05	56.62	-27.51	35.21	55.42
Maximum stress Secound Spar [5]	22.38	28.15	17.59	-21.60	27.40	17.04	21.27	26.79	16.65
Maximum stress Horizontal Rib [6]	25.9	19.26	14.17	26.05	19.23	14.8	26.04	19.17	14.56
Maximum stress Main spar curve [7]	12.2	20.1	65.25	13.25	11.2	53.04	5.959	16.2	54.02
Maximum stress Boom assembly region [8]	205.6	-221.6	147.3	205.3	-221.6	147.3	205.3	-221.6	147.3
Maximum stress Skin Vertical stabilizer-Boom [9]	205.4	-172.4	-319.0	179.8	-157.0	-279.0	179.8	-157.0	-279.0
Maximum stress Main spar hole [10]	6.675	5.281	16.6	7.56	6.225	17.77	6.78	4.908	13.51
Maximum deformation Total [cm]	28.71	30.81	20.31	28.7	30.8	20.31	28.69	30.79	20.29
Higher Hashin Value	0.284	0.423	0.2027	0.284	0.423	0.2027	0.284	0.423	0.2027
Location	[1]	[1]	[1]	[1]	[1]	[1]	[1]	[1]	[1]

In order to finalize this comparative study, we can see in Figure 6.13, two isometric views of a stress analysis for the Va+ case, with Figure 6.13b representing the case of a main spar in C-profile and Figure 6.13a , the respective main spar in I profile with 1.5x the thickness of the flange. As already observed in Table 6.11, we can see that although the requested regions are the same, the I-profile allows for a reduction in the overall magnitude of the skin in both the boom and the transition region.

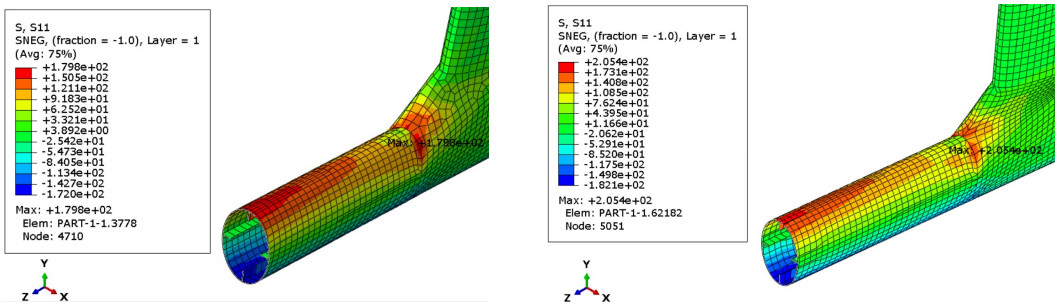

a) Spar I - 1.5x flange FEM model

b) Spar C FEM model

Figure 6.13: Isometric view - Stress analysis S11 point 8 - Load case Va+

Taking into account the advantages already mentioned, and since it was the company's objective to study I-Profile in more depth, C-Profile was discarded and Profile 3 was chosen over Profile 4, since it was considered that the added weight (480g) due to the increase in thickness from 1.5 times to 2 times would not justify the reduction in maximum stress observed in the structure (Table 6.11).

6.5 Ribs Analysis

Finally, having reached this point, the last comparative analysis proposed before the final structural version was the reduction of Ribs on the horizontal surface, which was initially oversized, defining a Rib every 1/4 Chord, corresponding to 13 Ribs. This led to the need to figure out how many ribs we could remove from the structure in order to reduce weight while maintaining structural integrity.

Before we begin this analysis, it is important to remember that the main role of the Ribs in the Tail structure is to support the inertial forces and reinforce the skin, avoiding phenomena such as buckling or deformations between sections, and it is necessary to ensure that these phenomena do not arise by reducing the number of Ribs.

Therefore, in Table 6.12 we can see the 3 cases tested, with the color map referring to the comparison with the reference case of 13 Ribs in the horizontal stabilizer. As we can see, the stress of the structure in general increases at all points, with the most significant increase being in the Ribs of the horizontal stabilizer, proving that reducing this component does not bring a major disadvantage in terms of the maximum stress of the structure. However, we can see that for the last iteration of 7 Ribs on the horizontal surface, the point of greatest stress in the Tail structure, which normally corresponds to the main spar, now corresponds to the holes in the horizontal Ribs, which is considered the stop criterion.

Table 6.12: Stress analysis S11 - Comparing 13/11/9/7 Ribs on the horizontal stabiliser

Points of analysis	13 Horizontal Ribs			11 Horizontal Ribs			9 Horizontal Ribs			7 Horizontal Ribs		
	Va+	Vd-	Rudder Vd	Va+	Vd-	Rudder Vd	Va+	Vd-	Rudder Vd	Va+	Vd-	Rudder Vd
	MPa			MPa			MPa			MPa		
Maximum Stress [1]	717	-780.5	-540	709.1	-781.3	-552.7	706.9	-782.0	-555.1	710.0	-782.6	-558.4
Maximum Stress, ignoring boundary conditions [1.1]	518.53	-561.23	-394.12	512.08	-567.23	-413.1	512.2	-568.2	-415.32	513.6	-573.2	-417.23
Maximum Stress Tail [2]	39.64	35.98	53.04	38.9	36.28	58.64	39.39	36.79	57.58	45.93	37.08	58.55
Maximum Stress Vertical Rib [3]	39.64	30.99	34.34	38.9	31.05	36.94	39.39	31.12	36.2	39.71	31.61	37.27
Maximum Stress Main Spar [4]	-28.17	36.05	56.02	-28.30	36.36	62.22	-28.58	36.69	61.11	-29.04	37.18	62.14
Maximum Stress Secound Spar [5]	-21.60	27.40	17.04	21.90	27.75	19.39	22.31	28.25	19.83	22.97	29.03	20.25
Maximum Stress Horizotnal Rib [6]	26.05	19.23	14.8	30.03	21.23	14.95	35.93	24.52	15.08	45.77	29.97	15.94
Maximum Stress Main spar curve [7]	13.25	11.2	53.04	14.25	16.24	58.64	14.45	20.12	57.58	12.29	20.52	58.55
Maximum Stress Boom assembly region [8]	205.3	-221.6	147.3	202.7	-221.9	148.7	202.5	-222.1	148.8	203.3	-222.2	150.2
Maximum Stress Skin Vertival Stabilizer-Boom [9]	179.8	-157.0	-279.0	-157.0	154.8	-289.2	178.5	-157.2	-286.1	180.8	-157.0	-293.8
Maximum Stress Main spar hole [10]	7.56	6.225	17.77	6.412	5.754	16.81	6.98	5.774	16.7	7.2	5.801	16.94
Maximum Total deformation [cm]	28.7	30.8	20.31	28.3	30.83	20.25	28.31	30.86	20.23	28.43	30.88	20.43
Higher Hashin Value	0.284	0.423	0.2027	0.2235	0.4239	0.2121	0.2221	0.4247	0.214	0.2241	0.4254	0.2166
Location	[1]	[1]	[1]	[1]	[1]	[1]	[1]	[1]	[1]	[1]	[1]	[1]

To conclude this study, we can see in Figure 6.14a the distribution of stress along the horizontal ribs for the case of 7 ribs, concluding that the greatest concentration of stress would be present in the hole in the central section, with the front hole being much less stressed. In addition, in Figure 6.14b we can see the general deformation of the structure, proving that reducing the ribs from 13 to 7 in the vertical stabilizer did not introduce any abnormal deformation phenomena in the Tail skin.

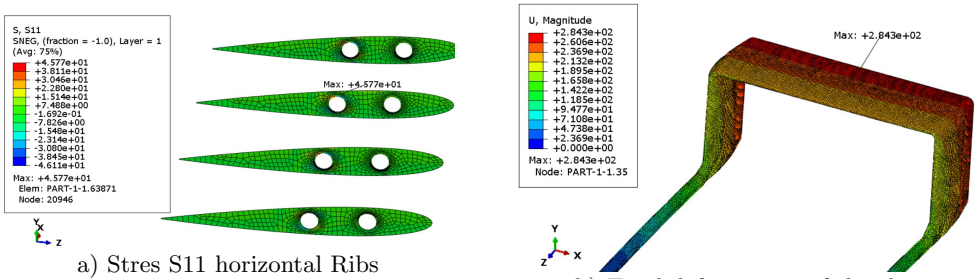

a) Stres S11 horizontal Ribs

b) Total deformation of the skin

Figure 6.14: Case of study 7 ribs - load case Va+

In Figure 6.15, we can see a more detailed analysis of the hole in the central section of the most stressed rib in the previous case of Figure 6.14a, and we can see that more than 95% of the stress concentrated in the hole is in the S11 direction corresponding to the vertical direction, which is justified by the shorter distance from the edge of the Rib.

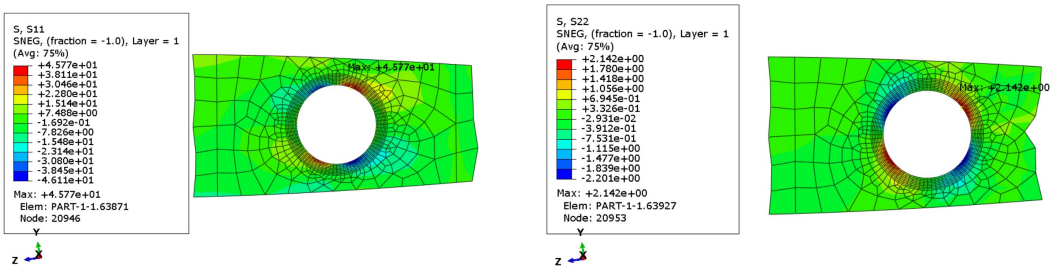

a) S11 Rib centre hole section

b) S22 Rib centre hole section

Figure 6.15: Stress analysis - Centre hole horizontal rib for the 7 Ribs analysis case - load case Va+

6.6 Final solution

After completing all the tests presented above, it was possible to carry out a final iteration of the Tail and Boom structure for the ARX aircraft, defining the end of the structural studies and the starting point for the weight reduction analysis with the help of the optimization tool in Chapter 7.

Therefore, 3 changes were taken into account compared to the structure of the last study presented in Section 6.5, the first of which was to reduce the ribs of the vertical stabilizer from 5 to 4 (Figure 6.16), since as we have seen over the last few analyses, the vertical ribs, with the exception of the rib next to the boom-vertical stabilizer transition, had a very low concentration of stress, so we could reduce the ribs in the central section from 2 to 1. The vertical stabilizer is at the limit of its optimization since all the other structural elements have a fixed position in order to delimit the Rudder control surface or to guarantee curvature in the connection zone between the vertical and horizontal stabilizers.

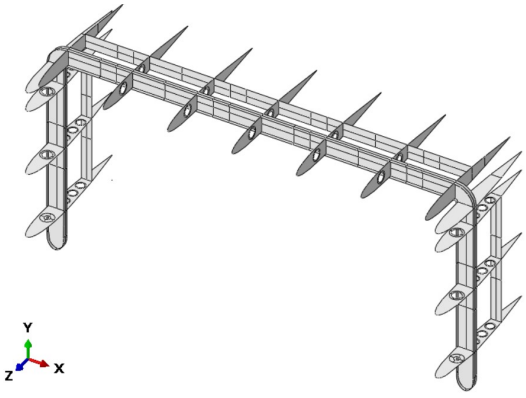

Figure 6.16: ARX final Tail structure

As for the second and third changes, since it was not possible for reasons of time in this work to investigate in terms of fatigue the regions of concentrated stress such as the holes in the Ribs, it was decided to conservatively reduce the diameter of the front hole of the vertical Rib near the boom-stabilizer transition from 25 to 15 [mm] and to reduce the hole in the central section

between the main spar and the reinforcement region (former secound spar) of the Ribs of the horizontal stabilizer from 25 [mm] to 20 [mm], in an attempt to solve what could be the most critical points of the structure at this level, and in Figure 6.16 we can see an illustration of Tail's final structure.

Therefore, in Table 6.13, we can see, as expected, a significant reduction in the concentration of stresses in the regions of the holes in the vertical and horizontal stabilizer ribs, and we can also see that the increase in stresses in the remaining points of analysis of the structure due to the reduction in the number of vertical stabilizer ribs was not significant, and these were never greater than 2 MPa compared to the height of the previous section.

Table 6.13: Stress analysis S11 Final iteration Tail boom ARX

	Final ARX Tail structure Ribs		
Points of analysis	Va+	Vd-	Rudder Vd
	MPa		
Maximum Stress [1]	714.2	-783.2	-562.5
Maximum Stress, ignoring boundary conditions [1.1]	516.22	-566.23	-423.4
Maximum Stress Tail [2]	38.89	37.41	60.78
Maximum Stress Vertical Rib [3]	30.44	23.94	28.6
Maximum Stress Main Spar [4]	-29.44	37.52	64.48
Maximum Stress Secound Spar [5]	23.23	29.30	20.76
Maximum Stress Horizotnal Rib [6]	-39.06	24.36	17.34
Maximum Stress Main spar curve [7]	16.2	16.21	60.78
Maximum Stress Boom assembly region [8]	204.5	-222.4	151.1
Maximum Stress Skin Vertival Stabilizer-Boom [9]	182.0	-157.4	-291.0
Maximum Stress Main spar hole [10]	6.915	5.669	16.89
Maximum Total deformation [cm]	28.59	30.9	20.53
Higher Hashin Value	0.2267	0.426	0.2218
Location	[1]	[1]	[1]

In more detail, we can see in Figure 6.17 the comparison of Stress S22 for the vertical Rib hole before the alteration (Figure 6.17a) and after the alteration (Figure 6.17b). We can see a decrease of approximately 5 MPa in the estimated maximum stress and a concentration of stress much further away from the edge of the Rib, which favors its resistance against the appearance of cracks that could cause the structure to fail.

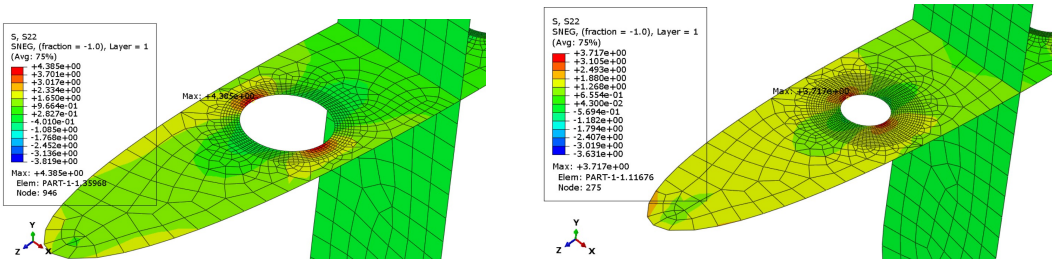

a) S11 Rib centre hole section

b) S22 Rib centre hole section

Figure 6.17: Stress analysis1 - Frontal hole Vetical Rib for the 7 Ribs analysis case - load case Vd-

6.6. Final solution

In Figure 6.18, we find the same analysis as before, but for Stress S11, where we can quickly identify that the greatest stress is in this direction, and we can see a decrease in the region of stress concentration near the borehole, although the estimated maximum value remains roughly the same due to a concentration of stress in the frontal region of the Rib due to deformation of the skin (vertical boom-stabilizer transition) in this region.

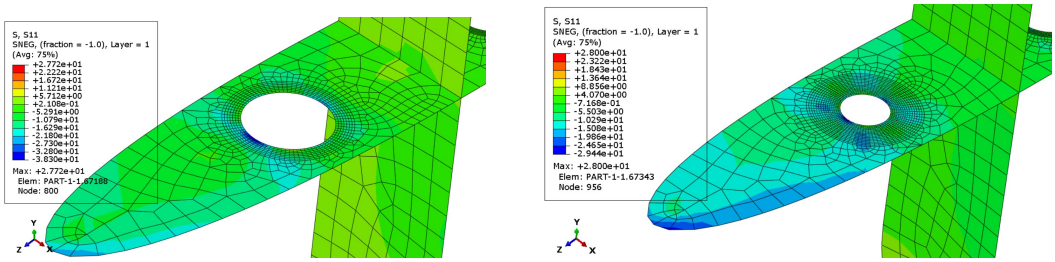

a) S11 Rib centre hole section b) S22 Rib centre hole section

Figure 6.18: Stress analysis2 - Frontal hole Vetical Rib for the 7 Ribs analysis case - load case Vd-

As a second analysis, we can see in Figure 6.19, an analysis of S22 and S11, for load case Vd-, where we can see the central section of the hole in the horizontal Ribs, corresponding to the second change made to the structure, where we can see by comparing with Figure 6.15, that as in the previous case, it was possible to successfully reduce the stress concentration created at the edge of the hole, and we can also see how in this case the S11 direction is the most dangerous for the structure.

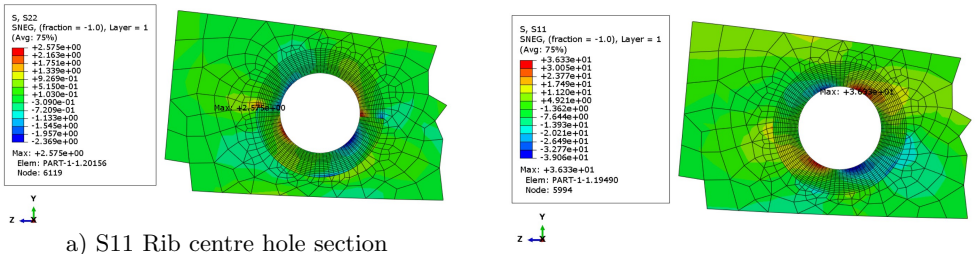

a) S11 Rib centre hole section b) S22 Rib centre hole section

Figure 6.19: Stress analysis - Section of the centre hole of the horizontal rib for the 7 Ribs analysis case

Looking more generally at other stressed regions of the structure, we can see in Figure 6.20, an S11 stress analysis for the Vd- load case, corresponding to the main spar and the reinforcement region , where we can see how the upper region of both structures is in tension and the lower region in compression.

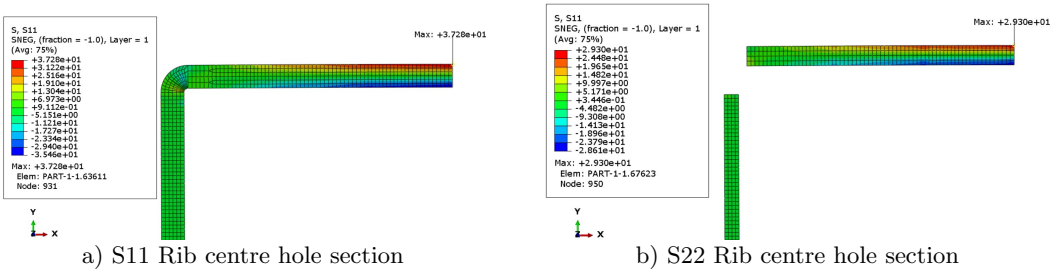

a) S11 Rib centre hole section b) S22 Rib centre hole section

Figure 6.20: Stress analysis - Main spar and control surface reforce for the 7 Ribs - load case Vd-

Finally, it is important to note in Figure 6.21, the boom region with the respective 4 stringers, where we can see through the S11 Stress analysis for the Vd- load case, that the upper region of the boom is in compression and the lower region is in tension, and we can also see the central neutral axis, following the behavior of the stringers and the skin. Also in Figure 6.21, we can see the concentration of tension that we have been analyzing throughout the comparative studies regarding the tension region inside the main spar in the region of the curve.

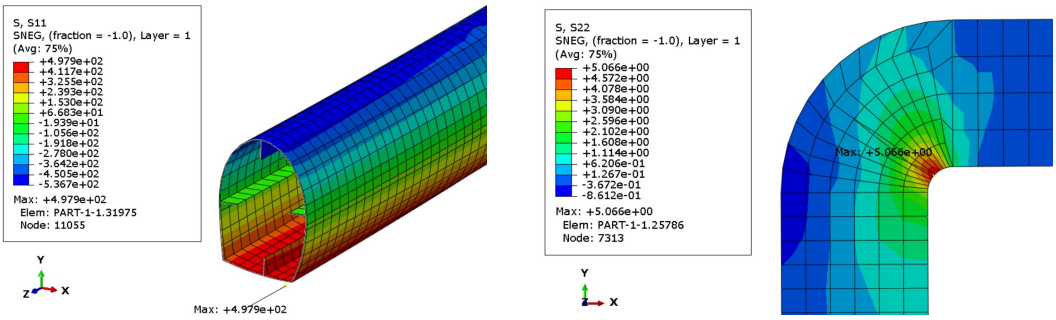

a) S11 Rib centre hole section b) S22 Rib centre hole section

Figure 6.21: Stress analysis - Boom and main spar curve for the 7 Ribs analysis case - load case Vd-

As a result, we have finalized the study phase, a structure reduced to the minimum structural components, capable of withstanding the 3 critical load cases identified without coming close to failure and with a total final weight of 40.3 [kg], which represents a decrease of approximately 3.9 [kg] compared to the initial structure.

Chapter 7

Carbon Fiber Reinforced Panel (CFRP) Optimization

After defining the final construction solution in Chapter 6, in this final chapter we will aim to optimise the weight of the most stressed sections of the structure. The starting point for this was the optimization code developed by engineers Douglas [3] and Dilki [4] in the 2022/2023 academic year, which already had the capacity to optimise composite materials in terms of number of layers and preferred layep orientation, which was tested by the engineers themselves in several case studies, concluding with the study of the fuselage and main wing of the aircraft developed, validating its correct operation. Therefore, throughout the initial section we will present the optimization tool's operating scheme, followed by its validation for two of the classic cases of known optimum value tested in the reference theses, in order to confirm the results obtained and allow improvements to be proposed, making it more geared towards the interests of the Tekever company and this case study.

7.1 Overview of the Optimization algorithmic

In Overview, the optimization tool is a single-objective tool that focuses on optimizing the orientation and number of layup layers for a given structure represented in a finite element software. This process can be carried out using a genetic optimization code, reinforced by an auxiliary surrogate model. We will therefore go through the tool's three processing phases in more detail below.

Design of Experiments and Finite element model

The sequence begins with the "Doe" script, which allows the generation of experiments (DoE) using Latin Hypercube Sampling (LHS), responsible for defining the sequence and configuration of the number of plys for each angle of study [0,45,90], which will be applied and analysed in the finite element model. It is important to note that this design of experiments is carried out taking into account three independent variables per analysis section, representative of the 3 analysis angles [0,45,90], the upper and lower limits defined for the independent variables and the number of samples, guaranteeing a design sample evenly distributed across the multidimensional input space.

The process then continues with the "Database" script, which acts as the tool's central data storage point, allowing the estimated results for the failure criterion to be saved for each simulation of the finite element model, which is defined in the "model" script where the CAE simulation process is programmed step by step, defining the geometry, mesh, loads and boundary conditions and composite material used.

Thus, after creating the finite element model in Abaqus, an iterative process is started taking into account the sample generated by the "Doe" script through the design of experiments (DoE), where after each analysis, the post-processing script extracts and processes the data from the Abaqus output databases, making it possible to identify the elements with a failure index greater than 1, according to the failure criterion defined for each layer orientation, retrieving this information from the Data base. As this process is time-consuming, the database generated allows the analysis to continue from the point of interruption, if necessary, and also checks for the existence of a combination of layers in the database, skipping iterations if found.

Once the initial iterative process has been completed, taking into account the number of samples defined, this process is repeated for a smaller number of samples, typically 20% of the value chosen for the first cycle, making it possible to generate an effective training database, guaranteeing the correct execution of the regression. The flow chart of the process explained above can be seen in Figure 7.1

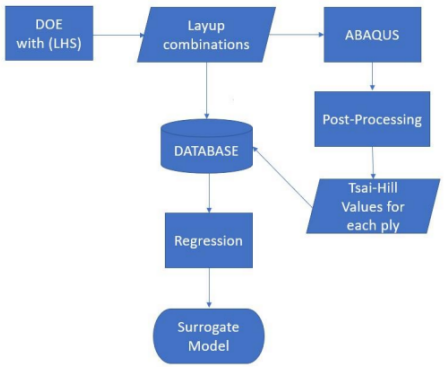

Figure 7.1: Flow Chart surrogate model [3]

Regression and Genetic Algorithm

Once the first phase has been completed, it is possible to run the Gaussian Regression (GPR) model, which adjusts a GPR model for each combination of section and angle, allowing the number of layers to be predicted and the model's performance to be assessed using the training data generated, evaluating the R-squared value and the root mean square error,

Finally, using this information, the developed Genetic Algorithm (GA) is applied, starting by defining the objective function which represents a linear and directly proportional relationship between the weight of the structure and the number of layers in each section, considering the area of each section (SArea in 7.1) that needs to be evaluated, the number of layers (Nlayers in 7.1) in each section and the area density of the laminate (Areal Densitylaminate in 7.1), which can be described by the following equation 7.1:

$$SW = \sum_{k=0}^{Nlayers} S_k * AreaDensity_{laminate} * Nlayers_k \tag{7.1}$$

Next, an initial population is randomly generated, ensuring adequate genetic diversity to effectively explore the solution space, avoiding premature convergence to suboptimal solutions and guaranteeing a comprehensive search for high-quality solutions. As for the selection of individuals, the roulette wheel method was implemented, where each individual's probability of selection is proportional to its fitness, which means that better adapted individuals have a greater chance of being selected for reproduction, preserving their valuable characteristics for future generations. Then in the reproduction process, the algorithm employs uniform crossover, which combines the genes of two parents in a uniform way to generate offspring, allowing the exploration of different genetic combinations and the generation of new solutions. Finally, flip-bit mutation is applied to introduce random variations in individuals, further promoting genetic diversity in the population. Therefore, in Figure 7.2 we can see the flow chart of the genetic code explained above in order to better understand how it works. It is important to note that all the methods explained here can be analyzed in more detail in Section 2.3.1 of this report.

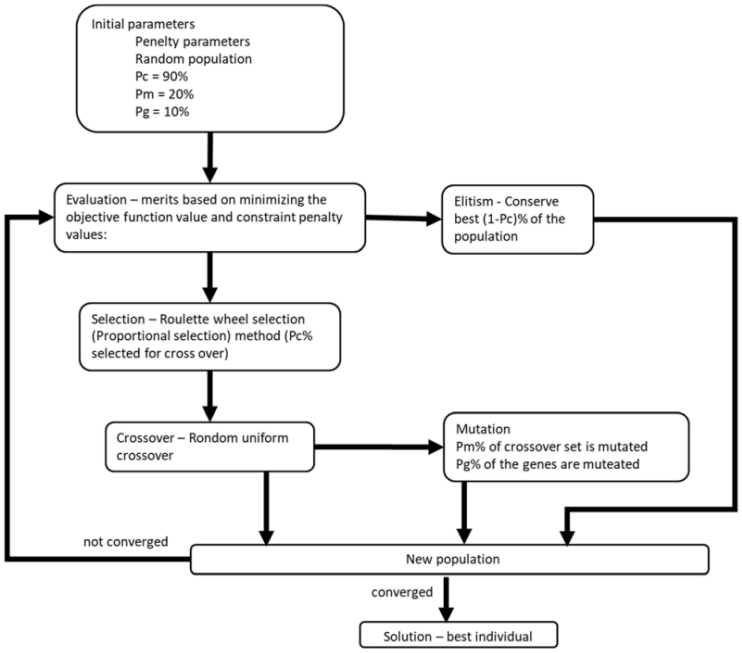

Figure 7.2: Representation line of thought Genetic code [4]

Finally, it is important to note that the algorithm has an elitist strategy, where the best individuals from the current population are preserved for the next generation, ensuring that valuable characteristics are not lost over the course of the algorithm's iterations, promoting convergence towards solutions of greater merit, making it possible to ensure that solutions with a failure criterion greater than 1 are penalised and removed from the population, and solutions that are closer and less than 1 are penalised, and the restrictions included in the problem are presented below:

- g1(x): Ensuring that the solution is below the upper boundery;
- g2(x): Ensuring that the solution is above the lower boundery;
- g3(x): Ensuring that there is at least one layer in each section;
- g4(x): Penalising solutions with Tsai-Hill ≥ 1, as shown in Equation 7.2.

Therefore, the penalty g4 (Equation 7.2), has a parameter that increases in magnitude taking into account the number of plys that fail, making it possible to distinguish between a situation where there is total failure of the structure and partial failure of only a small number of plys, which makes it easier to approximate the optimal solution to the value of 1 for the failure criterion estimate.

$$g_4(x) = g_4(x) + 10 + 1 * Numberof failingplies \tag{7.2}$$

7.1.1 Algorithm Validation

In order to confirm that the optimization tool was working properly and that we had a better understanding of it, we replicated two classic cases, the flat plate test on traction and then the flat plate test on shear, as taken into account in the reference theses [3], [4], considering a population size of 1000, 3 bits per variable and 200 samples. As for regression, only the Gaussian model was taken into account since it was the model that obtained the best efficiency and was closest to the theoretical values in the reference theses, compared to the other regressions Linear regression, Linear regression with polynomial features, Ridge model, Lasso model and Elastic Net, analyzed.

7.1.1.1 Traction Plate

Starting with the flat plate test on traction in Figure 7.3, we can observe the configurations and dimensions considered, corresponding to an area of 100 x 100 [mm^2], a layup of [± 45 , 90, 0]s, lower boundary of 0 and upper boundary of 15 layers, a tensile load of 1700 MPa and a boundary conditions of encasement at the center point and limitation of displacement U2 = U3 = 0 at the remaining vertices. In a theoretical context, we know that the preferred direction of the fibers should coincide with the direction of the force, due to the greater strength of composite materials in the direction of the fiber compared to the direction of the matrix. The number of layers is expected to be close to the average value of the upper and lower boundaries, assuming a good regression.

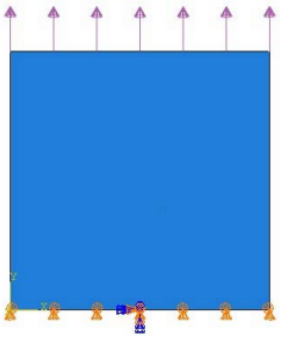

Figure 7.3: Test with plate in traction

Therefore, Figure 7.4a, Figure 7.4b and Figure 7.5 show the representative dispersion of the evaluations made by the Tsi-hill failure criterion for each sample generated by the Doe script. It can be seen that in the case of the 45 and 90 degree orientation, situations were found from 0 to 15 plys where the failure criterion is considerably exceeded, not representing the preferred direction of optimization. However, on the other hand, a clear convergence can be observed in the case of plys at 0 degrees, and it can be concluded that from approximately 9 ply, all the cases tested were

evaluated by the Tsi-hill criterion without breaking (≤ 1), defining it as the preferred direction of optimization.

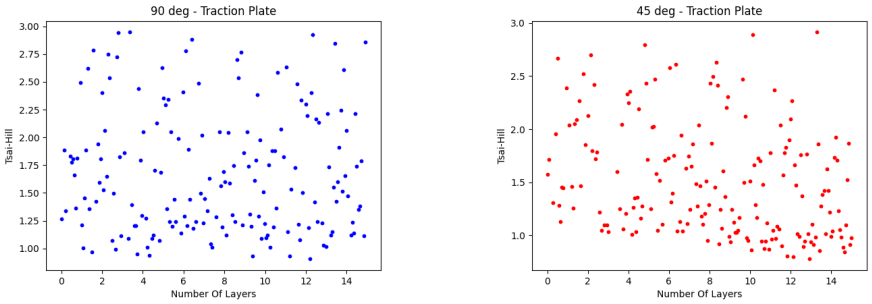

a) 90 degrees b) 45 degrees section

Figure 7.4: Tsi-Hill Failure Criteria - Plate in Traction

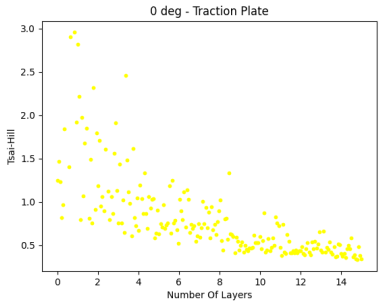

Figure 7.5: Tsi-Hill Failure Criteria - Plate in Traction for 0 degrees

The expected result of optimization at 0 degrees was therefore obtained, taking into account the reference axis aligned with the Y axis, corresponding to the direction of force application and a total of [0,0,9] plys, as obtained in the reference thesis [3] [4].

7.1.1.2 Plate in Shear

In the second case, a plate with the same dimensions, layep and upper and lower boundary was tested, but with a shear force of 600 MPa and a displacement restriction bondery condition U2 = U3 = 0 for the left vertical and U1 = U3 = 0 for the lower vertical, corresponding to a point pinned (U1 = U2 = U3 = 0) to the bottom left by the junction of the boundary conditions, the code is expected to be optimised for an optimal orientation of 45 degrees, following the same logic as previously mentioned for the tensile situation.

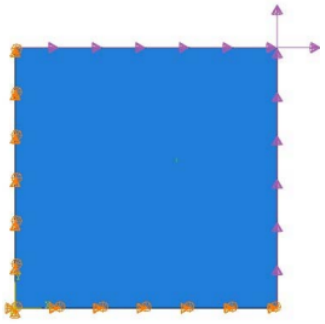

Figure 7.6: Test with plate in shear

Thus, as in the previous case, the three representative analyses of the samples evaluated in the case study are presented, and a clear convergence can be seen for the 45 degree ply direction (Figure 7.7), and it can be seen that from 7 plys no case was found that exceeded the failure criterion. On the other hand, for the ply direction of 90 degrees and 0 degrees, we can observe a diversity of points from [0-15]plys that exceed the failure criterion, Figure 7.8a and Figure 7.8b respectively.

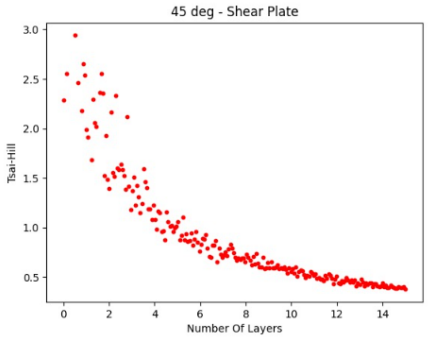

Figure 7.7: Tsi-Hill Failure Criteria - Plate in Shear for 45 degrees

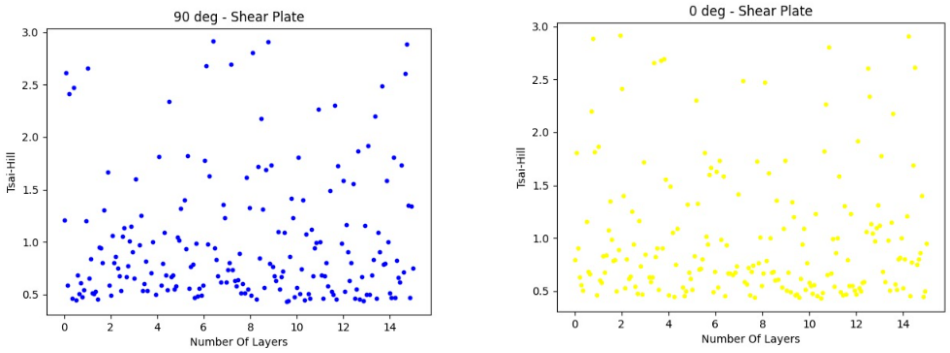

a) 90 degrees b) 0 degrees

Figure 7.8: Tsi-Hill Failure Criteria - Plate in Shear

Obtaining the expected result of optimization at $\pm 45^{o}$, taking into account the reference axis aligned with the X axis and a number of plys of [7,0,0], as per the reference thesis, validating the basic tool allowing for the evolution and integration of new functionalities in the following section.

7.2 Improved Optimization Code

When the first phase of validating the optimization tool was completed and the tool's strengths and weaknesses identified, the following improvements were taken into account:

Improving failure criteria

In the initial tool, the failure criterion responsible for evaluating each ply was the Tsi-hill criterion (discussed in Section 2.2.4), which, compared to more recent models such as LARC05 or Hashin, is less precise and efficient. In order to improve the analysis, the Hashin failure criterion was implemented, which currently represents the most efficient and evolved failure criterion present in Abaqus, considering multiple failure modes, such as fiber failure, matrix failure, compression and tension, allowing for a better assessment and determination of the structure. It should be noted

that the implementation of the LARC05 criterion through ply-in in Abaqus was also tested, but it was not possible to validate its proper functioning for more complex implementations, although the graphs obtained for the two classic cases of a flat plate in tension and a flat plate in shear are shown in Appendix E.

Improving genetic code efficiency

After analyzing the reference values found in the literature for the parameters of Crossover probability (Pc), Mutation probability (Pm), bits selected for mutation (Pg) and initial population size (n), it was considered that these could be balanced in a more efficient way, finding a better balance between diversity and demand. Therefore, below we will present the process carried out to test and improve the genetic code for the application of the classic cases.

Table 7.1: Genetic algorithmic parameters

Variable	Reference Values	Before	After
n	[20-200]	200	50
Pc	[0.5-0.7]	0.9	0.6
Pg	[0.05-0.3]	0.2	0.3
Pm	[0.1-0.3]	0.2	0.3
Lamb	———-	1	2
Tempo [s]	———-	21	6

So in the Table 7.1 , we can find possible reference values found in the literature for similar problems, [61] and the respective values used before and after the improvement, for the classic cases analysed above. It can be concluded that in the initial tool, the strategy involved a larger population, together with a high value of 90% for the Pc variable, which provided diversity to the population, which was balanced by introducing a considerably high value for the Pg and Pm variables, carrying out an aggressive mutation.

In the current case, a more elitist strategy was considered, reducing the population but maintaining a value within the reference parameters and reducing the value of Pc, increasing the probability of the best individuals remaining in the population. To balance this strategy, as mentioned above, the mutation parameters Pm and Pg were necessarily increased in order to introduce extra diversity and avoid weak exploitation. Finally, the value of Lamb was increased to 2, since it was observed that with these new parameters there was a greater tendency for the code to converge towards solutions with a lower objective value, i.e. in the case being analyzed, to assume situations at the failure limit or slightly higher, for example a failure criterion value of 1.05 or 1.1.

In this way, it was possible to obtain not only faster convergence, saving approximately 70% of the computational time of this phase of the algorithm for the classic cases analyzed, but also a greater probability of forcing the code to assume optimal values with an evaluation criterion by the failure criterion closer to 1.

Improving Versatility

Another problem with the initial tool was the need to manually program the finite element model, which complicated its implementation for more complex geometries, such as the case being analysed in this report. The solution adopted to overcome this problem was to implement the .cae files (Aabqus CAE files) directly in the tool, eliminating the need for manual programming. This change not only improved the ease of integration and changes to the finite element model, but also reduced the computational time required since the tool doesn't need to read the various lines of FEM model programming code.

7.2.1 Validating changes to the fault model

7.2.1.1 Hashin Plate in Traction

With regard to the Hashin criterion, when applied to the case of the flat plate, a situation similar to that of the Tsi-hill failure criterion can be observed, showing a dispersion of values towards 45 and 90 degrees (Figure 7.9a and Figure 7.9b), while maintaining convergence and preferential direction towards 0 degrees, as can be seen in Figure 7.10. However, unlike the Tsi-Hill criterion where only from 9 ply at 0 degrees could we observe convergence of all the points below the failure criterion, in the case of the Hashin criterion this does not happen, and we can observe convergence of points below the failure criterion from 7 ply in the same orientation, being able to estimate the value of 8 ply in the 0 degree direction compared to the 9 ply estimated in the case of Tsi-Hill, indicating better accuracy of the method.

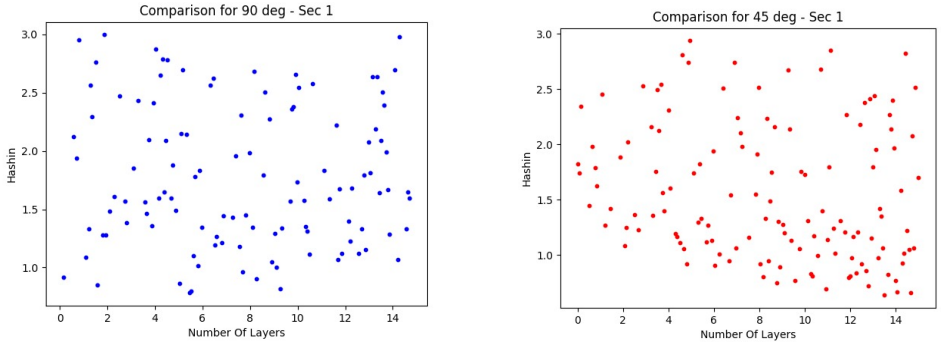

a) 90 degrees b) 45 degrees section

Figure 7.9: Hashin Failure Criteria - Plate in Traction

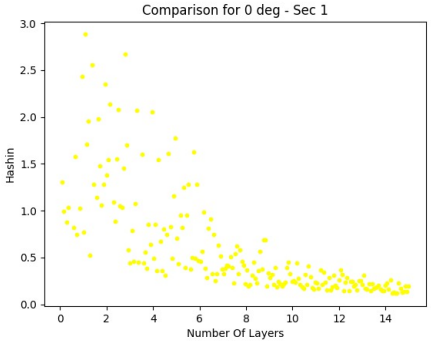

Figure 7.10: Hashin Failure Criteria - Plate in Shear for 0 degrees

7.2.1.2 Hashin Plate in Shear

In the case of the flat plate in shear, we can observe the same scenario as for the Tsi-Hill criterion, keeping the preferred direction at 45 degrees (Figure 7.11) and dispersion of [0-15]plys at 90 and 0 degrees (Figure 7.12a and Figure 7.12b respectively). As in the previous case, we can see a tendency to converge on values below the failure criterion, less than for the Tsi-hill criterion, and we can state that from 6 plys at 45 degrees no values were found that failed the criterion, while in Tsi-hill this was only proven from 7 ply at 45 degrees, the value of 7 plys being extended in this same direction, as obtained in the Tsi-Hill version.

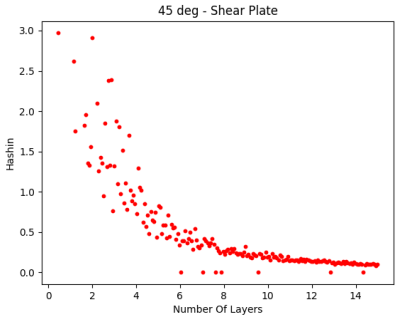

Figure 7.11: Hashin Failure Criteria - Plate in Shear for 45 degrees

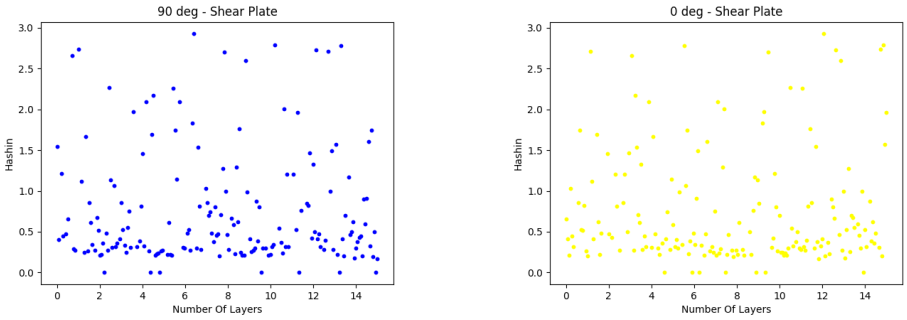

a) 90 degrees b) 0 degrees

Figure 7.12: Hashin Failure Criteria - Plate in Shear

7.3 ARX Skin Boom Optimization

After the validation and improvement of the genetic optimization tool in the previous sections, it was possible to start the optimization process in terms of orientation and number of layers of the last ARX construction iteration, obtained in Section 6.6. Since it would not be possible, for reasons of time, to carry out an individual optimization for all the structural components and different critical load cases, it was necessary to reduce the structure to the most critical section and load case. So, taking into account the analyses carried out in Chapter 6, we can easily identify the boom skin for load case Vd-, the critical point of the entire structure and the focus of our analysis. Bearing this in mind, before starting the optimization process, it's important to note that since the situation under analysis is symmetrical, the model was halved by applying a boundary condition to the central rib of the horizontal stabilizer on the XY plane (Figure 7.13).

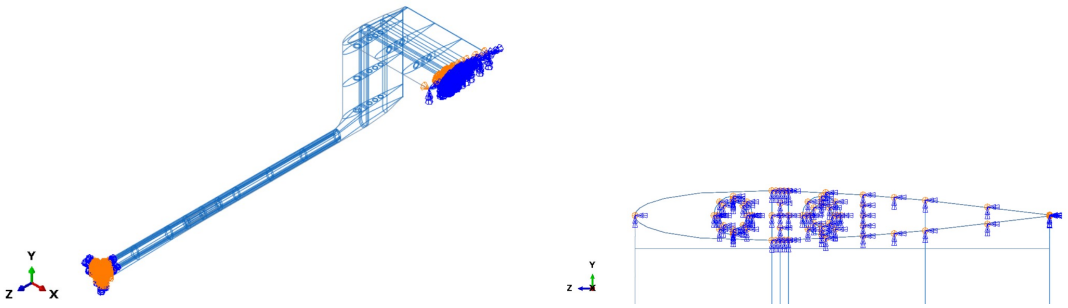

a) Isometic view b) Local View

Figure 7.13: Boundery conditions Symetric model

Maintaining all the other conditions previously presented in Chapter 5 allows the same analysis to be maintained, but with a smaller number of elements and a computational time per iteration of approximately 62% less.

With this in mind, the first step was to choose the analysis sections, since this will be one of the factors that most influences the final results of the optimization tool. Bearing in mind that the ARX will have the Boom divided into 2 sections, one at the front which is responsible for connecting the height to the main wing, and a second section at the rear which is responsible for connecting the vertical stabilizer to the first section of the Boom, it was considered pertinent to keep exactly this separation for our analysis. This allowed us to provide the company with feedback on the minimum number of plys in the respective preferred direction that each boom would have to contain in order to support the most critical load case for the boom's skin (Vd-). Thus, in Figure 7.14, we can see the aforementioned division, where the yellow region refers to the front boom, the blue region to the rear boom, and the grey region to the fixed sections that will not be used as variables in the optimization code, maintaining the configuration usually used up to now of 8 plys ([0,+-45,90]s).

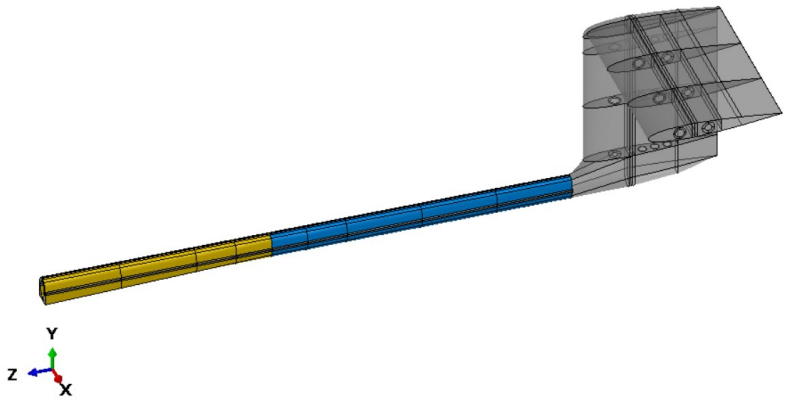

Figure 7.14: Analysis sections Front Boom (yellow) and Rear Boom (blue)

In Figure 7.15, we can also see the reference point that was taken into account for both analysis sections in the FEM model, which will be fundamental for us to be able to correctly interpret the results later on. We can see that the n-axis indicates the positive direction and that the 1-axis, which refers to the 0-degree orientation of the material, is in the direction of the length of the structure.

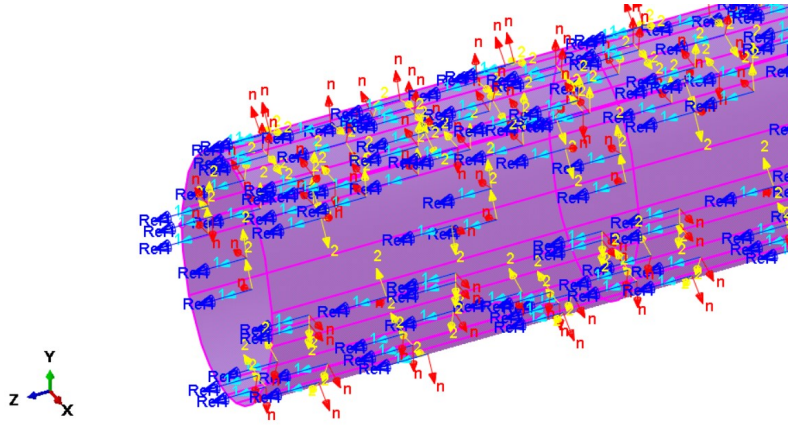

Figure 7.15: Fiber direction reference analysis section

7.3.1 Sampling parameters

Once the analysis sections had been defined and the reference orientation presented, the sampling criteria established for this analysis were defined, taking into account 3 analysis directions [0, 45, 90] and 2 sections, with a total of 6 independent variables. Looking at the reference theses [4],[3], where the optimization tool was initially applied, we could see that for the 4 analysis sections used, the value of 600 samples was not enough to obtain favorable results in the fuselage analysis carried out in [4], while the value of 2000 samples was enough to obtain a reasonable correlation in the main wing studied in [3]. Therefore, since the analysis case in this project includes only 2 analysis sections (the reference theses have 4 sections), the value of 700 samples for the initial iteration and 140 (representative of 20% of the initial samples) for the training values was considered reasonable. Finally, preliminary testing confirmed that the ideal number of layers would never exceed 3 plys, which allowed the upper limit for the Latin hypercube (LHS) to be set at 4 and the lower limit at 0.

7.3.2 Gaussian Regression Parameters

As for the Gaussian regression parameters, an iterative process of the Alpha, Lower boundary and Upper boundary parameters was taken into account in order to obtain the closest possible value to 1 for the R-squared metric and the closest value to 0 for the Average Mean Error metric, so as to be able to obtain the best possible regression, providing the genetic algorithm with the best possible basis for obtaining the optimal solutions.

Thus, the results obtained for the above metrics in the two analysis sections can be seen in Table 7.2, and the chosen parameters are shown below:

- Alpha = 0.1: This number limits predictions, especially when they are near to training data. It produces predictions that closely match the values observed in the training set.
- Upper boundary constant = 4: This constant sets the upper limit of the prediction range, affecting the greatest value that predictions can achieve.
- Lower boundary constant = 1e-10 sets the lower limit of the prediction range, preventing forecasts from approaching zero.

Table 7.2: Mean eror and R-squared value of each section of analysis

Sections	**R2s-0°**	**R2s-45°**	**R2s-90°**	**AME-0°**	**AME-45°**	**AME-90°**
Section1	0.8484	0.6737	0.8693	0.1303	0.0301	0.0231
Section2	0.7670	0.6649	0.6486	0.1022	0.1545	0.0898

7.3.3 Genetic Algorithmic Parameters

Following the completion of the Gaussian regression, the final step was to define the parameters of the improved genetic algorithm. This involved an iterative process of parameter testing in continuation of the improved method already explained in Section 7.2, seeking the best possible balance between computational resources and the final optimal result. Table 7.3 therefore shows a comparison between the computational time required to obtain the final optimal solution, using the parameters from the reference thesis [3] for the main wing skin and the parameters chosen for application in this project for the boom skin, bearing in mind that in both cases 2 bits per variable were taken into account, since preliminary testing confirmed that the value of layers would never exceed 3 plys.

Table 7.3: Genetic algorithmic parameters

Variable	Before	After
n	1000	100
Pc	0.9	0.6
Pg	0.2	0.3
Pm	0.2	0.3
Lamb	1	1
Tempo [s]	241	65

As a result, we can quickly see from the analysis carried out for the classic cases that the parameters chosen made it possible to obtain the same result for the optimal solution, in this case reducing the time required to obtain the same optimal solution by 73 %, validating the improvement implemented in more complex situations.

7.3.4 Skin Boom Optimization Results

After completing this process, it was then possible to obtain the optimum values for the number of layers and their preferred orientation for the skin of the bar in the case of Vd-load, with the genetic algorithm converging at iteration 102, indicating that a solution had been found that respected the projected objectives, in other words, the combination of layers and orientations that made it possible to have the lowest possible weight in the analysis sections without exceeding the failure criteria of the Hashin criterion. It was therefore possible to obtain the optimum solution from Table 7.4, and Appendix F shows the graphs of the number of layers versus the evaluation of the Hashin criterion, for each of the 3 directions [0,45,90] of section 1 and section 2.

Table 7.4: Optimized Layep skin of the Boom

Sections	**Nº of plyes - 0°**	**Nº of plyes - 45°**	**Nº of plyes - 90°**
Section 1	3	0	0
Section 2	2	0	0

Looking at the values obtained, we can quickly identify that both section 1 and section 2 have the angle of 0 degrees as their preferred direction, which is in line with what was expected, given that the stress induced by the load case Vd- in the structure is to a large extent a bending over the point of application of the boundary conditions, approximating a classic cantilever beam situation (Figure 7.16), the direction of the fibers aligned with the length of the Boom (0 degrees), guarantees better fiber performance. As for the number of plys, it is possible to observe a higher estimate for section 1, which is as expected since it proved to be a much more stressed region compared to section 2 throughout the analyses in chapter 6.

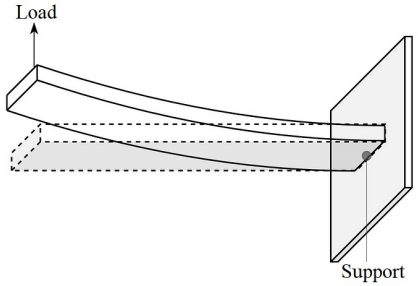

Figure 7.16: Schematic example cantilever beam

At this point, it is important to note that the optimization tool serves as a support for the designer, providing valuable information for more accurate and efficient decision making, so we can see in Table 7.5, the values of the different Hashin criteria for fiber and matrix for section 1 and section 2 under analysis, and in Figure 7.17 the visual representations refer to the highest evaluation criterion for both cases, which is close to the value of 0.8. Therefore, since the main factor in evaluating the merit of the population in the genetic code developed is to obtain a lower weight for a solution that respects the failure criterion, we can say that this would be the lightest solution for load case Vd-, which was proven by testing different decreases in the number of layers for section 1 and section 2 (e.g. 2 layers at 0 degrees section 1 and 2 layers at 0 degrees section 2), obtaining Hashin criteria greater than 1 in all cases.

Table 7.5: Hashin Failure criterion for optimized sections

Sections	**Matrix Tension**	**Matrix Compression**	**Fiber Tension**	**Fiber Compression**
Section 1	0.1294	0.1542	0.3266	0.8007
Section 2	0.3269	0.3093	0.4909	0.7653

In addition, since the composite used has a considerable thickness [0.25 mm], the decrease or increase of 1 ply creates a change in the analysis paradigm, making it difficult to approximate the material's failure limit.

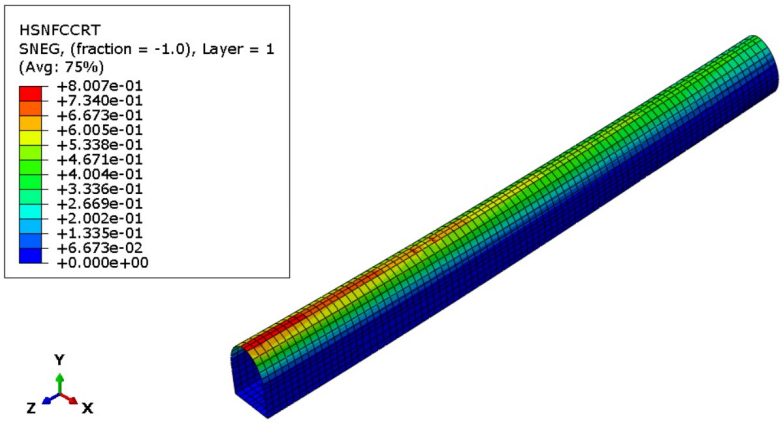

a) Section 1

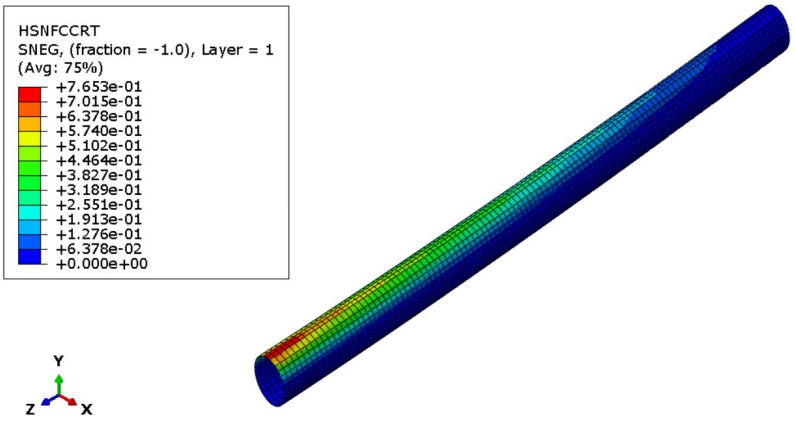

b) Section 2

Figure 7.17: Skin Boom Optimized regions

In a second analysis, we can also see in Figure 7.17, that both sections show the region of highest evaluation for the failure criterion in the central upper skin, which coincides with the reinforcement region of the stringers, so this can be a reference for the company, allowing it to apply the number of layers mentioned in the central region, looking into the possibility of reducing the number of layers of material in the sections between the reinforced stringers in future work.

To conclude the local analysis, it is important to note that the genetic code also tended to indicate plys for the 45 degree direction, especially for section 2, which is justified by the force generated by the vertical stabilizer on the rest of the structure, which is responsible for inducing a shear load on the surrounding areas, particularly section 2 of the boom. However, in terms of weight, this configuration proved to be less efficient, requiring more plys in order to meet the failure criterion, culminating in a value of 0 plys in the optimal solution. It is therefore important to point out that the solution obtained is subject to revision for the remaining load cases, with the expectation that there will be a need to increase the number of plys in the 90 degrees or 45 degrees direction in order to reinforce the structure in the transverse direction for load situations where the load induced by the vertical stabilizer and deflection of the Rudder control surface are greater.

Analyzing the structure in a general context, it can be seen that the reduction in the number of layers has resulted in a reduction in the structure's weight of approximately 2.15 [kg], with the final value of the optimized total structure being 38.05 [kg], which represents a reduction of [6.15 kg] compared to the first iteration analyses in Chapter 5 for the Tail and Boom structure reinforced by stringers.

As a final note, it is important to emphasis that since the initial ply configuration was maintained for the rest of the structure, there was no significant change in the Tail's stresses. It should also be noted that there was an increase in the structure's total deflection of approximately 1.2 [cm], compared to the last structural version presented in Chapter 6, which is insignificant compared to the weight gains achieved.

Chapter 8

Conclusions and future work

This work was carried out in the context of the development of the new Unmanned Aircraft developed by the company Tekever with a view to launch in 2025, in which the development of the tail and boom structure was intended, with the main focus on weight reduction while maintaining the structural reliability of the UAV, ensuring that the design met the various critical cases established by the ASTM F3116-18 standard for vertical and horizontal stabilizers. In addition, the aim of the second phase of the project was to validate and improve a heuristic algorithm optimization tool that began in the 2022/2023 academic year, to predict the minimum number of layers and the optimum orientations of the composite material fibres for the most critical structures identified, seeking to improve structural performance, reduce manufacturing costs and minimise the total weight of the ARX.

This work began with the successful conceptual study of the various types of twin-boom tails that could be applied to the ARX, followed by the respective conceptual studies of the various structural elements that make up the vertical stabilizers, horizontal stabilizers and Boom, culminating in iteration 1 structural which was later successfully refined to meet the company's manufacturing needs, concluding in 3 structural solutions.

After the conceptual phase was completed, the structural analysis phase began with the determination of the various critical load cases defined by the ASTM F3116-18 standard, culminating in the V-n diagram of the UAV and the respective calculation of the critical loads cases identified, using the XFLR5 software, as well as the calculation of the inertial loads. This allowed the finite element model to be modeled and validated, culminating in a comparison between the 3 structural solutions initially proposed, in which it was quickly concluded that the Boom reinforced by stringers would be the most efficient option, due to its lower weight and greater capacity to reinforce the skin that corresponded to the most critical region of the structure.

Following this, it was possible to start a structural optimization process in which it was possible to successfully study different positions for the main spar ([25/30/35]% chord), differences between spars with a C-profile flange and an I-profile flange, the possibility of using just 1 spar, the impact of reducing the Ribs of the vertical and horizontal stabilizer and comparisons between different thickness configurations for the I-profile. It was therefore possible to conclude that if 2 spars were to be used, the main spar in the 25% position of the chord would provide a good balance between reinforcing the structural elements of the Tail and the region of the transition skin between the vertical stabilizer and the boom, as well as offering greater scope for introducing hole regions in the Ribs due to the greater distance between spars.

However, directing the structure towards a situation where only 1 spar was used, it was possible to conclude that the position of the main spar at 35 % from the chord would be a better option, especially when combined with an I-profile flange, taking advantage of its greater static inertia to reinforce the structure, especially for load cases where the rudder control surface was deflected. With regard to the study of different configurations of the I-profile, it was possible to conclude that it would be more structurally advantageous to increase the thickness of the flange against the web, allowing for better reinforcement of the structure and less added weight. In the final phase, it was also possible to conclude, by reducing the Ribs of both the vertical stabilizer and the horizontal stabilizer, that their impact on the reinforcement of the structure was negligible, their main role being to support the weight of the constructive elements and avoid high deformation phenomena in the skin or buckling, allowing a structural solution to be achieved that was approximately 3.9 [kg] lighter than at the beginning of the study.

Finally, in the second phase of the project, it was possible to successfully validate and improve the optimization tool, implementing more precise failure criteria (Hashin and LARC05), improving the parameters and functioning of the genetic code used, allowing improvements of approximately 73% in terms of computational time and optimizing the simulation process, allowing the direct introduction of a CAE file, removing the need for manual programming of the FEM model, facilitating the implementation of the tool for more complex geometries and case studies. This culminated in the optimization of the most critical section of the structure developed for the respective critical load case, obtaining an optimal solution close to the failure of the material, and it was also possible to conclude that for this load case the preferred direction would be 0 degrees, requiring greater reinforcement of the boom section next to the main wing than the section next to the Tail, obtaining a final structure weighing 38.05 [kg] which represented an improvement of 6.15 [kg] compared to the initial iteration, allowing this project to be successfully completed.

As future work, it is important to highlight the need to apply the genetic algorithm to the other structural elements used (Ribs, spars, Formers), allowing for total optimization of the structure, in addition to evaluating the optimized solutions obtained with the help of the optimization tool for other critical load cases, namely those of deflection of the Rudder control surface, expecting, as in the example of the section under analysis in the project, a need to add plys at 90 or 45 degrees in order to be able to support loads in the transverse direction. In addition, it would be very important to improve the optimization tool for other fields, in order to find a balance between an optimal solution in terms of weight and other factors such as ease of manufacture, or the creation of reinforcement regions according to the regions of greatest demand, by modifying the way in which the objective function of the genetic code is defined. Finally, it is important to highlight the wide range of research possibilities in terms of fatigue of the most stressed areas of the Tail, such as the horizontal and vertical rib holes, which can not only design an efficient structure in terms of failure but also in terms of its fatigue resistance, taking optimization to the next level.

In conclusion, this work has successfully achieved its objectives, including the complete development of the new tail and boom structure for the Tekever UAV and the improvement of the computational tool making it more efficient and versatile to accommodate different constraints and exploit more advanced computational resources. As a result, an optimized structure was obtained, capable of guaranteeing structural integrity according to the parameters established in the ASTM F3116-18 standard and the manufacturing requirements established by the Tekever company. Thus, this approach not only sets a standard for structural efficiency and optimization of UAVs, but also lays the foundations for future advances at Tekever, allowing for even lighter solutions, improving the next generation of aircraft and making it a benchmark for technology and sustainability.

References

[1] TEKEVER . ARX. 2022. URL: https://www.tekever.com/projects/arx/.

[2] ASTM F3116/F3116M . Standard for Design Loads and Conditions. 2018. URL: https://cdn.standards.iteh.ai/samples/108102/dd0719212c75436cb9aee0e3820d0433/ASTM-F3116-F3116M-18e2.pdf.

[3] Nascimento DR. Optimization and analysis of uav wing for medical delivery 2023;.

[4] Arachchige DDS. Optimization and analysis of uav fuselage for medical deliveries 2023;.

[5] TEKEVER . Tekever's UAS used to survey the British Channel. 2021. URL: https://www.tekever.com/news/dsei-2021-tekevers-uas-used-to-survey-the-british-channel/.

[6] Geo Jobe . Multi-Rotor vs. Fixed Wing UAV Platforms: Considerations for Evaluating Capabilities and Limitations. 2021. URL: https://geo-jobe.com/drones-uav/multi-rotor-vs-fixed-wing-uav-platforms/.

[7] Boon M, Drijfhout A, Tesfamichael S. Comparison of a fixed-wing and multi-rotor uav for environmental mapping applications: A case study. The International Archives of the Photogrammetry, Remote Sensing and Spatial Information Sciences 2017;42:47–54.

[8] Telli K, Kraa O, Himeur Y, Ouamane A, Boumehraz M, Atalla S, et al. A comprehensive review of recent research trends on unmanned aerial vehicles (uavs). Systems 2023;11(8):400.

[9] TEKEVER . AR3. 2024. URL: https://www.tekever.com/models/ar3/; 14/02/2024.

[10] Misra A, Jayachandran S, Kenche S, Katoch A, Suresh A, Gundabattini E, et al. A review on vertical take-off and landing (vtol) tilt-rotor and tilt wing unmanned aerial vehicles (uavs). Journal of Engineering 2022;2022.

[11] Dalamagkidis K, Valavanis KP, Piegl LA, Dalamagkidis K, Valavanis KP, Piegl LA. Aviation history and unmanned flight. On Integrating Unmanned Aircraft Systems into the National Airspace System: Issues, Challenges, Operational Restrictions, Certification, and Recommendations 2012;:11–42.

[12] (EASA) EUASA. Concept of operations for drones: A risk based approach to regulation of unmanned aircraft. EASA Brochure 2019;:13doi:https://www.easa.europa.eu/en/document-library/general-publications/concept-operations-drones.

[13] Mitridis D, Kapsalis S, Terzis D, Panagiotou P. An evaluation of fixed-wing unmanned aerial vehicle trends and correlations with respect to nato classification, region, eis date and operational specifications. Aerospace 2023;10(4):382.

[14] TEKEVER . AR5. 2024. URL: https://www.tekever.com/models/ar5/; 14/02/2024.

References

[15] Northrop Grumman . RQ-4 Global Hawk. 2024. URL: https://www.northropgrumman.com/what-we-do/air/global-hawk.

[16] Mohammad Sadraey . Chapter 6-Tail Design. Daniel Webster College. URL: http://aero.us.es/adesign/Slides/Extra/Stability/Design_Tail/Chapter%206.%20Tail%20Design.pdf; 14/02/2024.

[17] Yayli UC, Kimet C, Duru A, Cetir O, Torun U, Aydogan AC, et al. Design optimization of a fixed wing aircraft. Advances in aircraft and spacecraft science 2017;4(1):65.

[18] Ariyanto M, Setiawan JD, Prabowo T, Haryanto I. Design of a low-cost fixed wing uav. In: MATEC Web of Conferences; vol. 159. EDP Sciences; 2018, p. 02045.

[19] Franco V. Design of a class i remotely piloted aircraft for maritime surveillance. Ph.D. thesis; Academia da Força Aérea; 2018.

[20] Nguyen D, Lowenberg M, Neild S. Derivation of control inputs for deep stall recovery using nonlinear frequency analysis. Aeronautical Journal -New Series- 2023;doi:10.1017/aer.2022.43.

[21] Ultralight Design . Design Concepts for Smaller Aircraft. 2017. URL: https://ultralightdesign.wordpress.com/2017/11/28/to-v-or-not-to-v/.

[22] Gudmundsson S. General aviation aircraft design: Applied Methods and Procedures. Butterworth-Heinemann; 2013.

[23] Nugroho G, Zuliardiansyah G, Rasyiddin AA. Performance analysis of empennage configurations on a surveillance and monitoring mission of a vtol-plane uav using a computational fluid dynamics simulation. Aerospace 2022;9(4):208.

[24] Portuguese Civil Aviation Authority (ANAC) . REGULAMENTO DE EXECUÇÃO (UE) 2019/947 DA COMISSÃO de 24 de maio de 2019. 2019. URL: https://eur-lex.europa.eu/legal-content/PT/TXT/HTML/?uri=CELEX:02019R0947-20200606&from=EN.

[25] Portuguese Civil Aviation Authority (ANAC) . Regulamento Delegado (UE) 2019/945 da Comissão, de 12 de março de 2019. 2019. URL: https://eur-lex.europa.eu/legal-content/PT/TXT/PDF/?uri=CELEX:02019R0945-20200809&from=EN.

[26] Laghari AA, Jumani AK, Laghari RA, Nawaz H. Unmanned aerial vehicles: A review. Cognitive Robotics 2023;3.

[27] Baker AA. Composite materials for aircraft structures. AIAA; 2004.

[28] Anand S, Mishra AK. High-performance materials used for uav manufacturing: Classified review. International Journal of All Research Education and Scientific Methods (IJARESM), ISSN 2022;:2455–6211.

[29] SÖNMEZ M, PELIN CE, GEORGESCU M, PELIN G, STELESCU MD, NITUICA M, et al. Unmanned aerial vehicles–classification, types of composite materials used in their structure and applications 2022;:1–6.

[30] Xiang T, Xia G, Zhang L. Mini-unmanned aerial vehicle-based remote sensing: techniques, applications, and prospects. Ieee Geoscience and Remote Sensing Magazine 2019;7:29–63. doi:10.1109/mgrs.2019.2918840.

[31] Goossens S. Barely visible impact damage detection in aerospace-grade carbon fibre reinforced polymer components with optical fibre sensors. Ph.D. thesis; Vrije Universiteit Brussel Brussels, Belgium; 2021.

[32] Bulut M, Erkliğ A, Yeter E. Experimental investigation on influence of kevlar fiber hybridization on tensile and damping response of kevlar/glass/epoxy resin composite laminates. Journal of Composite Materials 2015;50:1875–86. doi:10.1177/0021998315597552.

[33] Amiri A, Krosbakken T, Schoen W, Theisen D, Ulven C. Design and manufacturing of a hybrid flax/carbon fiber composite bicycle frame. Proceedings of the Institution of Mechanical Engineers Part P Journal of Sports Engineering and Technology 2017;232:28–38. doi:10.1177/1754337117716237.

[34] Starace F, Orlando S, Guida M, Marulo F. Experimental study of a virtual allowables approach for the design of composite aircraft structures. Proceedings of the Institution of Mechanical Engineers Part C Journal of Mechanical Engineering Science 2021;235:2529–41. doi:10.1177/0954406220987862.

[35] De Florio F. Airworthiness: An introduction to aircraft certification and operations. Butterworth-Heinemann; 2016.

[36] Butler R, Dodwell TJ, Haftka RT, Kim NH, Kim T, Kynaston S, et al. Uncertainty quantification of composite structures with defects using multilevel monte carlo simulations. In: 17th AIAA non-deterministic approaches conference. 2015, p. 1598.

[37] Dalamagkidis K, Valavanis KP, Piegl LA. On integrating unmanned aircraft systems into the national airspace system: issues, challenges, operational restrictions, certification, and recommendations. Springer; 2009.

[38] Hileman J, Spakovszky Z, Drela M, Sargeant M. Airframe design for" silent aircraft". In: 45th AIAA Aerospace Sciences Meeting and Exhibit. 2007, p. 453.

[39] Amirafshari P, Brenan F, Kolios A. A fracture mechanics framework for optimising design and inspection of offshore wind turbine support structures against fatigue failure. Wind Energy Science Discussions 2020;2020:1–31.

[40] Tavares S, De Castro P. An overview of fatigue in aircraft structures. Fatigue & Fracture of Engineering Materials & Structures 2017;40(10):1510–29.

[41] Swift T. Fail-safe design requirements and features, regulatory requirements. In: AIAA International Air and Space Symposium and Exposition: The Next 100 Years. 2003, p. 2783.

[42] Swift T. Damage tolerance capability. International Journal of Fatigue 1994;16(1):75–94.

[43] Rana S, Fangueiro R. Advanced composite materials for aerospace engineering: processing, properties and applications. Woodhead Publishing; 2016.

[44] Wang CH, Duong CN. Chapter 2 - failure criteria. In: Wang CH, Duong CN, editors. Bonded Joints and Repairs to Composite Airframe Structures. Oxford: Academic Press. ISBN 978-0-12-417153-4; 2016, p. 21–45. URL: https://www.sciencedirect.com/science/article/pii/B9780124171534000025. doi:https://doi.org/10.1016/B978-0-12-417153-4.00002-5.

[45] Aboudi J, Arnold S, Bednarcyk B. 4 - failure criteria and margins of safety. In: Aboudi J, Arnold S, Bednarcyk B, editors. Practical Micromechanics of Composite Materials. Butterworth-Heinemann. ISBN 978-0-12-820637-9; 2021, p. 161–214. URL: https:

//www.sciencedirect.com/science/article/pii/B9780128206379000088. doi:https://doi.org/10.1016/B978-0-12-820637-9.00008-8.

[46] Staab GH. 5 - lamina failure theories. In: Staab GH, editor. Laminar Composites (Second Edition); second edition ed. Butterworth-Heinemann. ISBN 978-0-12-802400-3; 2015, p. 139–87. URL: https://www.sciencedirect.com/science/article/pii/B9780128024003000052. doi:https://doi.org/10.1016/B978-0-12-802400-3.00005-2.

[47] Ziadoon A, Chwei Z. Effect the stacking sequences of composite laminates under low velocity impact on failure modes by using carbon fiber reinforced polymer. Int J Eng Sci 2016;5(2):53–62.

[48] Davila CG, Camanho PP, Rose CA. Failure criteria for frp laminates. Journal of Composite materials 2005;39(4):323–45.

[49] Nali P, Carrera E. A numerical assessment on two-dimensional failure criteria for composite layered structures. Composites Part B: Engineering 2012;43(2):280–9.

[50] Hinton M. Failure criteria in fibre reinforced polymer composites: the world-wide failure exercise. Elsevier; 2004.

[51] Davila C, Jaunky N, Goswami S. Failure criteria for frp laminates in plane stress. In: 44th AIAA/ASME/ASCE/AHS/ASC structures, structural dynamics, and materials conference. 2003, p. 1991.

[52] Grasso A. Implementation of classical and advanced failure criteria for composite layered structures in femap and assessment of results. Ph.D. thesis; Politecnico di Torino; 2018.

[53] ABAQUS . Damage initiation for fiber-reinforced composites. 2022. URL: https://docs.software.vt.edu/abaqusv2022/English/SIMACAEMATRefMap/simamat-c-damageinitfibercomposite.htm.

[54] Sigmund O, Bondsgc M. Topology optimization. State-of-the-Art and Future Perspectives, Copenhagen: Technical University of Denmark (DTU) 2003;.

[55] Virtualcae . Virtual.PYXIS. 2022. URL: https://virtualcae.com.br/nossos-softwares/virtual-pyxis/.

[56] Formlabs . Topology Optimization 101: How to Use Algorithmic Models to Create Lightweight Design. 2024. URL: https://formlabs.com/eu/blog/topology-optimization/.

[57] Zhou M, Fleury R, Kemp M. Optimization of composite-recent advances and application. In: 13th AIAA/ISSMO multidisciplinary analysis optimization conference. 2010, p. 9272.

[58] Ansys . Ansys optiSLang Process Integration Design Optimization. 2022. URL: https://www.ansys.com/products/connect/ansys-optislang.

[59] Dassault Systemes . Isight the SIMULIA Execution Engine. 2022. URL: https://www.3ds.com/products/simulia/isight.

[60] Altair . Altair OptiStruct. 2022. URL: https://altair.com/optistruct-applications.

[61] António CAC. Otimização de sistemas em engenharia-fundamentos e algoritmos para o projeto ótimo 2020;.

[62] Koza J. Genetic programming as a means for programming computers by natural selection. Statistics and Computing 1994;4. doi:10.1007/bf00175355.

[63] Fischer S, Oliveira J, Mumford J, Kell L. Using a genetic algorithm to optimize a data-limited catch rule. Ices Journal of Marine Science 2021;78:3013–4. doi:10.1093/icesjms/fsab070.

[64] Mirjalili S, Mirjalili S. Genetic algorithm. Evolutionary Algorithms and Neural Networks: Theory and Applications 2019;:43–55.

[65] Zhou Y, Kang J, Zhang X. A cooperative coevolutionary approach to discretization-based feature selection for high-dimensional data. Entropy 2020;22:613. doi:10.3390/e22060613.

[66] Lambora A, Gupta K, Chopra K. Genetic algorithm-a literature review. In: 2019 international conference on machine learning, big data, cloud and parallel computing (COMITCon). IEEE; 2019, p. 380–4.

[67] Audet C, Denni J, Moore D, Booker A, Frank P. A surrogate-model-based method for constrained optimization. In: 8th symposium on multidisciplinary analysis and optimization. 2000, p. 4891.

[68] Koziel S, Ciaurri DE, Leifsson L. Surrogate-based methods. Computational optimization, methods and algorithms 2011;:33–59.

[69] Forrester A, Sobester A, Keane A. Engineering design via surrogate modelling: a practical guide. John Wiley & Sons; 2008.

[70] Alizadeh R, Allen JK, Mistree F. Managing computational complexity using surrogate models: a critical review. Research in Engineering Design 2020;31:275–98.

[71] Condra L. Reliability improvement with design of experiment. Crc Press; 2018.

[72] Afzal A, Kim KY, Seo Jw. Effects of latin hypercube sampling on surrogate modeling and optimization. International Journal of Fluid Machinery and Systems 2017;10(3):240–53.

[73] Preece R, Milanović JV. Efficient estimation of the probability of small-disturbance instability of large uncertain power systems. IEEE Transactions on Power Systems 2015;31(2):1063–72.

[74] Li CQ, Yang W. Time-dependent reliability theory and its applications. Elsevier; 2022.

[75] Youssef SA, Paik JK, Kim YS, Kim MS, Cheng F. Probabilistic selection of ship-ship collision scenarios. In: International Conference on Offshore Mechanics and Arctic Engineering; vol. 55324. American Society of Mechanical Engineers; 2013, p. V02AT02A027.

[76] Cozad A, Sahinidis NV, Miller DC. Learning surrogate models for simulation-based optimization. AIChE Journal 2014;60(6):2211–27.

[77] Ryan TP. Modern regression methods; vol. 655. John Wiley & Sons; 2008.

[78] Young DS. Handbook of regression methods. CRC Press; 2018.

[79] Su X, Yan X, Tsai CL. Linear regression. Wiley Interdisciplinary Reviews: Computational Statistics 2012;4(3):275–94.

[80] Groß J. Linear regression; vol. 175. Springer Science & Business Media; 2003.

[81] scikit-learn . Regression-Linear Models. 2024. URL: https://scikit-learn.org/stable/modules/linear_model.html#regression.

[82] McDonald GC. Ridge regression. Wiley Interdisciplinary Reviews: Computational Statistics 2009;1(1):93–100.

[83] Ranstam J, Cook J. Lasso regression. Journal of British Surgery 2018;105(10):1348–.

[84] Madhuri CR, Anuradha G, Pujitha MV. House price prediction using regression techniques: A comparative study. In: 2019 International conference on smart structures and systems (ICSSS). IEEE; 2019, p. 1–5.

[85] Raymer D. Aircraft design: a conceptual approach. American Institute of Aeronautics and Astronautics, Inc.; 2012.

[86] Raymer D. Aircraft design: a conceptual approach. American Institute of Aeronautics and Astronautics, Inc.; 2012.

[87] Sadraey MH. Aircraft design: A systems engineering approach. John Wiley & Sons; 2012.

[88] Roskam J, Lan CTE. Airplane aerodynamics and performance. DARcorporation; 1997.

[89] Khadka S, Abeygoonewardene J, Liyanage N. Conceptual design of boom mounted inverted v-tail in the searcher mk ii uav 2020;.

[90] Coelho V. Aerodynamic detailed design of an unmanned aerial vehicle with vtol capabilities. Ph.D. thesis; Academia da Força Aérea; 2021.

[91] Antonio CRV, Yan S. Preliminary design and performance-stability analysis of a fixed-wing uav using xflr5 2023;.

[92] Mouritz AP. Introduction to aerospace materials. Elsevier; 2012.

[93] Abbott, Richard . Analysis and design of composite and metallic flight vehicle structures -THIRD EDITION. 2019. URL: https://www.abbottaerospace.com/aa-sb-001/.

[94] Federal Aviation Administration . Aircraft Maintenance Handbook: Volume.1. 2012. URL: https://www.abbottaerospace.com/downloads/faa-h-8083-31-2-aircraft-maintenance-handbook-vol-1/.

[95] Kaur R, Ambri A. Spars and stringers-function and designing. Int J Aerosp Mech Eng 2014;1(1):58–61.

[96] Carta F, Pirondi A. Damage tolerance analysis of aircraft reinforced panels. Frattura ed Integrità Strutturale 2011;5(16):34–42.

[97] Airfoil Tools . NACA 0012 AIRFOILS (n0012-il). 2024. URL: http://airfoiltools.com/airfoil/details?airfoil=n0012-il#polars.

[98] Güzelbey IH, Eraslan Y, DOĞRU MH. Numerical investigation of different airfoils at low reynolds number in terms of aerodynamic performance of sailplanes by using xflr5. Karadeniz Fen Bilimleri Dergisi 2018;8(1):47–65.

[99] ABAQUS version 6.6 Documentation . Define a distributing coupling constraint. 2024. URL: https://classes.engineering.wustl.edu/2009/spring/mase5513/abaqus/docs/v6.6/books/key/default.htm?startat=ch04abk25.html#usb-kws-mdistributing.

APPENDIX

Appendix A

XFLR5 Load Cases Results Horizontal Stabilizer

Table A.1: Cl, Cd and Cm along the semi-span of Horizontal stabilizer- XFLR5 data for Vd+

Span [mm]	CL	CD	Cm@25%c
0	-0.299	0.000476	0.077668
0.025	-0.299	0.000476	0.077668
0.075	-0.29869	0.00049	0.077632
0.125	-0.29807	0.000518	0.077558
0.175	-0.29712	0.000561	0.077442
0.225	-0.29584	0.000621	0.07728
0.275	-0.2942	0.000699	0.077063
0.325	-0.29217	0.0008	0.076777
0.375	-0.28972	0.000929	0.076401
0.425	-0.28679	0.001182	0.075927
0.4738	-0.28278	0.000839	0.074613
0.5212	-0.2791	0.001296	0.074088
0.5687	-0.27458	0.001496	0.073275
0.6162	-0.2692	0.001706	0.072223
0.6638	-0.26279	0.001932	0.070857
0.7113	-0.25507	0.002177	0.069064
0.7588	-0.24565	0.002439	0.066672
0.8063	-0.23392	0.002709	0.06341
0.8538	-0.21885	0.002967	0.058835
0.9013	-0.19858	0.00316	0.052141
0.9487	-0.16908	0.003152	0.041661
0.9963	-0.11912	0.002522	0.023305
1.02	-0.11912	0.002522	0.023305

Table A.2: Cl, Cd and Cm along the semi-span of Horizontal stabilizer- XFLR5 data for Rudder Vd

Span [mm]	CL	CD	Cm@25%c
-1.02	0.171758	0.012122	-0.005884
-0.9963	0.171758	0.012122	-0.005884
-0.9487	0.22293	0.015514	-0.015729
-0.9013	0.252776	0.017116	-0.020486
-0.8538	0.275592	0.018149	-0.023933
-0.8063	0.294617	0.018885	-0.026747
-0.7588	0.311033	0.019427	-0.029114
-0.7113	0.325428	0.01983	-0.031119
-0.6638	0.338164	0.020131	-0.032823
-0.6162	0.349494	0.020353	-0.034271
-0.5687	0.359605	0.020508	-0.035506
-0.5212	0.368646	0.020605	-0.036561
-0.4738	0.376712	0.020501	-0.03743
-0.425	0.3845	0.020876	-0.038627
-0.375	0.391378	0.020893	-0.039373
-0.325	0.397482	0.020901	-0.039999
-0.275	0.402902	0.020905	-0.040528
-0.225	0.407703	0.020905	-0.04098
-0.175	0.411931	0.0209	-0.041368
-0.125	0.415627	0.020891	-0.041702
-0.075	0.418824	0.020877	-0.04199
-0.025	0.421547	0.020859	-0.042238
0.025	0.423819	0.020839	-0.042451
0.075	0.425656	0.020815	-0.042634
0.125	0.427069	0.020789	-0.04279
0.175	0.428066	0.020761	-0.042923
0.225	0.428645	0.020732	-0.043035
0.275	0.4288	0.020706	-0.043127
0.325	0.428513	0.020685	-0.043196
0.375	0.427745	0.020674	-0.04323
0.425	0.426407	0.020651	-0.043209
0.4738	0.424298	0.020246	-0.042807
0.5212	0.42207	0.020438	-0.042832
0.5687	0.419087	0.020437	-0.042766
0.6162	0.415233	0.020425	-0.042616
0.6638	0.410291	0.020417	-0.042332
0.7113	0.403938	0.020431	-0.04183
0.7588	0.395673	0.020484	-0.040971
0.8063	0.384698	0.020598	-0.039513
0.8538	0.36967	0.020782	-0.037033
0.9013	0.348136	0.020955	-0.032757
0.9487	0.314514	0.020606	-0.024967
0.9963	0.246435	0.017185	-0.006663
1.02	0.246435	0.017185	-0.006663

Table A.3: Cl, Cd and Cm along the semi-span of Horizontal stabilizer- XFLR5 data for Va-

Span [mm]	CL	CD	Cm@25%c
0	1.428533	0.170153	-0.232459
0.025	1.428533	0.170153	-0.232459
0.075	1.427033	0.17021	-0.23231
0.125	1.424021	0.170324	-0.232009
0.175	1.419476	0.170493	-0.231557
0.225	1.413372	0.170721	-0.230957
0.275	1.405704	0.171033	-0.230228
0.325	1.396565	0.171591	-0.229458
0.375	1.386539	0.173835	-0.229033
0.425	1.380625	0.219212	-0.231999
0.4738	1.336912	0.11041	-0.212407
0.5212	1.330757	0.174666	-0.217738
0.5687	1.31242	0.174483	-0.216486
0.6162	1.289488	0.173927	-0.213837
0.6638	1.262427	0.1734	-0.21032
0.7113	1.230713	0.172611	-0.205905
0.7588	1.193323	0.171277	-0.200379
0.8063	1.148609	0.169033	-0.193363
0.8538	1.093771	0.165245	-0.18418
0.9013	1.023356	0.158418	-0.171433
0.9487	0.924047	0.143134	-0.151491
0.9963	0.748017	0.086103	-0.111995
1.02	0.7	0.086103	-0.111995

Table A.4: Cl, Cd and Cm along the semi-span of Horizontal stabilizer- XFLR5 data for Va+

Span [mm]	CL	CD	Cm@25%c
0	-1.25491	0.097683	0.23278
0.025	-1.25491	0.097683	0.23278
0.075	-1.25327	0.097814	0.232611
0.125	-1.24996	0.098075	0.232268
0.175	-1.24494	0.098469	0.231742
0.225	-1.23816	0.099	0.231023
0.275	-1.22956	0.099688	0.230108
0.325	-1.21913	0.10065	0.229041
0.375	-1.20727	0.102886	0.228105
0.425	-1.19791	0.135973	0.229795
0.4738	-1.15654	0.059393	0.212063
0.5212	-1.14521	0.106109	0.2153
0.5687	-1.12247	0.106936	0.212544
0.6162	-1.09421	0.10757	0.208035
0.6638	-1.06036	0.108207	0.201999
0.7113	-1.01982	0.108543	0.194103
0.7588	-0.97084	0.108206	0.183732
0.8063	-0.91073	0.106641	0.169943
0.8538	-0.83539	0.102929	0.151326
0.9013	-0.73807	0.095507	0.125766
0.9487	-0.60658	0.081597	0.090132
0.9963	-0.41283	0.054925	0.039835
1.02	-0.41283	0.054925	0.039835

Table A.5: Cl, Cd and Cm along the semi-span of Horizontal stabilizer- XFLR5 data for Rudder Va

Span [mm]	CL	CD	Cm@25%c
-1.02	0.030548	0.002756	-0.00251
-0.9963	0.030548	0.002756	-0.00251
-0.9487	0.050991	0.002756	-0.00251
-0.9013	0.070112	0.003775	-0.00444
-0.8538	0.088372	0.004723	-0.00694
-0.8063	0.105725	0.005578	-0.00957
-0.7588	0.12209	0.006331	-0.01211
-0.7113	0.137428	0.00698	-0.01447
-0.6638	0.151742	0.007531	-0.0166
-0.6162	0.165063	0.007993	-0.01851
-0.5687	0.177442	0.008375	-0.02021
-0.5212	0.188946	0.008685	-0.02171
-0.4738	0.199667	0.008927	-0.02305
-0.425	0.209928	0.009174	-0.02444
-0.375	0.219641	0.009371	-0.02557
-0.325	0.228659	0.009506	-0.02656
-0.275	0.237068	0.009611	-0.02743
-0.225	0.244935	0.009691	-0.02822
-0.175	0.252317	0.009748	-0.02893
-0.125	0.259268	0.009785	-0.02959
-0.075	0.265837	0.009804	-0.03021
-0.025	0.272068	0.009806	-0.0308
0.025	0.278001	0.009793	-0.03136
0.075	0.283672	0.009765	-0.03192
0.125	0.289111	0.009722	-0.03247
0.175	0.294341	0.009666	-0.03304
0.225	0.299378	0.009597	-0.03362
0.275	0.304227	0.009517	-0.03422
0.325	0.308876	0.009429	-0.03484
0.375	0.313275	0.009334	-0.03547
0.425	0.317282	0.009139	-0.03604
0.4738	0.320898	0.008988	-0.0365
0.5212	0.324048	0.008911	-0.03709
0.5687	0.326522	0.008854	-0.0376
0.6162	0.327992	0.00884	-0.03792
0.6638	0.327981	0.008921	-0.03786
0.7113	0.32578	0.009174	-0.03714
0.7588	0.320322	0.009708	-0.03531
0.8063	0.310084	0.01064	-0.03169
0.8538	0.293174	0.011971	-0.02546
0.9013	0.268087	0.013256	-0.01621
0.9487	0.234693	0.013436	-0.00494
0.9963	0.185568	0.011094	-0.00494
1.02	0.185568	0.011094	-0.00494

Appendix B

Aero loads FEM model Horizontal Stabilizer

Table B.1: Aerodynamic Loads equivalent for the Finite Element Model - Load case Vd+

Main spar at 30% of chord	Rib1	Rib2	Rib3	Rib4	Rib5	Rib6	Rib7
VZ1 CS H	11.61874	11.59657	11.46441	11.02857	10.12365	7.668981	1.296668
VZ1 CS V	145.3373	145.7046	146.6305	144.7916	141.1872	120.0942	30.00702
VZ2 CS V	-384.713	-383.93	-380.69	-370.287	-351.642	-300.03	-92.9367
VZ2 CS H	-31.7779	-31.7132	-31.4456	-30.5863	-29.0462	-24.783	-7.67672

Table B.2: Aerodynamic Loads equivalent for the Finite Element Model - Load case rudder Vd

Main spar at 30% of chord	Rib1	Rib2	Rib3	Rib4	Rib5	Rib6	Rib7	Rib8	Rib9	Rib10	Rib11	Rib12	Rib13
VZ1 CS H	-1.14253	-4.69259	-5.3796	-5.10306	-4.76766	-4.25186	-3.918773219	-3.73348	-3.73398	-3.78946	-4.46498	-5.22279	-1.3126
VZ1 CS V	57.98493	122.9989	131.2129	139.6509	146.2927	152.4689	156.0750537	157.622	156.7941	153.7128	145.3915	138.6284	79.24128
VZ2 CS V	25.49635	106.1379	141.6337	161.3883	173.9614	180.3587	183.7407442	185.9086	187.5715	186.7641	184.4289	163.1104	39.76006
VZ2 CS H	2.106038	8.767153	11.69916	13.33092	14.36948	14.8979	15.1772695	15.35633	15.49369	15.427	15.23411	13.47317	3.284242

Table B.3: Aerodynamic Loads equivalent for the Finite Element Model - Load case Va-

Main spar at 30% of chord	Rib1	Rib2	Rib3	Rib4	Rib5	Rib6	Rib7
VZ1 CS H	-47.0148	-47.1403	-47.7588	-46.7753	-48.5214	-46.66044	-17.51579164
VZ1 CS V	18.93042	18.03663	14.01568	15.74206	8.44994	4.407199	7.194837336
VZ2 CS V	386.3835	385.3428	382.8485	365.6881	350.5204	313.2524	118.2966162
VZ2 CS H	22.59676	22.53589	22.39002	21.38643	20.49939	18.31985	6.918306499

Table B.4: Aerodynamic Loads equivalent for the Finite Element Model - Load case Va+

Main spar at 30% of chord	Rib1	Rib2	Rib3	Rib4	Rib5	Rib6	Rib7
VZ1 CS H	-25.2266	-25.3414	-26.5137	-25.5436	-27.9299	-27.7729	-11.4773
VZ1 CS V	41.13845	42.0658	45.85359	43.25092	44.27016	24.43441	-13.4627
VZ2 CS V	-393.096	-391.876	-388.144	-368.438	-341.585	-267.22	-66.1957
VZ2 CS H	-22.9893	-22.918	-22.6997	-21.5472	-19.9768	-15.6278	-3.8713

Table B.5: Aerodynamic Loads equivalent for the Finite Element Model - Load case Rudder Va

Main spar at 30% of chord	Rib1	Rib2	Rib3	Rib4	Rib5	Rib6	Rib7	Rib8	Rib9	Rib10	Rib11	Rib12	Rib13
VZ1 CS H	-0.19971	-0.40256	-1.00658	-1.30703	-1.36266	-1.26235	-1.10204	-0.92783	-0.76663	-0.60751	-0.60019	-0.65791	-0.09982
VZ1 CS V	3.277181	13.96058	16.64938	19.05684	21.99188	25.38252	28.5225	31.00122	32.51582	33.13997	33.3526	43.33736	28.66414
VZ2 CS V	1.750688	8.692352	22.64406	33.32797	40.46036	44.98283	48.25824	51.19537	54.38481	57.58737	58.82527	40.97364	3.228421
VZ2 CS H	0.102385	0.508352	1.324286	1.94911	2.366231	2.630718	2.822273	2.994044	3.180571	3.367866	3.440261	2.39625	0.188807

Appendix C

XFLR5 Load Cases Results Vertical Stabilizer

Table C.1: Cl, Cd and Cm along the semi-span of Vertical stabilizer- XFLR5 data for Vd-

Span [mm]	CL	CD	Cm@25%c
1.0066	-0.02275	0.005069	0
1.0347	-0.02275	0.005069	0
1.0603	-0.03908	0.005069	0
1.1076	-0.0563	0.005068	0
1.1695	-0.07348	0.005066	0
1.2365	-0.09008	0.005065	0
1.2984	-0.10507	0.005064	0
1.3457	-0.11702	0.005062	0
1.3713	-0.12465	0.005062	0
1.3999	-0.1328	0.005061	0
1.4436	-0.14458	0.005059	0
1.4874	-0.15692	0.005057	0
1.5311	-0.16981	0.005054	0
1.5749	-0.18331	0.00505	0
1.6186	-0.1975	0.005046	0
1.6624	-0.21248	0.005042	0
1.7061	-0.22843	0.005038	0
1.7494	-0.24569	0.005033	0
1.7921	-0.26585	0.005035	0
1.8349	-0.29543	0.00504	0
1.8776	0.005329	0.005044	0

Table C.2: Cl, Cd and Cm along the semi-span of Vertical stabilizer- XFLR5 data for Vd+

Span [mm]	CL	CD	Cm@25%c
1.0066	0.014201	0.005069	0
1.0347	0.014201	0.005069	0
1.0603	0.024434	0.005069	0
1.1076	0.03489	0.005068	0
1.1695	0.04438	0.005066	0
1.2365	0.052505	0.005065	0
1.2984	0.059045	0.005064	0
1.3457	0.063802	0.005062	0
1.3713	0.066652	0.005062	0
1.3999	0.069655	0.005061	0
1.4436	0.073682	0.005059	0
1.4874	0.077603	0.005057	0
1.5311	0.081377	0.005054	0
1.5749	0.084968	0.00505	0
1.6186	0.088299	0.005046	0
1.6624	0.091222	0.005042	0
1.7061	0.093458	0.005038	0
1.7494	0.094473	0.005033	0
1.7921	0.093302	0.005035	0
1.8349	0.087695	0.00504	0
1.8776	0.071015	0.005044	0

Table C.3: Cl, Cd and Cm along the semi-span of Vertical stabilizer- XFLR5 data for rudder Vd

Span [mm]	CL	CD	Cm@25%c
-1.8555	0.01783	0.001196	0
-1.7685	0.01783	0.001196	0
-1.7033	0.01783	0.001196	0
-1.6599	0.038605	0.002497	0
-1.6166	0.060747	0.003844	0
-1.5732	0.079959	0.004956	0
-1.5298	0.096004	0.005834	0
-1.4864	0.109159	0.006517	0
-1.4431	0.119702	0.007038	0
-1.3997	0.127831	0.007399	0
-1.3713	0.133292	0.009232	0
-1.3457	0.135323	0.007852	0
-1.2984	0.138128	0.00803	0
-1.2365	0.137247	0.00807	0
-1.1695	0.129106	0.007788	0
-1.1076	0.11123	0.006955	0
-1.0603	0.083351	0.00538	0
-1.0347	0.050183	0.002933	0
-0.9845	0.050183	0.002933	0
0.9845	-0.07987	0.00341	0
1.0347	-0.07987	0.00341	0
1.0603	-0.13413	0.006972	0
1.1076	-0.18464	0.009018	0
1.1695	-0.22547	0.01018	0
1.2365	-0.25618	0.010778	0
1.2984	-0.27769	0.011113	0
1.3457	-0.29165	0.011347	0
1.3713	-0.30202	0.02002	0
1.3997	-0.30517	0.011395	0
1.4431	-0.31249	0.011947	0
1.4864	-0.31774	0.012373	0
1.5298	-0.32014	0.012868	0
1.5732	-0.3184	0.013458	0
1.6166	-0.30969	0.014095	0
1.6599	-0.28634	0.014326	0
1.7033	-0.21916	0.011632	0
1.7685	-0.26676	0.011632	0
1.8555	-0.39456	0.011632	0

Table C.4: Cl, Cd and Cm along the semi-span of Vertical stabilizer- XFLR5 data for Va-

Span [mm]	CL	CD	Cm@25%c
1.0066	-0.06186	0.005068	0
1.0347	-0.06186	0.005068	0
1.0603	-0.10632	0.005068	0
1.1076	-0.15299	0.005068	0
1.1695	-0.19873	0.005068	0
1.2365	-0.24211	0.005069	0
1.2984	-0.28075	0.005069	0
1.3457	-0.31137	0.005069	0
1.3713	-0.33084	0.005069	0
1.3999	-0.35173	0.00507	0
1.4436	-0.38191	0.00507	0
1.4874	-0.41369	0.005071	0
1.5311	-0.44715	0.005071	0
1.5749	-0.48267	0.005072	0
1.6186	-0.52082	0.005072	0
1.6624	-0.56265	0.005073	0
1.7061	-0.61065	0.005074	0
1.7494	-0.61938	0.005074	0
1.7921	0.020323	0.005075	0
1.8349	0.103242	0.005077	0
1.8776	0.092773	0.00508	0

Table C.5: Cl, Cd and Cm along the semi-span of Vertical stabilizer- XFLR5 data for Va+

Span [mm]	CL	CD	Cm@25%c
1.0066	0.040733	0.005068	0
1.0347	0.040733	0.005068	0
1.0603	0.069963	0.005068	0
1.1076	0.1	0.005068	0
1.1695	0.127998	0.005068	0
1.2365	0.152778	0.005069	0
1.2984	0.173244	0.005069	0
1.3457	0.18834	0.005069	0
1.3713	0.197439	0.005069	0
1.3999	0.206965	0.00507	0
1.4436	0.219734	0.00507	0
1.4874	0.231994	0.005071	0
1.5311	0.243484	0.005071	0
1.5749	0.253924	0.005072	0
1.6186	0.262867	0.005072	0
1.6624	0.269591	0.005073	0
1.7061	0.272915	0.005074	0
1.7494	0.270876	0.005074	0
1.7921	0.260331	0.005075	0
1.8349	0.234707	0.005077	0
1.8776	0.177465	0.00508	0

Table C.6: Cl, Cd and Cm along the semi-span of Vertical stabilizer- XFLR5 data for rudder Va

Span [mm]	CL	CD	Cm@25%c
-1.8555	0.015918	-3E-06	0
-1.7685	0.029143	0.000078	0
-1.7033	0.264992	0.045629	0
-1.6599	0.380259	0.065967	0
-1.6166	0.453691	0.076506	0
-1.5732	0.504617	0.082457	0
-1.5298	0.540853	0.085867	0
-1.4864	0.566428	0.087667	0
-1.4431	0.58382	0.088134	0
-1.3997	0.594719	0.08038	0
-1.3713	0.646597	0.219022	0
-1.3457	0.60098	0.092555	0
-1.2984	0.583362	0.087871	0
-1.2365	0.554648	0.085846	0
-1.1695	0.503028	0.080864	0
-1.1076	0.422148	0.070573	0
-1.0603	0.312517	0.052218	0
-1.0347	0.194093	0.012208	0
-0.9845	0.194093	0.012208	0
0.9845	-0.20618	0.010563	0
1.0347	-0.20618	0.010563	0
1.0603	-0.33288	0.05353	0
1.1076	-0.45214	0.072628	0
1.1695	-0.54308	0.083383	0
1.2365	-0.60465	0.088768	0
1.2984	-0.64249	0.091203	0
1.3457	-0.66795	0.097169	0
1.3713	-0.72327	0.255991	0
1.3997	-0.66911	0.083264	0
1.4431	-0.66338	0.09415	0
1.4864	-0.65072	0.095036	0
1.5298	-0.62879	0.094604	0
1.5732	-0.59408	0.092466	0
1.6166	-0.54068	0.087252	0
1.6599	-0.45725	0.075963	0
1.7033	-0.31845	0.051897	0
1.7685	-0.17544	-0.00047	0
1.8555	-0.26469	-0.00521	0

Appendix D

Aero Loads FEM model Vertical Stabilizer

Table D.1: Aerodynamic Loads equivalent for the Finite Element Model - Load Vd+

Main spar at 30% of chord	Rib1	Rib2	Rib3	Rib4	Rib5
VZ1 CS V	4.856917	30.68284	75.5241	102.8624	89.9697
VZ1 CS H	-1.22207	-4.016274	-5.584284	-5.571479	-4.420857
VZ2 CS V	-0.53966	-3.4092	-8.39157	-11.4292	-9.99663

Table D.2: Aerodynamic Loads equivalent for the Finite Element Model - Load case Rudder Vd

Main spar at 30% of chord	Rib1	Rib2	Rib3	Rib4	Rib5
VZ1 CS V Left	-25.4019	-180.9625143	-358.3924	-378.3376206	-296.123
VZ1 CS H Left	-1.0403	-7.360324226	-13.7713949	-14.58808151	-10.28111
VZ2 CS V Left	2.822432	20.10694603	39.8213773	42.0375134	32.90259
VZ1 CS V Right	22.68713	113.4458059	165.67863	86.15871798	13.61152
VZ1 CS H Right	-1.331334	-6.099266179	-8.85353519	-4.742162456	-0.707162
VZ2 CS V Right	-2.52079	-12.60508954	-18.408737	-9.573190887	-1.51239

Table D.3: Aerodynamic Loads equivalent for the Finite Element Model - Load case Va+

Main spar at 30% of chord	Rib1	Rib2	Rib3	Rib4	Rib5
VZ1 CS V	4.160711	31.0006	78.1255	107.7049	89.17089
VZ1 CS H	-0.429227	-1.411081	-1.9642	-1.965121	-1.564707
VZ2 CS V	-0.4623	-3.44451	-8.68061	-11.9672	-9.90788

Table D.4: Aerodynamic Loads equivalent for the Finite Element Model - Load Va-

Main spar at 30% of chord	Rib1	Rib2	Rib3	Rib4	Rib5
VZ1 CS V	-6.31945	-47.7792	-128.827	-204.174	-103.549
VZ1 CS H	-0.429227	-1.411081	-1.9642	-1.965121	-1.564707
VZ2 CS V	0.702161	5.308803	14.31411	22.68599	11.50549

Table D.5: Aerodynamic Loads equivalent for the Finite Element Model - Load Rudder Va

Main spar at 30% of chord	Rib1	Rib2	Rib3	Rib4	Rib5
VZ1 CS V Left	-19.646	-124.122	-276.68	-265.156	-103.396
VZ1 CS H Left	-2.182886	-13.79132	-30.74223	-29.46178	-11.48843
VZ2 CS V Left	2.182886	13.79132	30.74223	29.46178	11.48843
VZ1 CS V Right	64.71259	228.3145	250.6939	117.1342	21.35834
VZ1 CS H Right	-9.32476	-32.10225	-40.11983	-16.36898	-1.894374
VZ2 CS V Right	-7.19029	-25.3683	-27.8549	-13.0149	-2.37315

Appendix E

Classical Optimization cases- LARC05 Failure Criteria

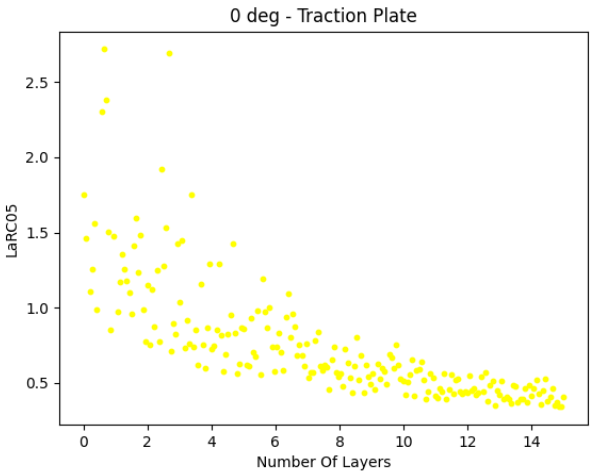

Figure E.1: LARC05 Failure Criteria- Plate in Traction for 0 degrees

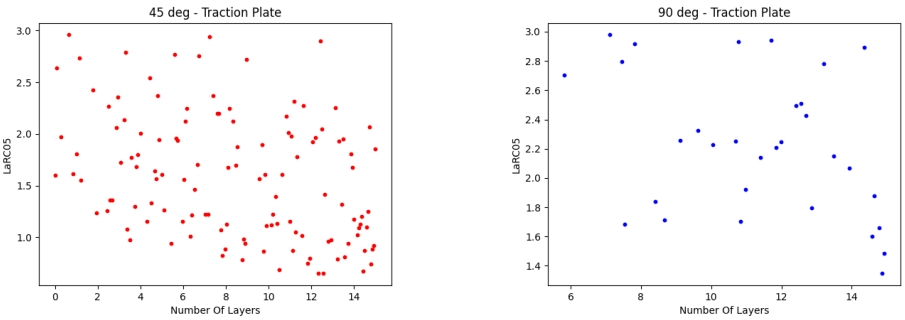

a) 45 degrees b) 90 degrees

Figure E.2: LARC05 Failure Criteria- Plate in traction

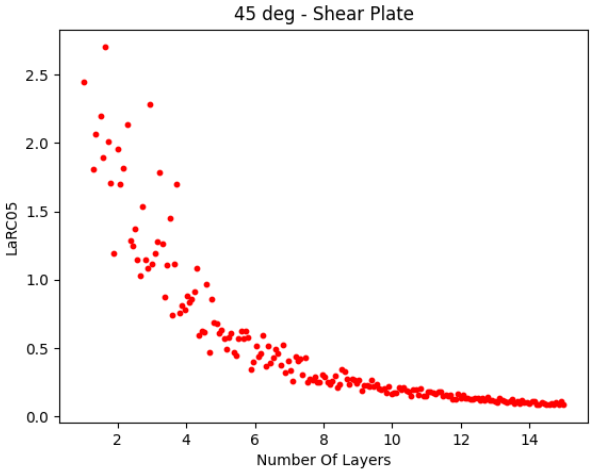

Figure E.3: LARC05 Failure Criteria- Plate in shear for 45 degrees

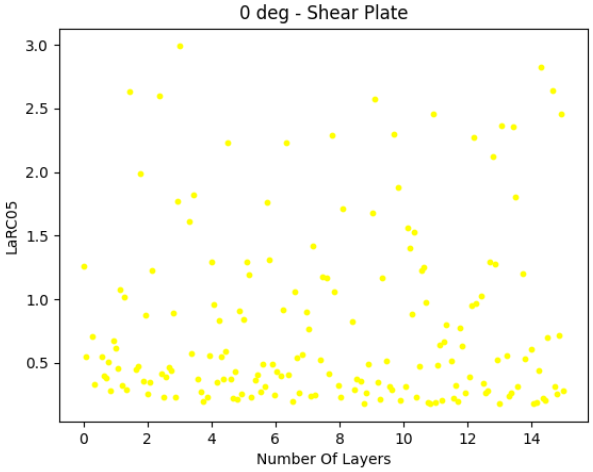

a) 0 degrees

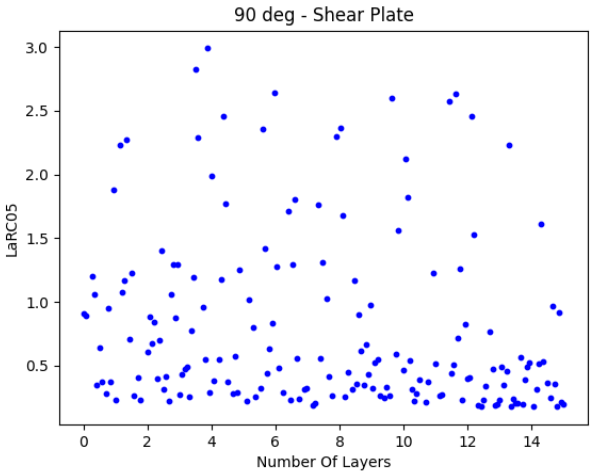

b) 90 degrees

Figure E.4: LARC05 Failure Criteria- Plate in shear

Appendix F

Skin Boom Optimization case - Hashin Failure Criteria

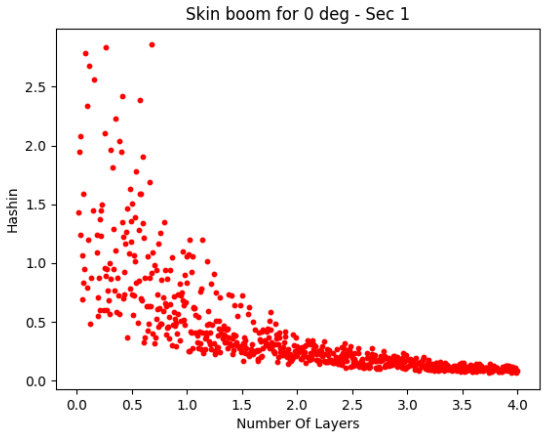

Figure F.1: Hashin Failure Criteria- skin boom section1 for 0 degrees

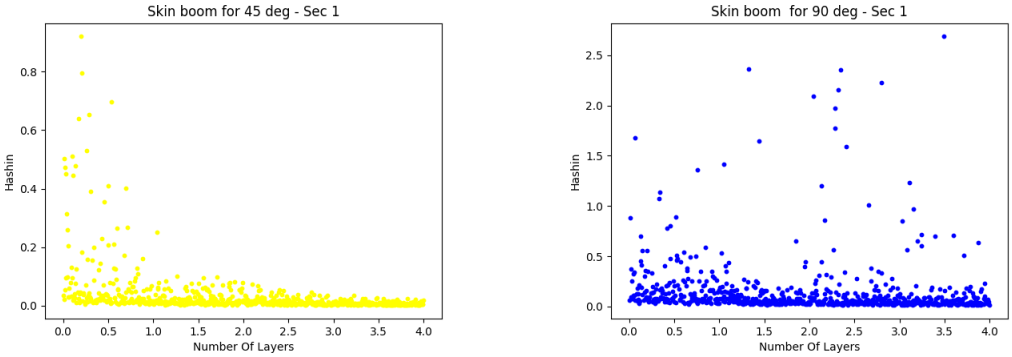

a) 45 degrees b) 90 degrees

Figure F.2: Hashin Failure Criteria- skin boom section1

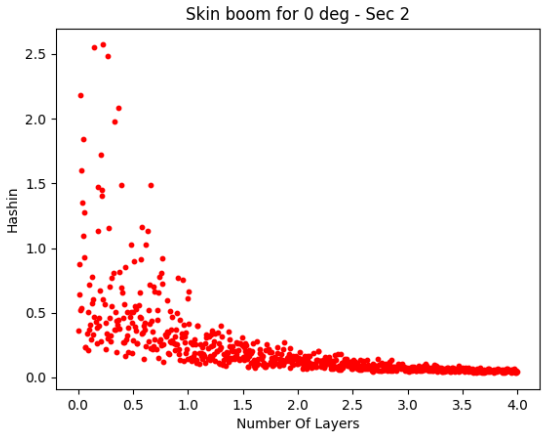

Figure F.3: Hashin Failure Criteria- skin boom section2 for 0 degrees

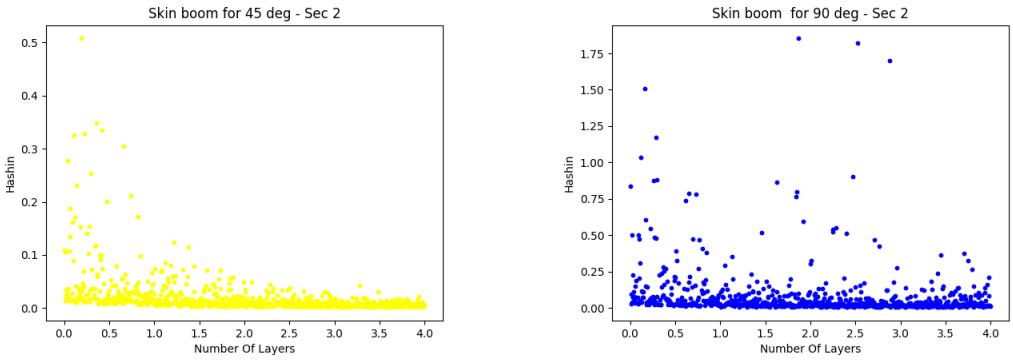

a) 45 degrees b) 90 degrees

Figure F.4: Hashin Failure Criteria- skin boom section2